(NASA-CR-165196) NUMERICAL COMPUTATIONS OF SWIRLING RECIRCULATING FLOW Final Report (Airesearch Mfg. Co., Phoenix, Ariz.) 167 p HC A08/MF A01 CSCL 20D

N81-14267

Unclas G3/34 29643

NASA CR- 165196
AIRESEARCH 21-3517

NASA

NUMERICAL COMPUTATIONS OF SWIRLING RECIRCULATING FLOW FINAL REPORT

by

R. SRINIVASAN
H.C. MONGIA

AIRESEARCH MANUFACTURING COMPANY OF ARIZONA
A DIVISION OF THE GARRETT CORPORATION

SEPTEMBER 1980

Prepared for

National Aeronautics and Space Administration
NASA-Lewis Research Center

Contract NAS3-21254

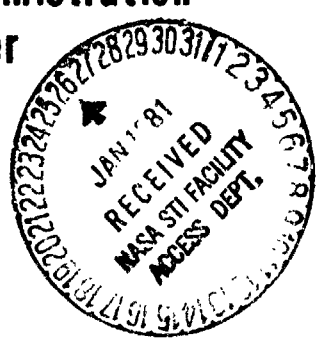

1 Report No.	2. Government Accession No.	3. Recipient's Catalog No.

4. Title and Subtitle	5. Report Date
Numerical Computations of Swirling Recirculating Flow Final Report	September 1980
	6. Performing Organization Code
7. Author(s) R. Srinivasan H. C. Mongia	8. Performing Organization Report No. AiResearch 21-3517
	10. Work Unit No.
9 Performing Organization Name and Address AiResearch Manufacturing Company of Arizona A Division of the Garrett Corporation Phoenix, Arizona 85010	11. Contract or Grant No. NAS3-21254
	13. Type of Report and Period Covered Project Completion Report
12 Sponsoring Agency Name and Address National Aeronautics and Space Administration Washington, D.C. 20546	14. Sponsoring Agency Code

15. Supplementary Notes

Project Manager: Dr. C. J. Marek,
NASA-Lewis Research Center,
Cleveland, Ohio

16. Abstract

Numerical computations are made for swirling, recirculating, nonreacting flows using the AiResearch 2-D elliptic program. This computational program consisted of three tasks. The computations in Task I and II were made using an independent analysis for the two coaxial swirling flows. In Task II, computations were made using the measured profiles of the mixing region. In Task III, a modified 2-D elliptic program was employed to include the effects of interaction between the inner and outer streams.

17. Key Words (Suggested by Author(s))	18. Distribution Statement
Recirculation Flow-Analysis Final-Report	

19 Security Classif (of this report)	20. Security Classif. (of this page)	21. No. of Pages	22. Price*
Unclassified	Unclassified	169	

* For sale by the National Technical Information Service, Springfield, Virginia 22161

NASA-C-168 (Rev 10-75)

TABLE OF CONTENTS

LIST OF ILLUSTRATIONS

LIST OF ILLUSTRATIONS (CONTD)

LIST OF ILLUSTRATIONS (CONTD)

LIST OF ILLUSTRATIONS (CONTD)

LIST OF TABLES

SUMMARY

Numerical computations are made for swirling, recirculating, nonreacting flows using the AiResearch two-dimensional (2-D) elliptic program. The predicted results are compared with experimental data taken by Vu and Gouldin (ref. 26). The geometry of the experimental apparatus consists of a central 1.465-inch (3.72-cm) diameter swirling jet mixing into a coaxial co- or counterswirling flow with 5.75-inch (14.6-cm) outer diameter.

The computational program consists of three tasks. In Task I, only the geometry of the test apparatus and the mass flow rates and vane angles were specified. The predictions in this task were obtained using estimated inlet profiles determined from vane angle and mass flow rates. These predictions did not show any flow reversal for both co- and counterswirling cases. The experimental data showed a flow reversal for the counterflow case. In Task II, the measured velocity profiles at the center stream exit plane were used as boundary conditions. Predictions were obtained using the original K-ϵ turbulence model and a modified K-ϵ model. The original K-ϵ model results did not show any flow reversal for co-swirl as well as counterswirl cases, while the modified K-ϵ model predicted an elongated recirculation bubble.

In Task III, the 2-D elliptic program was further modified to simulate the center jet and the coaxial outer swirling streams more accurately, and predictions were obtained for co- and counterswirling cases. The Task III velocity profile predictions agreed with the data within about 10 percent of the average flow velocity in the counterswirl case. The predictions for the co-swirl case showed a recirculation region, while the test data did not show any flow reversal.

This program was conducted by AiResearch Manufacturing Company of Arizona under contract NAS3-21254 with the NASA-Lewis Research Center. The NASA Program Manager was Dr. C. J. Marek.

INTRODUCTION

Background

Swirler stabilized combustion systems have become a common feature in turbo-propulsion systems. Design procedures for such combustors have, in the past, depended upon empirical data (refs. 1-5) and experimental correlations based on past development experience. These approaches have been quite useful for preliminary design predictions entailing iterative series of development tests. Due to the increasing demands for improvements in the combustor performance, there has been a recognized need for a better understanding of complex combustor flows. Although several models have been developed for analyzing swirling flows (refs. 6-11), physical and mathematical modeling difficulties still exist.

The axial velocity, u, for swirling flows in long ducts assumes a fully developed distribution at large downstream distances, and the swirl velocity asymptotically decays to zero. If the swirl number is sufficiently large, stagnation regions and flow reversal may exist in the entrance region. This phenomenon, known as vortex breakdown, helps to stabilize flames in combustion chambers. A review article on vortex bursting has been written by Hall (ref. 12) and later by Leibovich (ref. 13).

The effect of streamline curvature on turbulent flow was studied by Wattendorf (ref. 14) by using a curved channel of constant cross section. He observed that for fully developed curved internal flows, the turbulent viscosity was less than that for a straight flow near the inner wall and greater near the outer wall. This observation was in accordance with the stability criteria suggested by Rayleigh (ref. 15). The dependence of turbulence structure on the shape of angular momentum profile was

demonstrated by Eskinazi and Yeh (ref. 16) and later by Margolis and Lumley (ref. 17). These analyses were concerned with flows in curved channels. Bradshaw (ref. 18) later generalized the streamline curvature effects to include the influence of swirl on turbulence. He used the Richardson numbers to account for the effects of streamline curvature on turbulence.

Despite these theoretical studies, there are very few successful turbulence models that are sufficiently general and account for the effects of streamline curvature. Most of the existing turbulence models (ref. 13) generally assume that the turbulent exchange coefficients are isotropic. Recent experimental works have disputed this assumption for swirling flows. Although more complex Reynolds stress models are being developed (refs. 20,21) to overcome these difficulties, none of these models has shown significant improvement over the K-ϵ two-equation model. The K-ϵ model is perhaps the most proven among the existing turbulence models.

The mathematical approaches employed to analyze swirl flows have evolved from 2-D parabolic to 3-D elliptic procedures. Owen (ref. 22) applied the original Patankar and Spalding (ref. 23) finite-difference method to predict the turbulent swirling boundary layer on a plane rotor disc system. For swirling and recirculating flows, 2-D elliptic codes have been developed. Mongia and Reynolds (ref. 24) have used a variant of the numerical scheme described by Patankar (ref. 25) to analyze practical gas turbine combustors. However, these models give, at best, qualitative predictions.

Although swirler-stabilized combustion systems are widely prevalent, most of the current design methods are based upon empirical correlations. A major reason for this is due to insufficient understanding of swirler-stabilized combustion

systems in view of measurement complexities and a lack of analytical validation. The program presented herein is an attempt towards validating and refining an existing analytical model.

Objectives

The objective of this program was to obtain predictions of swirling, recirculating, nonreacting turbulent flows from existing AiResearch computer codes and compare the results with experimental measurements (ref. 26). Predictions are presented for both co-swirling and counterswirling conditions.

The approach used in this program can be categorized under three tasks.

Task I - Computations with given geometry

Task II - Computations with given measured inlet profiles

Task III - Computations with a more accurate simulation of the geometry of the flow assembly

Each of these tasks involved a series of computations and comparison of the predictions with the experimental data.

In Task I, only the geometry of the mixing region was specified. The inlet profiles for this region were estimated from the mass flow rates and the swirler vane angles. The flow field in the mixing region was predicted using the estimated inlet profiles. In Task II, the measured velocity profiles near the exit plane of the inner jet were specified in addition to the geometry of the mixing region. In Task III computations, the 2-D

elliptic program was modified to simulate the geometry of the whole flow assembly more accurately. The inlet profiles for the inner jet and the outer stream in this task were estimated based upon the mass flow rates and the vane angles.

DESCRIPTION OF EXPERIMENTAL TEST GEOMETRY AND THE ANALYTICAL MODEL

This section discusses the overall physical and numerical approach adopted for predicting swirling recirculating flow. A brief description of the experimental test geometry and computer program used in this program is described in the following paragraphs.

Description of the Flow Assembly Configuration

A sketch of the flow assembly used by Vu and Gouldin (ref. 26) is shown in Figure 1. The assembly has two main segments: (1) the inner flow passage and (2) the outer flow channel. The inner passage is a circular tube with 1.465-inch (3.72-cm) inner diameter and 1.5-inch (3.8-cm) outer diameter. A sketch of the inner flow passage is shown in Figure 2. The inner tube has a swirl generator located 4.7-inches (11.9-cm) upstream of the discharge end of the tube The swirl generator, as shown in Figure 3, consists of 12 equally spaced vanes with a 68.5-degree swirl angle and a vane thickness of 0.02 inch (0.5 cm).

The outer channel (Figure 4) is a 30-inch diameter (76-cm) radial inflow passage with adjustable vane swirlers. The outer passage has 24 swirler vanes located near the entrance of the channel. The vanes in the outer channel are adjustable to produce any desired swirl direction and velocity. The outer flow has a turning channel which turns the flow from the radial direction at the inlet to the axial direction at the exit of the annular passage. At the exit plane, the outer flow enters through a 5.75-inch (14.6-cm) diameter pipe where the mixing between the two swirling streams takes place.

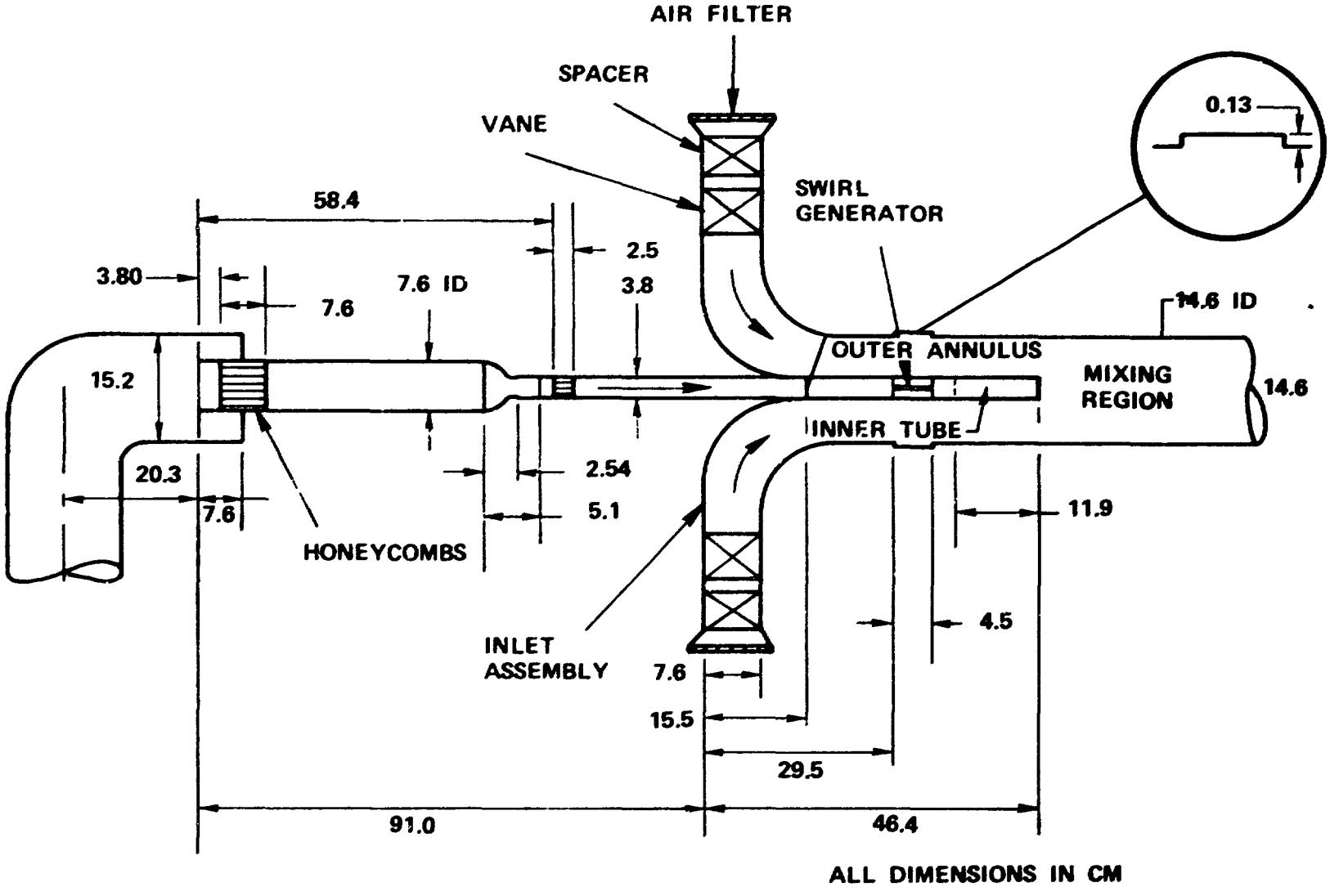

Figure 1. Flow Assembly.

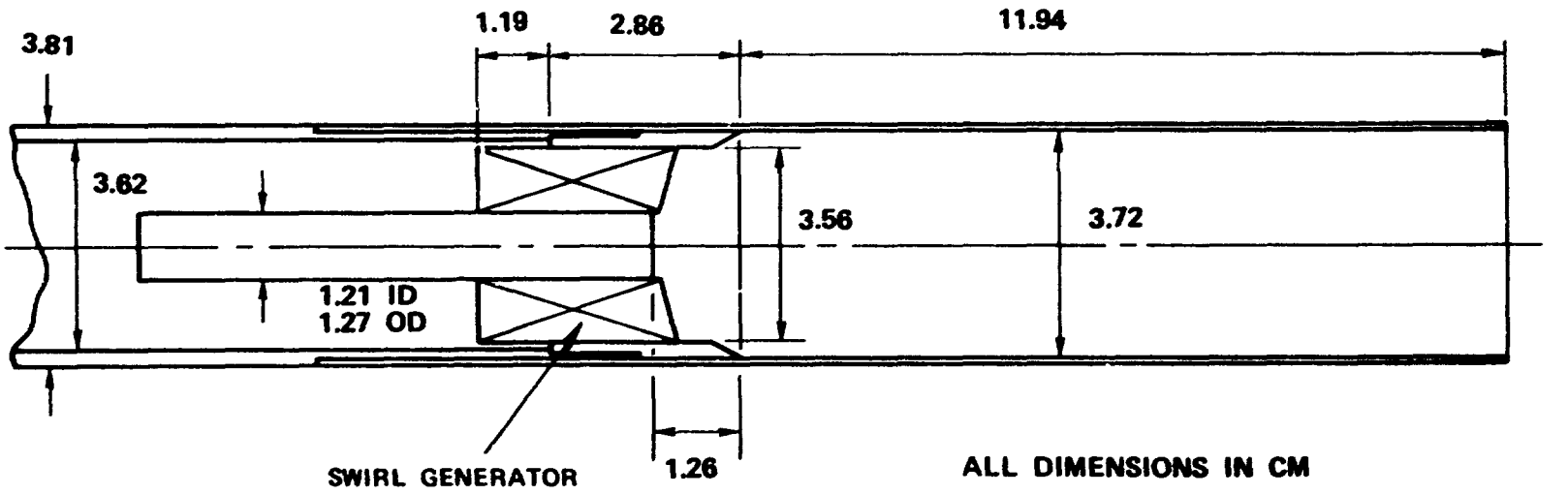

Figure 2. Inner Tube and Swirl Generator.

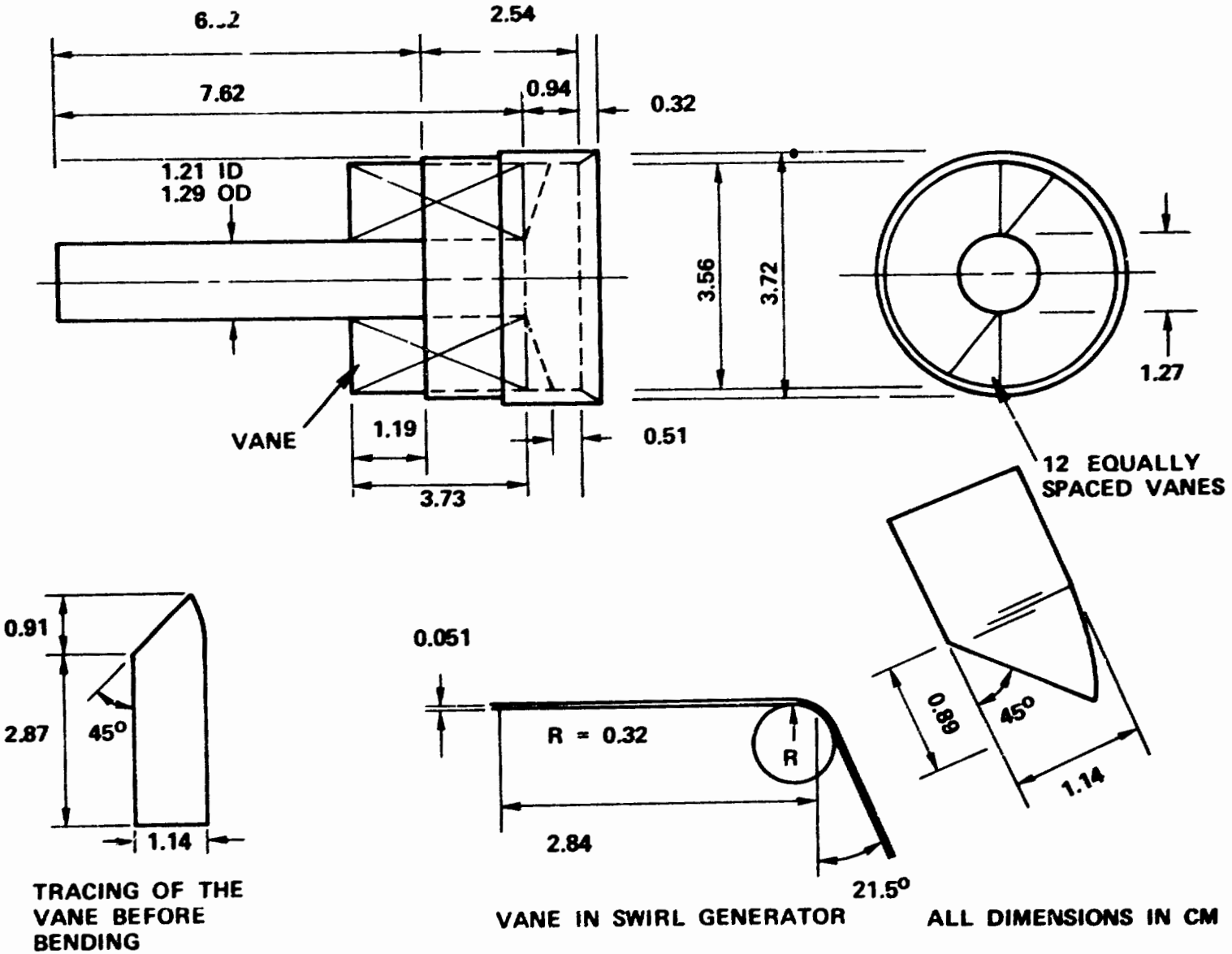

Figure 3. Swirl Generator for Inner Flow.

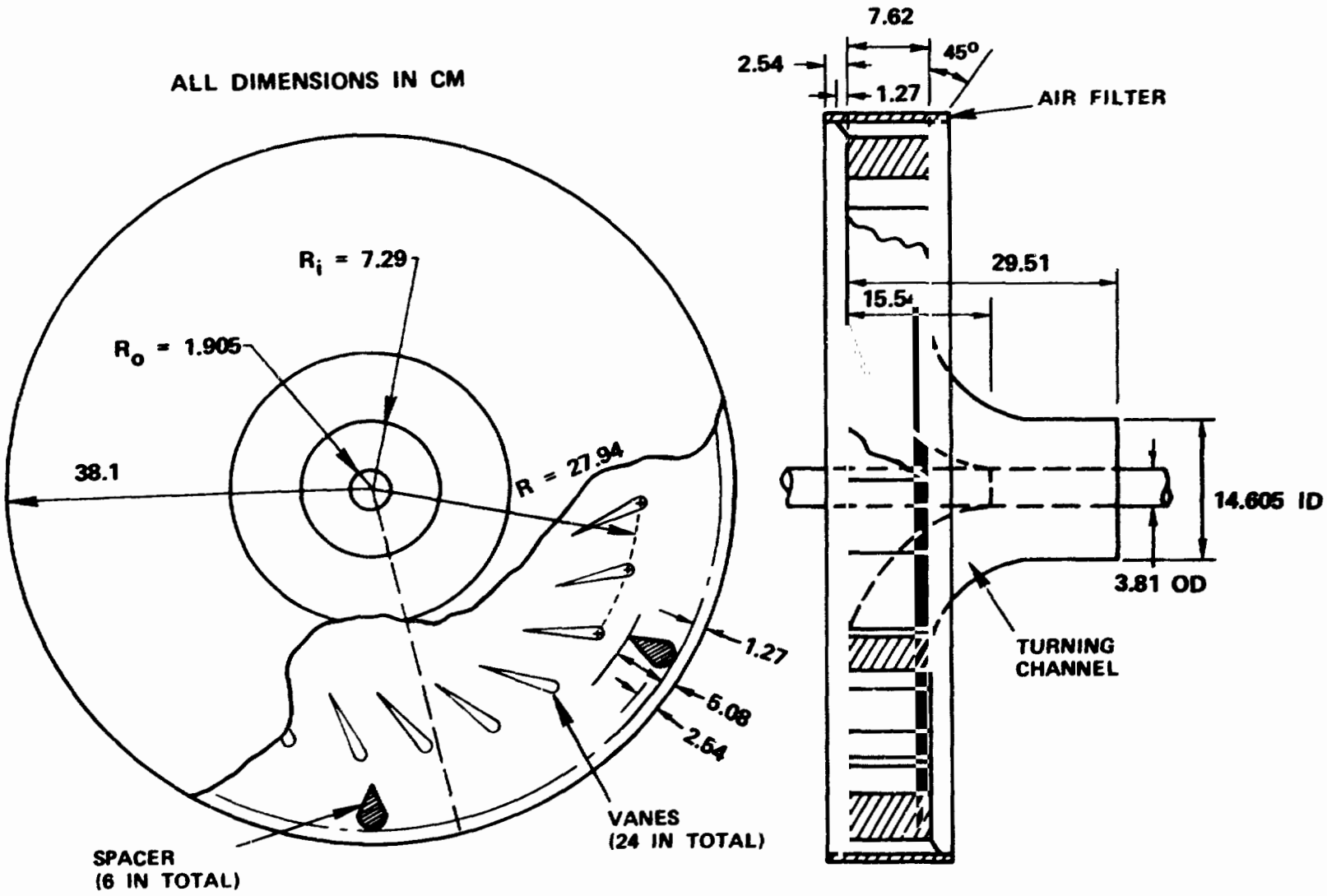

Figure 4. Outer Flow Passage.

Description of the Computer Program

The AiResearch 2-D elliptic (recirculation) flow program was used for predicting the internal swirling flow fields of the geometry as specified in the paragraph titled Description of the Flow Assembly Configuration. This program computes the following variables in the region of interest:

- Axial-, radial-, and swirl-velocity components
- Pressure correction
- Turbulence kinetic energy and its dissipation rate (alternately, the length scale of turbulence).

A brief description of the transport equation, formulation of the relevent difference equations, boundary conditions, and the solution procedure are given in the following paragraphs.

Governing Equations

The time-averaged transport equations for mass conservation, axial velocity (u), radial velocity (v), tangential velocity (v_θ), turbulence kinetic energy (k) and its dissipation rate (ϵ) can be cast in the following generalized variable form:

$$\frac{\partial}{\partial x}(\rho u \phi) + \frac{1}{r}\frac{\partial}{\partial r}(\rho v r \phi) = \frac{\partial}{\partial x}\left(\Gamma_{eff,\phi}\frac{\partial \phi}{\partial x}\right) + \frac{1}{r}\frac{\partial}{\partial r}\left(\Gamma_{eff,\phi}\, r\, \frac{\partial \phi}{\partial r}\right) + S_\phi \qquad (1)$$

Here ρ, $\Gamma_{eff,\phi}$ and S_ϕ denote the fluid density, the local effective exchange coefficient of variable ϕ, sources/sinks, and the terms that do not fall under convection and diffusion terms.

The source terms for the dependent variables are:

- u - velocity component

$$S_u = \frac{\partial}{\partial x}\left(\mu_{eff}\frac{\partial u}{\partial x}\right) + \frac{1}{r}\frac{\partial}{\partial r}\left(\mu_{eff}\, r\,\frac{\partial v}{\partial x}\right) - \frac{\partial p}{\partial x} \qquad (2)$$

- v - velocity component

$$S_v = \frac{\partial}{\partial x}\left(\mu_{eff}\frac{\partial u}{\partial r}\right) + \frac{1}{r}\frac{\partial}{\partial r}\left(\mu_{eff}\, r\,\frac{\partial v}{\partial r}\right) - 2\mu_{eff}\frac{v}{r^2} + \frac{\rho v_\theta^{\,2}}{r} - \frac{\partial p}{\partial r} \qquad (3)$$

- v_θ - velocity component

$$S_{v_\theta} = -\left[\frac{\mu_{eff}}{r^2} + \frac{\rho v}{r} + \frac{1}{r}\frac{\partial}{\partial r}\left(\mu_{eff}\right)\right] v_\theta \qquad (4)$$

- Kinetic energy of turbulence

$$S_k = G_k - \rho\epsilon \qquad (5)$$

where:

$$G_k = \mu_{eff}\left\{2\left[\left(\frac{\partial u}{\partial x}\right)^2 + \left(\frac{\partial v}{\partial r}\right)^2 + \left(\frac{v}{r}\right)^2\right] + \left(\frac{\partial v_\theta}{\partial x}\right)^2 + \left[r\,\frac{\partial}{\partial r}\left(\frac{v_\theta}{r}\right)\right]^2 + \left(\frac{\partial u}{\partial r} + \frac{\partial v}{\partial x}\right)^2\right\} \qquad (6)$$

- Dissipation rate of k

$$S_\epsilon = \frac{\epsilon}{k}\left(C_1 G_k - C_2\,\rho\epsilon\right) \qquad (7)$$

The effective viscosity is obtained from the relation:

$$\mu_{eff} = \mu + \mu_t \tag{8}$$

where μ and μ_t are the molecular and turbulent viscosities, respectively. μ_t is related to k and via

$$\mu_t = C_D \rho k^2/\epsilon \tag{9}$$

The exchange coefficients are defined as:

$$\Gamma_{eff,\phi} = \mu_{eff}/\sigma_{eff,\phi} \tag{10}$$

Recommended values[25] for the stants appearing in the above equations are:

$C_D = 0.09$
$C_1 = 1.44$
$C_2 = 1.92$
$\sigma_{eff,k} = 0.9$

$\sigma_{eff,\epsilon}$ is calculated from

$$\sigma_{eff,\epsilon} = \frac{\kappa^2}{(C_2-C_1)\ C_D^{1/2}} \tag{11}$$

where κ is the von Karman constant taken to be equal to 0.41.

Finite-Difference Solution of the Equations

The numerical solution of the above nonlinear, coupled, partial differential equations are obtained by using a finite-difference method described in reference 25. The finite-difference equations are derived for a box-shaped flow domain.

Over the region of interest, a number of grid planes, parallel to the two coordinates, are placed. For each grid node, the finite-difference equations are set up for each of the flow variables to be solved. Since the governing equations for axial- and radial-velocities (eq. 1) contain pressure gradient terms, these two variables are solved along planes staggered with respect to the main grid planes described above.

A typical grid node spacing for the swirling flow problem is shown in Figure 5. A total of 30 x 25 nonuniformly spaced nodes are shown here although the maximum number of nodes the program can handle is 50 x 25 with 148,000 octal words of computer memory required.

Finite-difference equations for a node are obtained by integrating the differential equations over a control volume enclosing a grid node. For evaluating the convection and diffusion fluxes through a control volume face, a linear variation (in the direction normal to the face) of the flow properties is assumed. For other purposes, a stepwise variation with discontinuities at control-volume boundaries is assumed. Net rate of flow of ϕ into the control volume around a node P (Figure 5) by convection and diffusion in the x-direction is

$$[T_{X-} + (1 - f_{X-})\ L_{X-}]\ \phi_{X-} + [T_{X+} - f_{X+}\ L_{X+}]\ \phi_{X+}$$

$$- [T_{X-} - f_{X-}\ L_{X-} + T_{X+} + (1 - f_{X+})\ L_{X+}]\ \phi_P \qquad (12)$$

where

$$T_X = \Gamma_{eff,\phi}\ A_X/\delta_X$$

$$L_X = \dot{m}_X''/\delta_X$$

$$A_X = 0.5\ (r_+ + r_-)\ \Delta Y$$

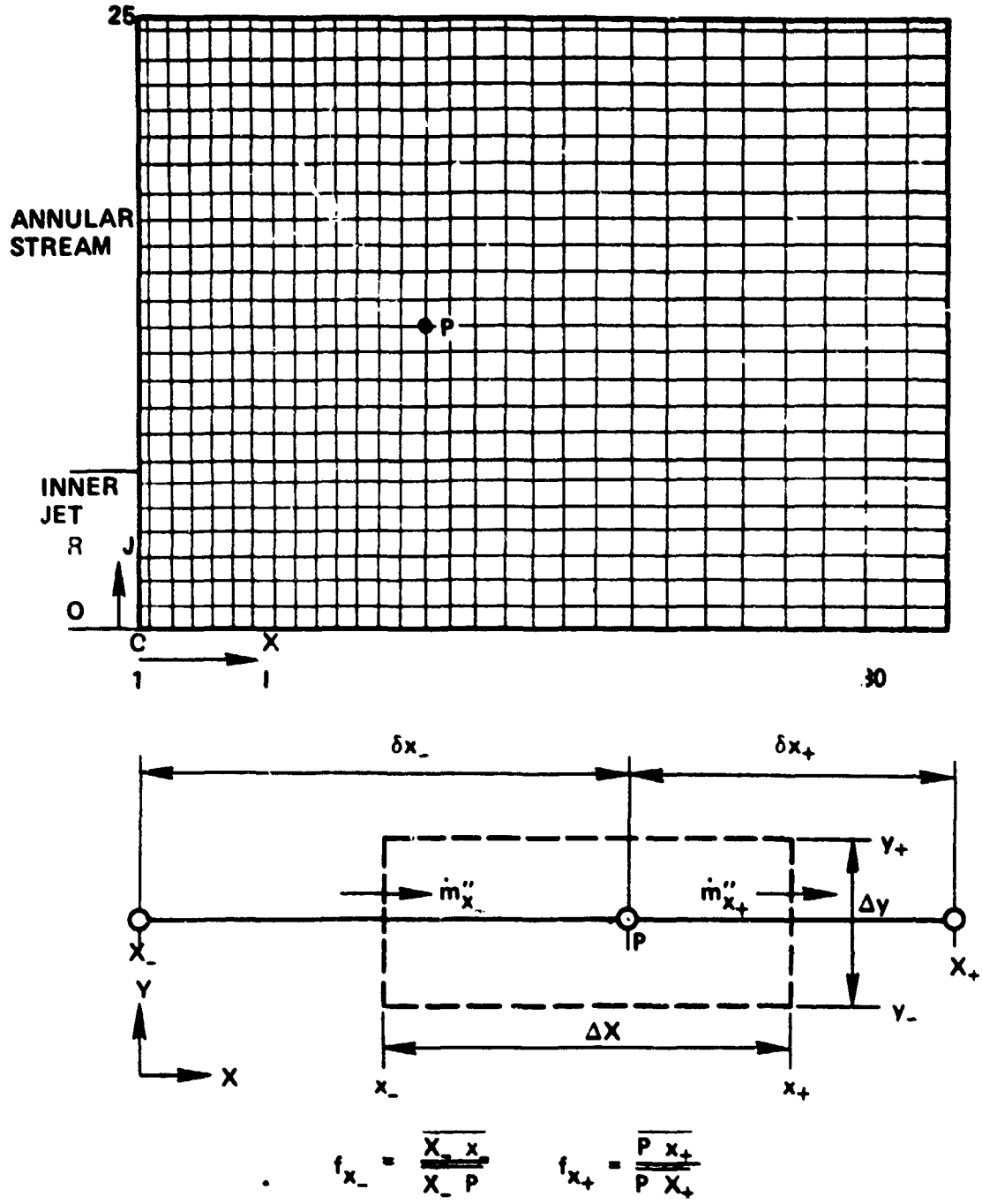

Figure 5. Typical Grid Spacing of the Swirling Flow Problem and Control Value Around a Point P.

Defining $\iiint S_\phi dV = S_u + S_p\phi_p$, the one-dimensional transport equation for the variable ϕ becomes

$$[T_{X-} + (1 - f_{X-})\ L_{X-} + T_{X+} - f_{X+}\ L_{X+} - S_p]\ \phi_p$$

$$= [T_{X-} + (1 - f_{X-})\ L_{X-}]\ \phi_{X-} + [T_{X+} - f_{X+}\ L_{X+}]\ \phi_{X+} + S_u \qquad (13)$$

The linear-profile assumption becomes unacceptable when $f_{X+}\ L_{X+}$ is large compared with T_{X+} because the weighting factor $(T_{X+} - f_{X+}\ L_{X+})$ then becomes negative, implying an unrealistic physical process through which raising the value of ϕ_{X+} could lower the value of ϕ_p. Therefore, it is assumed that if the convective flow rates (L) are large compared to the diffusion coefficients (T), the diffusion across the control-volume face is zero and the value of ϕ convected is equal to the value at the node on the upwind side of the face. With this assumption, the coefficient $T_{X+} - f_{X+}\ L_{X+}$ is replaced by $T^*_{X+} - f_{X+}\ L_{X+}$ where

$$T^*_{X+} = [T_{X+}, - (1 - f_{X+})\ L_{X+}, f_{X+}\ L_{X+}]$$

Here $[a_1, a_2, a_3]$ stands for the largest of the three quantities a_1, a_2, and a_3.

Using a similar procedure for the fluxes in the radial direction, the final finite-difference equation is reduced to

$$A_p\phi_p = A_{X+}\phi_{X+} + A_{X-}\phi_{X-} + A_{Y+}\phi_{Y+} + A_{Y-}\phi_{Y-} + S_u \qquad (14)$$

The solution of the above equation is obtained by line-by-line relaxation using an efficient tri-diagonal matrix algorithm. By this method, a traverse along one direction, for example, the X-direction, is made with old values for the y-direction nodes.

Using this solution as the best estimate, the y-direction is then traversed. The solution method adopted is based on the SIMPLE (Semi-Implicit Method for Pressure Linked Equations) algorithm of Patankar and Spalding as described in reference 25.

Boundary Conditions

The boundary conditions are enforced by appropriately modifying the finite-difference coefficients at the first interior point adjacent to the boundary. For the inlet boundaries, the velocity components, density, and the turbulence profiles are either experimentally known or estimated. At the inlet boundary, if pressure is specified, the pressure correction is set to zero. When the normal velocities at the boundary point are specified, the coefficients in the pressure correction are modified in such a way that the mass fluxes through the control volume satisfy the overall continuity equation.

For boundaries of the second kind, where gradients and not the values of the variables are specified, the program uses one of the following two approaches. In the first approach, the boundary value is guessed and continually updated so as to satisfy the given gradient condition. The second approach breaks the link through the boundary to all adjoining external control volumes by first arranging for the finite-difference coefficient connecting the boundary node to an internal node to be zero, and then inserting the correct flux at the boundary as a source of diffusion and/or convection for that internal node.

At the symmetry plane, the convection and diffusion fluxes in the radial direction are zero. Therefore, the finite-difference coefficients containing these fluxes are set to zero at the axis of symmetry. For the exit plane, information about some of the variables is not available. However, since it is the

process occurring in the calculation domain that decides values of the variables which the outgoing fluid will carry, there is no need for information at such boundaries. These boundaries are simply treated by neglecting the diffusion at the exit boundary.

The near-wall region is given a special treatment in the program. Since the expression for Γ_{eff} is accurate for turbulent flows only, a means is provided for the inclusion of the correct shear stresses and other fluxes at the wall. Therefore, the nodes next to the wall are assigned the following values as per an empirical wall law:

$$y^+ \leq 11.5 \qquad \Gamma_{\phi,wall} = \frac{\mu}{\sigma_\phi}$$

$$y^+ > 11.5 \qquad \Gamma_{\phi,\,wall} = \frac{\mu}{\sigma_\phi} \quad \frac{y^+}{\frac{1}{\kappa} \ln (9y^+) + P_\phi}$$

$$y^+ = \rho k^{1/2} C_D^{1/4} \frac{\delta}{\mu}$$

$$P_\phi = 9.0 \left(\frac{\sigma}{\sigma_{eff}} - 1\right) \left(\frac{\sigma}{\sigma_{eff}}\right)^{-1/4}$$

where δ is the normal distance of the wall from the first interior adjacent node. The kinetic energy of turbulence has small diffusion near the wall; hence, Γ_{wall} for k is set equal to zero. Instead of computing Γ_{wall} for ϵ, it is calculated for the near-wall node by assuming a linear variation of the length scale giving the following expression:

$$\epsilon = C_D^{3/4} k^{3/2} / (\kappa \delta)$$

ANALYSIS AND DISCUSSION

The geometry of the flow assembly was discussed previously in the paragraph titled Description of the Flow Assembly Configuration and is shown schematically in Figure 1. The flow assembly consists of three segments; namely, (1) inner tube, (2) outer channel, and (3) mixing region. Due to the complex nature of the flow assembly, a modular analytical approach was taken for Task I computations. In this approach, the two streams in the inner tube and the outer channel were separately analyzed up to the start of the mixing region so as to estimate the inlet profile for the mixing region. The mixing region was subsequently analyzed using the 2-D elliptic code with the estimated inlet station profiles. Such an approach did not allow upstream influences exerted by the outer stream on the inner tube flow field.

A brief discussion on the convergence criteria adapted in this study is presented in the following paragraphs by illustrating computed radial profiles of axial velocities at different streamwise stations for a straight-tube flow at several values of swirl numbers, SN, defined as

$$SN = \frac{\int_0^R \rho u r^2 V_\theta \, dr}{R \int_0^R \rho u r^2 dr}$$

Figures 6 and 7 represent axial velocity profiles for a 45 degree tip vane swirler with a resultant swirl number of 0.51. The predictions shown are the results after 150 iterations with a cumulative mass error of 0.1 percent. The streamwise distances shown in these figures are measured from the lip of the inner tube. Increasing the tip vane angle to 63.4 degrees (SN = 0.62) introduces a velocity deficit near the centerline as shown in Figures 8 and 9. But the convergence rate was slightly poorer

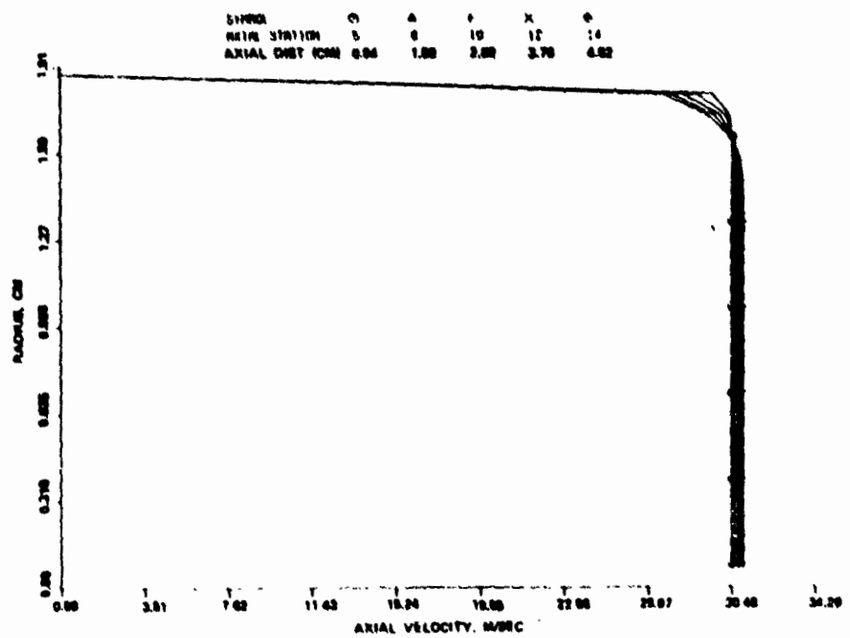

Figure 6. Axial Velocity Profiles for Flow in a Straight Tube with 0.31 Swirl Number.

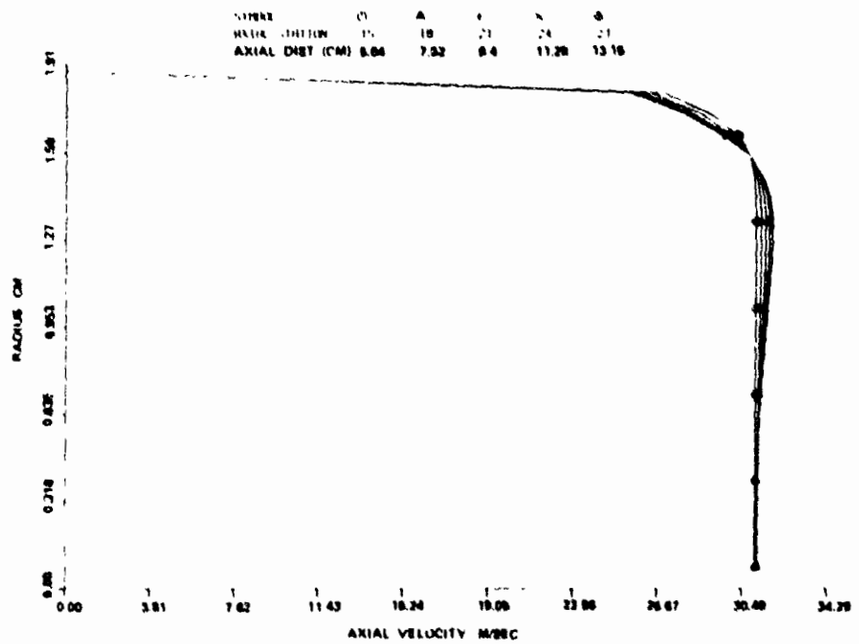

Figure 7. Axial Velocity Profiles for Flow in a Straight Tube with 0.31 Swirl Number.

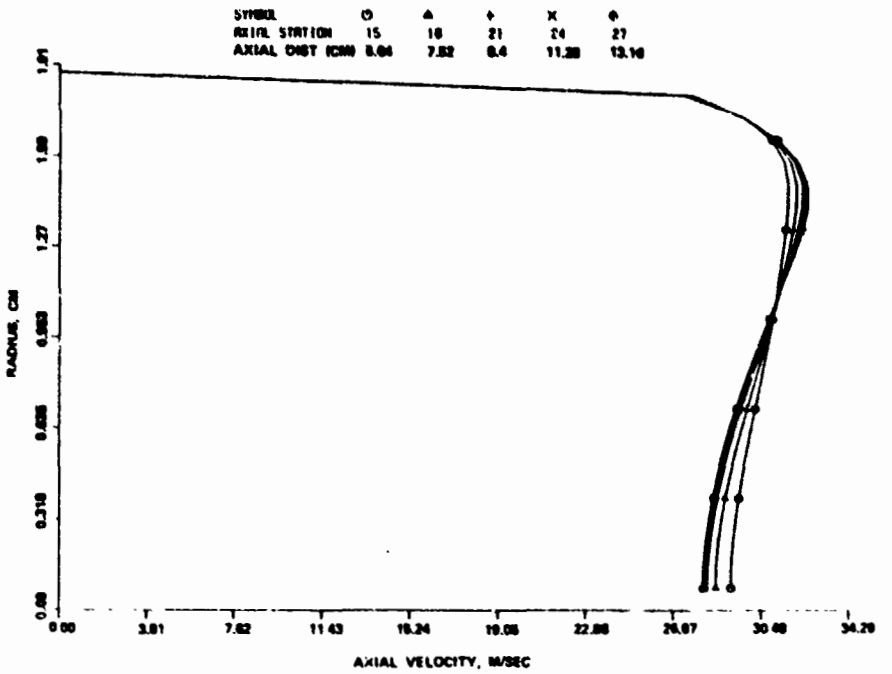

Figure 8. Axial Velocity Profiles for Flow in a Straight Tube with a 0.62 Swirl Number.

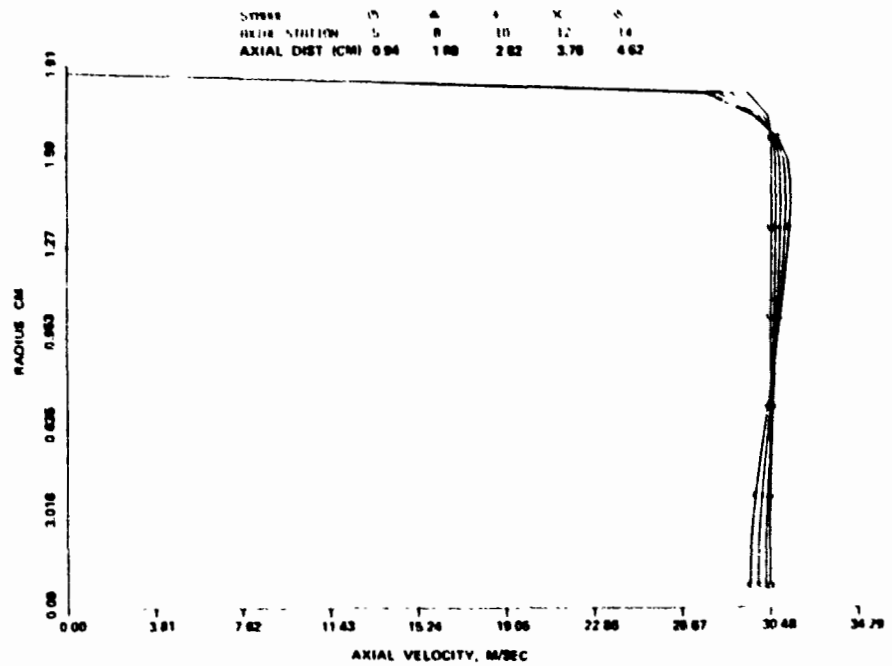

Figure 9. Axial Velocity Profiles for Flow in a Straight Tube with 0.62 Swirl Number.

than that for a swirl number of 0.31. The cumulative mass residual after 150 iterations is 0.25 percent. A further increase in swirler tip vane angle to 83.4 degrees (SN = 3.11) seemed to indicate the presence of a reverse flow region after 150 iterations, as seen in Figures 10 and 11. The mass residual after 150 iterations for this case was 1.92 percent. Continuation of the calculations up to 300 iterations resulted in a mass residual of 1.3 percent and the resulting solutions are shown in Figures 12 and 13. These predictions were considerably different from the results after 150 iterations. The results after 300 iterations indicated no recirculation in the main flow field with the exception of a small region near the exit. There was no discernible change in computed profiles as the computations continued for another 150 iterations. Therefore, in the study, the solution was considered converged if the cumulative mass residual was less than 1 percent and the variation in the field variables at the node of maximum local mass residual was within 0.1 percent.

Task I - Results

The flow conditions for the inner and the outer streams for both co-swirl and counterswirl case are shown in Table I.

TABLE I. FLOW CONDITIONS FOR THE INNER AND THE OUTER STREAMS

	Inner Flow		Outer Flow	
	Axial Velocity, M/S	Swirl No.	Axial Velocity, M/S	Swirl No.
Co-Swirl Case	29.65	0.577	20.3	0.536
Counterswirl Case	30.33	0.49	20.2	-0.507

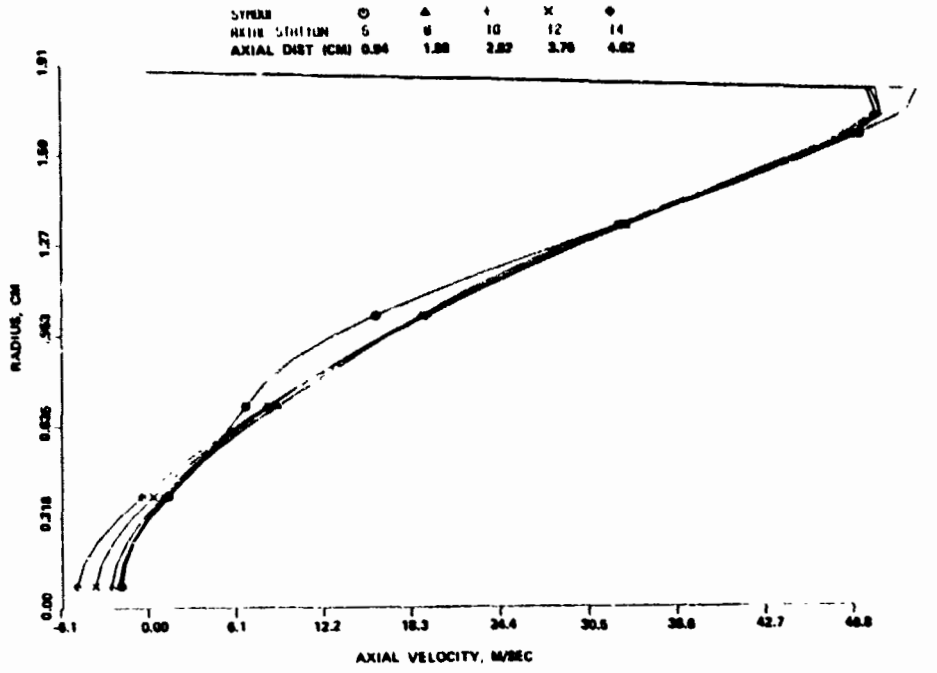

Figure 10. Axial Velocity Profiles for 3.11 Swirl Number Flow in a Straight Tube After 150 Iterations.

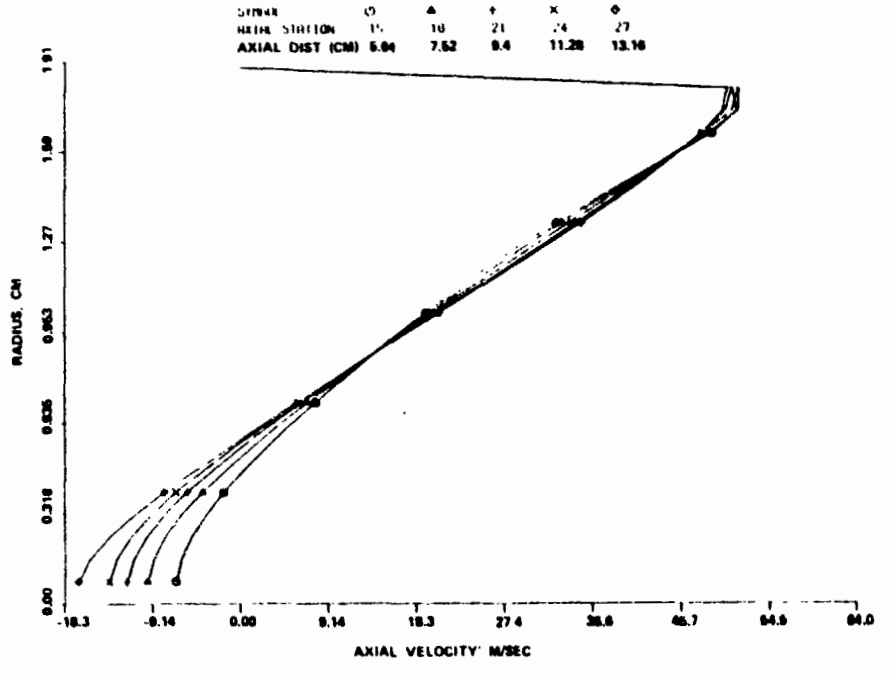

Figure 11. Axial Velocity Profiles for 3.11 Swirl Number Flow in a Straight Tube After 150 Iterations.

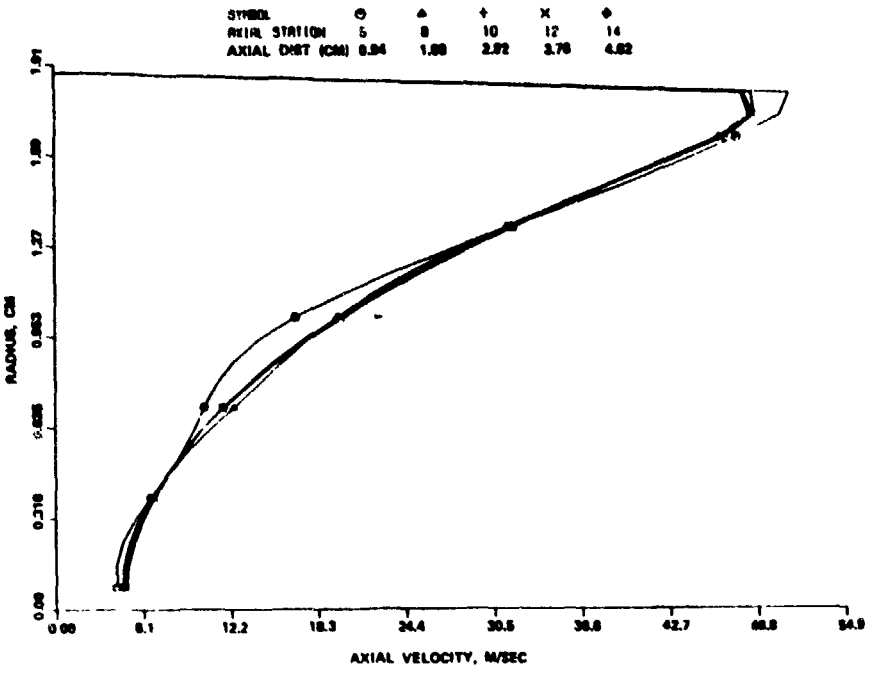

Figure 12. Axial Velocity Profiles for 3.11 Swirl Number Flow in a Straight Tube After 300 Iterations.

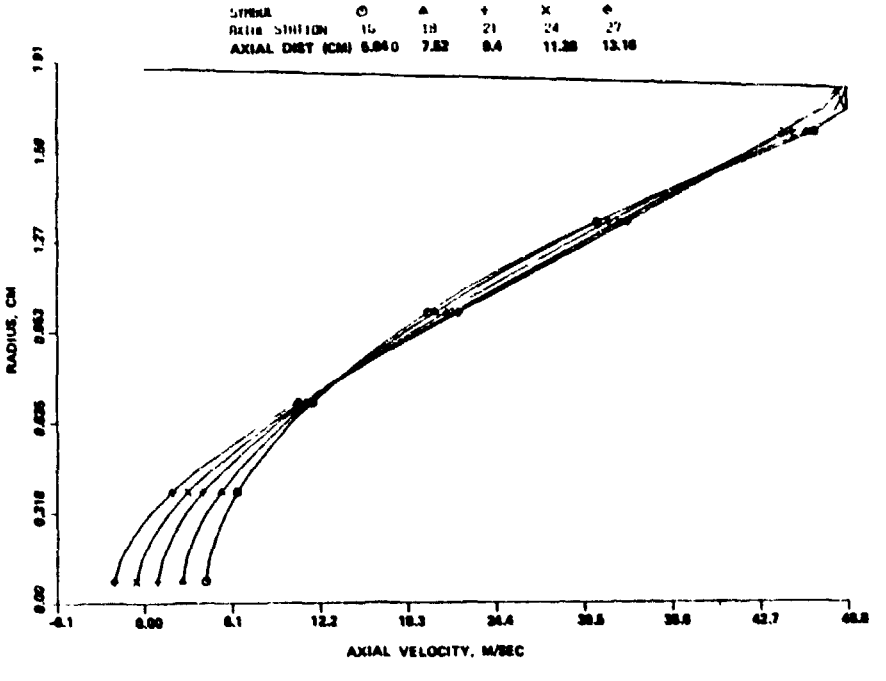

Figure 13. Axial Velocity Profiles for 3.11 Swirl Number Flow in a Straight Tube After 300 Iterations.

In order to estimate radial profiles of axial, radial, and tangential velocity components, turbulence kinetic energy, and length scale at the inlet to the mixing region (Figure 1), separate flow calculations were performed for the inner tube and the outer annulus of the flow assembly. The 2-D elliptic code was used to compute the inner tube flow field corresponding to an inner swirl number of 0.573 for co-swirl case and 0.491 for counterswirl case.

The flow through the radial inflow swirler is very difficult to analyze in view of the large change in curvature of the duct. Major modifications in the 2-D elliptic program would be necessary if elliptic effects were to be included in this analysis. This effort was considered beyond the scope of this program. The alternate procedure employed was to adopt a 2-D parabolic approach for the outer flow. However, because of the flow separation caused by the large curvature of the channel, the 2-D parabolic approach could not be used up to the mixing region inlet. An AiResearch Compressor Aerodynamic Performance Simulation (CAPS) program was, therefore, used to predict the flow field in the outer channel. This program solves the potential flow equations with appropriate near-wall modifications to correct for boundary layer effects. In order to define turbulence kinetic energy and dissipation for the outer stream at the mixing region inlet, a fully developed pipe flow approximation was invoked.

Figures 14 and 15 represent the comparison between predicted and measured axial velocity profiles at different axial stations for co-swirling and counterswirling conditions, respectively. The corresponding results for the tangential velocity profiles are shown in Figures 16 and 17.

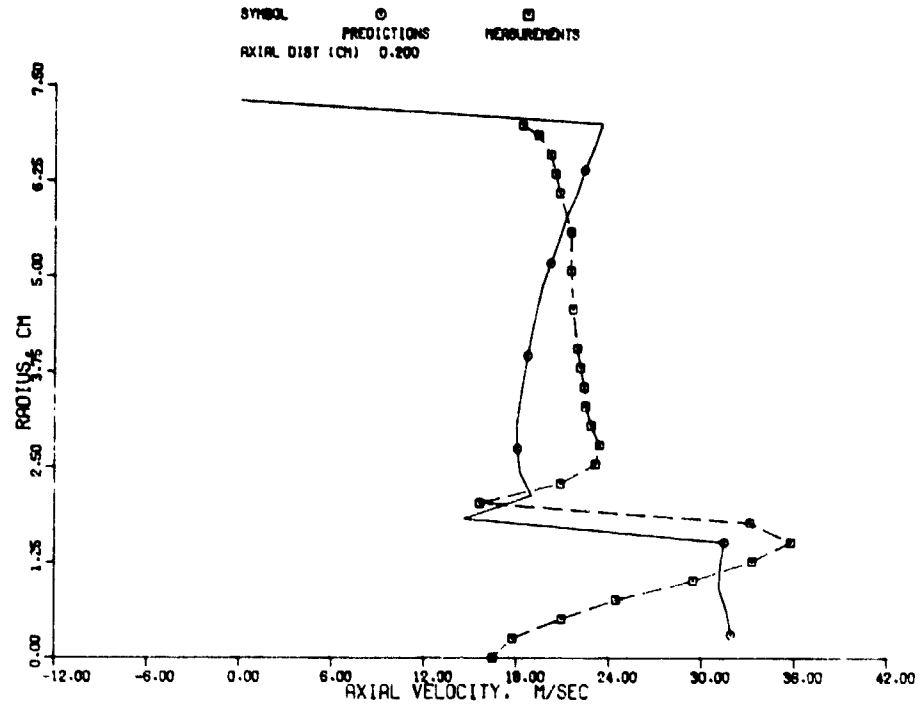

(a)

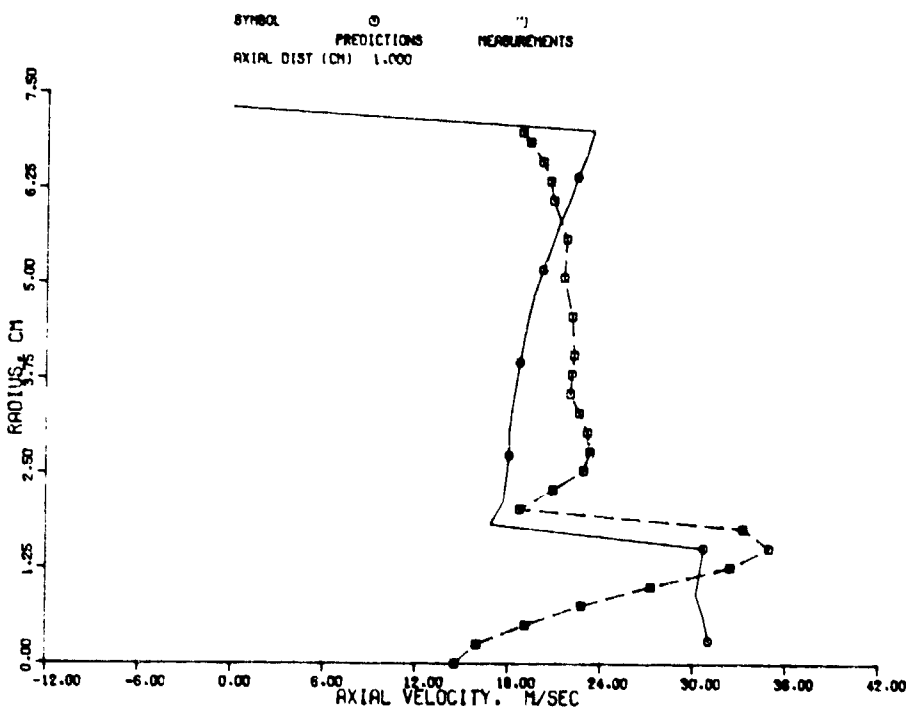

(b)

Figure 14. Axial Velocity Profiles for Co-Swirl Case with Predicted Inlet Profiles: Original K-ϵ Model.

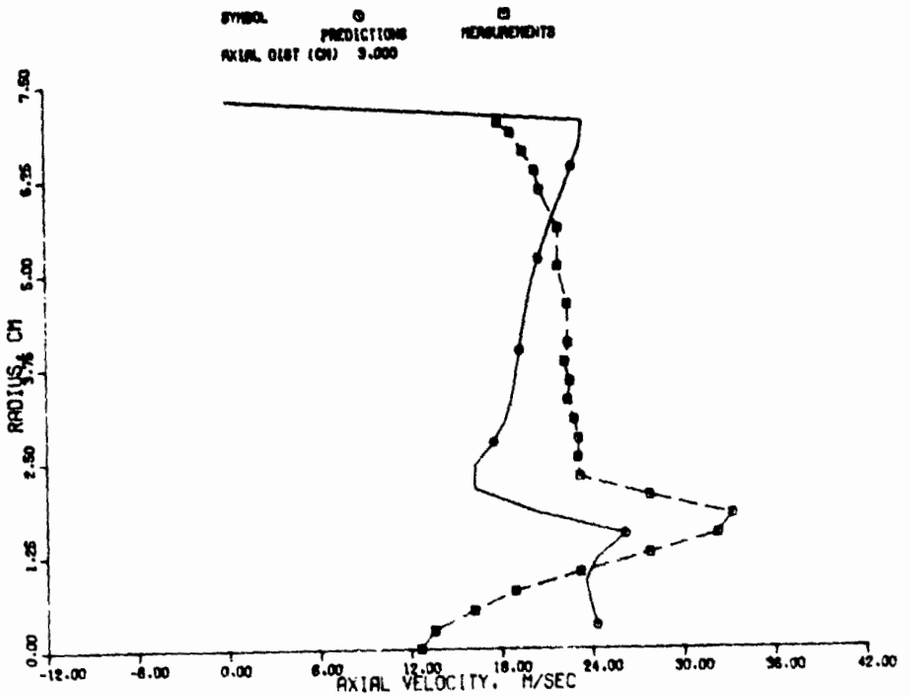

(c)

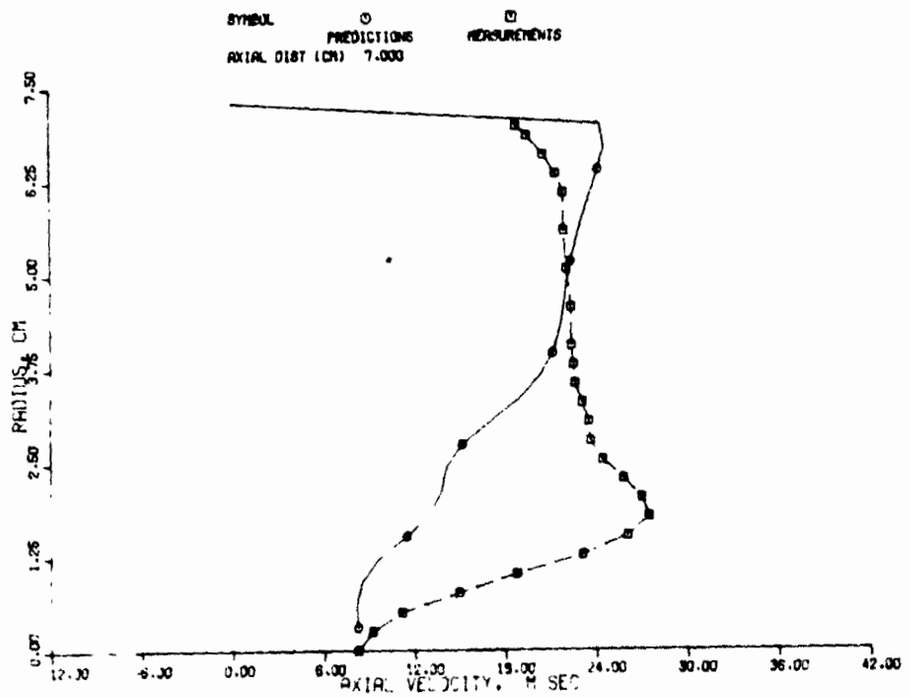

(d)

Figure 14. Axial Velocity Profiles for Co-Swirl Case with Predicted Inlet Profiles: Original K-ε Model (Contd).

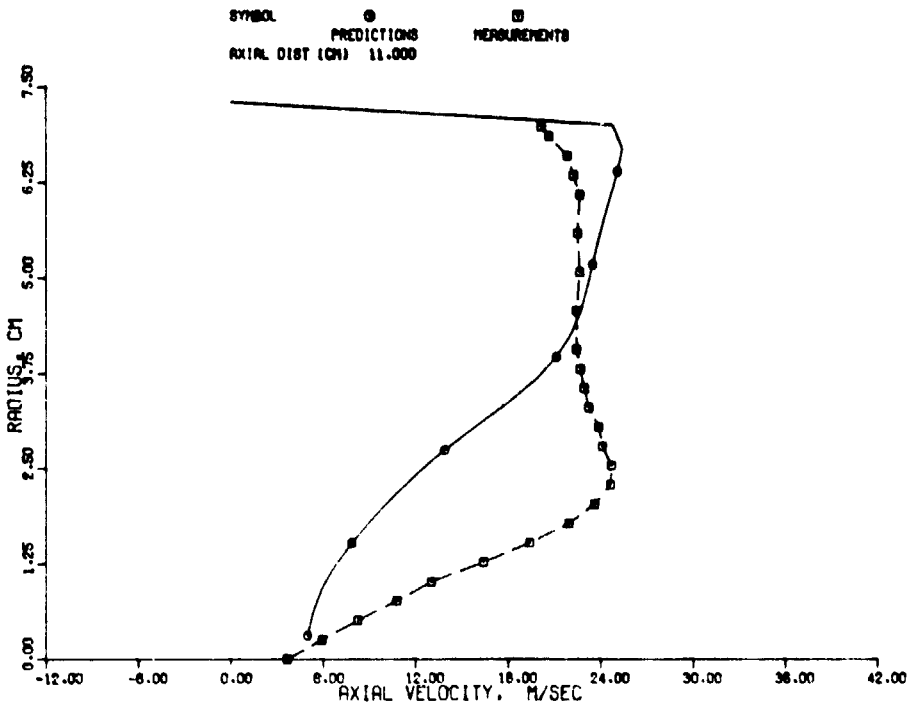

(e)

Figure 14. Axial Velocity Profiles for Co-Swirl Case with Predicted Inlet Profiles: Original K-ϵ Model (Contd).

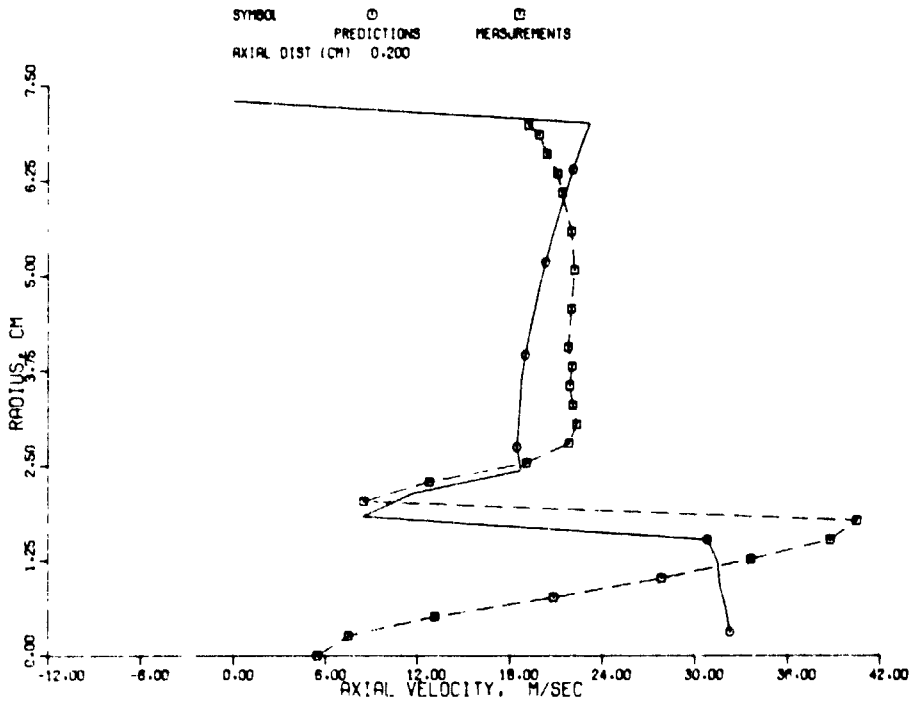

(a)

Figure 15. Axial Velocity Profiles for Counter-Swirl Case with Predicted Inlet Profiles: Original K-ϵ Model.

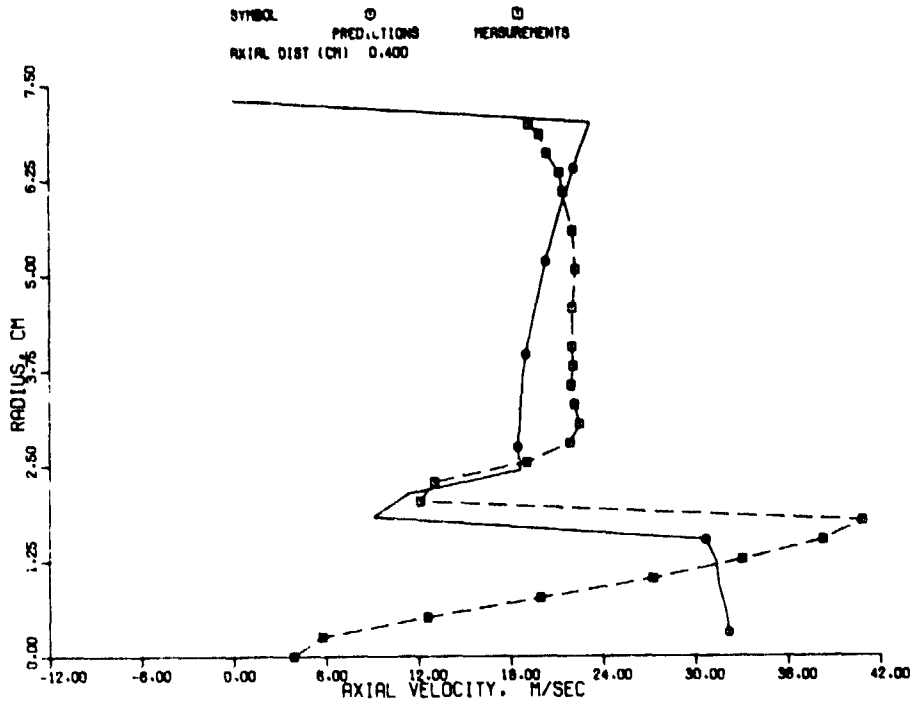

(b)

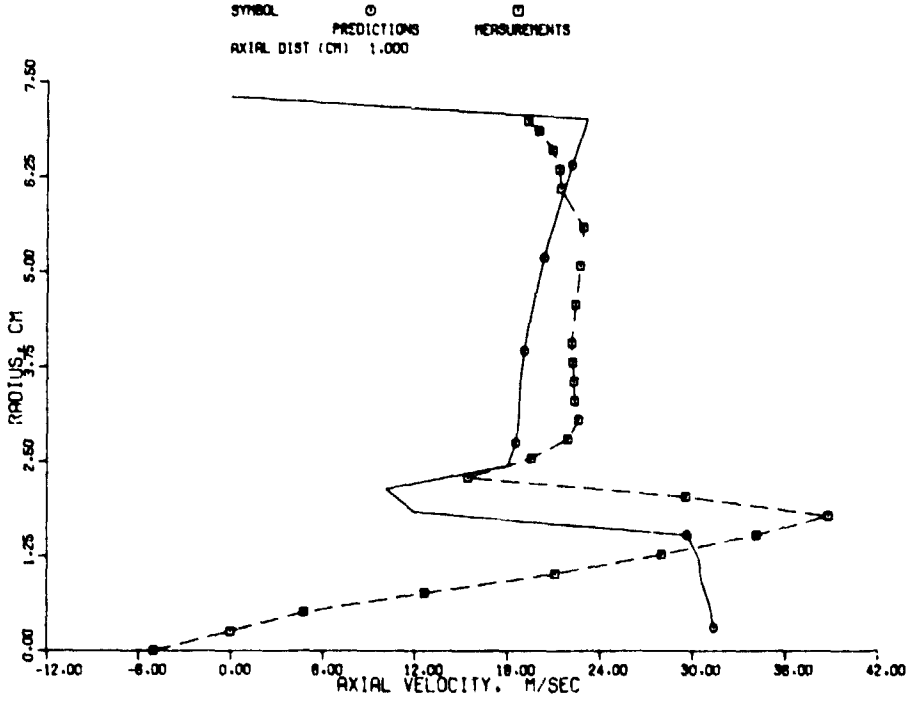

(c)

Figure 15. Axial Velocity Profiles for Counterswirl Case with Predicted Inlet Profiles: Original K-ε Model (Contd).

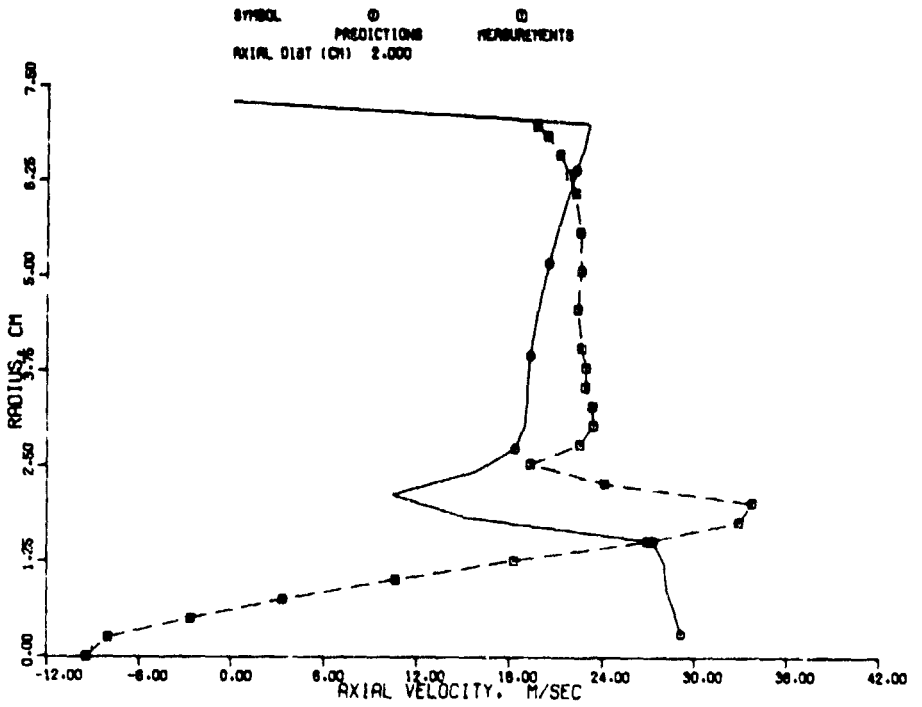

(d)

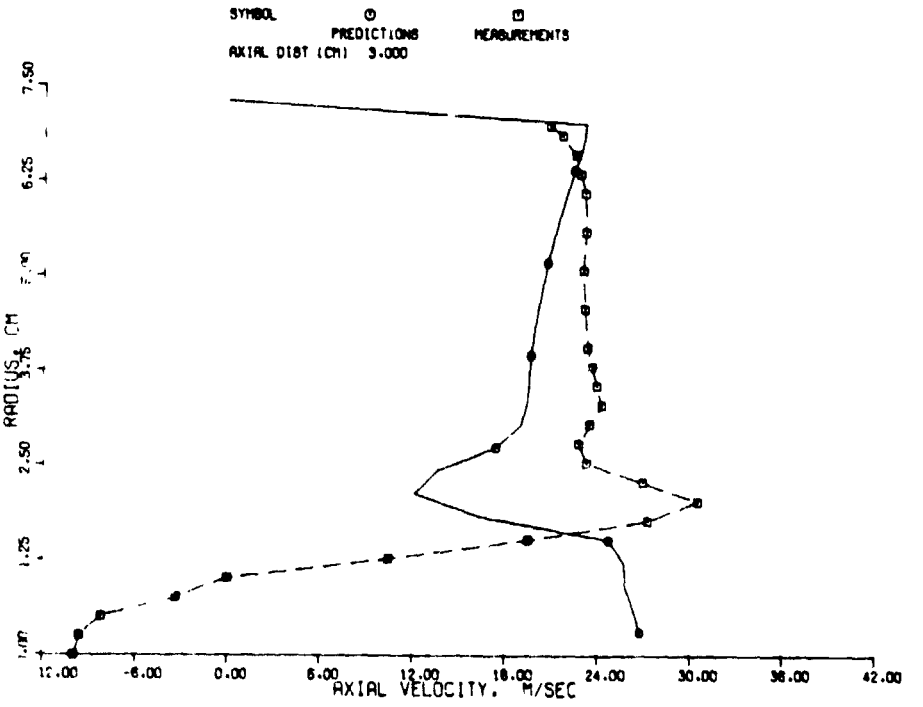

(e)

Figure 15. Axial Velocity Profiles for Counterswirl Case with Predicted Inlet Profiles: Original K-ε Model (Contd).

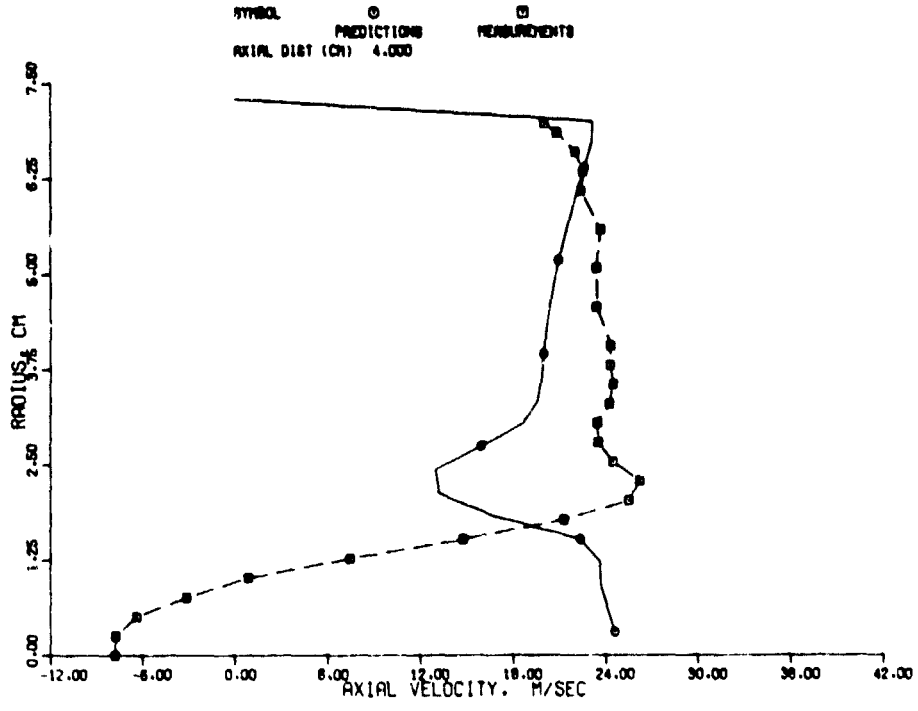

(f)

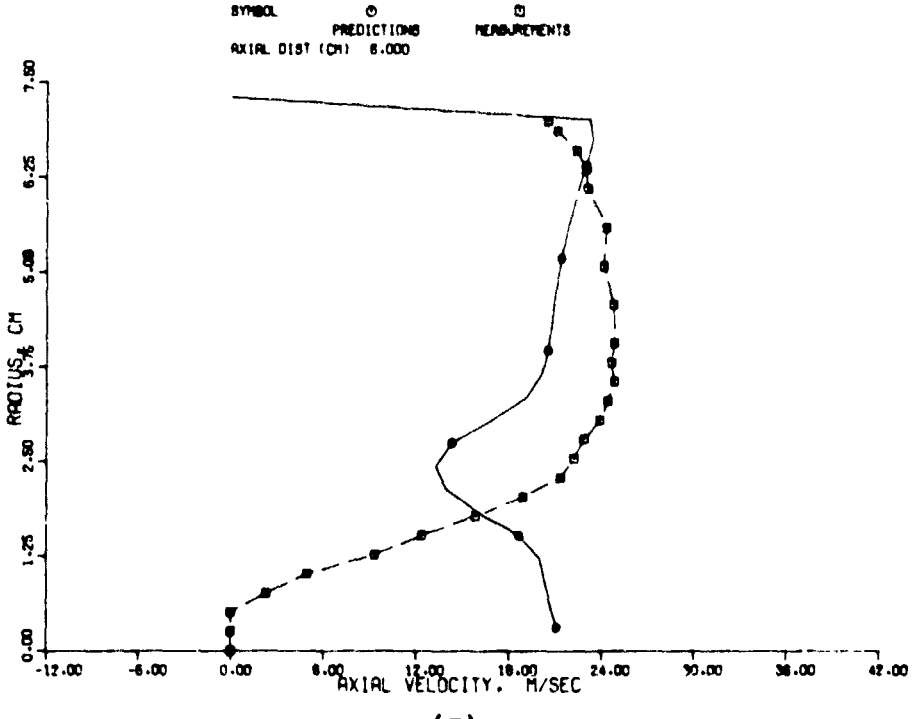

(g)

Figure 15. Axial Velocity Profiles for Counterswirl Case with Predicted Inlet Profiles: Original K-ε Model (Contd).

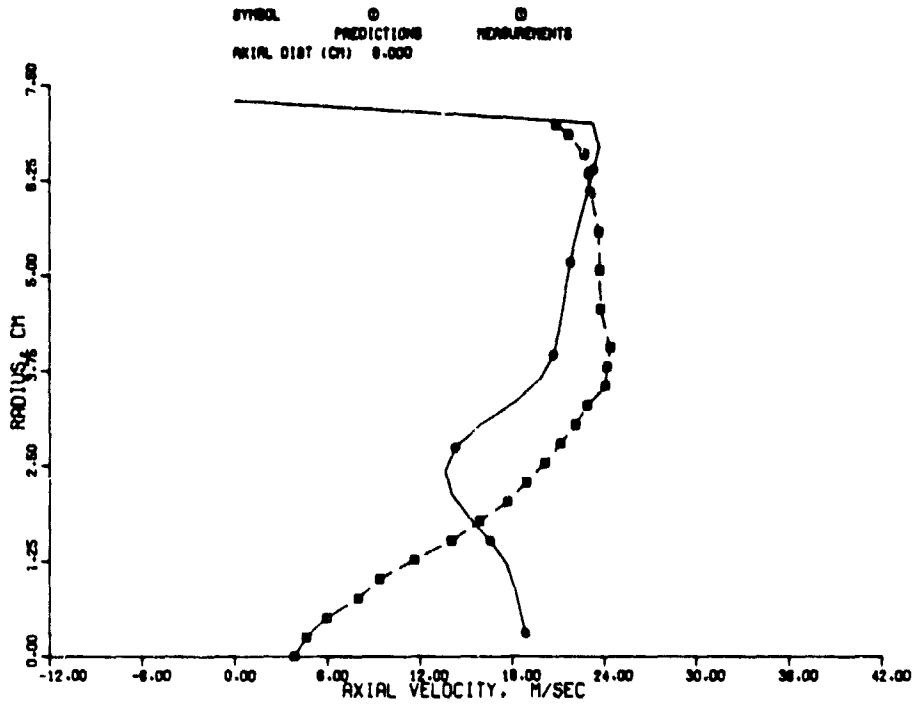

(h)

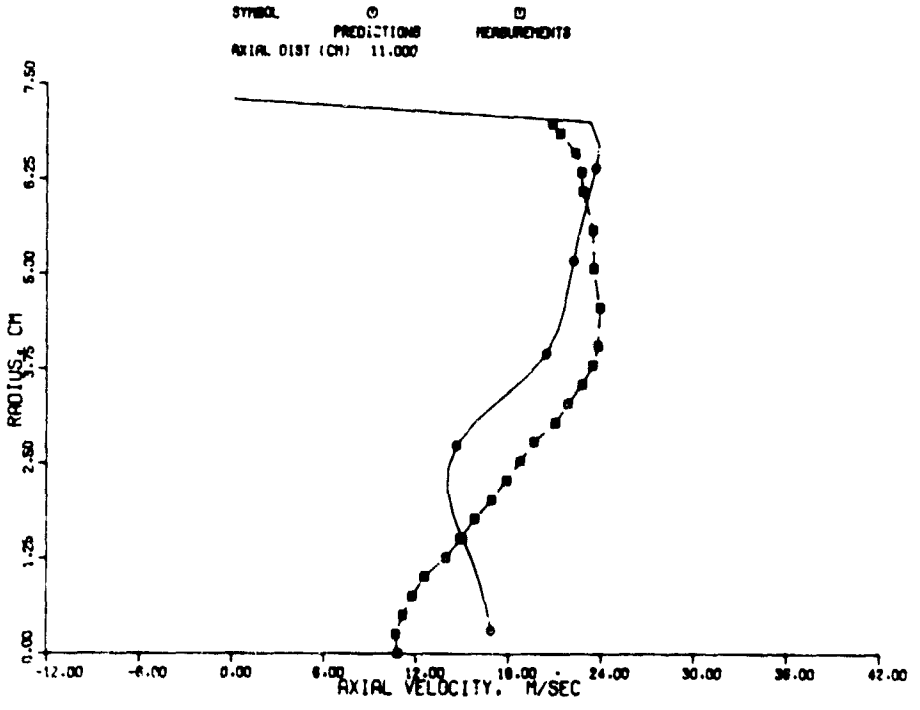

(i)

Figure 15. Axial Velocity Profiles for Counterswirl Case with Predicted Inlet Profiles: Original K-ε Model (Contd).

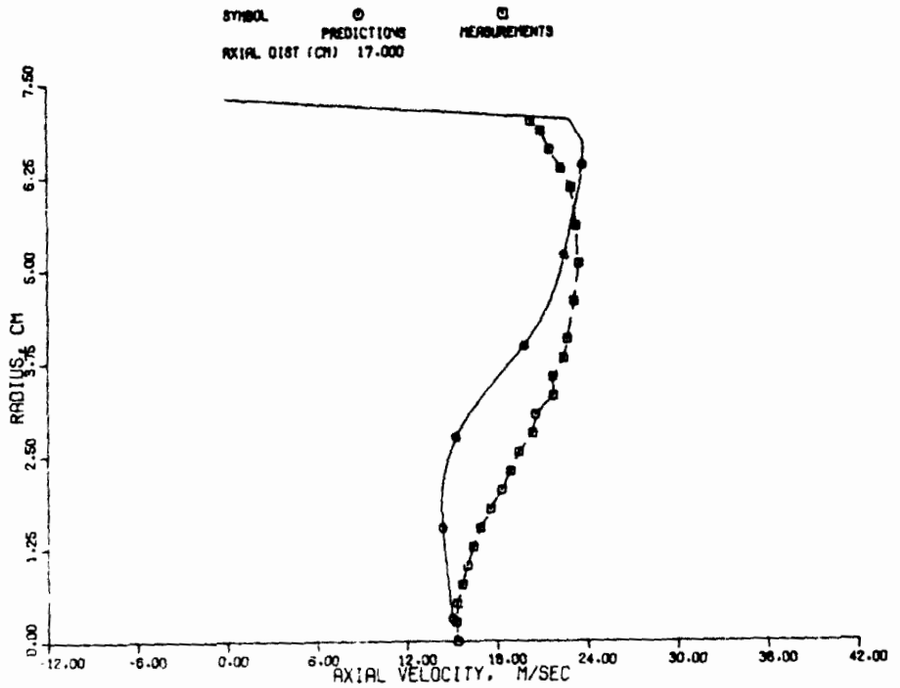

(j)

Figure 15. Axial Velocity Profiles for Counterswirl Case with Predicted Inlet Profiles: Original K-ϵ Model (Contd)

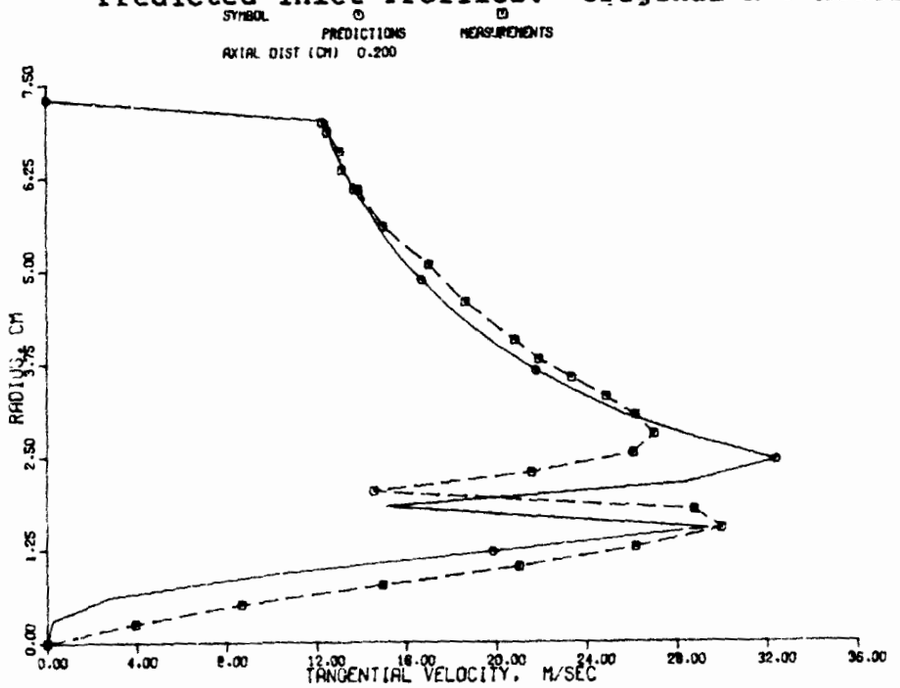

(a)

Figure 16. Tangential Velocity Profiles for Co-Swirl Case with Predicted Inlet Profiles: Original K-ϵ Model.

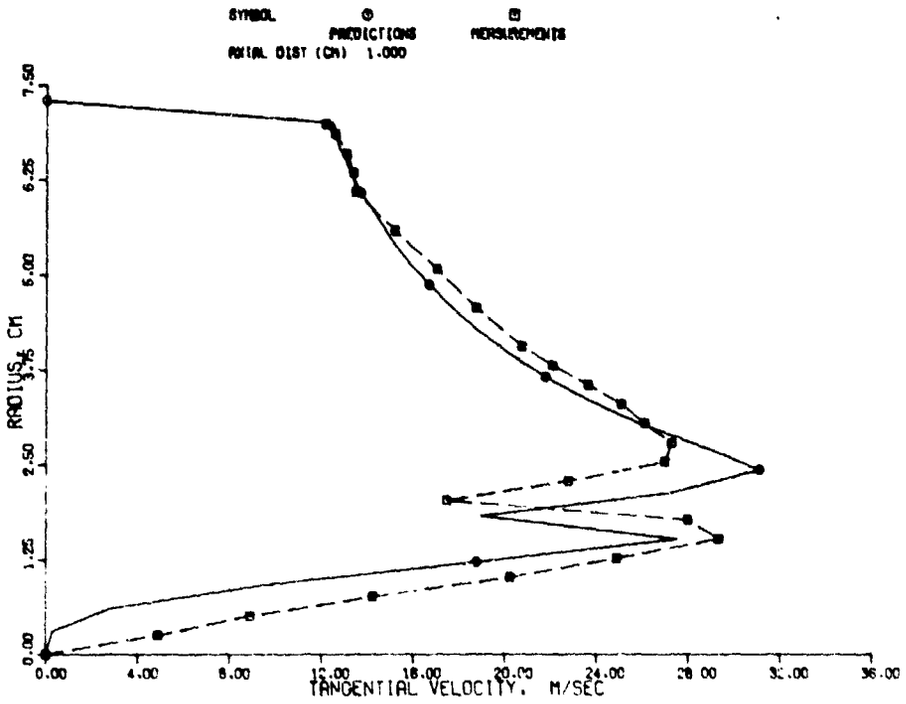

(b)

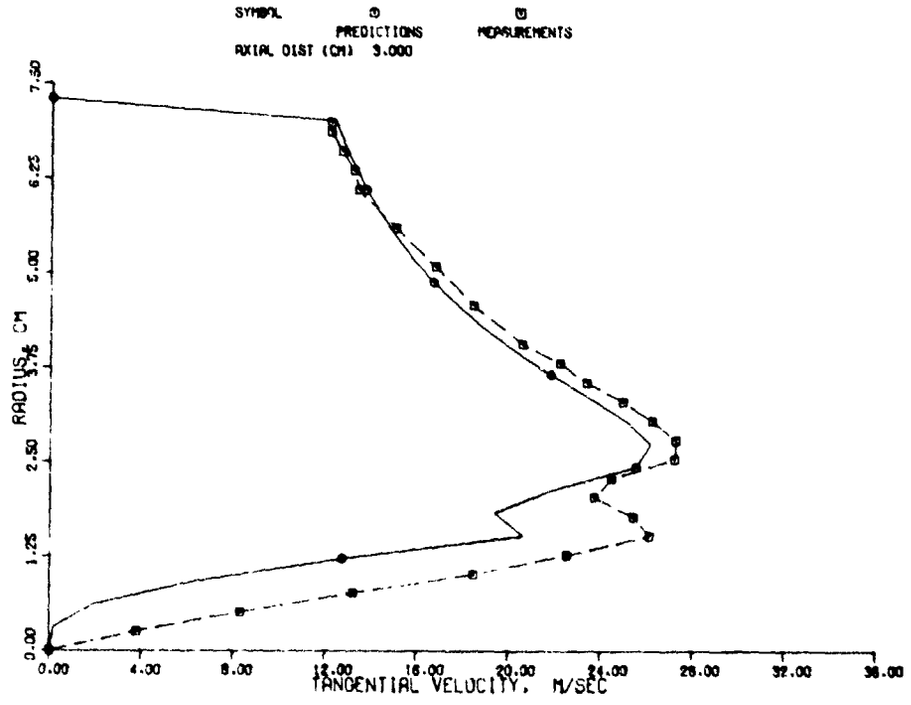

(c)

Figure 16. Tangential Velocity Profiles for Co-Swirl Case with Predicted Inlet Profiles: Original K-ε Model (Contd).

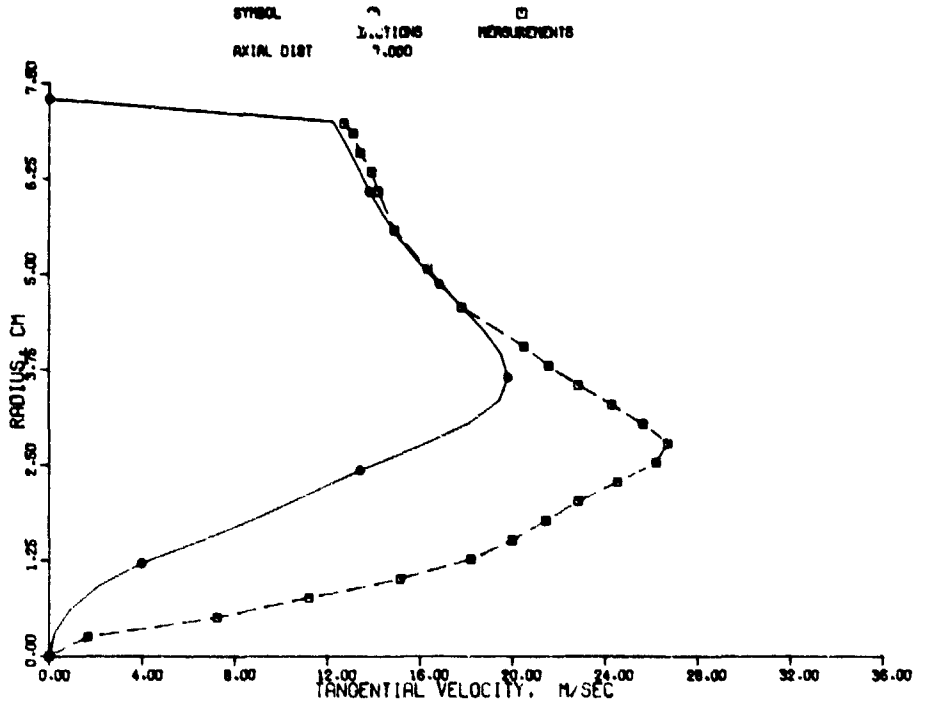

(d)

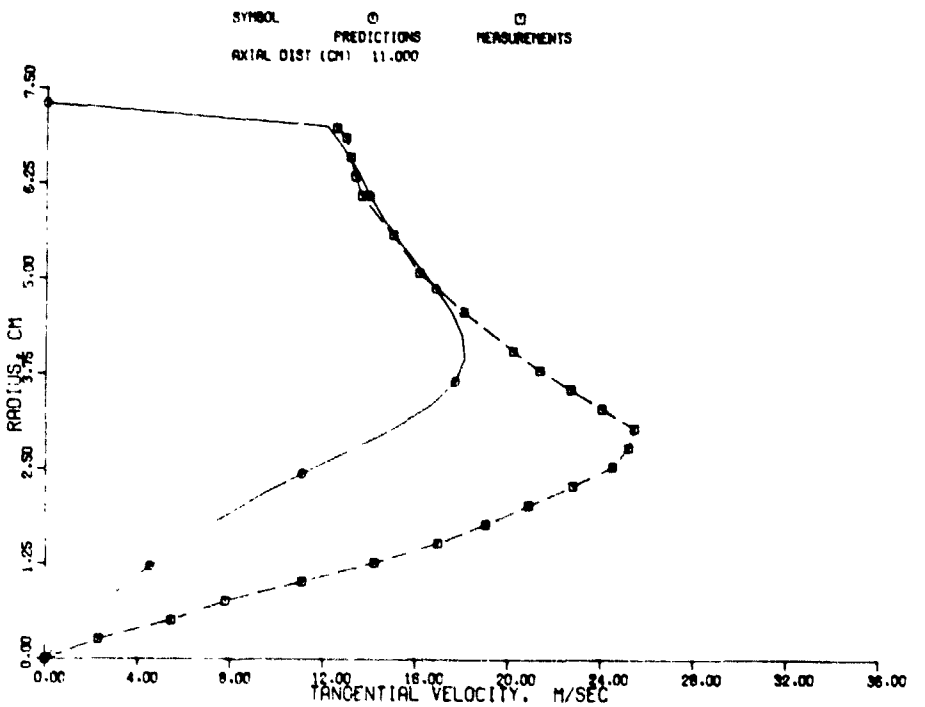

(e)

Figure 16. Tangential Velocity Profiles for Co-Swirl Case with Predicted Inlet Profiles: Original K-ϵ Model (Contd).

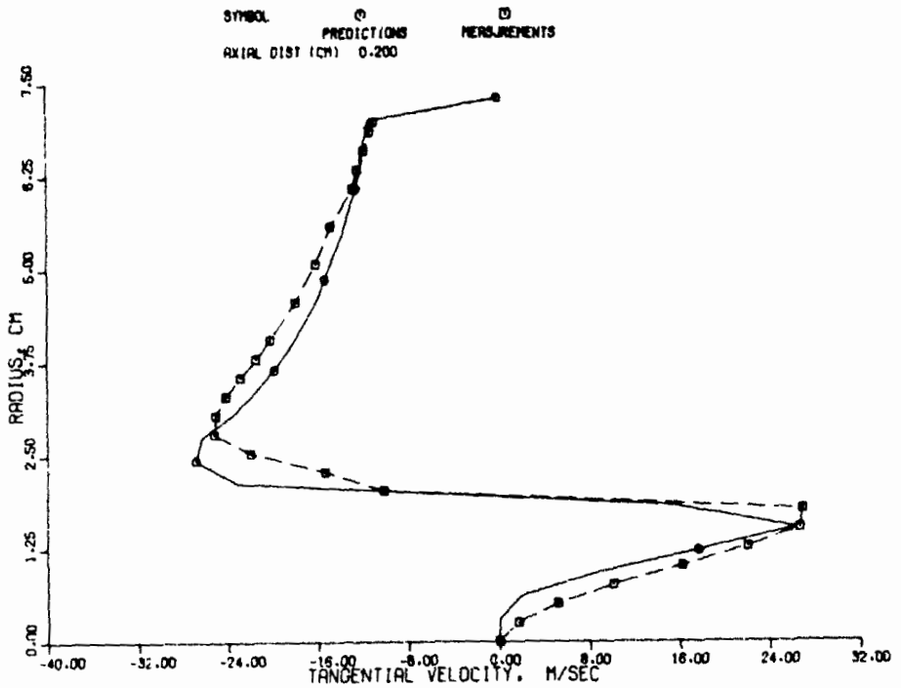

(a)

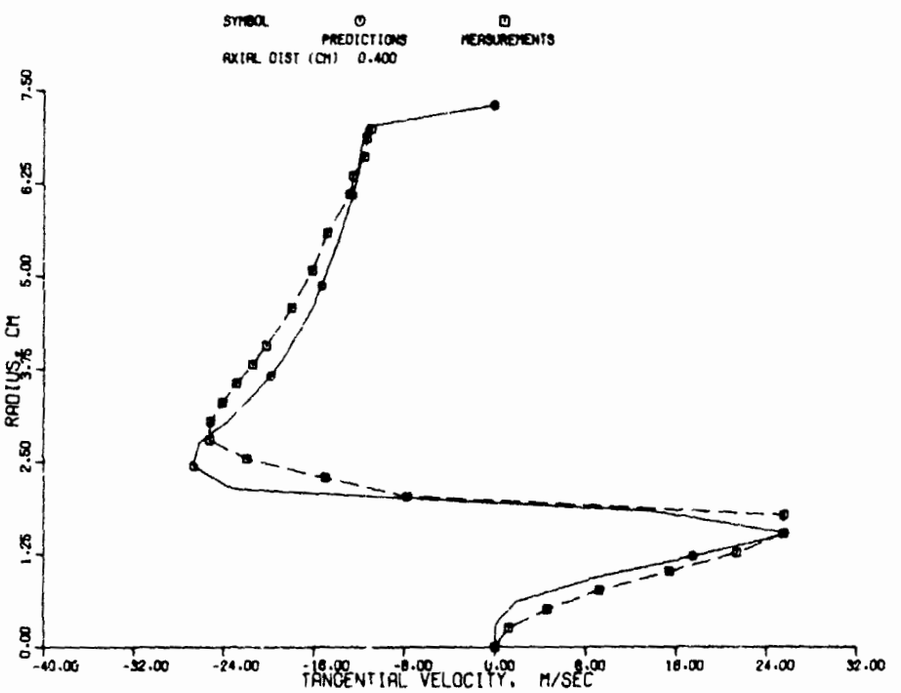

(b)

Figure 17. Tangential Velocity Profiles for Counterswirl Case with Predicted Inlet Profiles: Original K-ϵ Model.

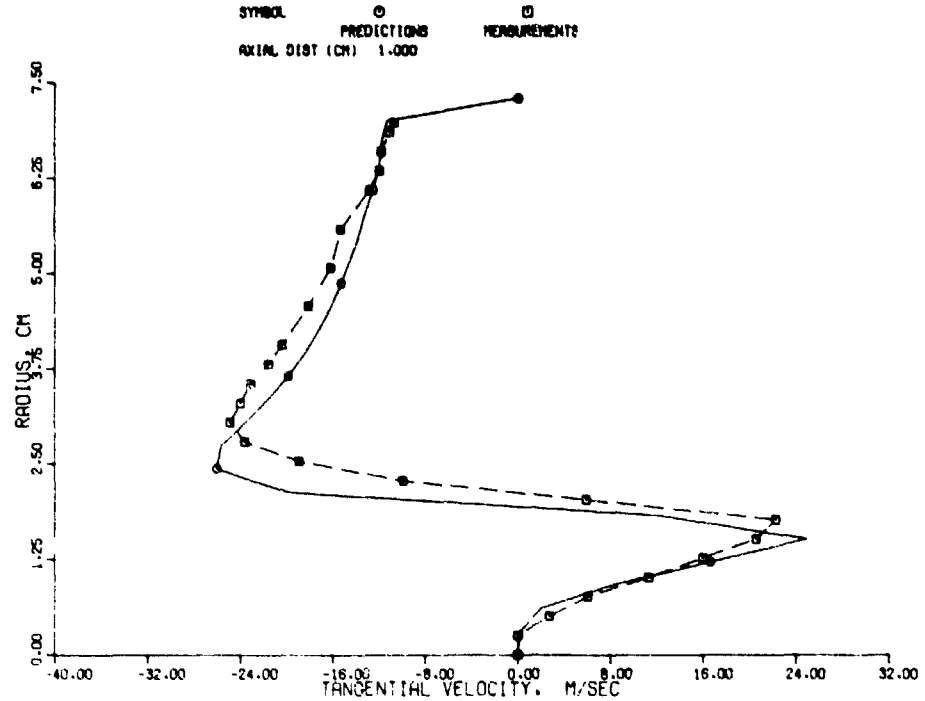

(c)

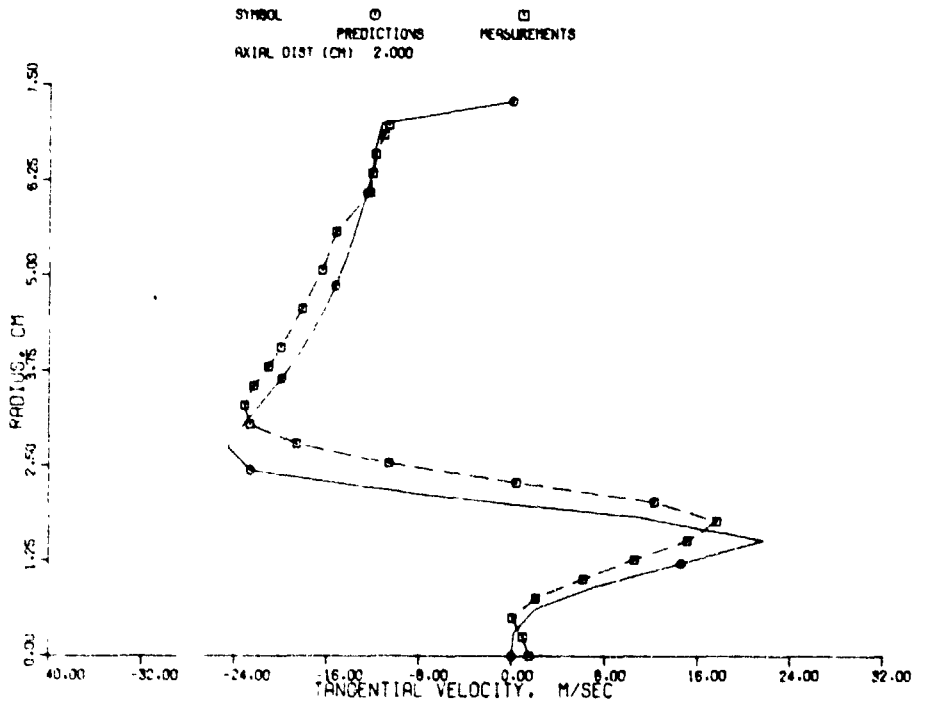

(d)

Figure 17. Tangential Velocity Profiles for Counterswirl Case with Predicted Inlet Profiles: Original K-ϵ Model (Contd).

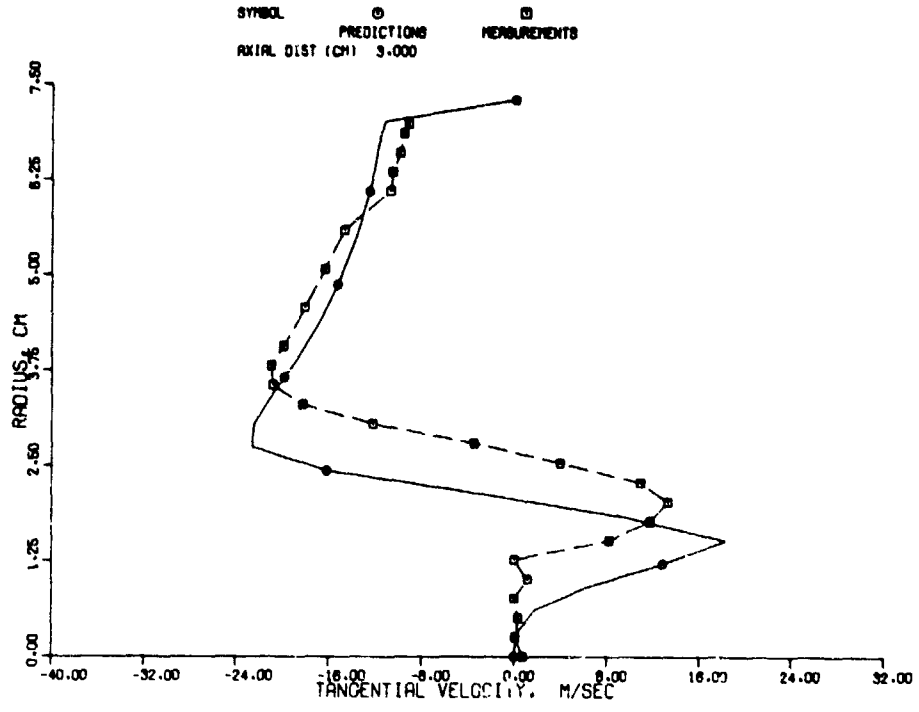

(e)

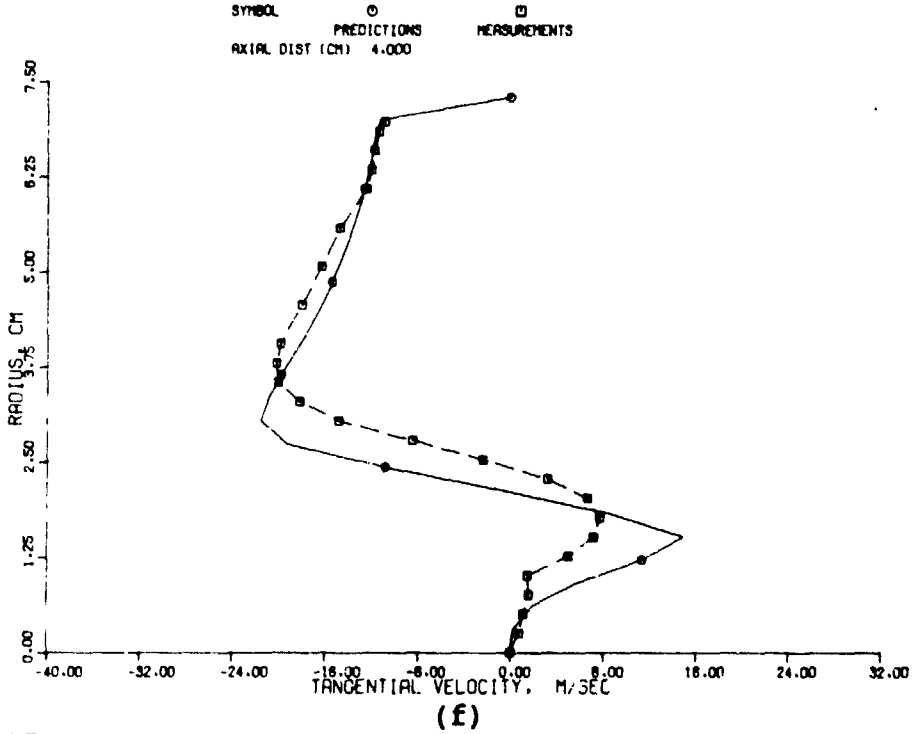

(f)

Figure 17. Tangential Velocity Profiles for Counterswirl Case with Predicted Inlet Profiles: Original K-ϵ Model (Contd).

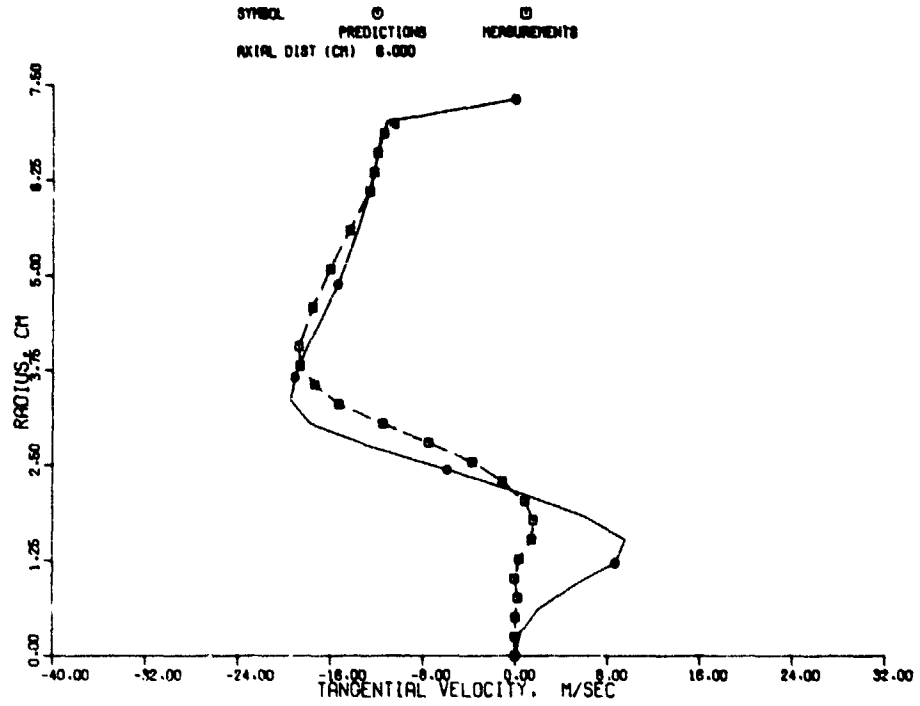

(g)

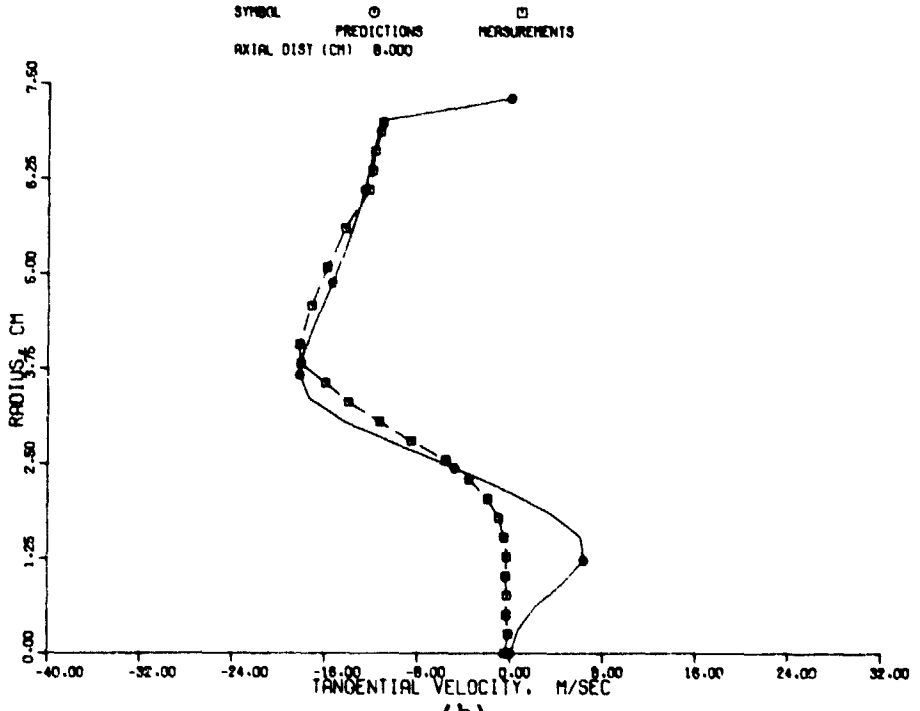

(h)

Figure 17. Tangential Velocity Profiles for Counterswirl Case with Predicted Inlet Profiles: Original K-ε Model (Contd).

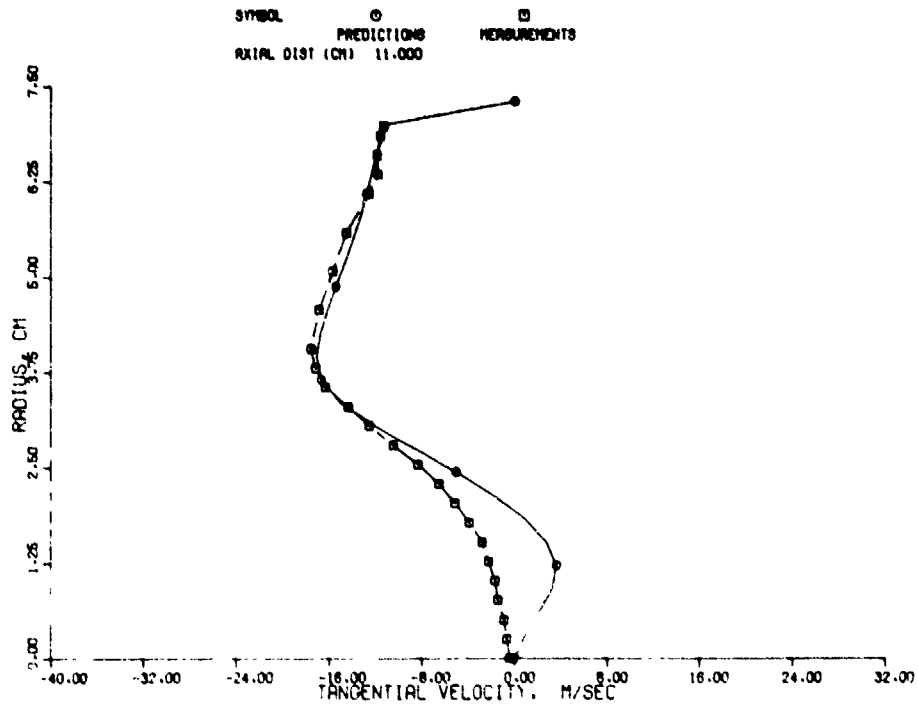

(i)

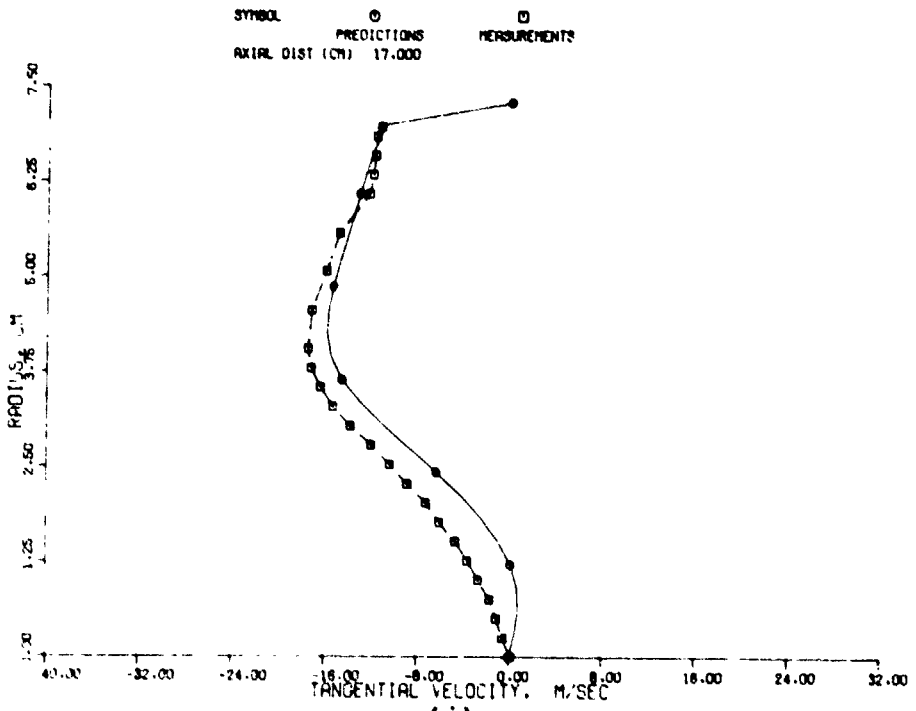

(j)

Figure 17. Tangential Velocity Profiles for Counterswirl Case with Predicted Inlet Profiles: Original K-ε Model (Contd).

The predicted axial-velocity profile development trends for the outer stream are in qualitative agreement with the measurements in regard to velocity deficit caused by the inner tube walls and the outer mixing layer between the two streams. However, the correlation for the inner stream development is rather poor.

The comparison between computed and measured tangential velocity profiles close to the mixing region inlet (up to 3-cm downstream from the inlet) is reasonably good but becomes progressively worse further downstream. The latter is believed to be due to the inability of the model to get good correlation for the axial velocity development for the inner tube.

In order to ensure that computed results are grid independent with minimal false diffusion, calculations were made with three sets of grid spacing with an increasing number of finite-difference nodes. The results presented were found to be grid independent, thus, indicating that poor correlations in the inner jet development are attributable to the mathematical modeling of turbulence and the flow assembly and not the numerical inaccuracy.

Task II - Computations for Given Inlet Velocity Profiles

One of the reasons for the inferior quantitative agreement between the Task I predictions and the measurements is due to the differences in the inlet velocity profiles. The main cause of the difference stems from neglecting the elliptic effects of the interaction between the inner and the outer streams. If this were the case, then the use of the measured values near the entrance plane of the mixing region as the inlet profiles should predict a better agreement with the measurements further downstream.

A series of computations, therefore, were made with the measured velocity profiles at x = 0.2 cm as the input profile for the mixing region, and the flow field predictions were compared with the measurements downstream. The comparison between these results and the measurements are shown in Figures 18 through 21. Figures 18 and 19 show the axial velocity profile comparisons for co-swirling and counterswirling cases, respectively. Although these predictions show an improvement over Task I calculations, they do not predict any recirculation, while the measurements indicate flow reversal for the counterswirling case from x = 1 cm to x = 4 cm. In this region, the comparison between the predictions and measurements were poorer than elsewhere. The comparison of the tangential velocity profiles for co-swirling and counterswirling cases is shown in Figures 20 and 21, respectively.

These figures indicate some of the shortcomings in the turbulence model. In the vicinity of the recirculating region, the K-ϵ model seems to underpredict diffusion. This is seen more clearly in the tangential velocity profiles downstream of x = 1 cm. The addition of swirl on the flow should cause a streamline curvature on the whole flow system. Streamline curvature should in turn result in a significant change in the Reynolds stresses, thereby increasing the diffusion rate.

An elucidation of the effect of swirl was afforded by representing the radial flux of angular momentum, $T^{y}_{V_\theta}$, by

$$T^{y}_{V_\theta} = A\, T^{y}_{k-\epsilon}, \tag{15}$$

where A is an empirical constant, and $T^{y}_{k-\epsilon}$ is the radial momentum flux as predicted by the k-ϵ model. Computer runs were made for different values of A and swirl numbers for studying the swirling flow field in a straight pipe. The inlet profiles to a 1.42-inch (3.61-cm) diameter pipe were assumed to be a uniform axial

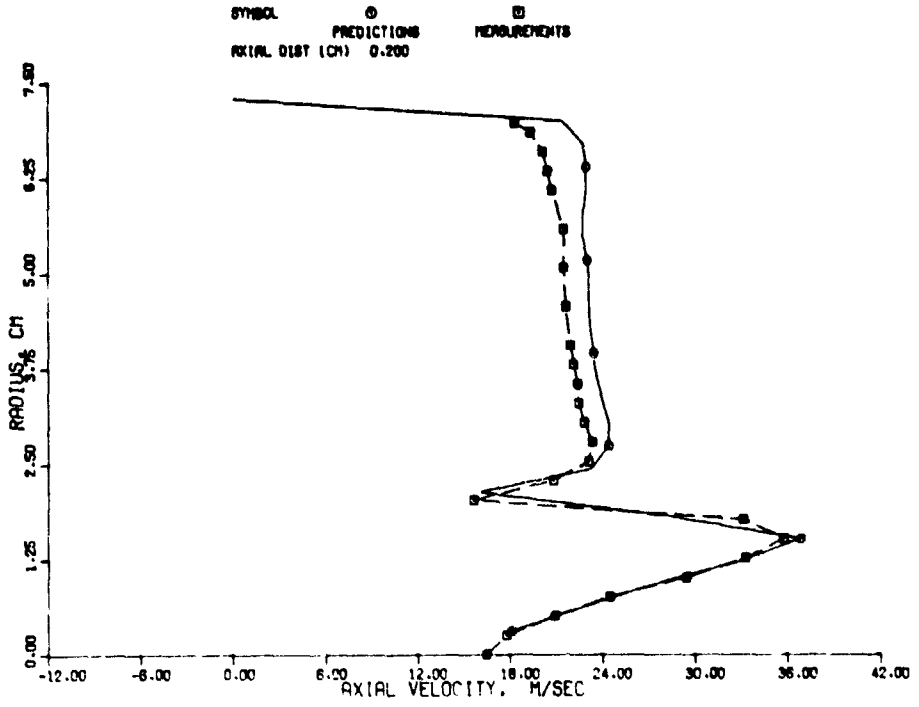

(a)

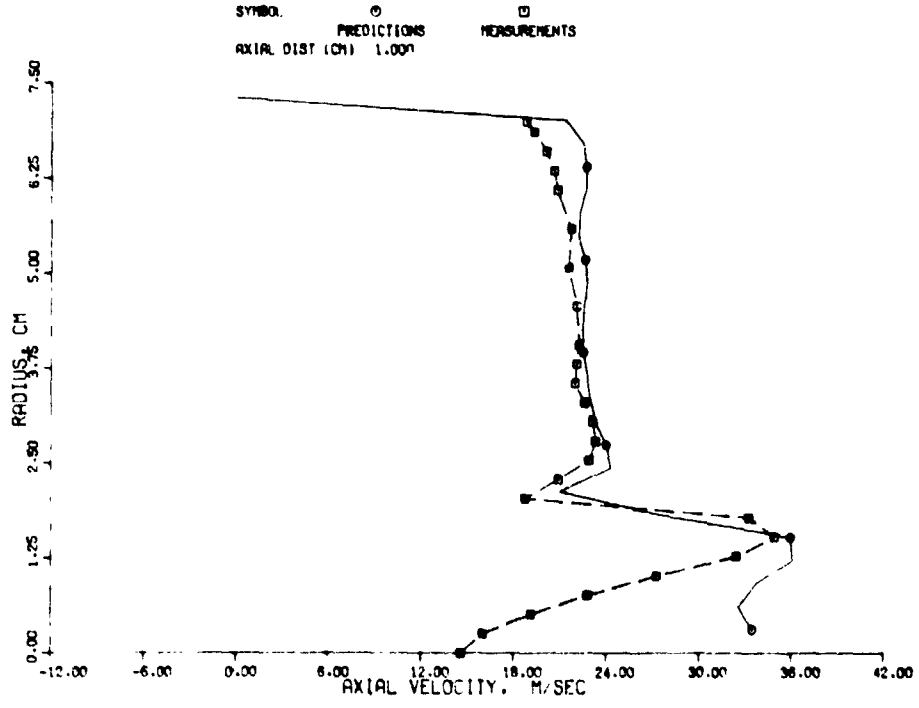

(b)

Figure 18. Axial Velocity Profiles for Co-Swirl Case with Measured Inlet Profiles: Original K-ϵ Model.

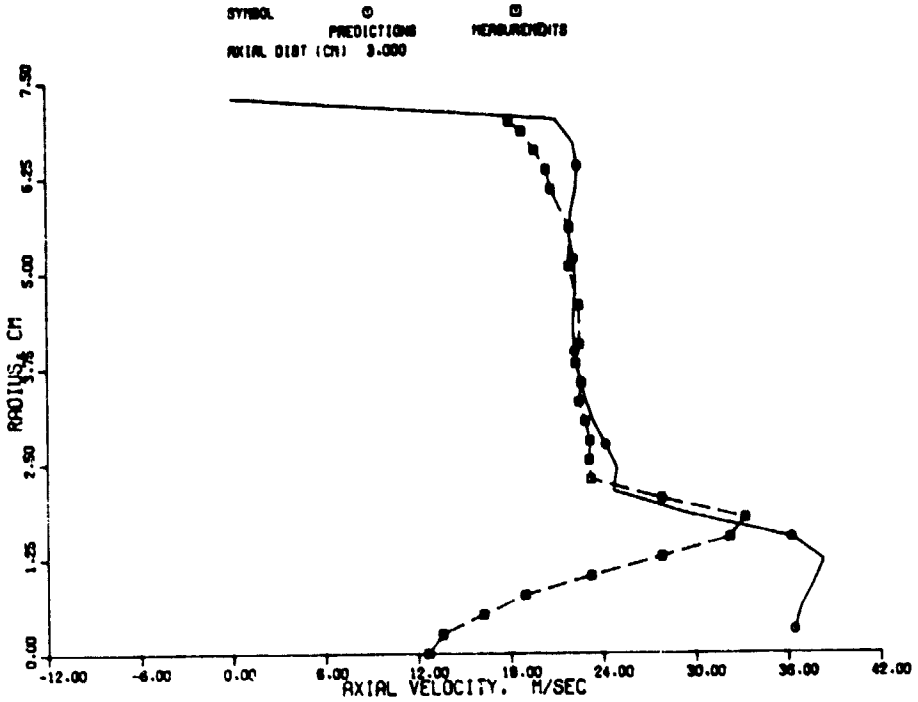

(c)

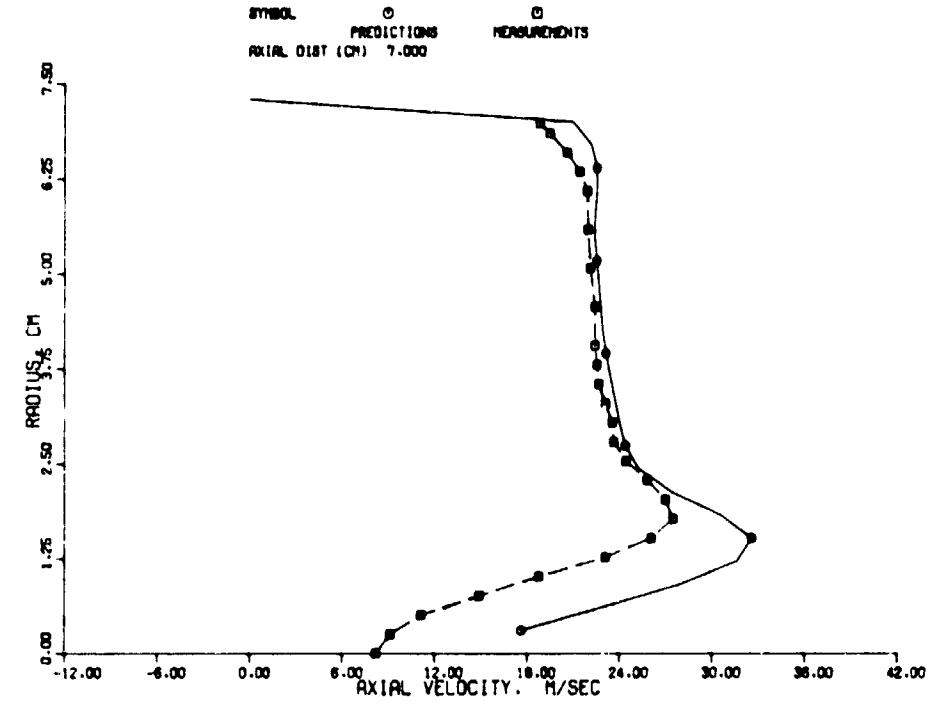

(d)

Figure 18. Axial Velocity Profiles for Co-Swirl Case with Measured Inlet Profiles: Original K-ϵ Model (Contd).

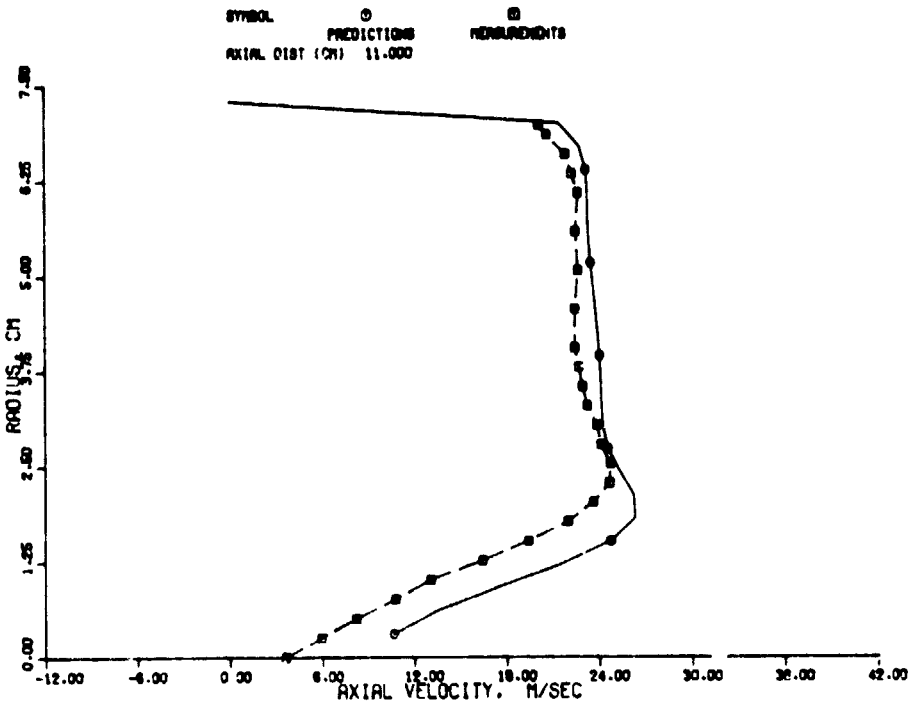

(e)

Figure 18. Axial Velocity Profiles for Co-Swirl Case with Measured Inlet Profiles: Original K-ε Model (Contd).

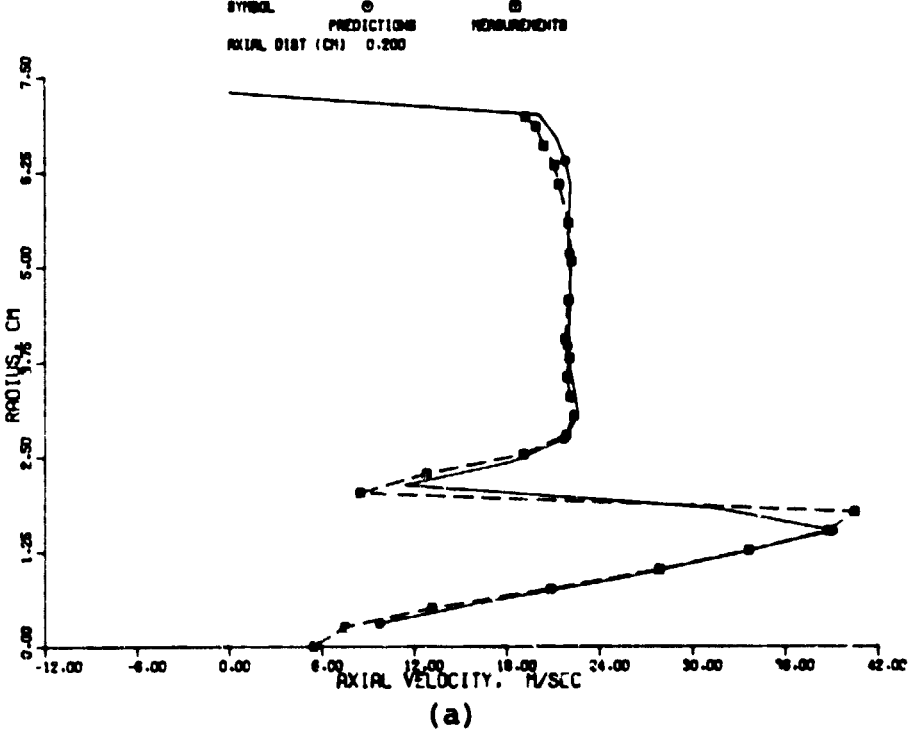

(a)

Figure 19. Axial Velocity Profiles for Counterswirl Case with Measured Inlet Profiles: Original K-ε Model.

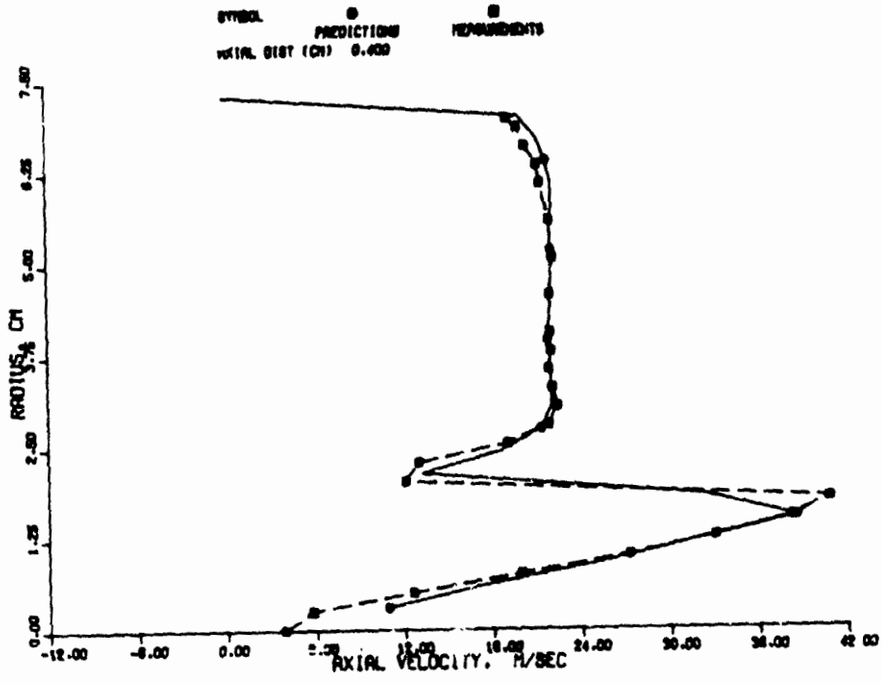

(b)

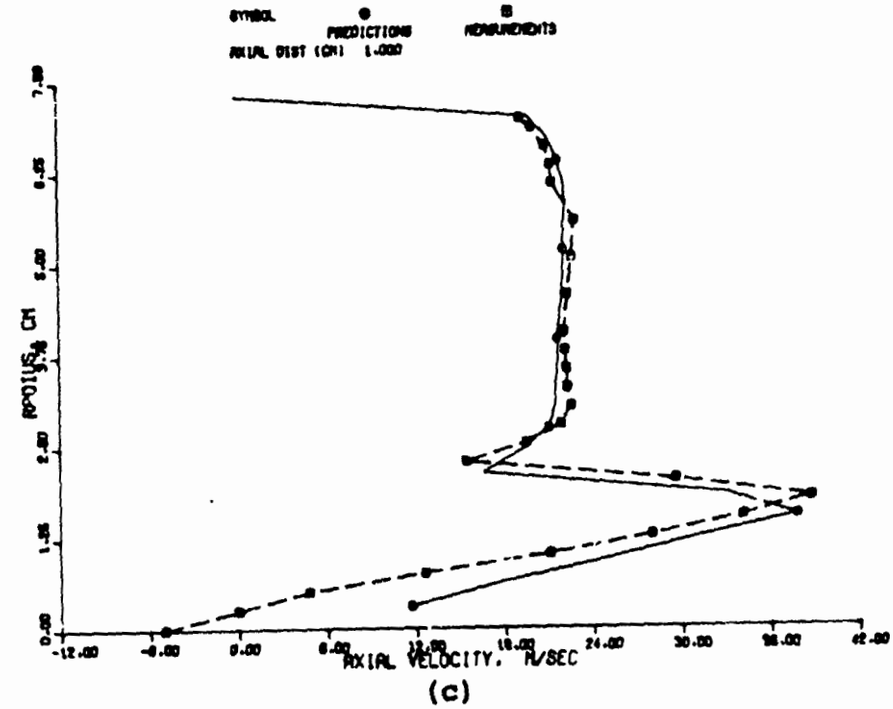

(c)

Figure 19. Axial Velocity Profiles for Counterswirl Case with Measured Inlet Profiles: Original K-ε Model (Contd).

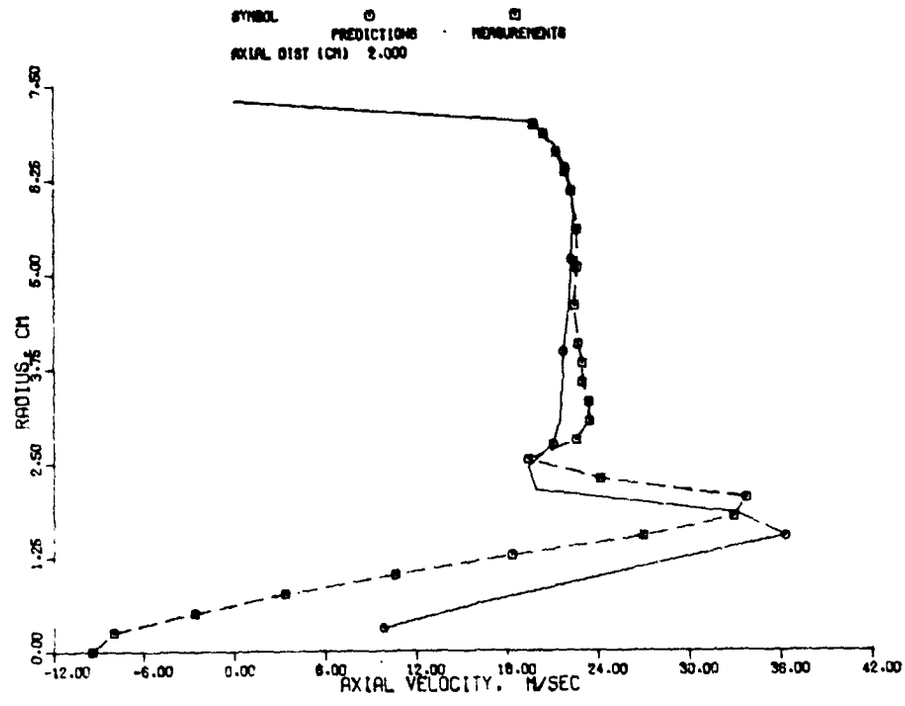

(d)

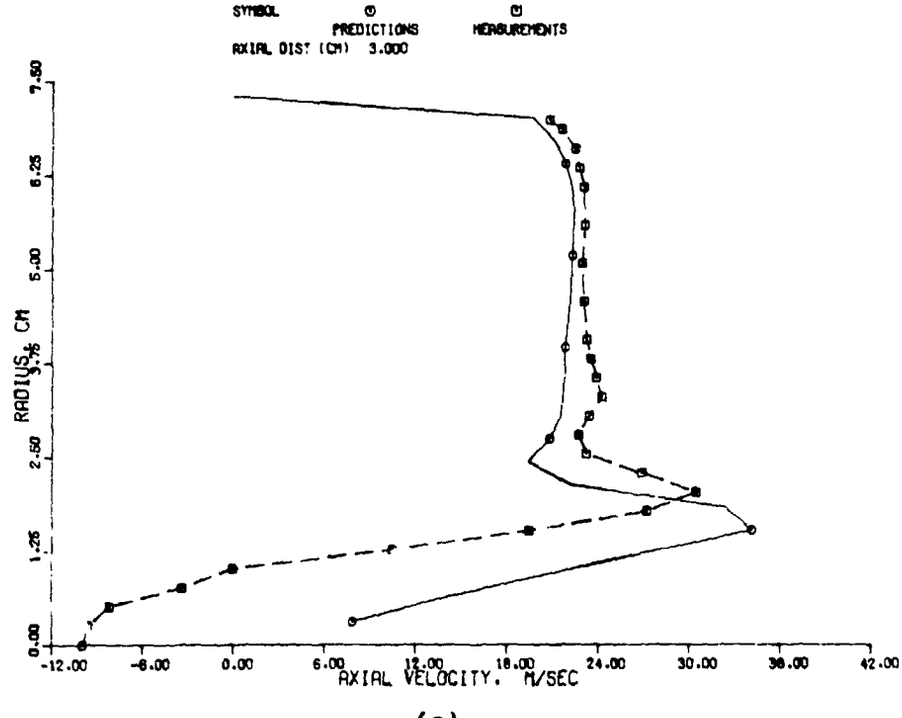

(e)

Figure 19. Axial Velocity Profiles for Counterswirl Case with Measured Inlet Profiles: Original K-ϵ Model (Contd).

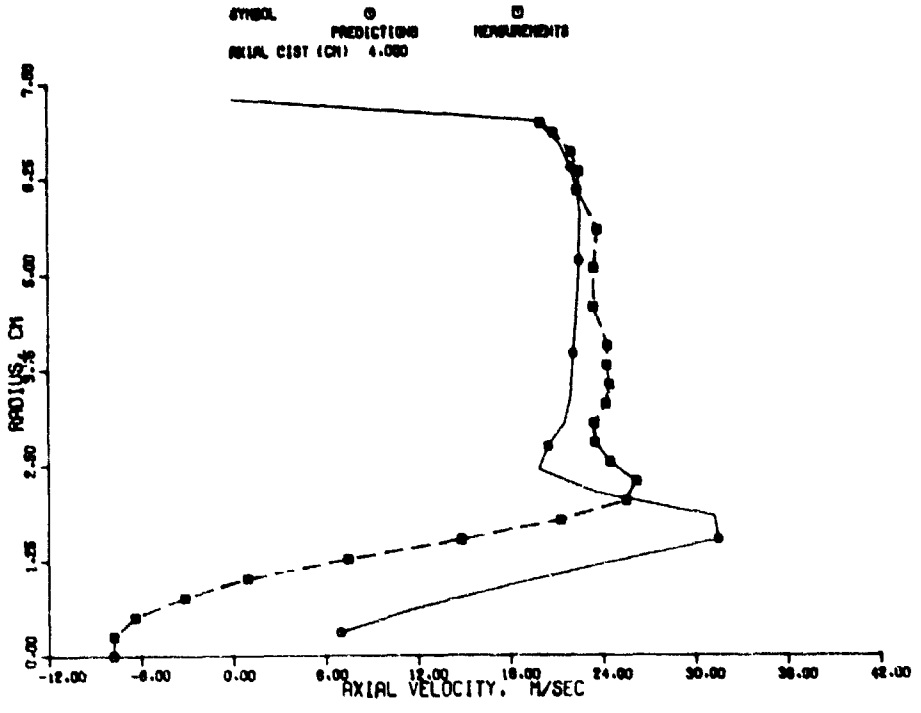

(f)

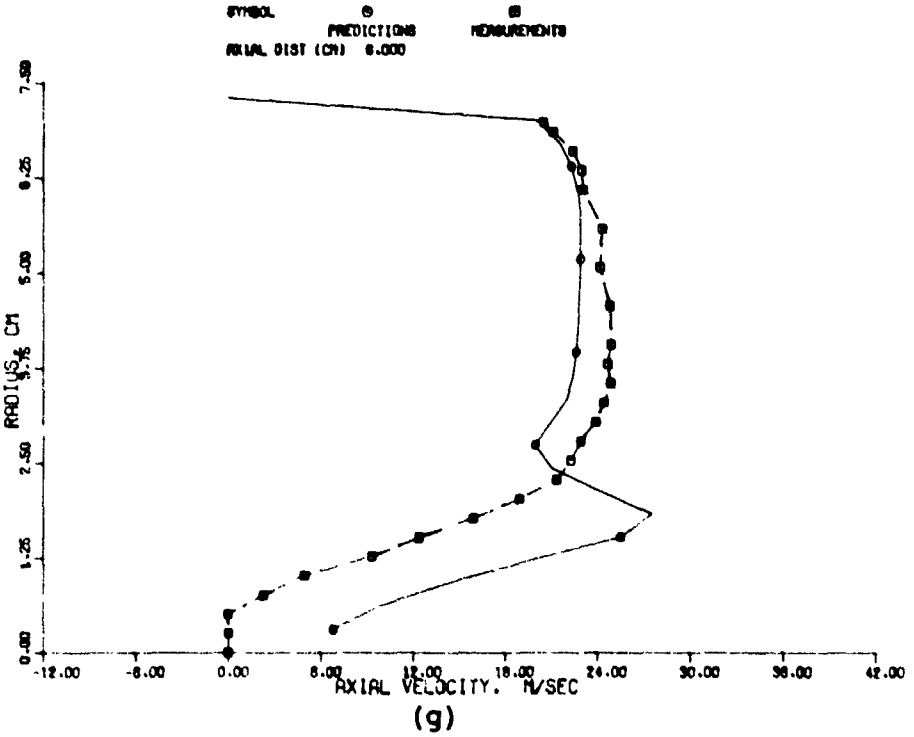

(g)

Figure 19. Axial Velocity Profiles for Counterswirl Case with Measured Inlet Profiles: Original K-ϵ Model (Contd).

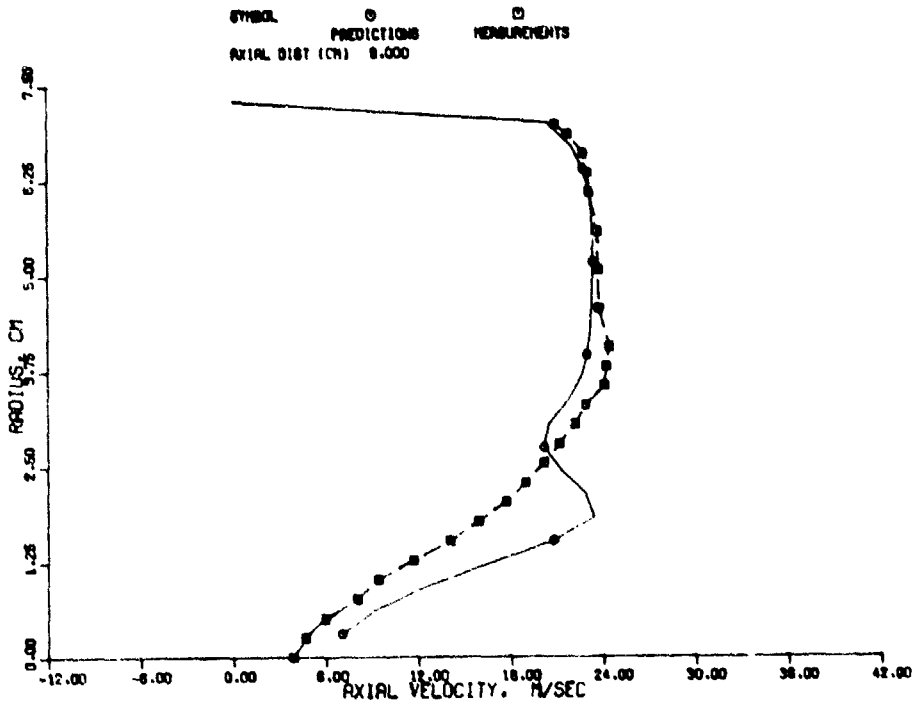

(h)

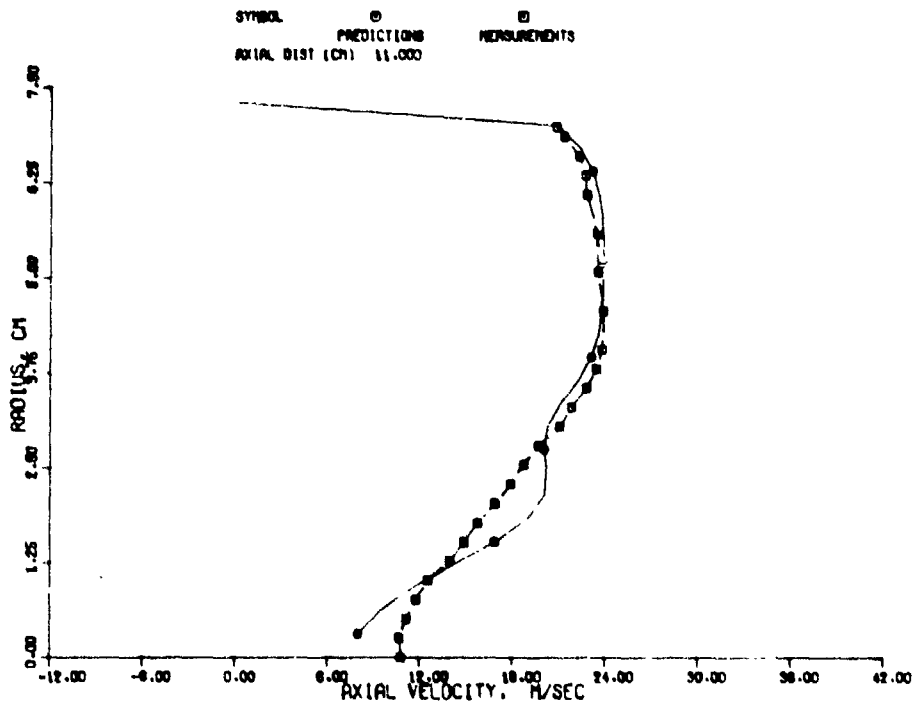

(i)

Figure 19. Axial Velocity Profiles for Counterswirl Case with Measured Inlet Profiles: Original K-ε Model (Contd).

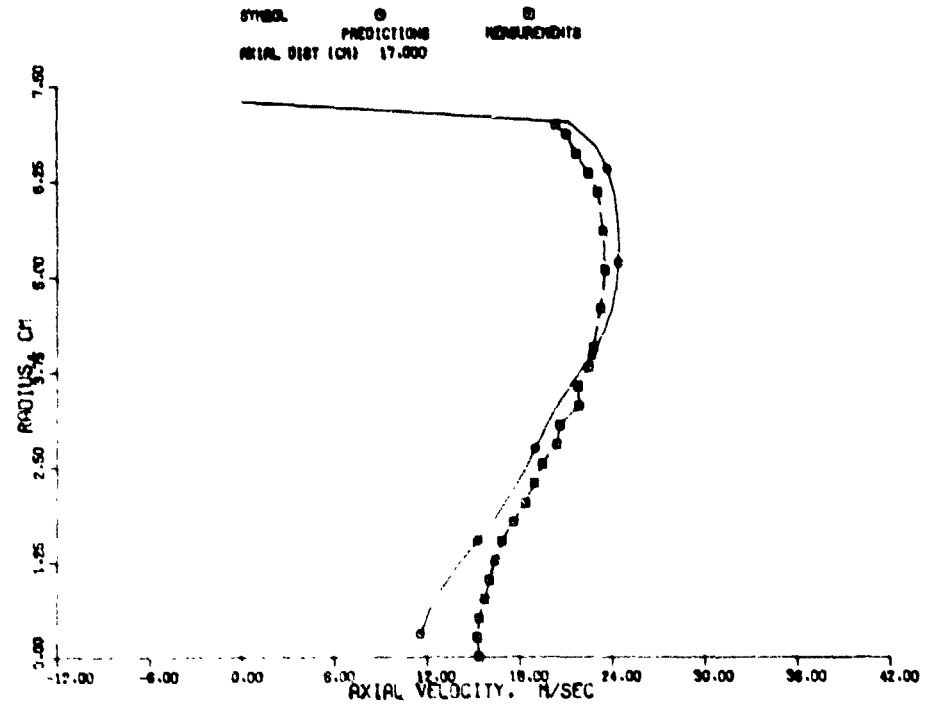

(j)

Figure 19. Axial Velocity Profiles for Counterswirl Case with Measured Inlet Profiles: Original K-ε Model (Contd).

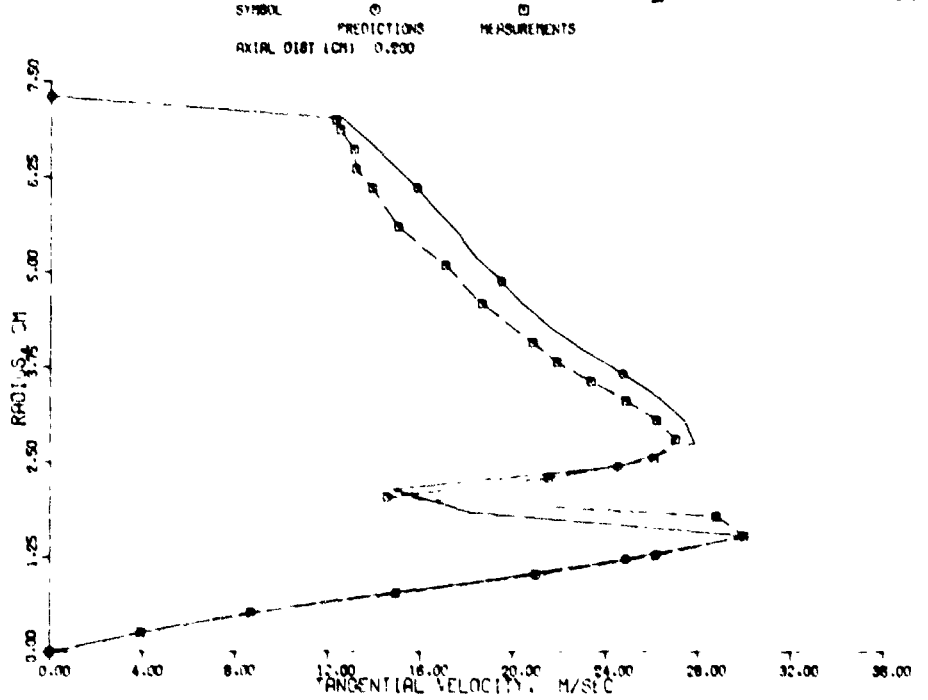

(a)

Figure 20. Tangential Velocity Profiles for Co-Swirl Case with Measured Inlet Profiles: Original K-ε Model.

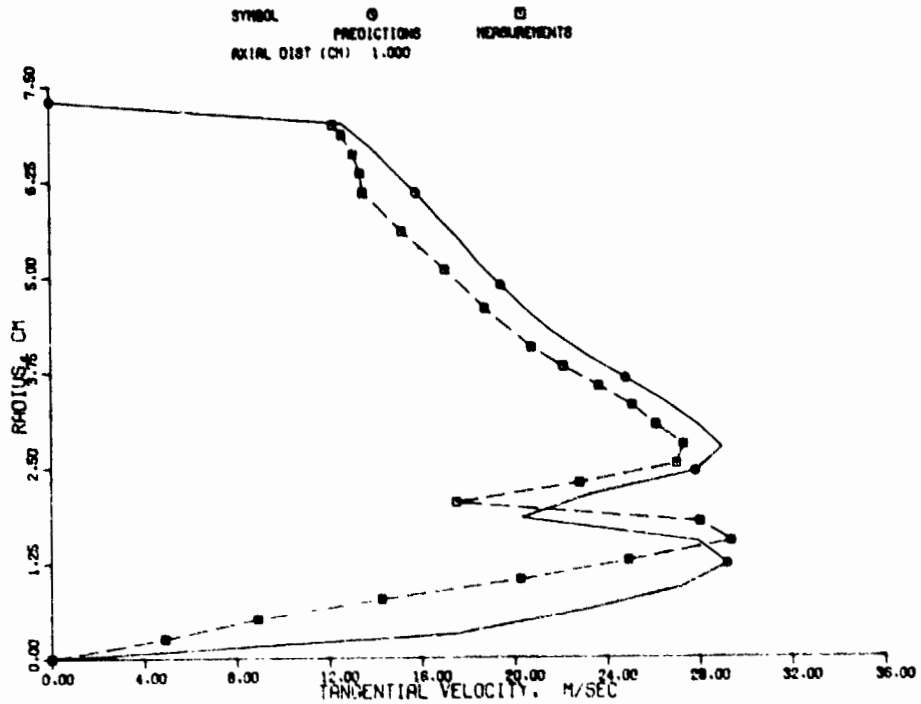

(b)

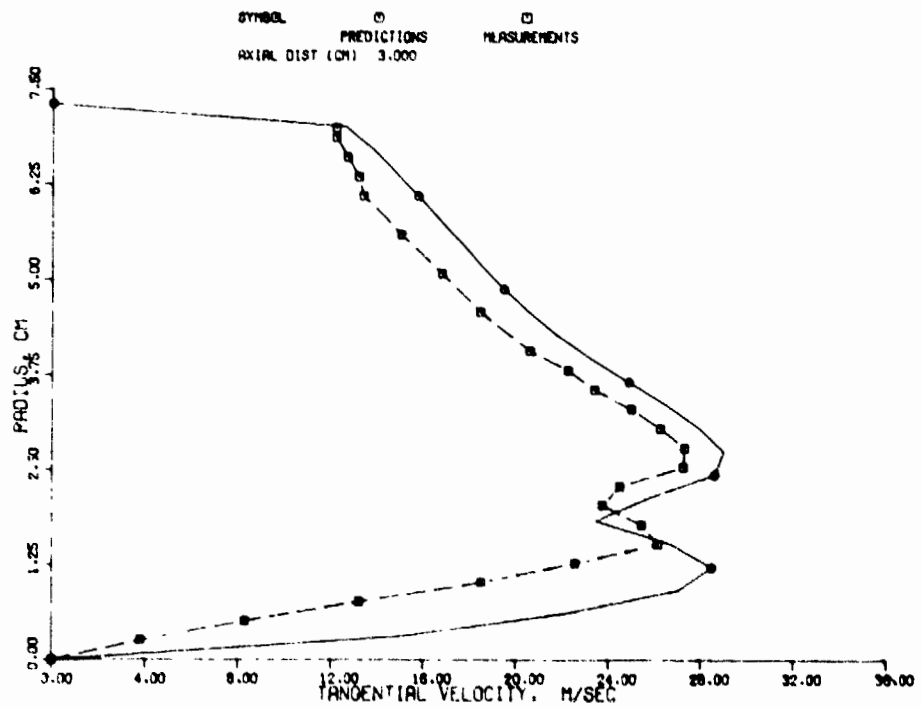

(c)

Figure 20. Tangential Velocity Profiles for Co-Swirl Case with Measured Inlet Profiles: Original K-ϵ Model (Contd).

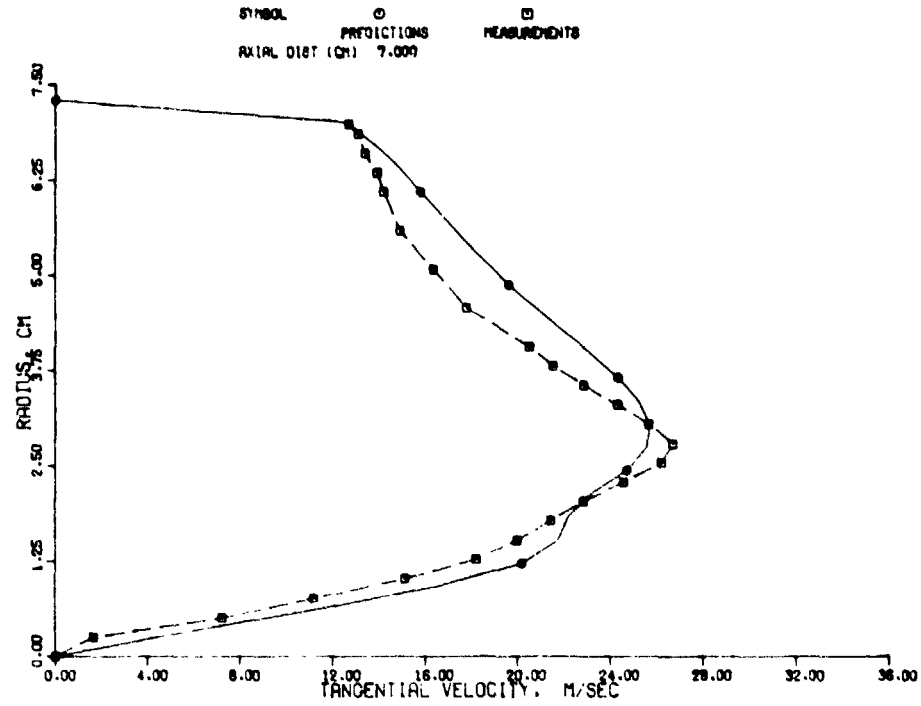

(d)

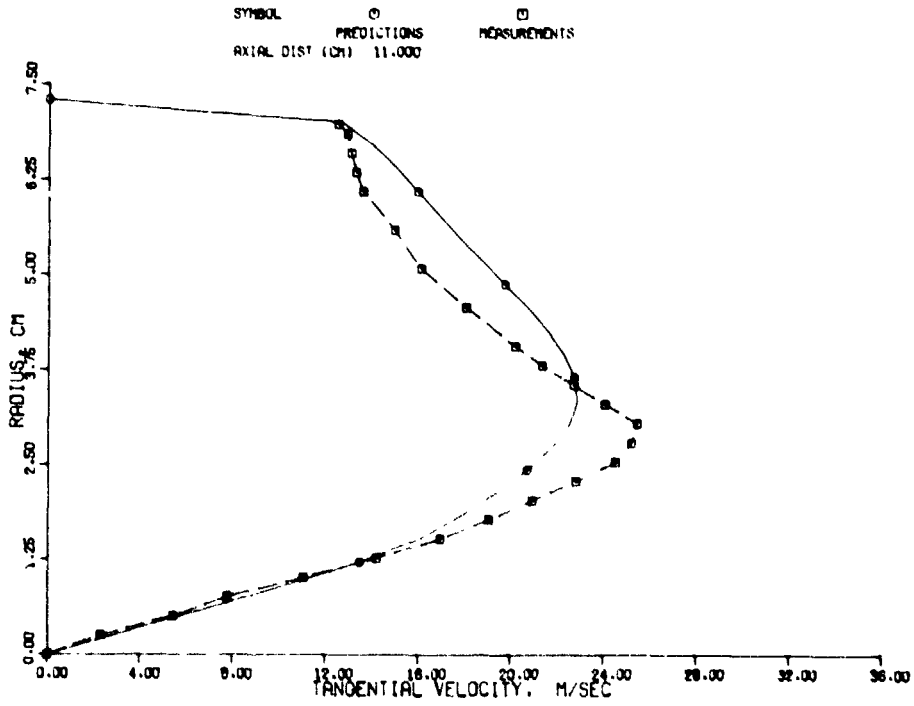

(e)

Figure 20. Tangential Velocity Profiles for Co-Swirl Case with Measured Inlet Profiles: Original K-ϵ Model (Contd).

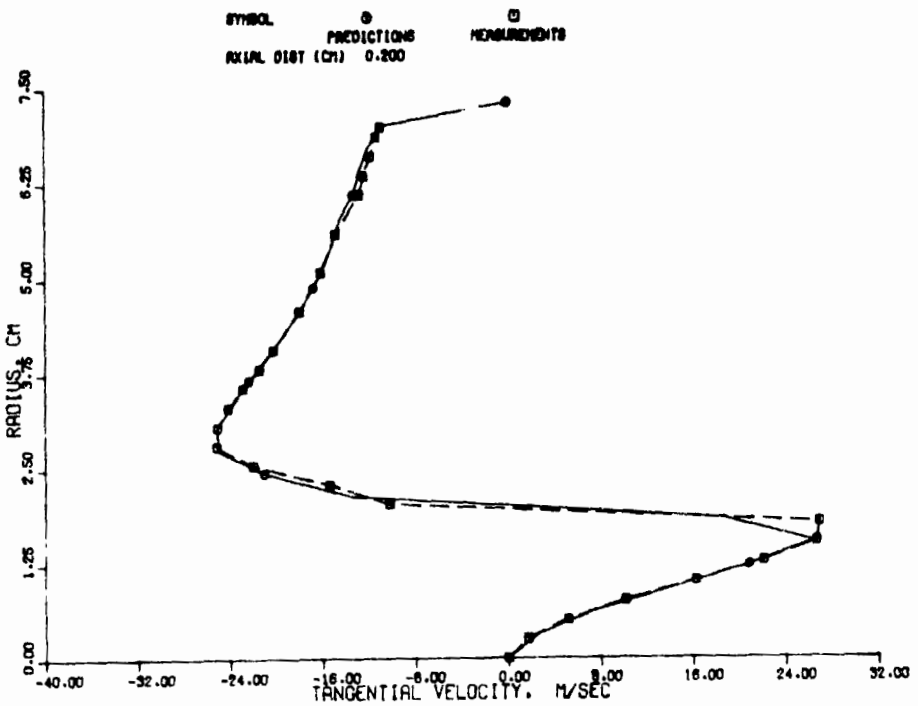

(a)

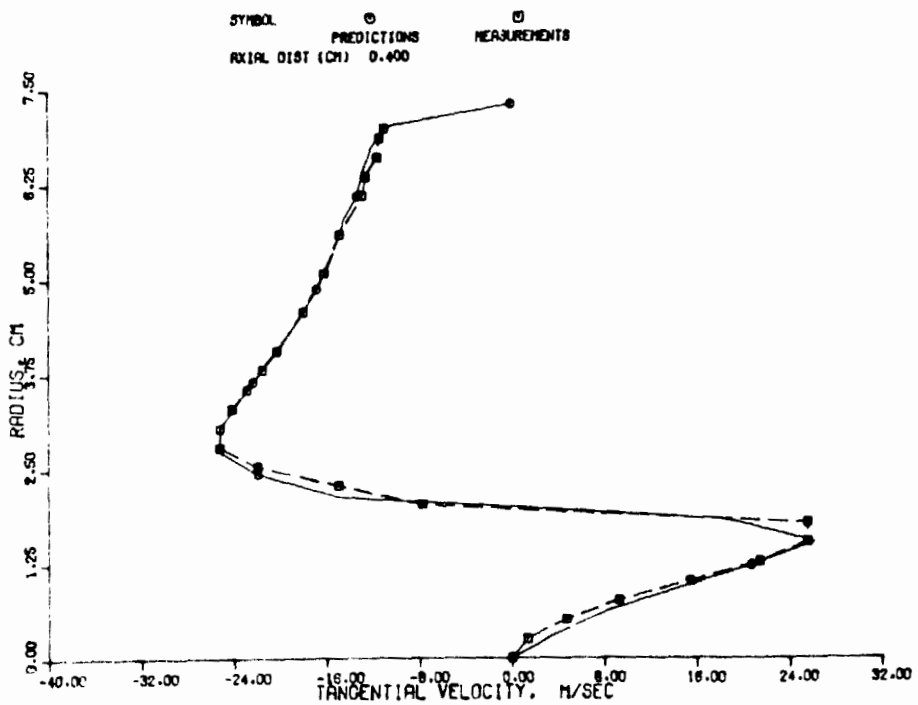

(b)

Figure 21. Tangential Velocity Profiles for Counterswirl Case with Measured Inlet Profiles: Original K-ε Model.

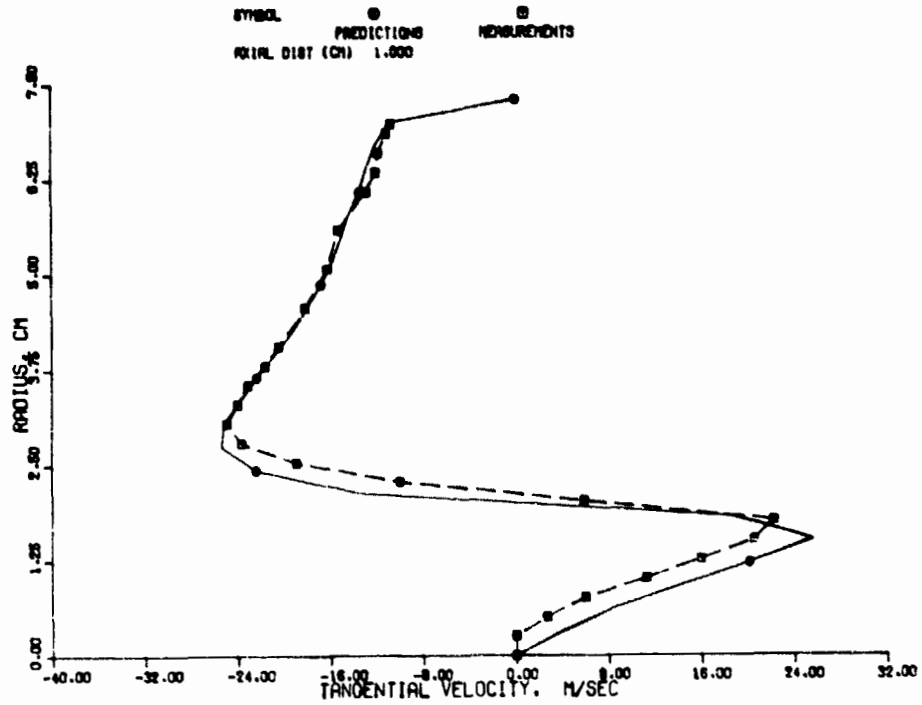

(c)

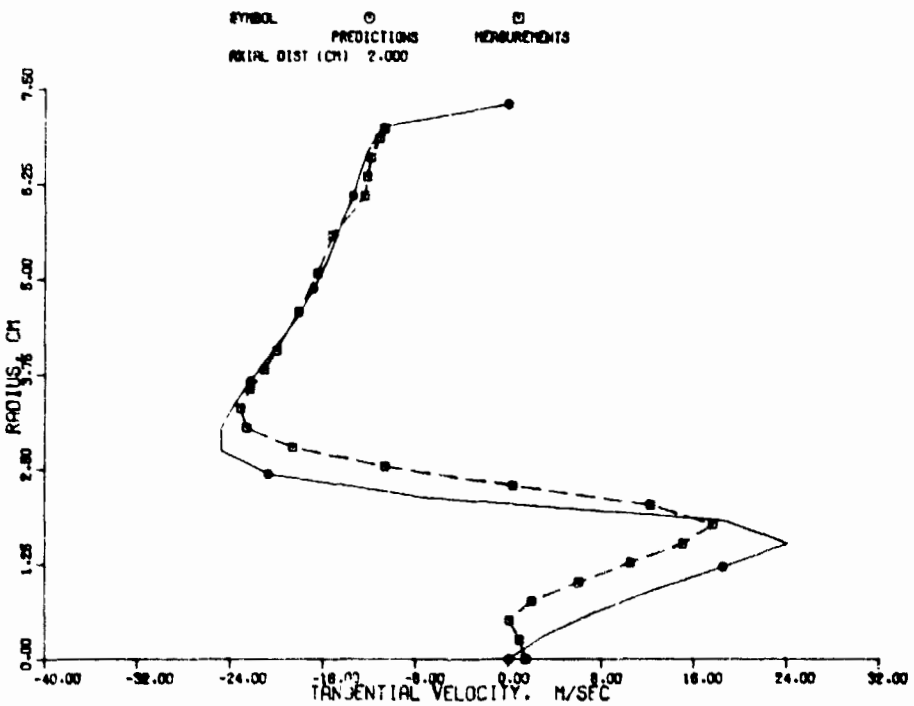

(d)

Figure 21. Tangential Velocity Profiles for Counterswirl Case with Measured Inlet Profiles: Original K-ϵ Model (Contd).

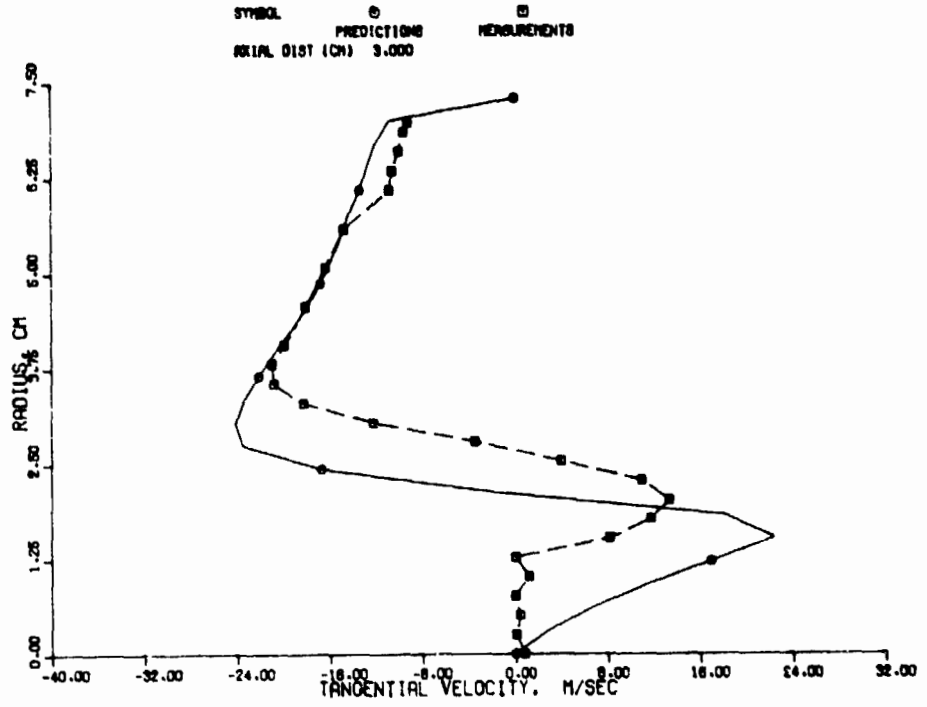

(e)

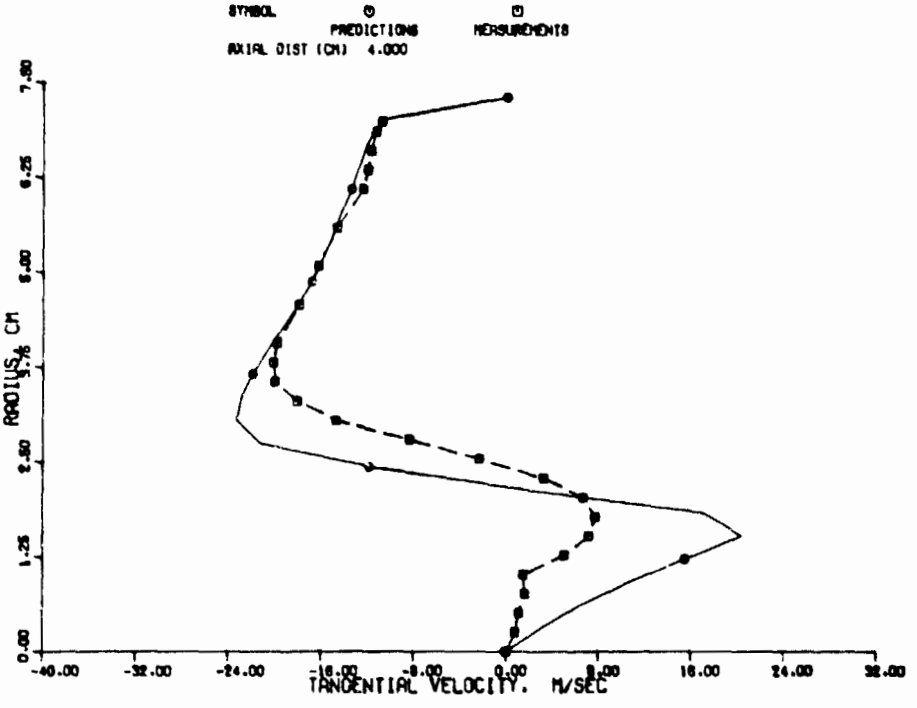

(f)

Figure 21. Tangential Velocity Profiles for Counterswirl Case with Measured Inlet Profiles: Original K-ε Model (Contd).

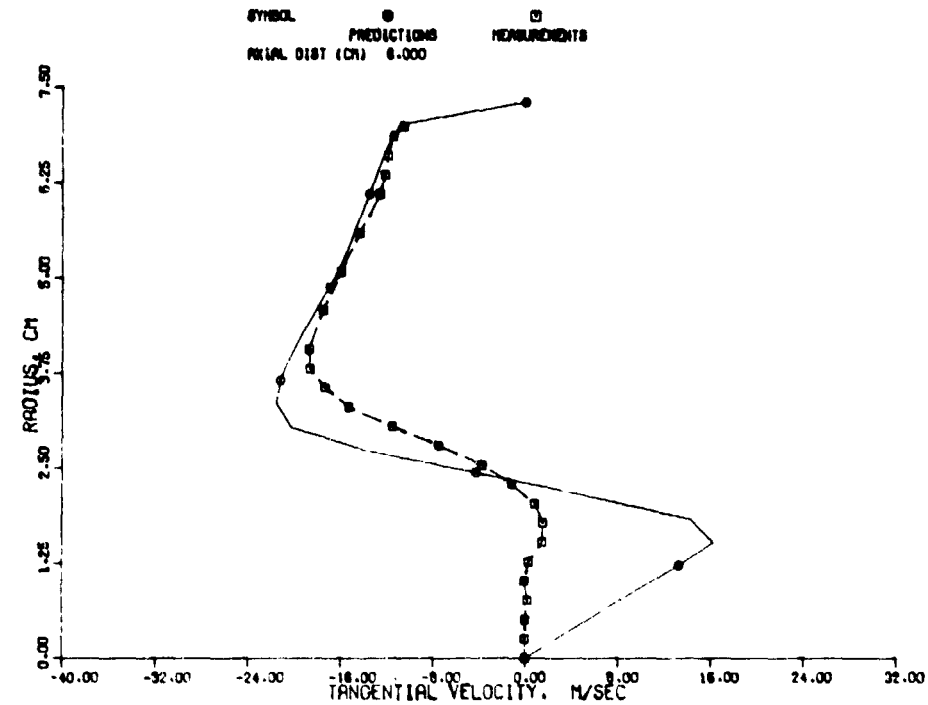

(g)

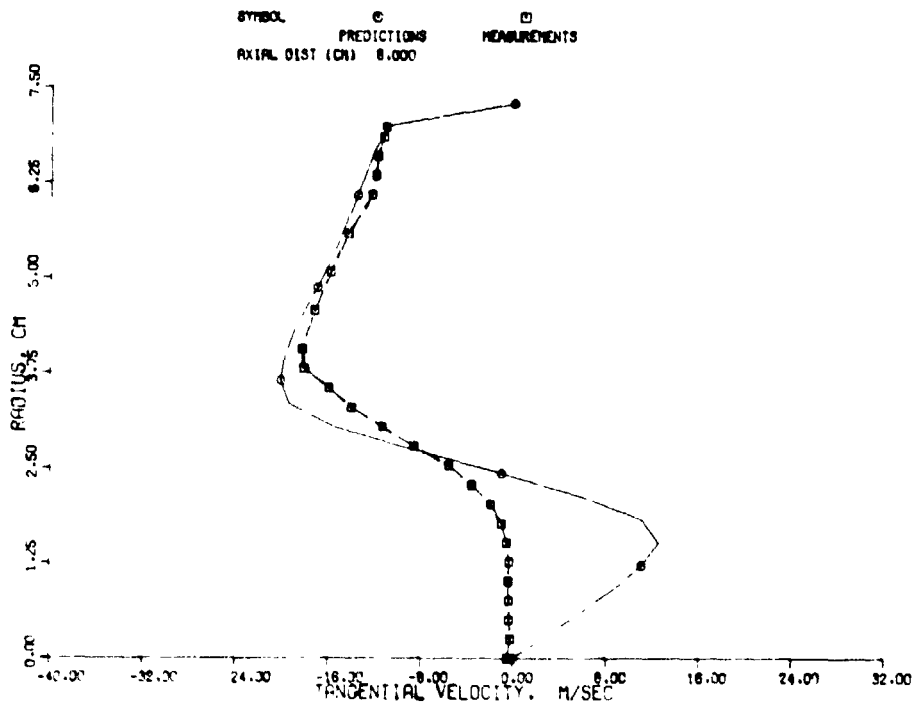

(h)

Figure 21. Tangential Velocity Profiles for Counterswirl Case with Measured Inlet Profiles: Original K-ϵ Model (Contd).

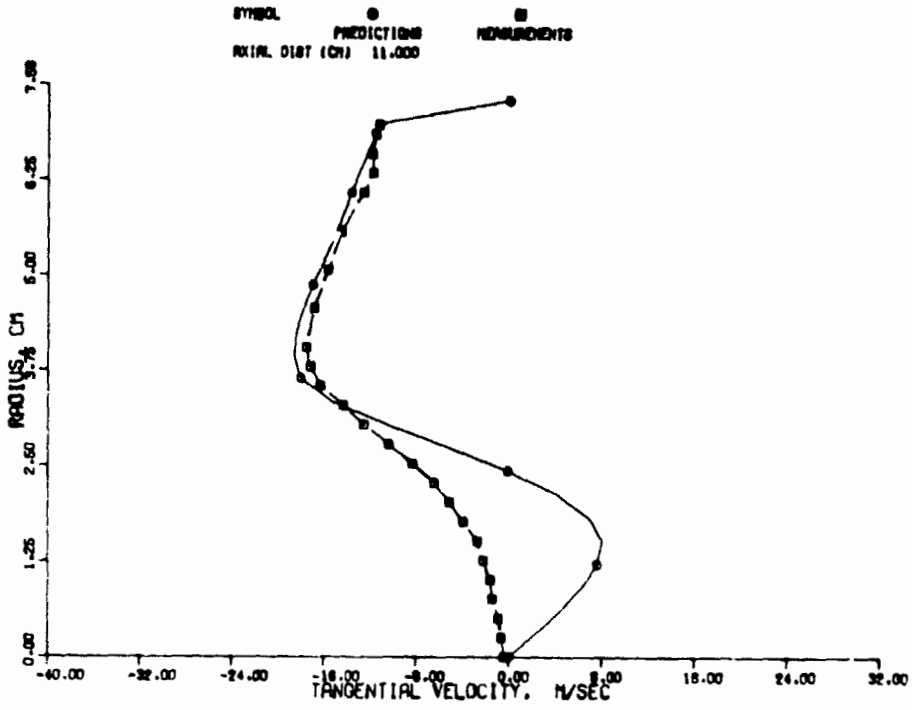

(i)

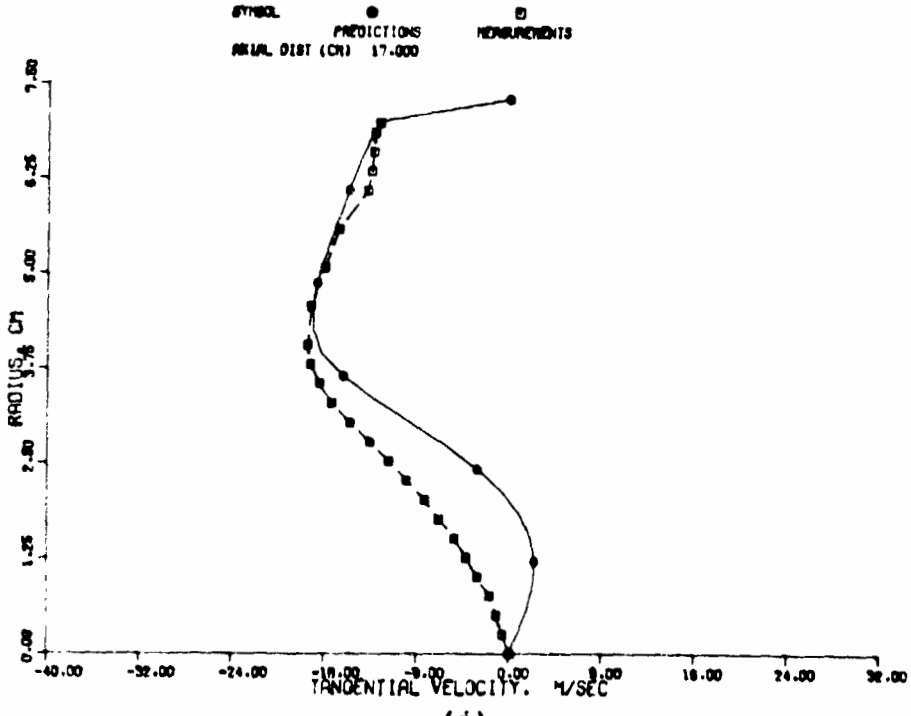

(j)

Figure 21. Tangential Velocity Profiles for Counterswirl Case with Measured Inlet Profiles: Original K-ϵ Model (Contd).

velocity of 99.74 fps (32.4 m/s), forced vortex (wherein V_θ is proportional to radius), turbulence kinetic energy of 30 $(fps)^2$ (2.8 m^2/S^2) and length scale equal to 0.014 inch (0.036 cm). Figures 22 through 24 show the axial velocity predictions at x = 0.37 (0.94 cm), 0.74 (1.88 cm), 1.11 (2.82 cm), 1.48 (3.76 cm) and 1.82 inches (4.62 cm) for a swirl number of 0.99 and different values of A. For A = 1, the predictions correspond to that of the original k-ϵ model. It should be emphasized that increasing the value of A increases only the angular momentum flux in the radial direction and does not directly alter the flux of any other quantity. As seen in these figures, increases in the value of A causes considerable changes in the profiles, although the trend near the pipe centerline does not appear to be realistic. The predictions for angular momentum, corresponding to a swirl number of 0.99 are shown in Figures 25 through 27.

Figures 28 through 30 show the axial velocity predictions for a 2.98 swirl number flow with different values for the empirical constant A. These figures show that increasing the radial transport of angular momentum tends to cause a flow reversal due to increased diffusion. This parametric study was made to demonstrate the shortcomings of the original k-ϵ model in handling complex flows with significant streamline curvature, thereby illustrating a need for an improved turbulence model to treat such flows.

Modified k-ϵ Model for Swirling Flows

Although the k-ϵ model accurately predicts the flow field for simple flows, any simple extension of the turbulence model to handle complex flows can at best be expected to give qualitative agreement with measurements (ref. 18), especially with regard to the turbulence parameters.

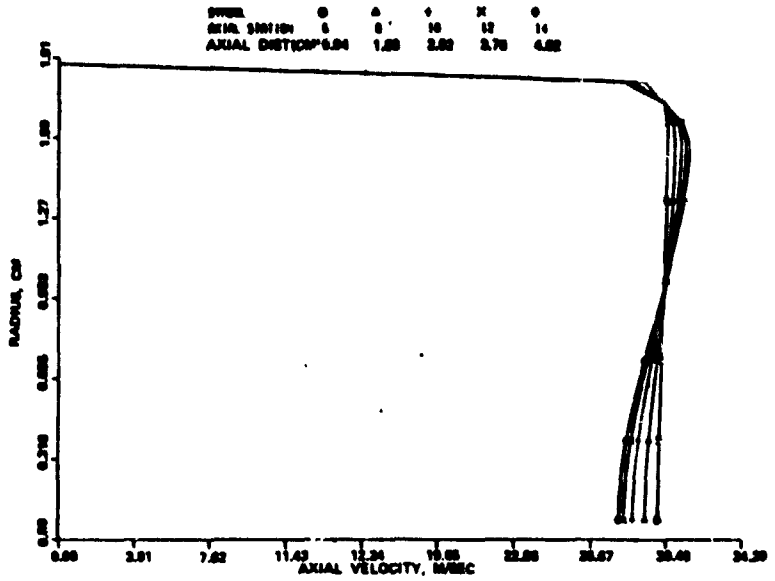

Figure 22. Axial Velocity Profiles for 0.99 Swirl Number Forced Vortex Plug Flow.

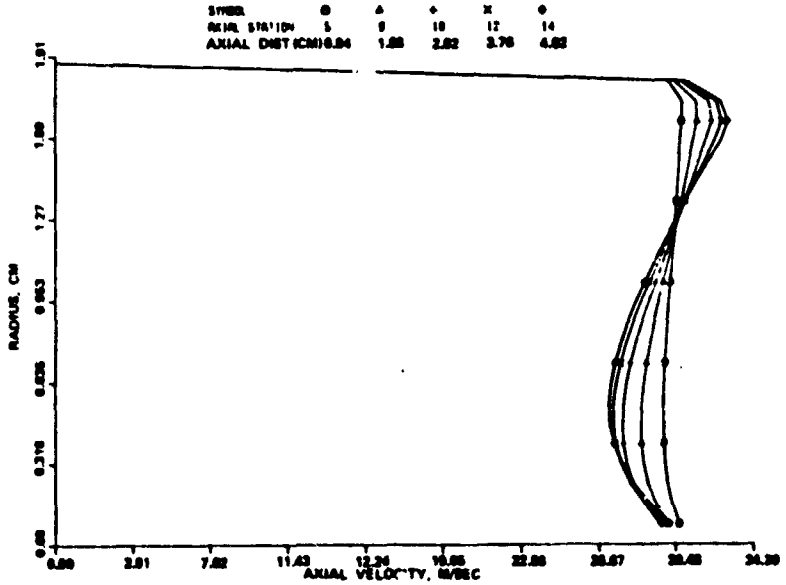

Figure 23. Axial Velocity Profiles for 0.99 Swirl Number Forced Vortex Flow 2 Times TY.

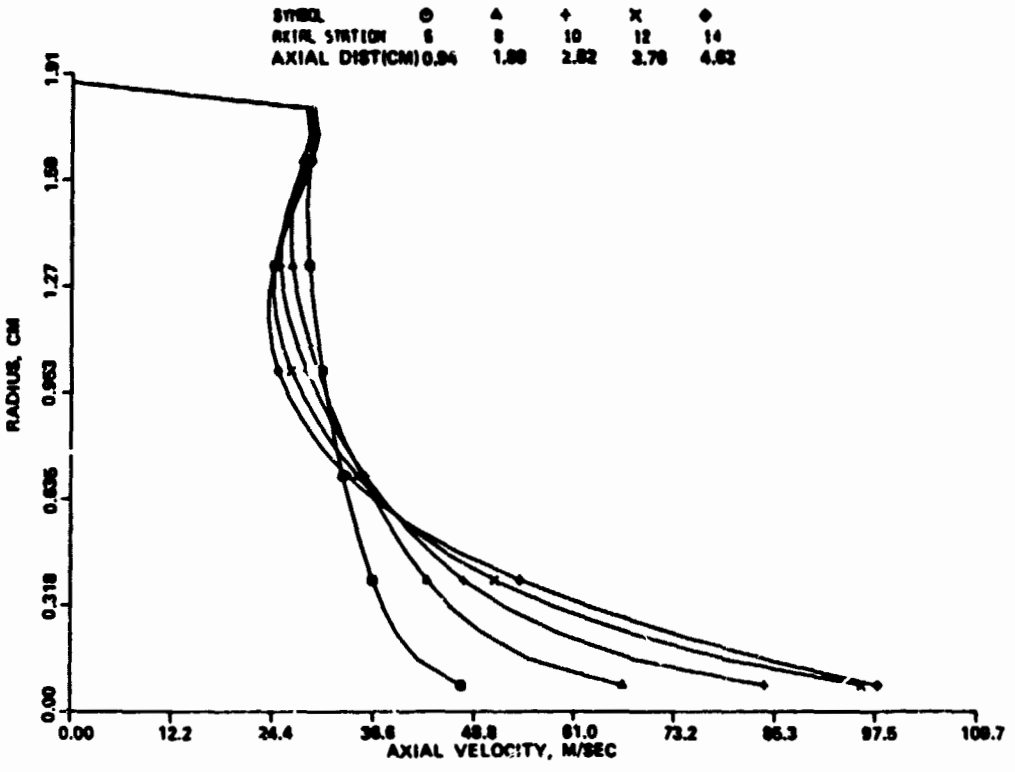

Figure 24. Axial Velocity Profiles for 0.99 Swirl Number Forced Vortex Flow 5 Times TY.

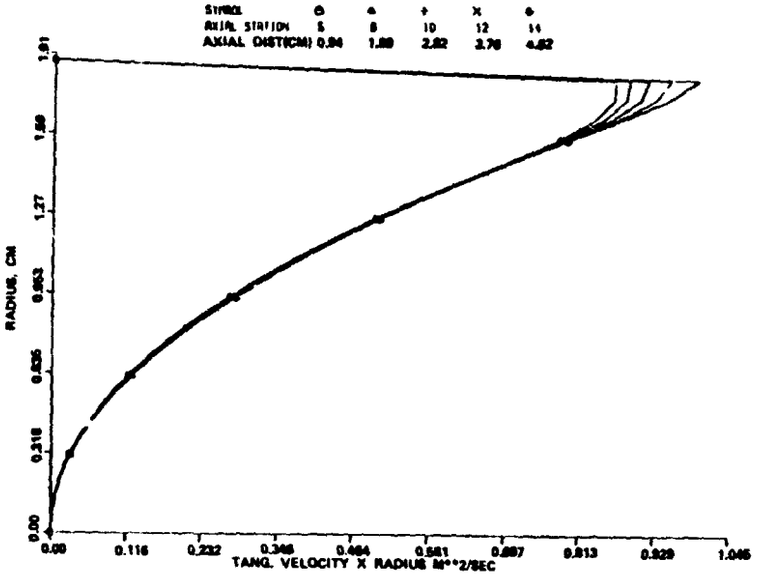

Figure 25. Tangential Velocity Profiles for 0.99 Swirl Number Forced Vortex Plug Flow.

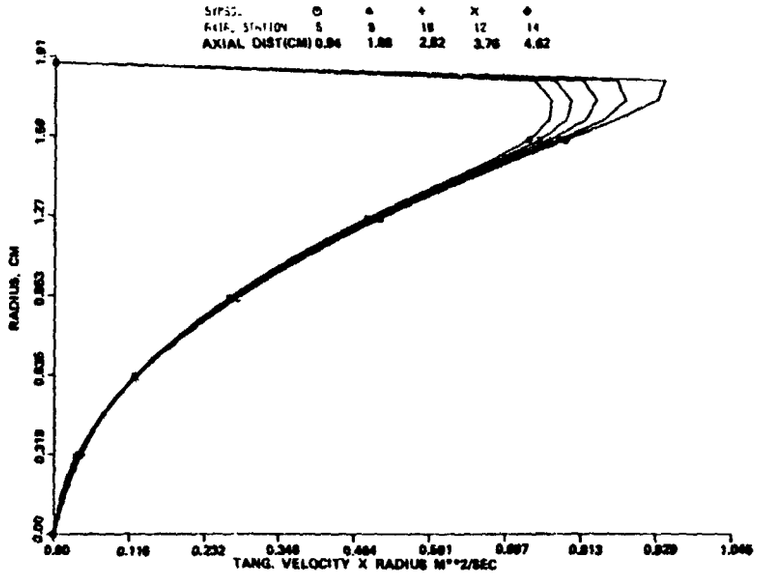

Figure 26. Tangential Velocity Profiles for 0.99 Swirl Number Forced Vortex Plug Flow 2 Times TY.

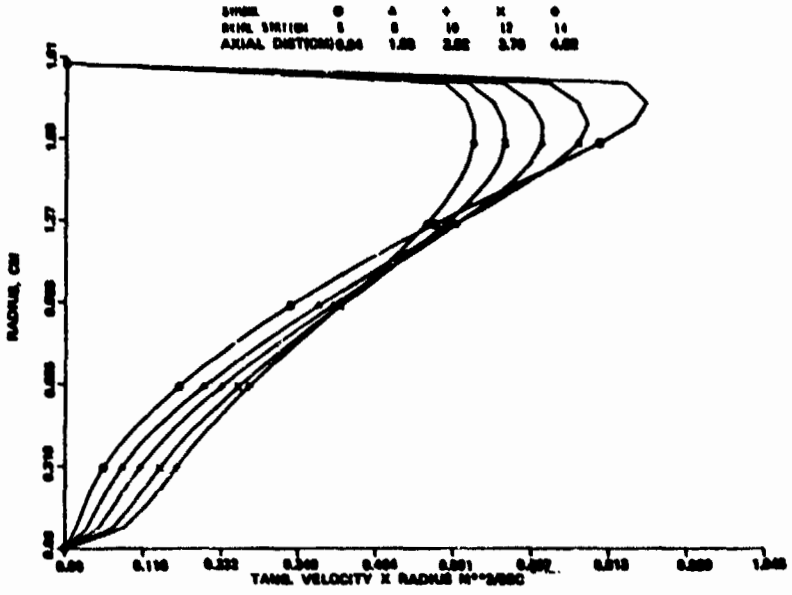

Figure 27. Tangential Velocity Profiles for 0.99 Swirl Number Forced Vortex Plug Flow 5 Times TY.

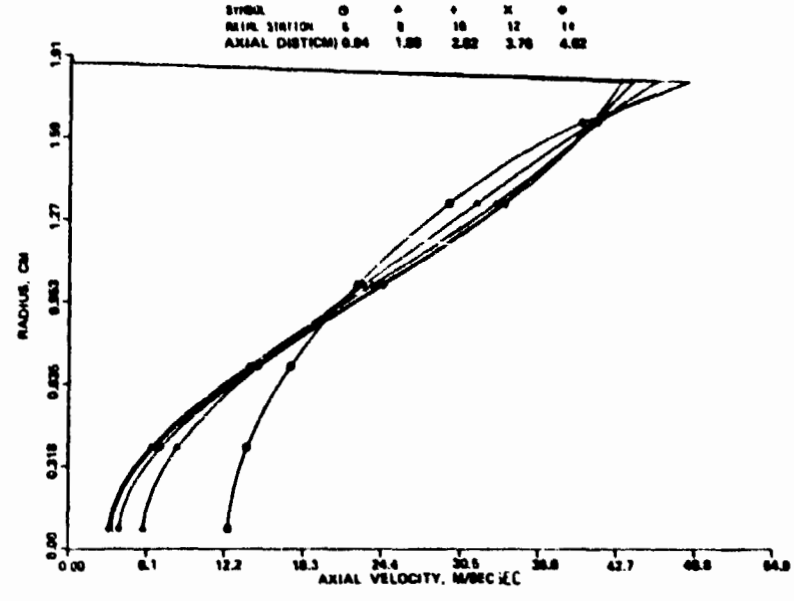

Figure 28. Axial Velocity Profiles for 2.98 Swirl Number Forced Vortex Plug Flow 1 Time TY.

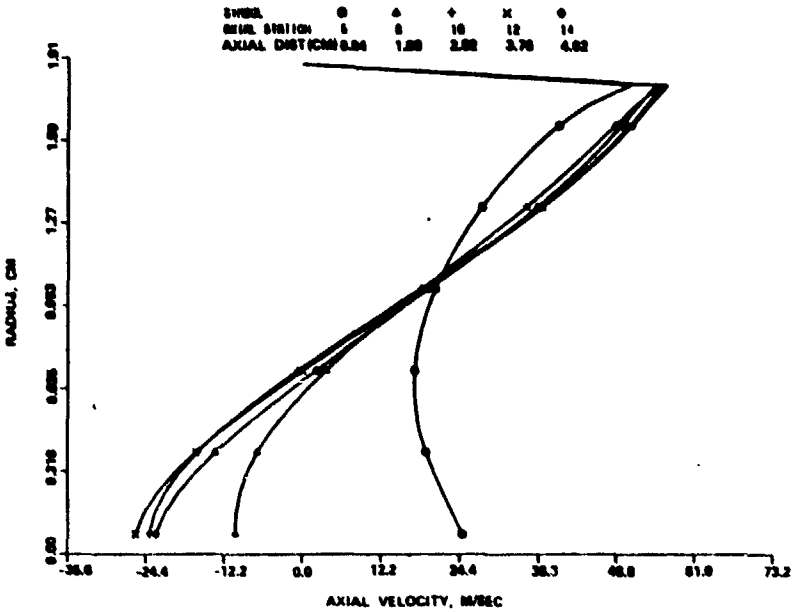

Figure 29. Axial Velocity Profiles for 2.98 Swirl Number Forced Vortex Plug Flow 2 Times TY.

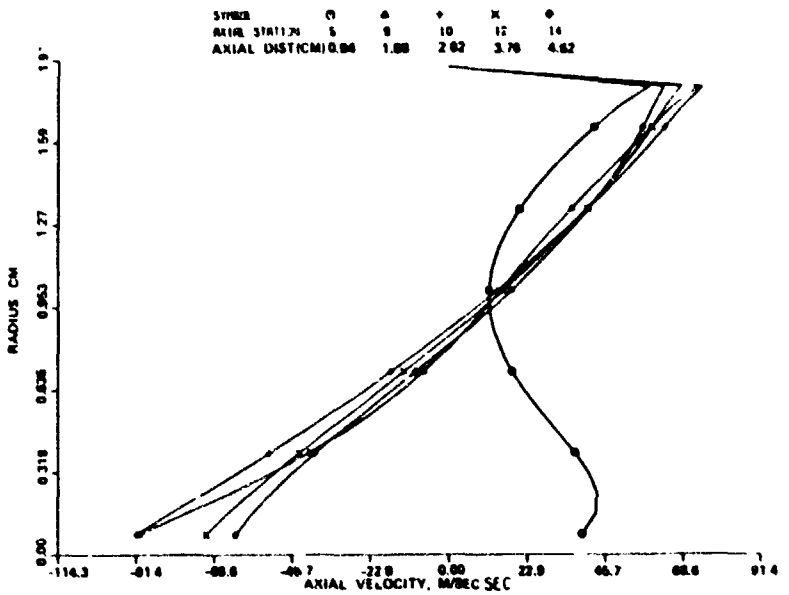

Figure 30. Axial Velocity Profiles for 2.98 Swirl Number Forced Vortex Plug Flow 5 Times TY.

The turbulence modeling approach employed in this study was based upon the suggestions by Bradshaw (ref. 18), where the effect of streamline curvature on the turbulence scale is expressed by

$$l = l_o\ (1-\beta R_i) \tag{16}$$

where l_o is the mixing length in a simple flow, β and Ri are the empirical constant and the appropriate Richardson number. The Richardson number is a measure of the extra strain rate associated with the streamline curvature.

Militzer, Nicoll, and Alpay (ref. 30) followed the approach of modifying the source term, G_K, in the transport equation for turbulence kinetic energy for obtaining good correlations with measurements in the recirculating region produced by two plane parallel unconfined jets. The modified source term G_K' obtained by them was given by

$$G_K' = S_c\ G_K \tag{17}$$

$$S_c = A_1\ (1 - \exp[A_2(F-A_3)]) \tag{18}$$

$$F = \frac{\sqrt{U^2 + V^2}}{R(\frac{\partial U}{\partial Y} + \frac{\partial V}{\partial X})} \tag{19}$$

$$\frac{1}{R} = \frac{UV(\frac{\partial V}{\partial y} - \frac{\partial U}{\partial X})}{(U^2 + V^2)^{3/2}} \tag{20}$$

$$G_K = \mu_{eff}\left\{2(\frac{\partial U}{\partial X})^2 + 2(\frac{\partial V}{\partial Y})^2 + (\frac{\partial U}{\partial Y}+\frac{\partial V}{\partial X})^2\right\} \tag{21}$$

The empirical constants A_1, A_2 ,and A_3 were equal to 1.15, 11.3 and 0.18, respectively. S_c was set equal to zero for F values greater than or equal to A_3. With this modification, the 2-D elliptic program using the upwind difference scheme resulted in poor comparison with measurements (ref. 31). However, by utilizing the skewed upwind numerical scheme developed by Raithby (ref. 32), excellent agreement between predictions and experiment was reported. The method employed by Militzer et.al. was limited to nonswirling flows.

Launder (ref. 33) proposed a simple modification to the constant C_2 in the k-ϵ turbulence model, of the form

$$C_2 = 1.92 - C_{2_{V_\theta}} \, Ri_{V_\theta}, \tag{22}$$

where

$$Ri_{V_\theta} = \frac{\left(\frac{V_\theta}{r^2}\right)\frac{\partial}{\partial r}(rV_\theta)}{\left(\frac{\partial U}{\partial r}\right)^2 + \left[r\frac{\partial}{\partial r}\left(\frac{V_\theta}{r}\right)\right]^2} \tag{23}$$

and $C_{2_{V_\theta}}$ is an empirical constant. It is noted that the original k-ϵ model is recovered by setting $C_{2_{V_\theta}} = 0$.

A series of computations were made with Morse's modification and using the measured velocity profiles as input. Several different values of $C_{2_{V_\theta}}$ were used in this series of computations. Morse's recommended value for $C_{2_{V_\theta}}$ is 0.36. The predicted results for counterswirl case using $C_{2_{V_\theta}} = 1.62$ are presented in Figures 31 and 32. The value of 1.62 for $C_{2_{V_\theta}}$ gave by far the best agreement with the data.

Figure 31 shows a comparison of the axial velocity profiles, at several axial stations, between the predictions and measurements. It is interesting to note that Morse's model does

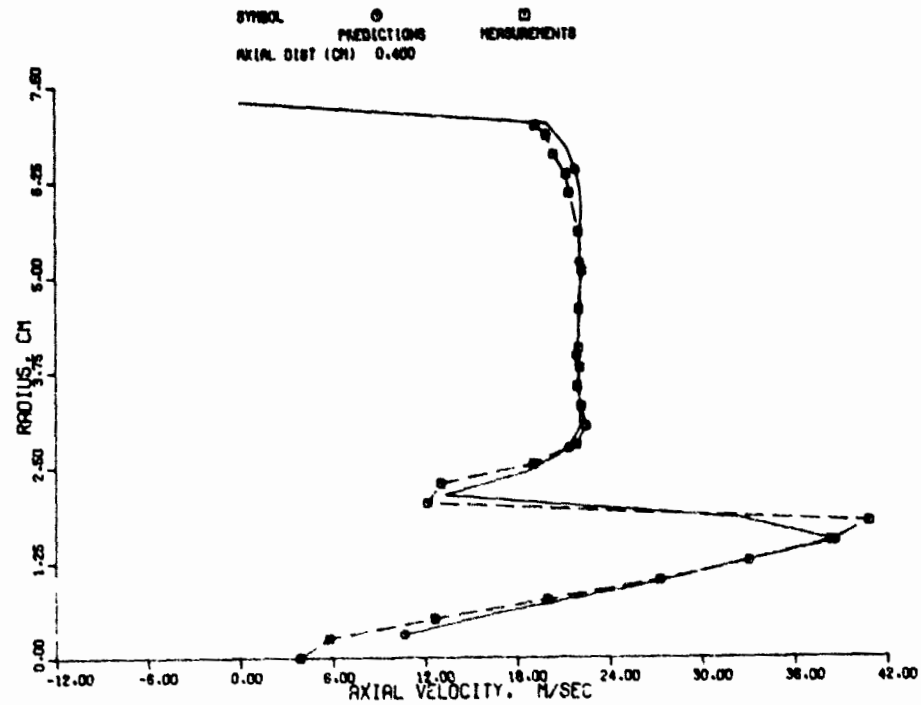

(a)

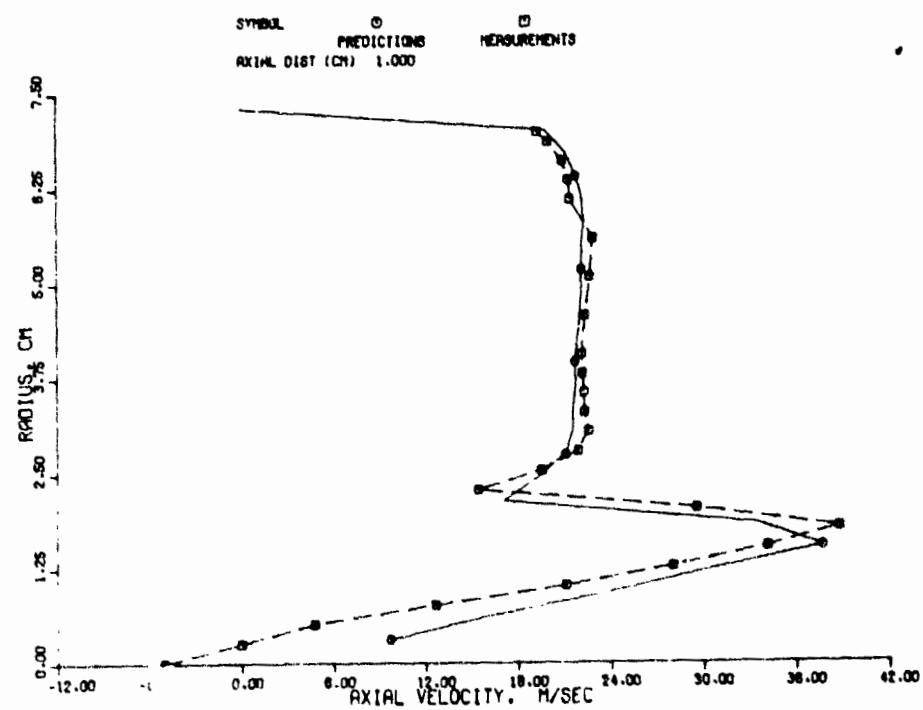

(b)

Figure 31. Axial Velocity Profiles for Counterswirl Case; Morse's Model, $C_{2_{V_\theta}} = 1.62$.

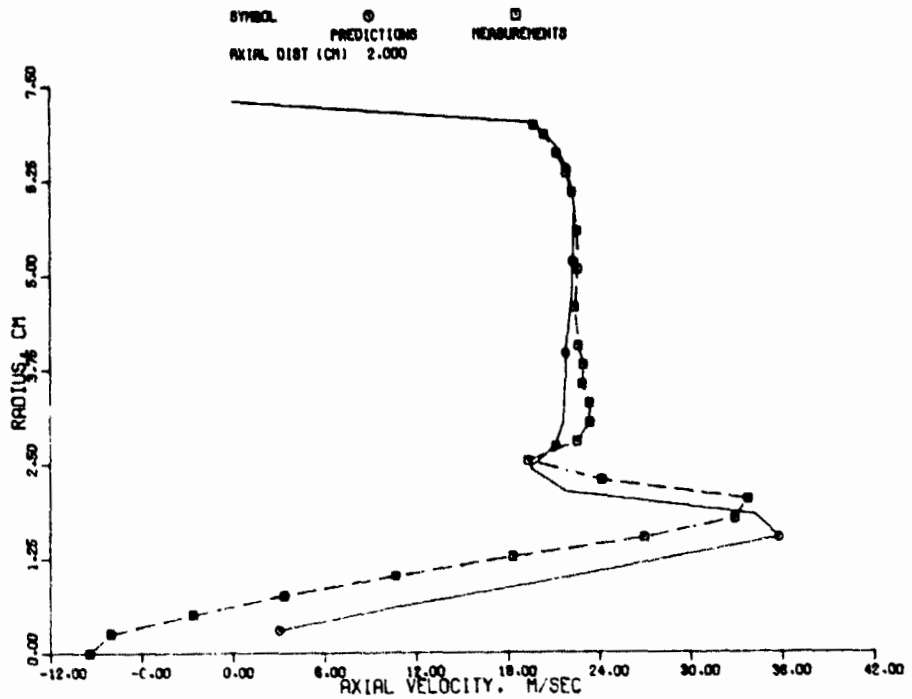

(c)

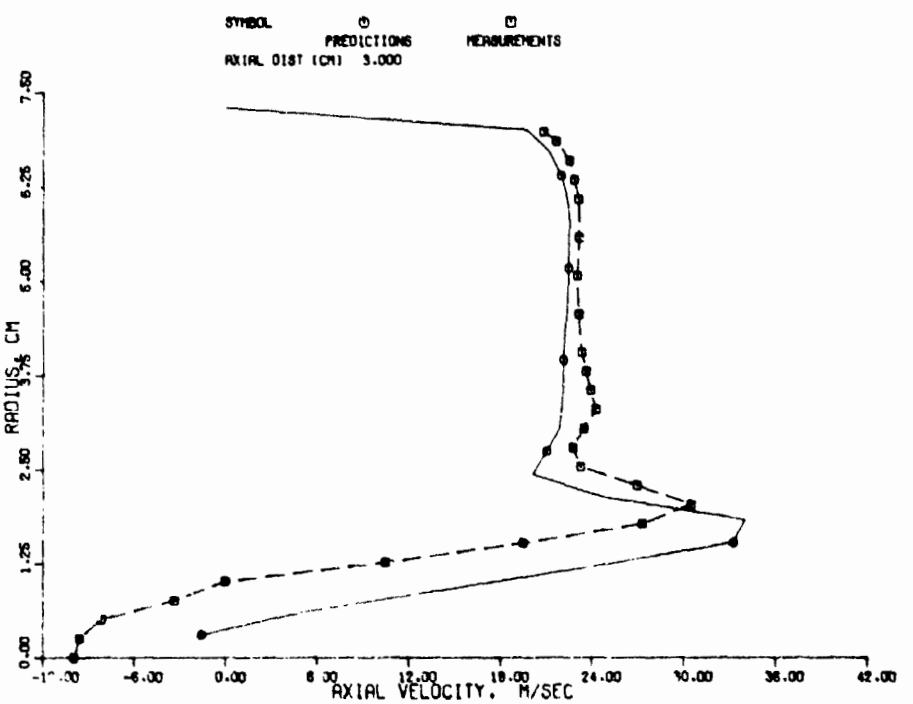

(d)

Figure 31. Axial Velocity Profiles for Counterswirl Case; Morse's Model, $C_{2_{V_\theta}} = 1.62$ (Contd).

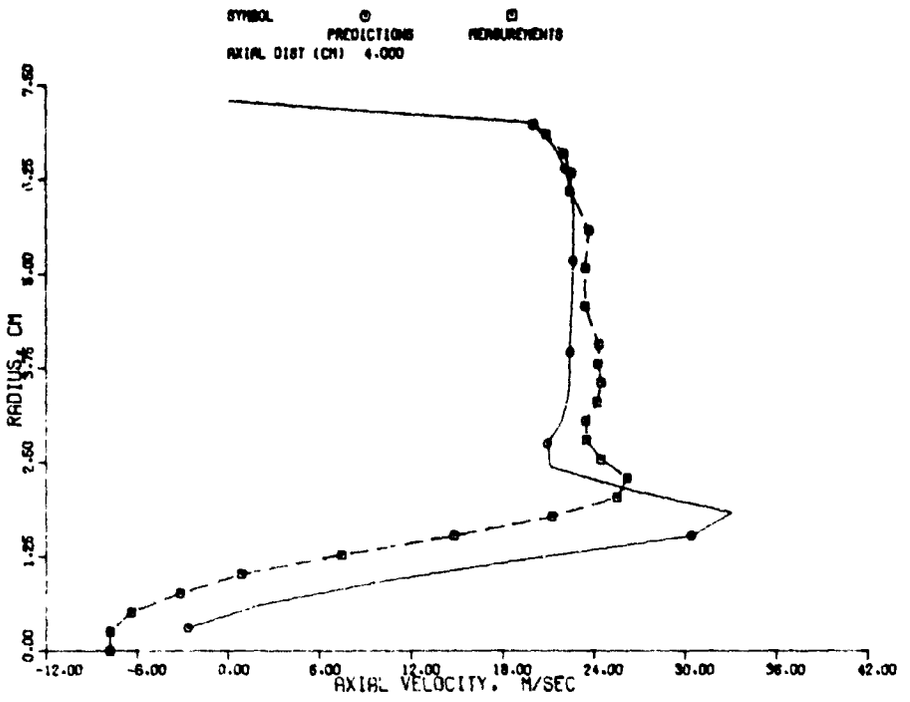

(e)

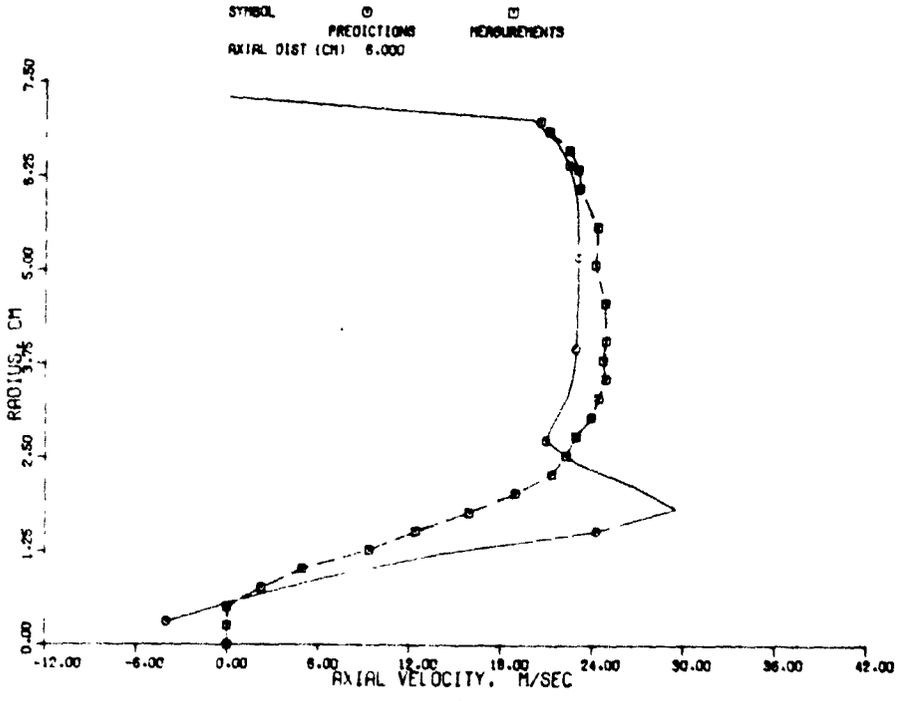

(f)

Figure 31. Axial Velocity Profiles for Counterswirl Case; Morse's Model, $C_{2_{V_\theta}} = 1.62$ (Contd).

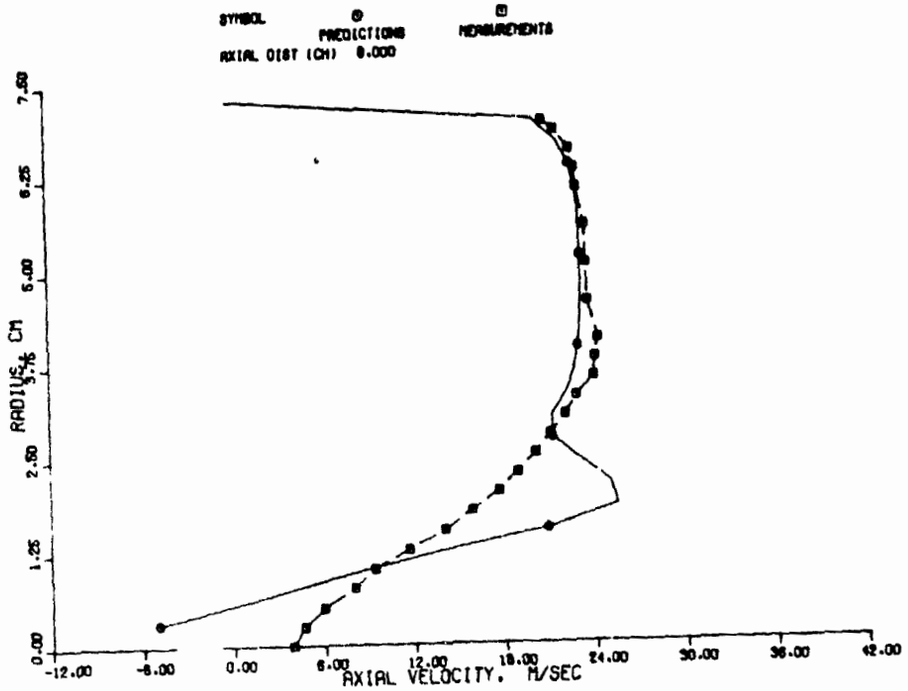

(g)

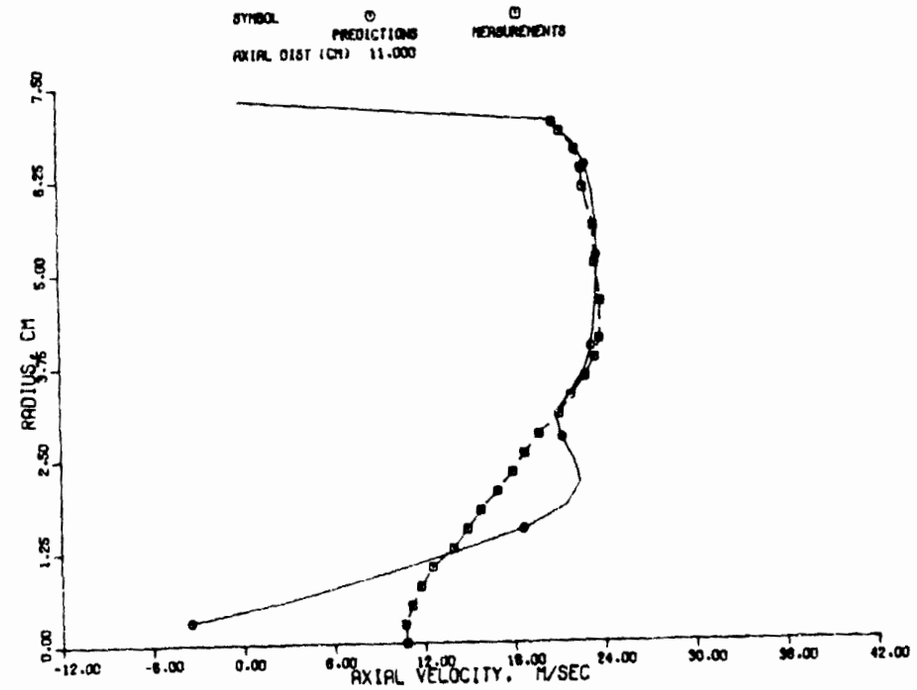

(h)

Figure 31. Axial Velocity Profiles for Counterswirl Case; Morse's Model, $C_{2_{V_\theta}} = 1.62$ (Contd).

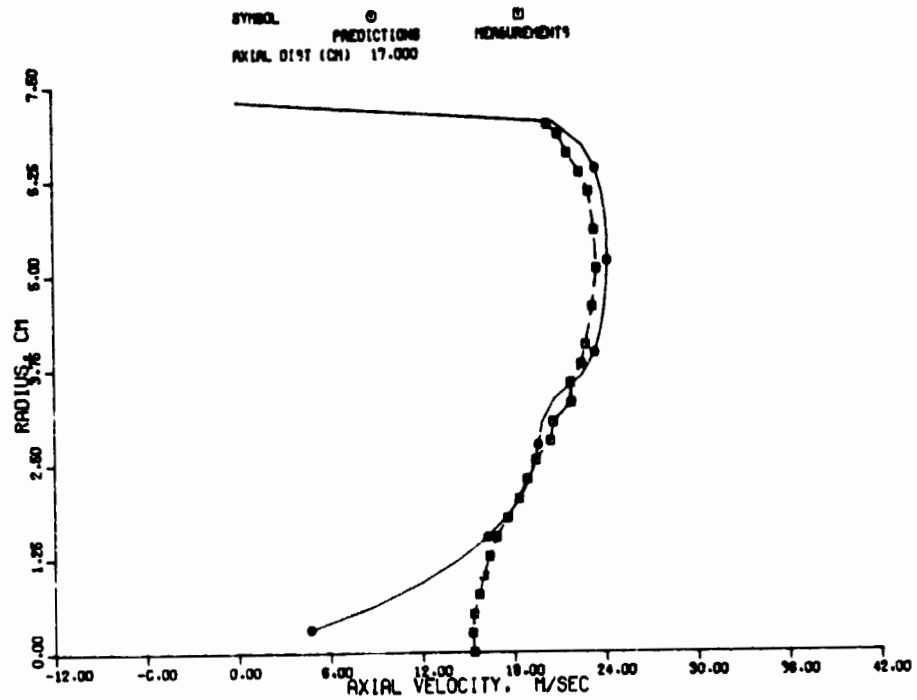

(i)

Figure 31. Axial Velocity Profiles for Counterswirl Case; Morse's Model, $C_{2_{V_\theta}}$ = 1.62 (Contd)

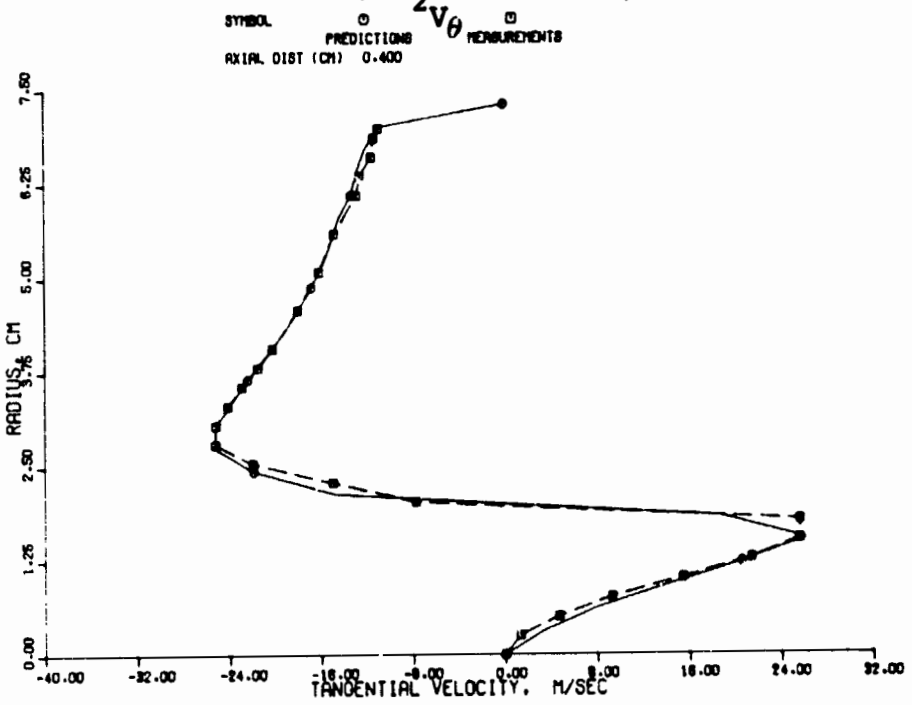

(a)

Figure 32. Tangential Velocity Profiles for Counterswirl Case; Morse's Model, $C_{2_{V_\theta}}$ = 1.62.

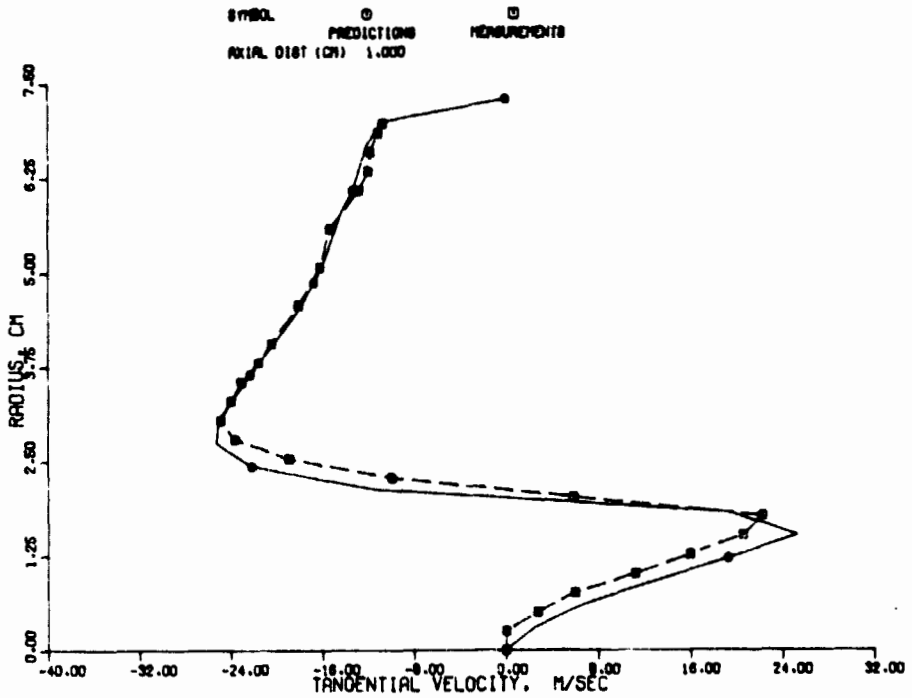

(b)

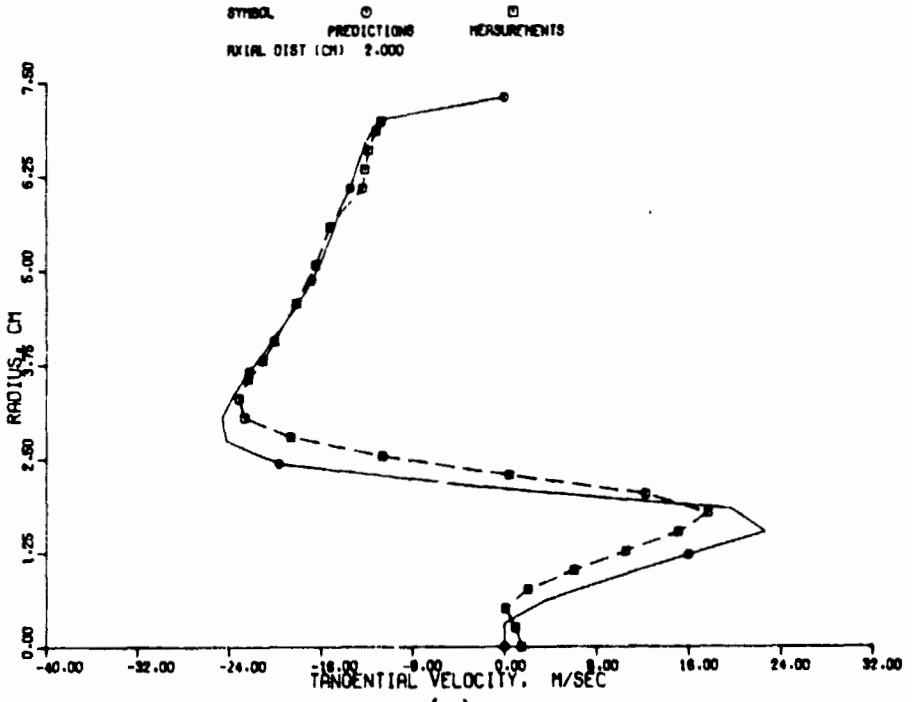

(c)

Figure 32. Tangential Velocity Profiles for Counterswirl Case; Morse's Model, $C_{2_{V_\theta}} = 1.62$ (Contd).

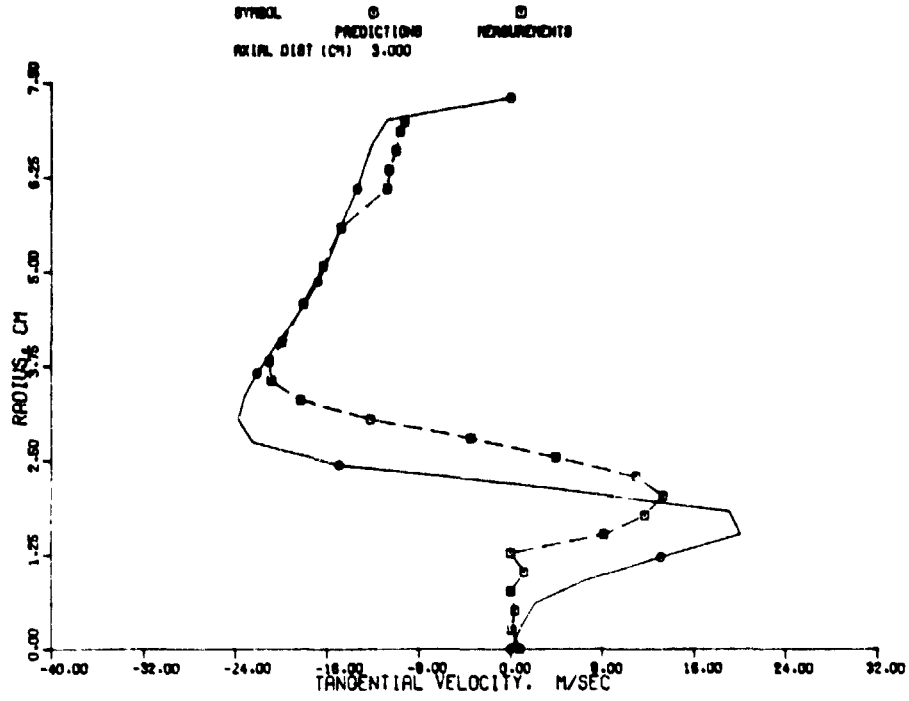

(d)

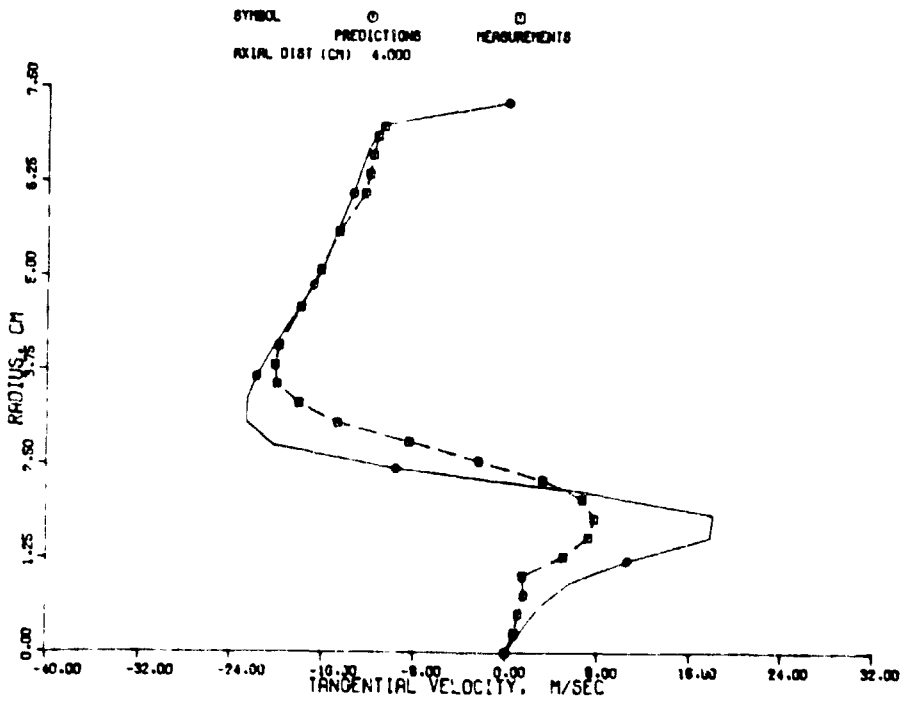

(e)

Figure 32. Tangential Velocity Profiles for Counterswirl Case; Morse's Model, $C_{2_{V_\theta}} = 1.62$ (Contd).

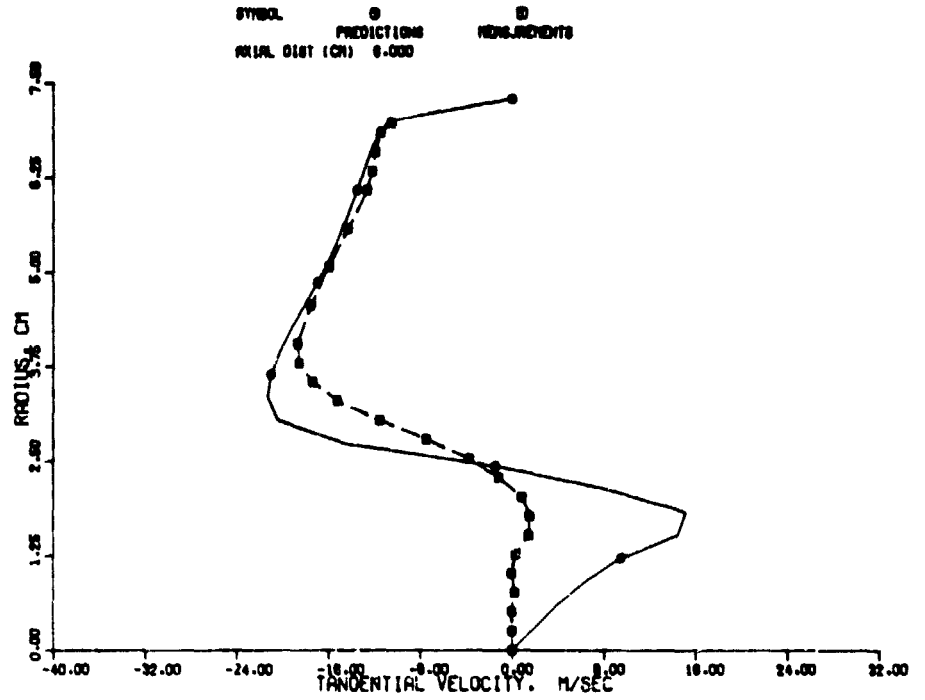

(f)

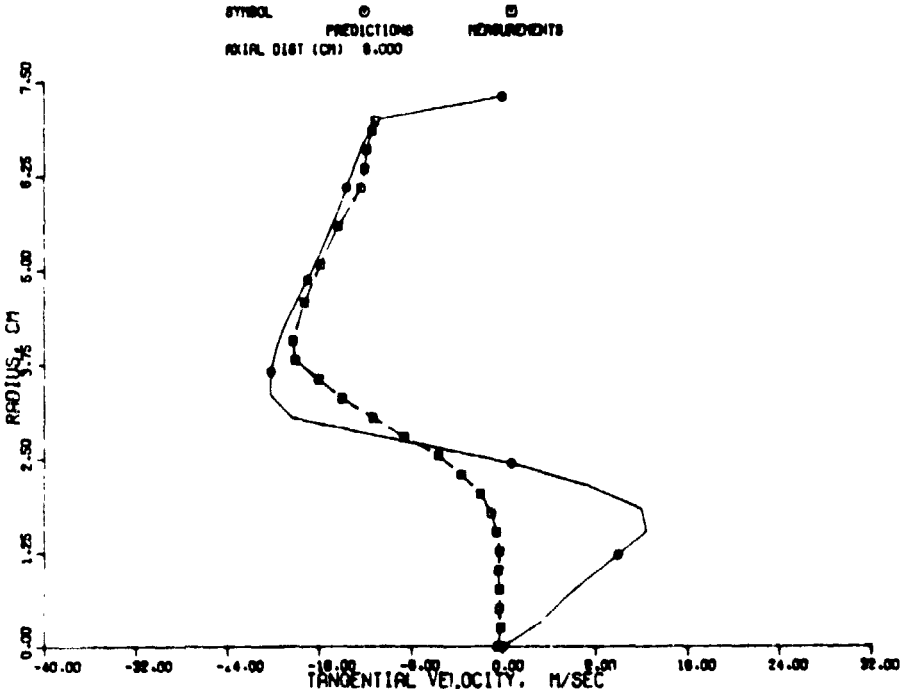

(g)

Figure 32. Tangential Velocity Profiles for Counterswirl Case; Morse's Model, $C_{2_{V_\theta}}$ = 1.62 (Contd).

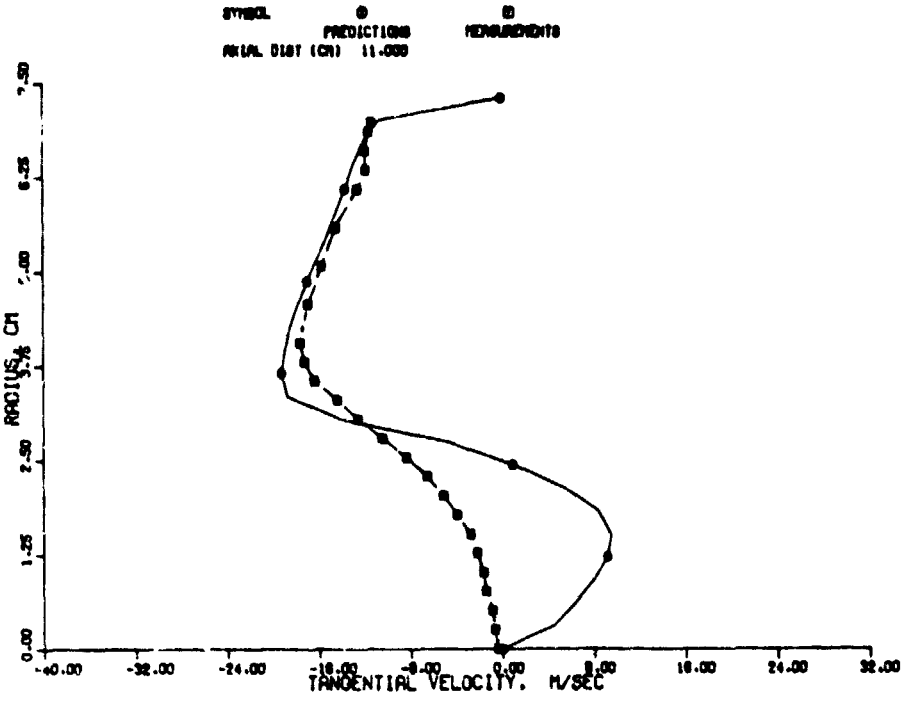

(h)

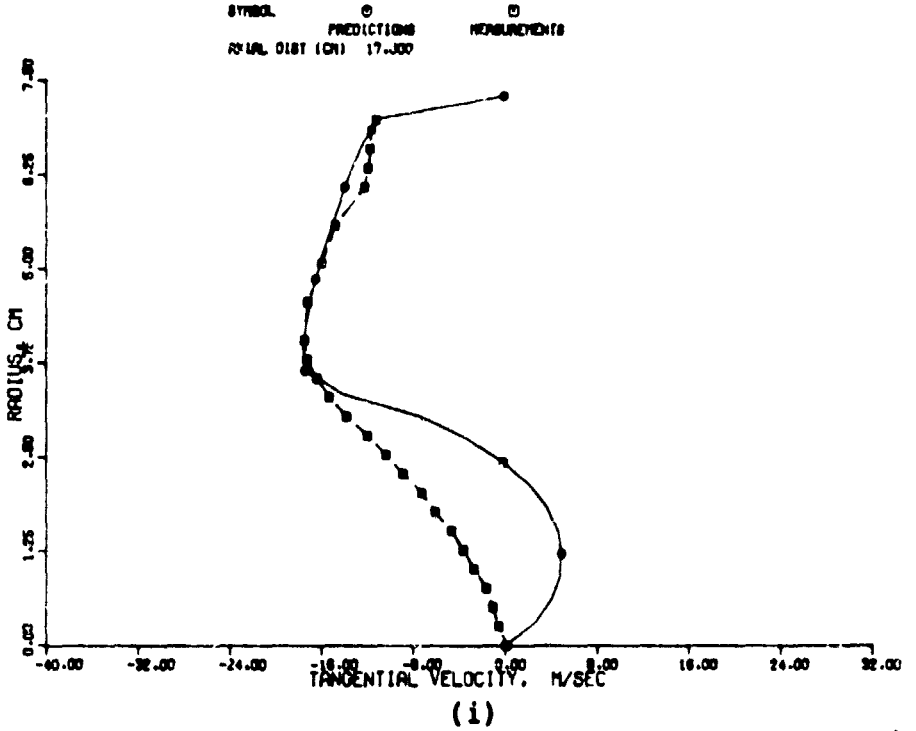

(i)

Figure 32. Tangential Velocity Profiles for Counterswirl Case; Morse's Model, $C_{2_{V_\theta}} = 1.62$ (Contd).

predict a recirculation zone. Although this model shows improvements in the agreement with the data, particularly in the recirculation zone (x between 1 cm and 6 cm), still better agreement is desirable near the centerline of the tube.

Figure 32 represents a comparison between the predicted and the measured data for tangential velocities. These figures show a noticeable improvement in the results in the proximity of the recirculation zone. Despite these improvements, still better agreement is deemed necessary.

This series of tests revealed that, as the value of C_{2_V} was increased, the agreement between predictions and the measurements gradually improved. But, for values of C_{2_V} larger than 1.62, the recirculation zone gradually became smaller and smaller. This trend was detected to be associated with C_2 becoming negative at some point in the flow field, which is unrealistic.

This difficulty was overcome by adopting the following modification:

$$C_2 = 1.92 \exp(2\alpha_{V_\theta} \, Ri_{V_\theta} + 2\alpha_c \, Ri_c) \tag{24}$$

where α_{V_θ} and α_c are empirical constants, Ri_{V_θ} is the swirl Richardson number and Ri_c is the curvature Richardson number. The definition of Ri_{V_θ} is given in Equation (24); Ri_c is obtained by adopting the method of Militzer, et.al. (ref. 31) as

$$Ri_c = \frac{\sqrt{U^2 + V^2}}{R\left[\frac{1}{r}\frac{\partial}{\partial r}(rU) + \frac{\partial V}{\partial x}\right]} \tag{25}$$

where, the radius of curvature, R, is defined by

$$\left(\frac{1}{R}\right) = \frac{UV\left[\frac{1}{r}\frac{\partial}{\partial r}(rU) - \frac{\partial U}{\partial x}\right]}{(U^2 + V^2)^{3/2}} \qquad (26)$$

The exponential form adopted in this model ensures that C_2 can never become negative. In order to establish the relative magnitudes of Ri_c and Ri_{V_θ}, computations were made with several values of α_{V_θ} and α_c. For reasons of brevity, only some of these results are presented in this report.

The predicted axial velocity profiles for the counterswirl case with $\alpha_{V_\theta} = -0.75$ and $\alpha_c = 0$ are compared with measurements in Figure 33. The inlet profiles for the mixing region used in these computations were obtained from measurements. The predicted profiles for this case indicate a much better agreement in the recirculation zone than the original k-ϵ model. In the initial mixing region, including the recirculation zone, the modified k-ϵ model with $\alpha_{V_\theta} = -0.75$ and $\alpha_c = 0$ gives better correlation than the original k-ϵ model. But, in the region downstream of the recirculation zone (x>8 cm), the modified k-ϵ model is in poorer agreement with measurements than the original k-ϵ model. This trend is also exhibited in the tangential velocity predictions as shown in Figure 34. The modified k-ϵ model predictions show kinks in the tangential velocity profiles especially in the recirculation zone. These kinks in the profiles were not observed in the original k-ϵ model predictions. The modified k-ϵ model showed improvements in the agreement in the recirculation zone. In addition, the centerline axial velocity recovery is much slower than that predicted by the original k-ϵ model and is in better agreement with the trends seen in the data.

To illustrate the effects of the curvature of the streamlines on the turbulent transport, a non-zero value for α_c was

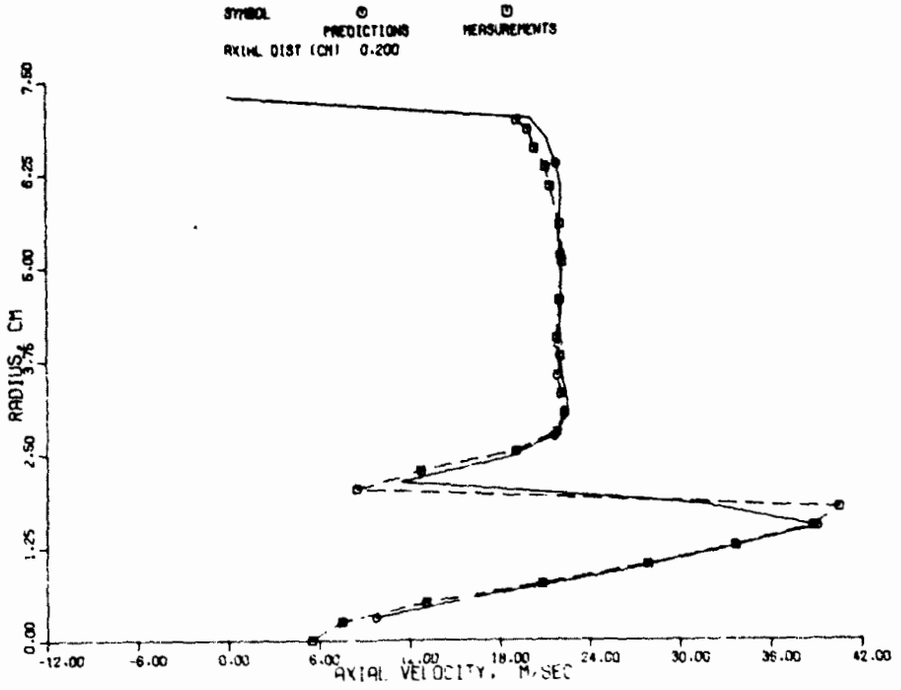

(a)

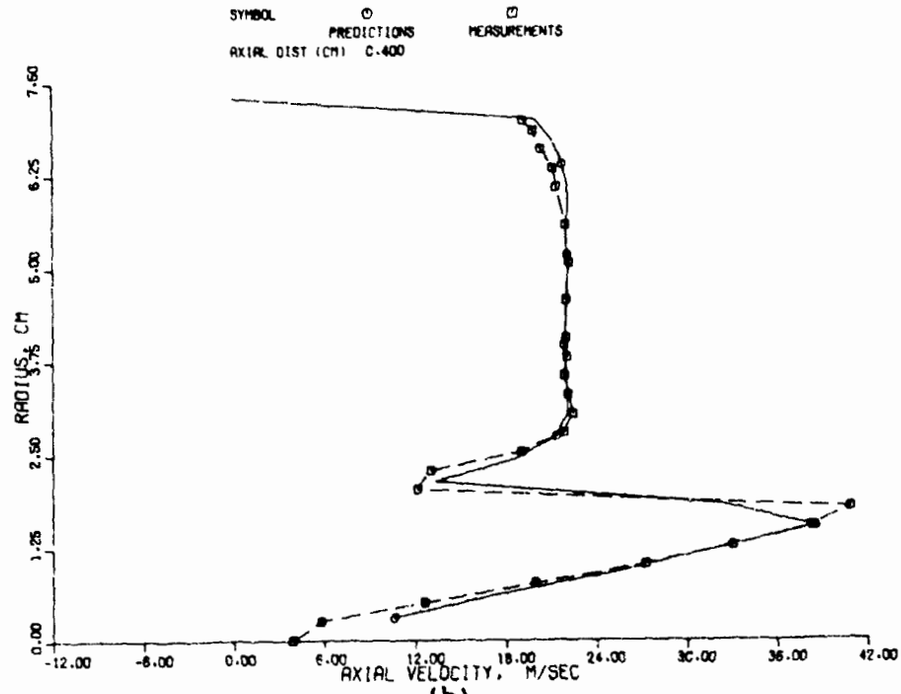

(b)

Figure 33. Axial Velocity Profiles for Counterswirl Case with Measured Inlet Profiles, Modified K-ϵ Model; $\alpha_{V_\theta} = -0.75$, $\alpha_C = 0$.

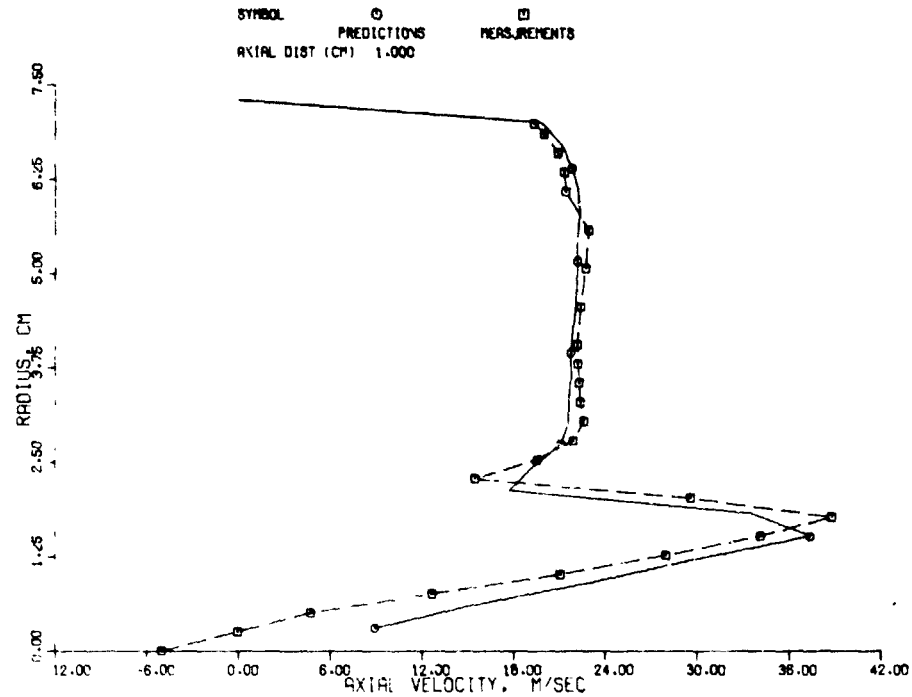

(c)

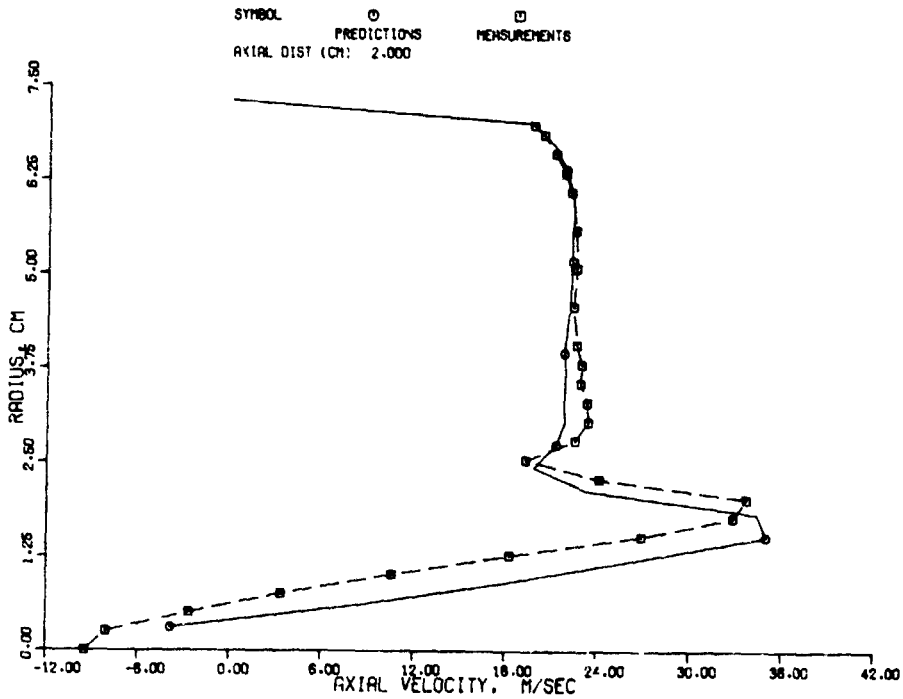

(d)

Figure 33. Axial Velocity Profiles for Counterswirl Case with Measured Inlet Profiles, Modified K-ε Model; $\alpha_{V_\theta} = -0.75$, $\alpha_c = 0$ (Contd).

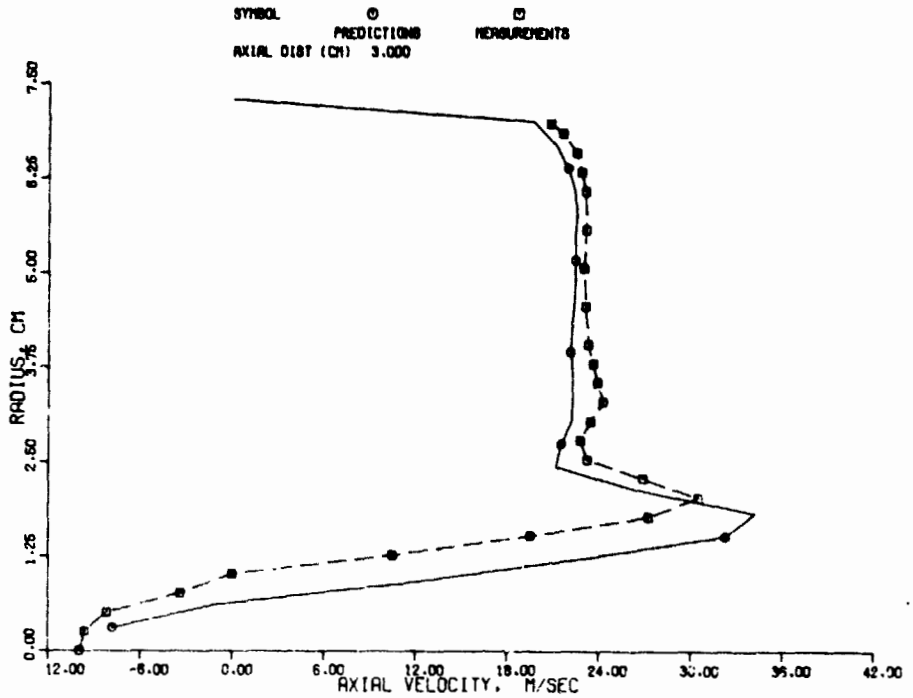

(e)

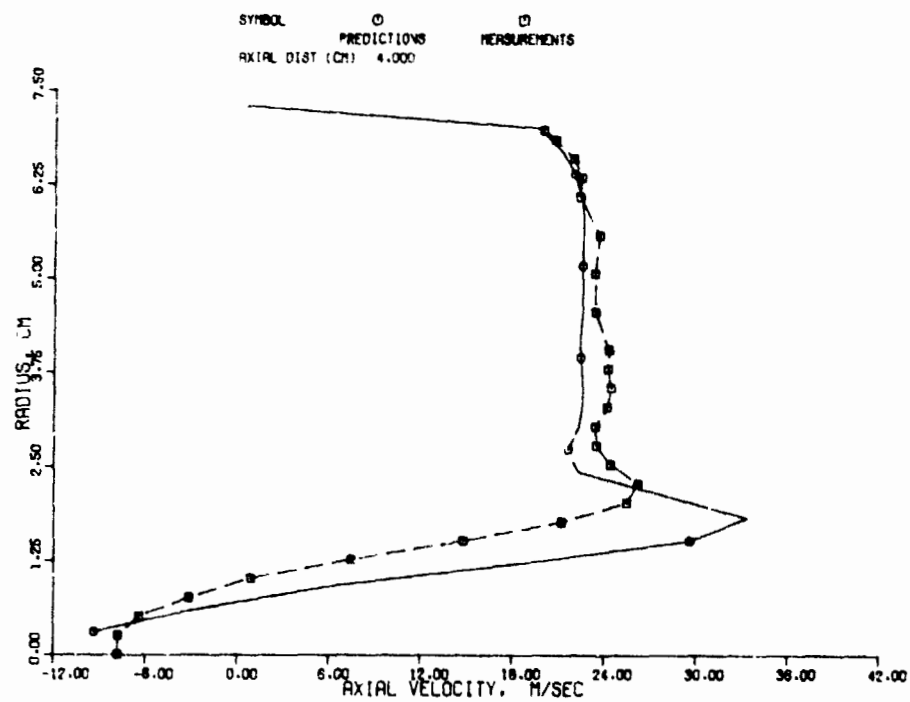

(f)

Figure 33. Axial Velocity Profiles for Counterswirl Case with Measured Inlet Profiles, Modified K-ε Model; $\alpha_{V_\theta} = -0.75$, $\alpha_c = 0$ (Contd).

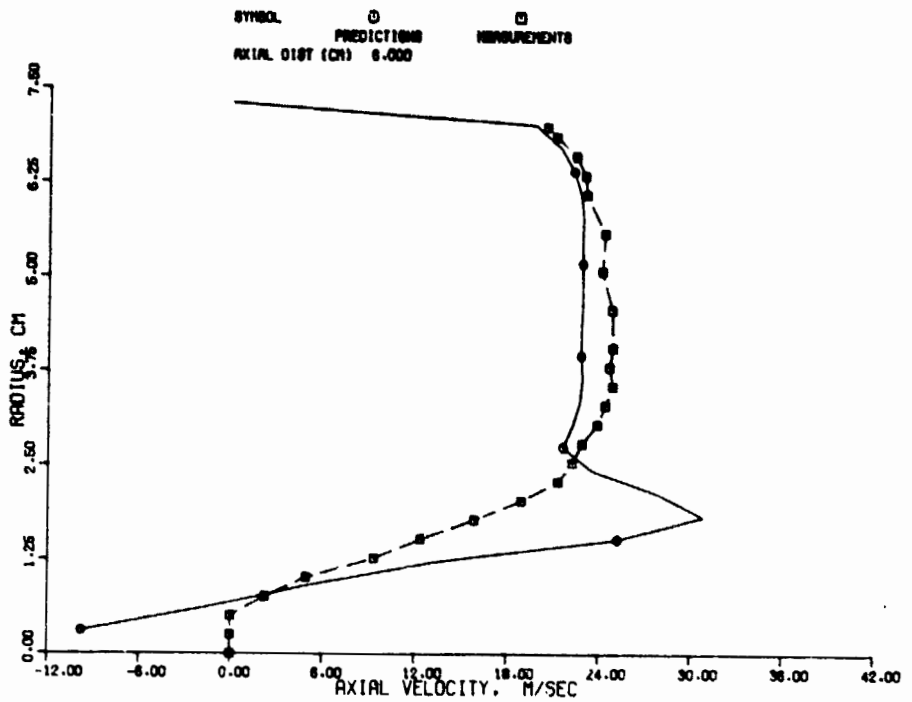

(g)

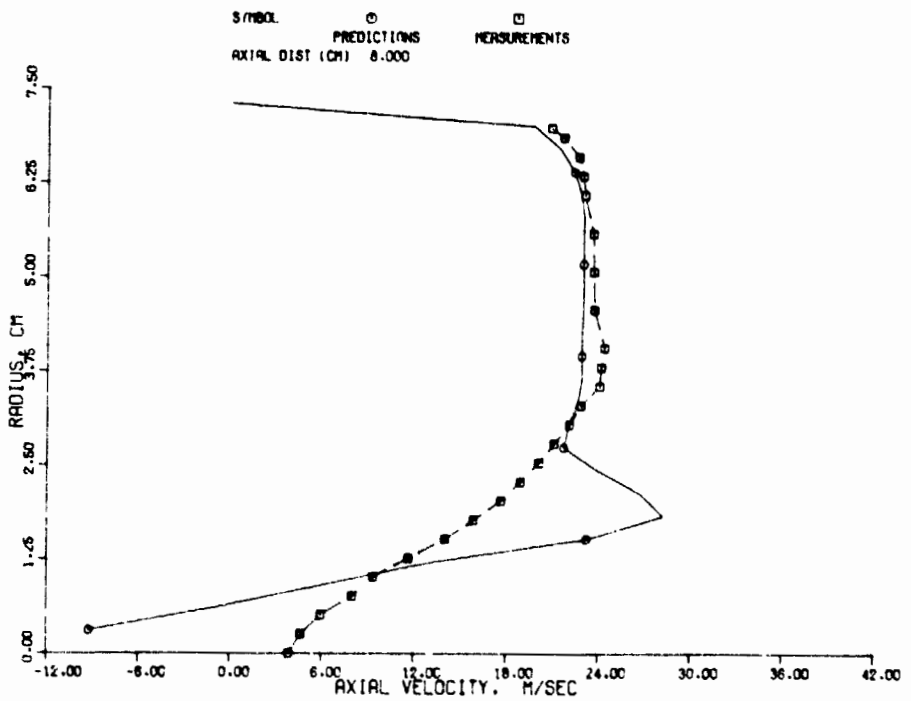

(h)

Figure 33. Axial Velocity Profiles for Counterswirl Case with Measured Inlet Profiles, Modified K-ε Model; $\alpha_{V_\theta} = -0.75$, $\alpha_c = 0$ (Contd).

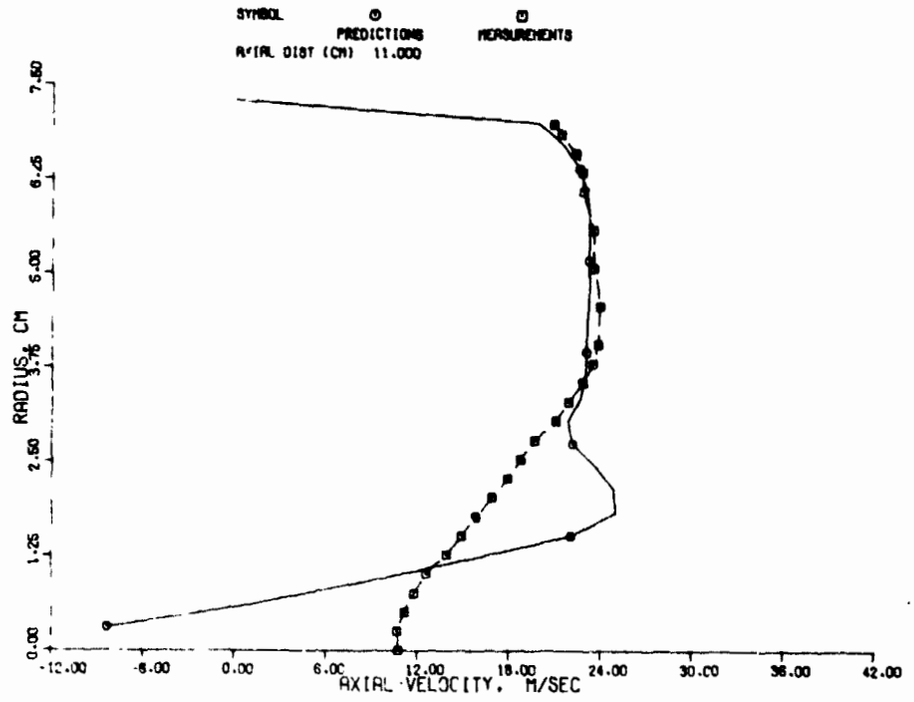

(i)

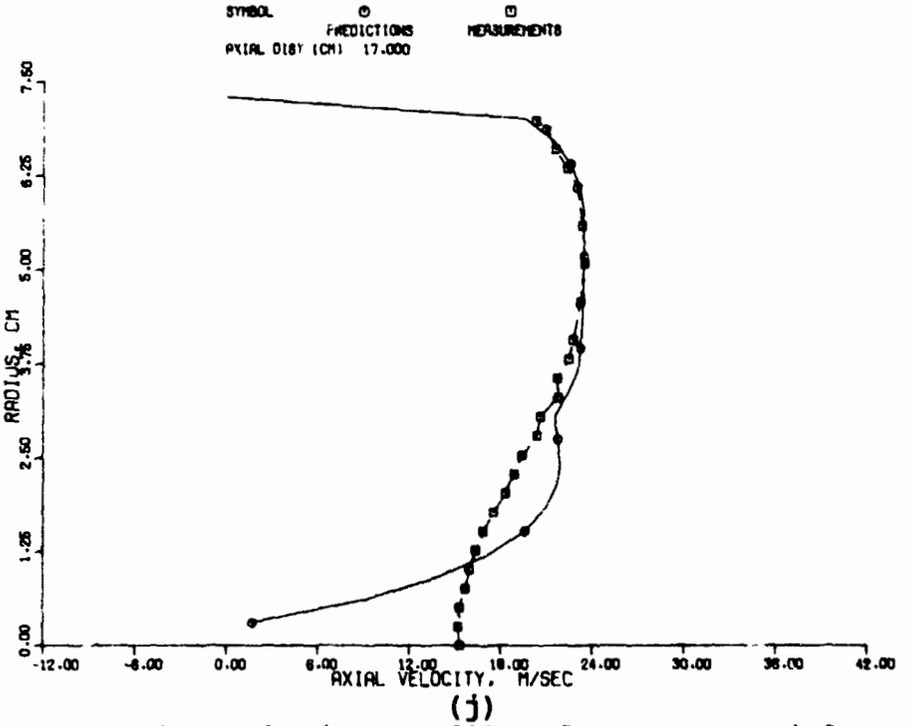

(j)

Figure 33. Axial Velocity Profiles for Counterswirl Case with Measured Inlet Profiles, Modified K-ϵ Model; $\alpha_{V_\theta} = -0.75$, $\alpha_c = 0$ (Contd).

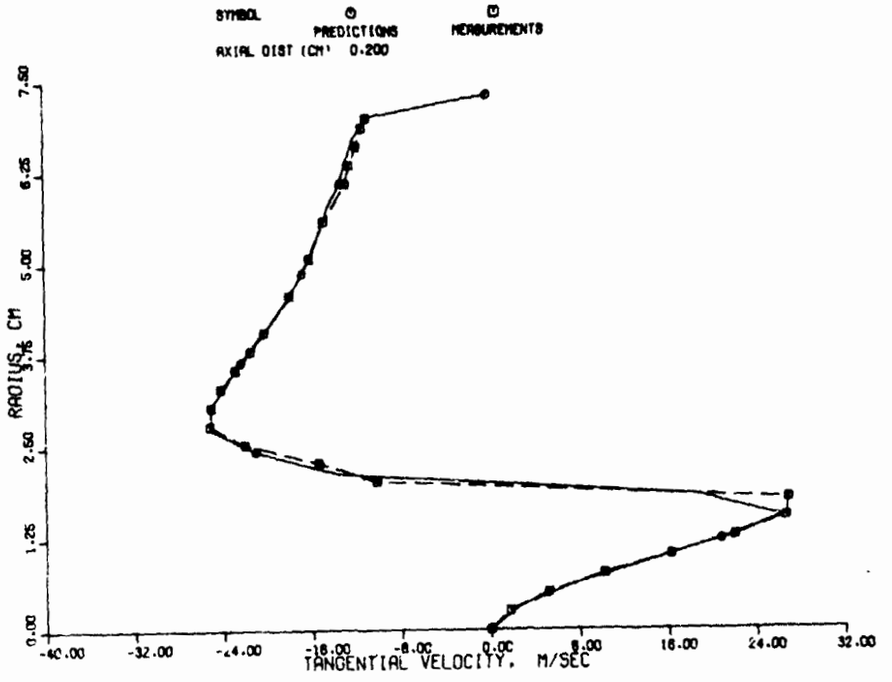

(a)

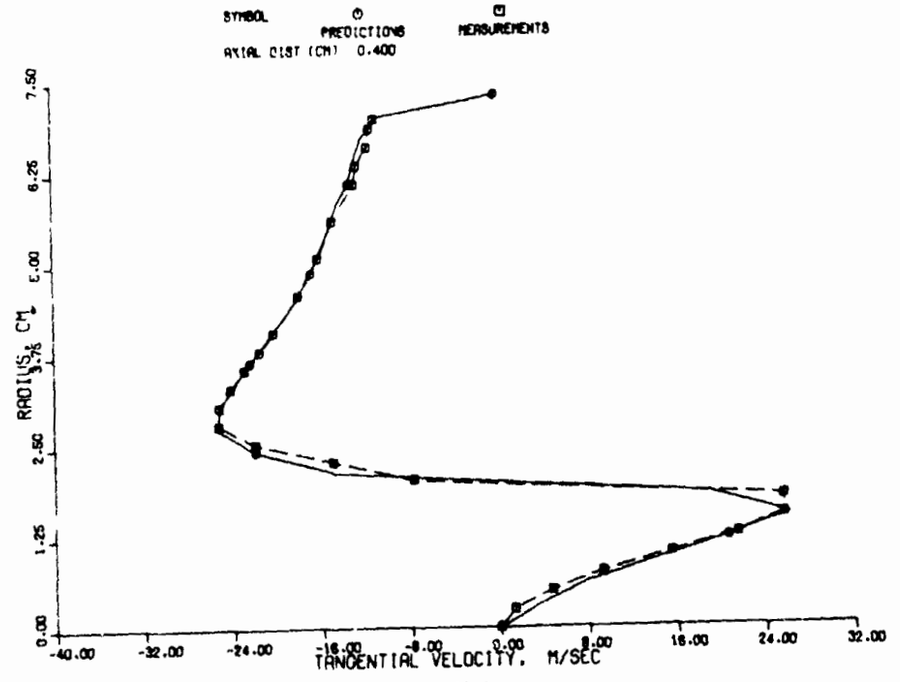

(b)

Figure 34. Tangential Velocity Profiles for Counterswirl Case with Measured Inlet Profiles; Modified K-ϵ Model; $\alpha_{V_\theta} = -0.75$, $\alpha_C = 0$.

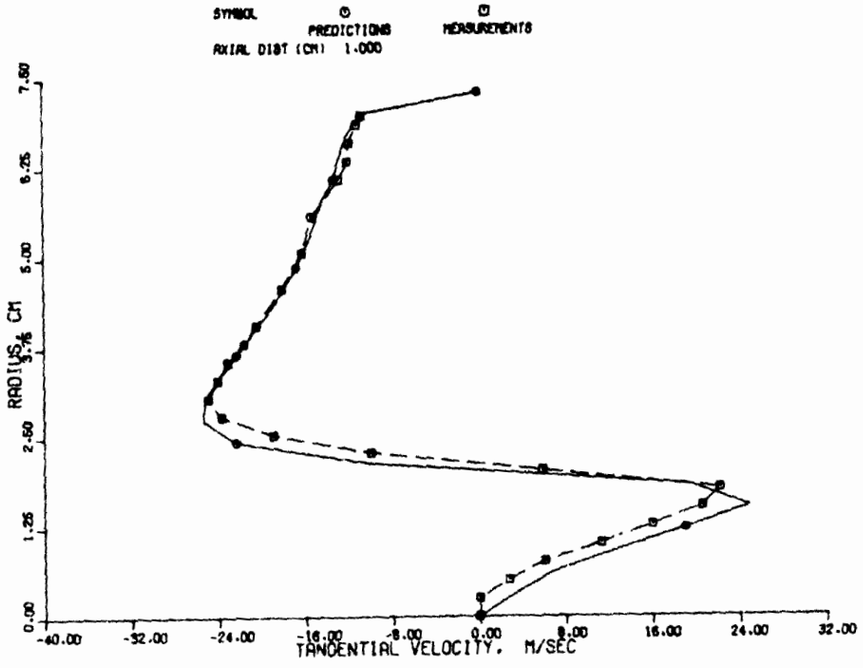

(c)

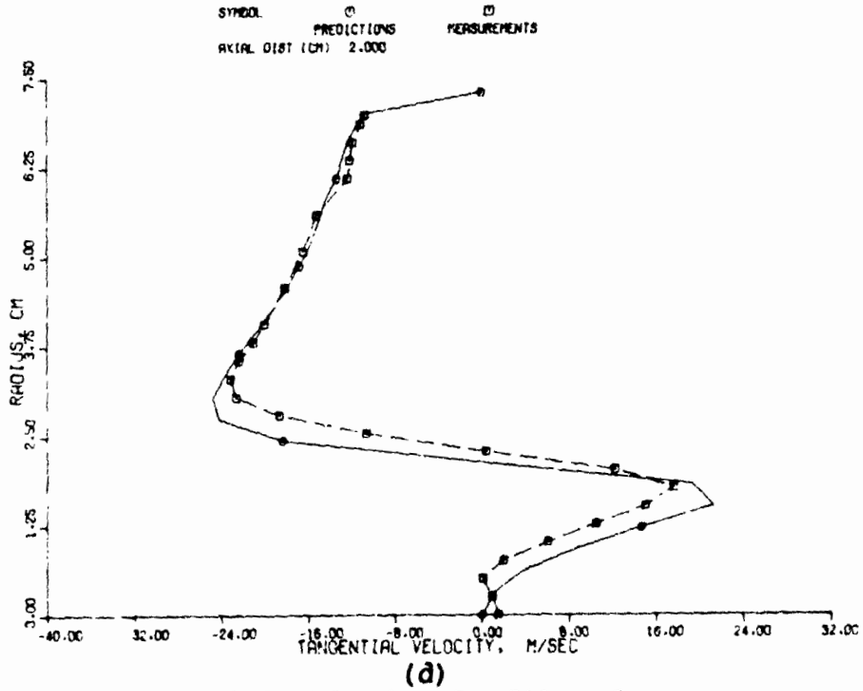

(d)

Figure 34. Tangential Velocity Profiles for Counterswirl Case with Measured Inlet Profiles; Modified K-ϵ Model; $\alpha_{V_\theta} = -0.75$, $\alpha_C = 0$ (Contd).

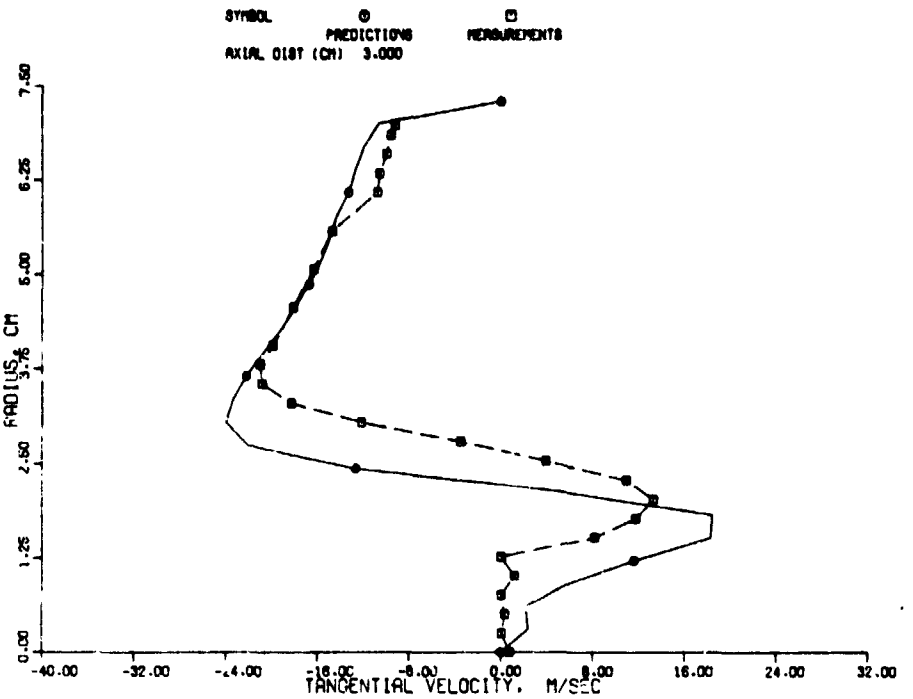

(e)

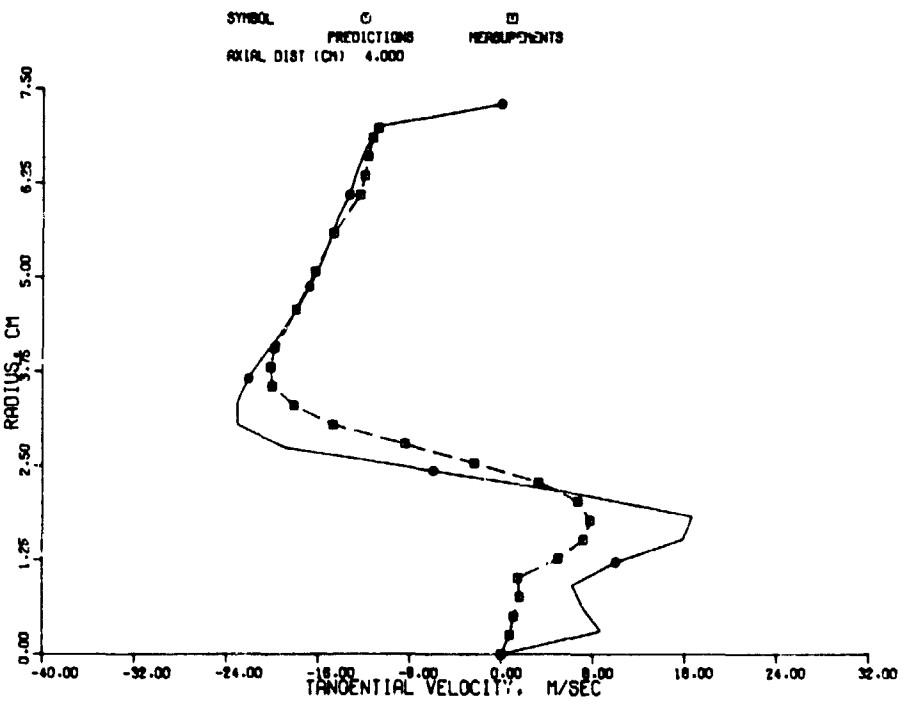

(f)

Figure 34. Tangential Velocity Profiles for Counterswirl Case with Measured Inlet Profiles; Modified K-ϵ Model; $\alpha_{V_\theta} = -0.75$, $\alpha_C = 0$ (Cont'd).

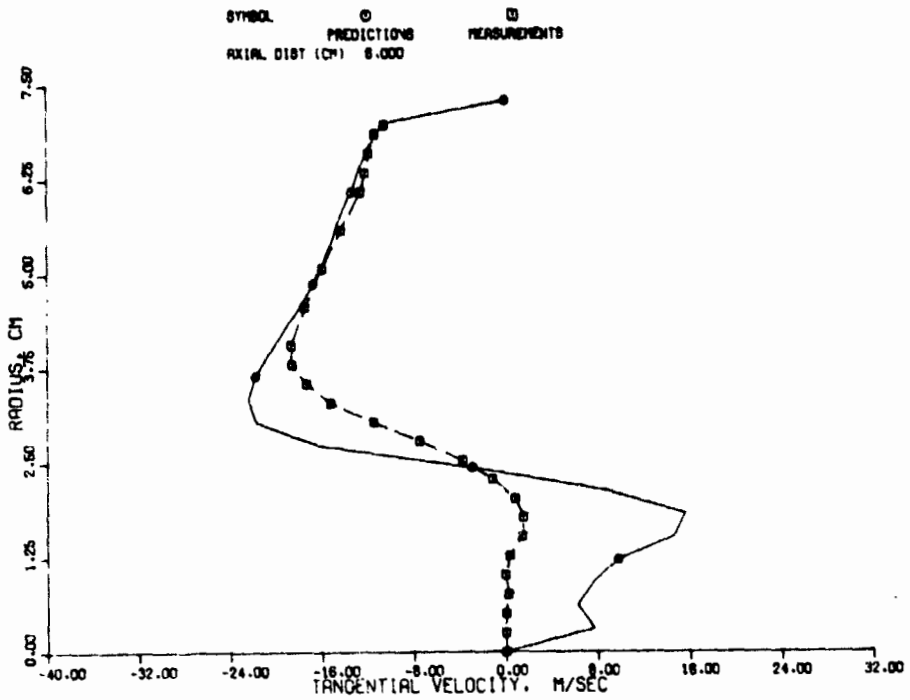

(g)

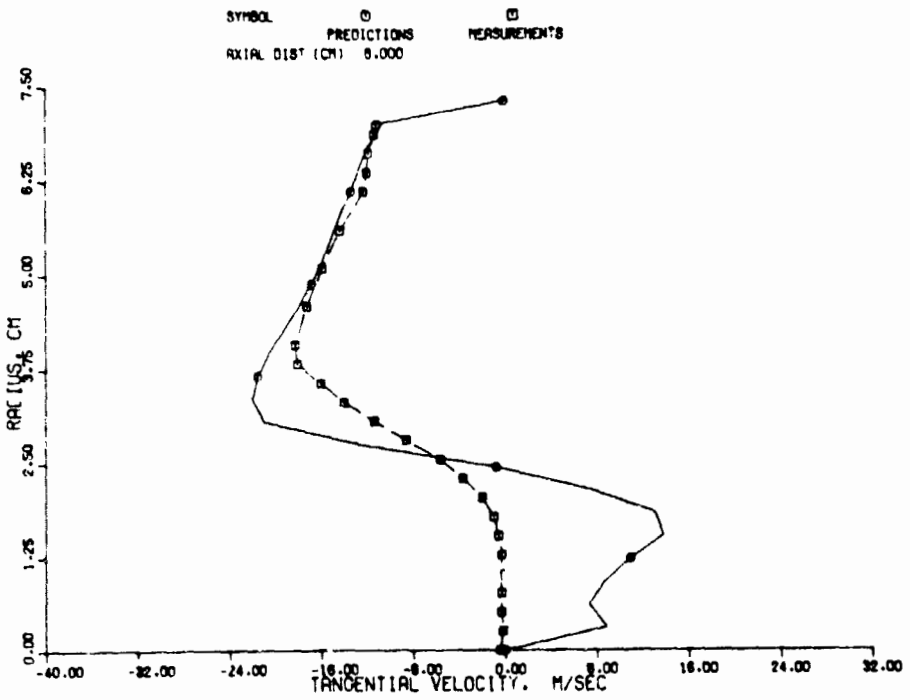

(h)

Figure 34. Tangential Velocity Profiles for Counterswirl Case with Measured Inlet Profiles; Modified K-ϵ Model; $\alpha_{V_\theta} = -0.75$, $\alpha_C = 0$ (Contd).

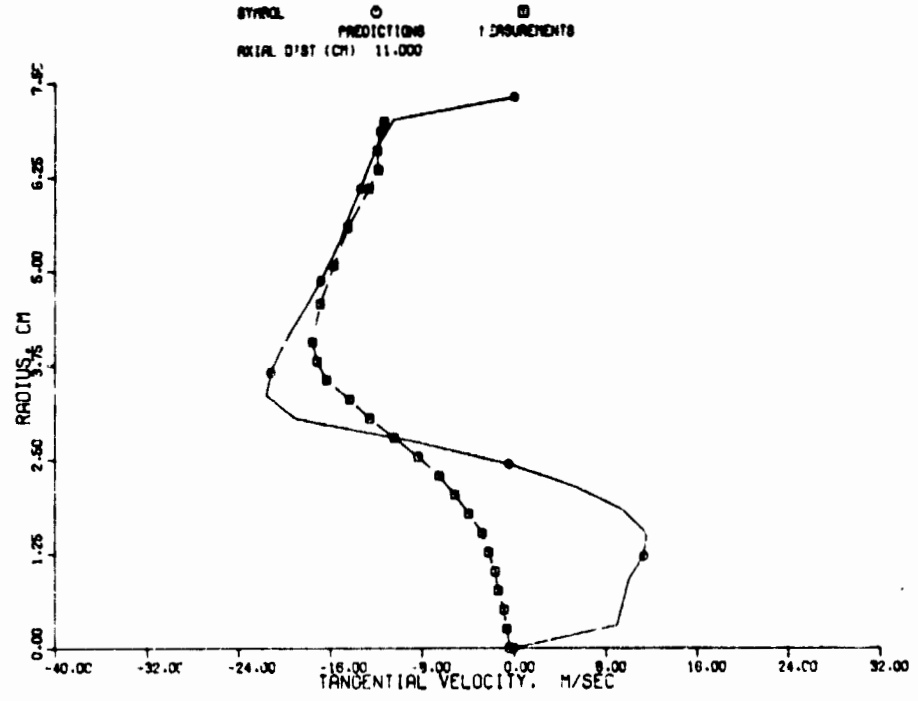

(i)

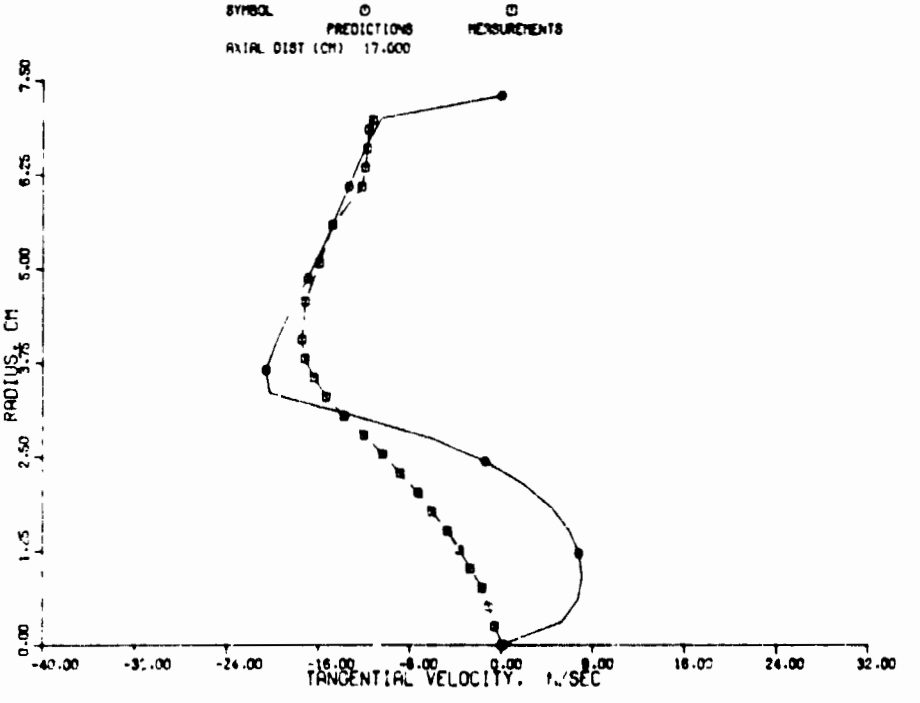

(j)

Figure 34. Tangential Velocity Profiles for Counterswirl Case with Measured Inlet Profiles; Modified κ-ϵ Model; $\alpha_{V_\theta} = -0.75$, $\alpha_C = 0$ (Contd).

selected. Several different values of α_C were tried out in the test runs, and among those, by far the best comparison with measurements was obtained for the case of $\alpha_{V_\theta} = -0.75$ and $\alpha_C = -2.0$. A comparison of the predicted results for axial velocity with the measurements for the counterswirl case are shown in Figure 35. A comparison of the results presented in Figure 33 and those shown in Figure 35 reveals marginal improvement in the agreement with data. This implies that in a strongly swirling flow, like in the test case, the Richardson Number due to swirl has a dominant effect on turbulent transport and the effect of the curvature of streamlines is quite small. This observation was also reported by Bradshaw (ref. 18). The predicted tangential velocity profiles for $\alpha_{V_\theta} = -0.75$ and $\alpha_C = -2.0$, as seen in Figure 36, show improvements inside and downstream of the recirculation zone. The effect of the length scale modification based upon the extra strain rate is seen in the recirculation zone, where kinks in the profiles are predicted. Comparison of Figures 36 and 34 shows that the effect of streamline curvature (α_C) on the tangential velocity profile is minimal.

Although the modified k-ε model gave improved correlations with the counter-swirling flow data, it failed to give a converged solution for the co-swirl case, even after a limited number of attempts were made to improve convergence by using different under-relaxation factors and initial profile development. This effort was not pursued to the point where specific conclusions could be made as to why the modified k-ε turbulence model was triggering a numerical instability.

Another potential area of inaccuracy in the computations lies in the specification of inlet turbulence kinetic energy and length scale profiles. The 2-D elliptic program, as a default option, assumes uniform profiles for inlet turbulence kinetic energy and length scale, corresponding to a fully developed flow, i.e.,

$$k_{inlet} = 0.003\ (U_{inlet})^2_{av}$$

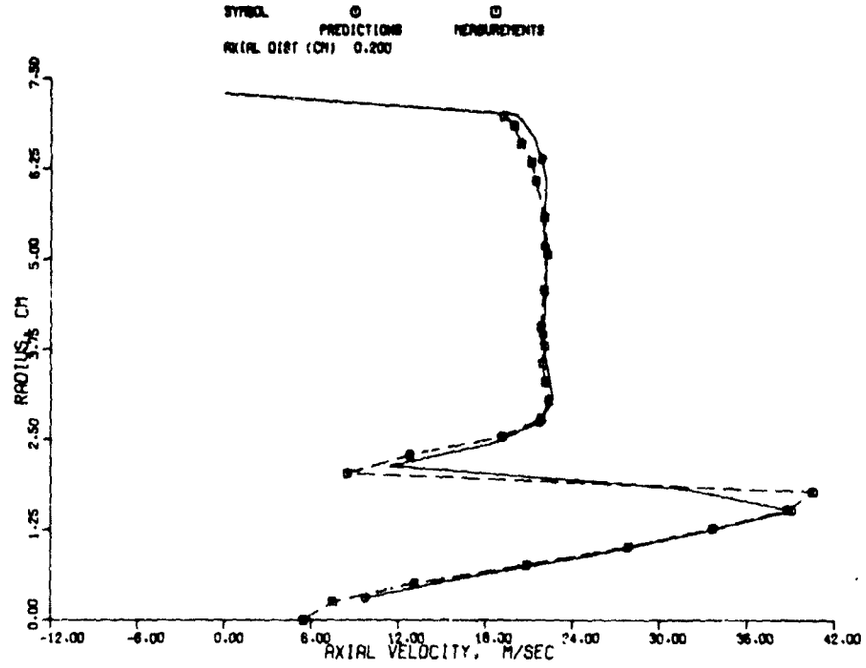

(a)

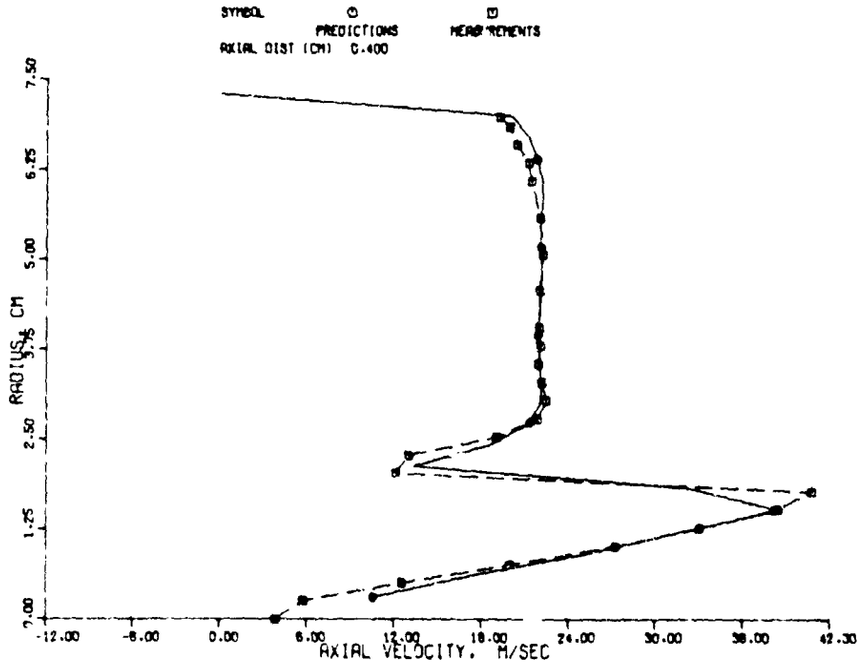

(b)

Figure 35. Axial Velocity Profiles for Counterswirl Case with Measured Inlet Profiles; Modified K-ε Model; $\alpha_{V_\theta} = -0.75$, $\alpha_C = -2.0$.

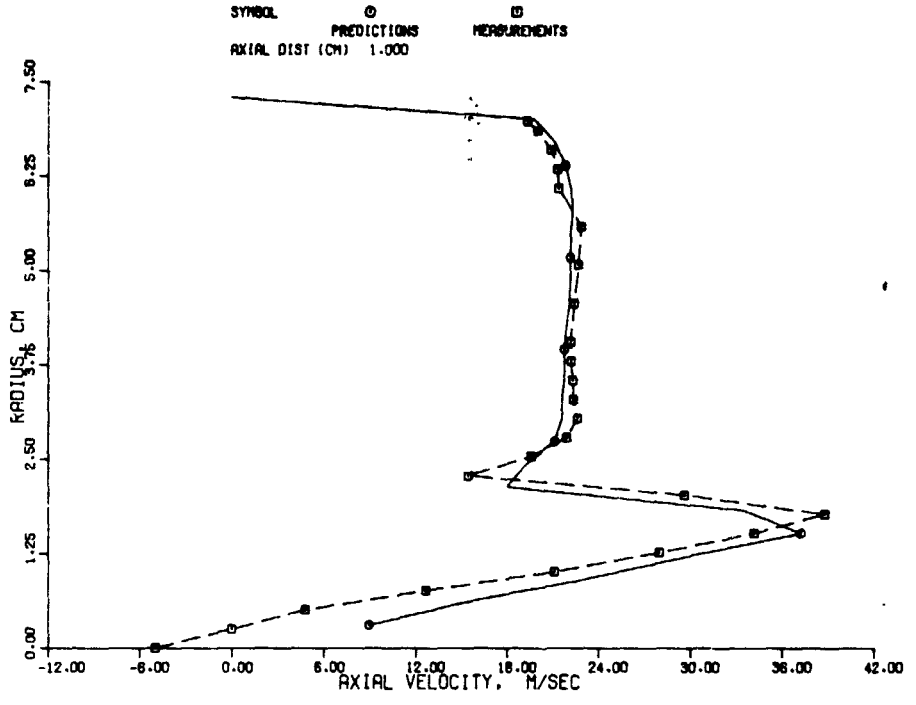

(c)

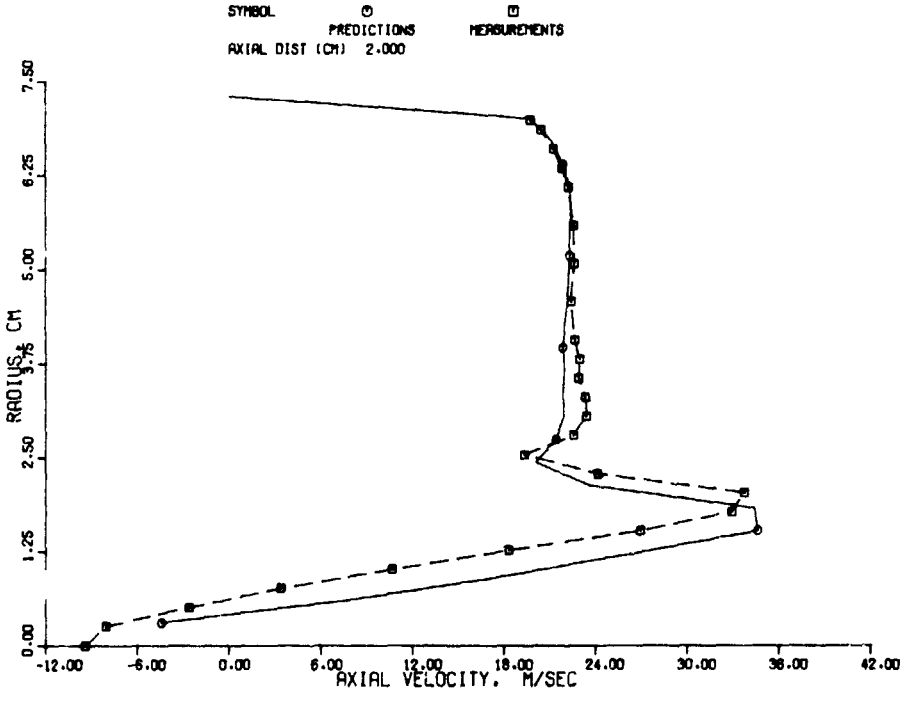

(d)

Figure 35. Axial Velocity Profiles for Counterswirl Case with Measured Inlet Profiles; Modified K-ϵ Model; $\alpha_{V_\theta} = -0.75$, $\alpha_C = -2.0$ (Contd).

C-2

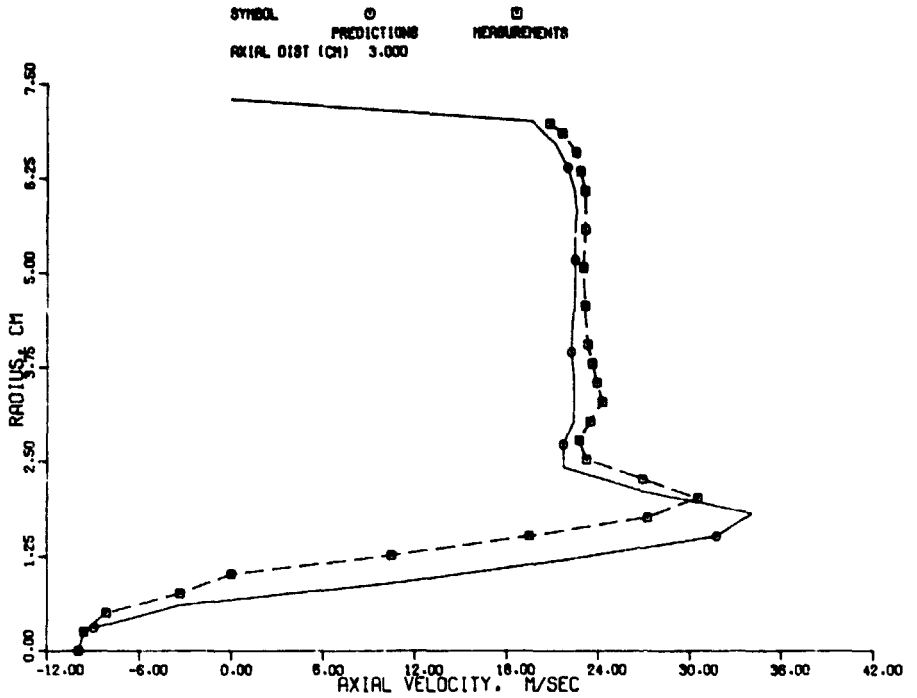

(e)

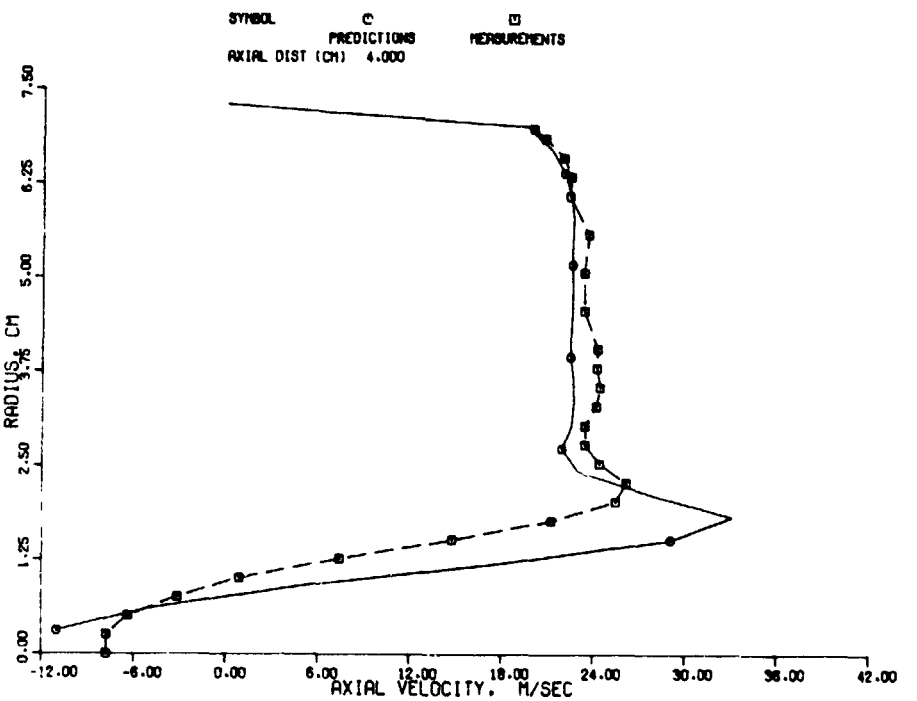

(f)

Figure 35. Axial Velocity Profiles for Counterswirl Case with Measured Inlet Profiles; Modified K-ϵ Model; $\alpha_{V_\theta} = -0.75$, $\alpha_C = -2.0$ (Contd).

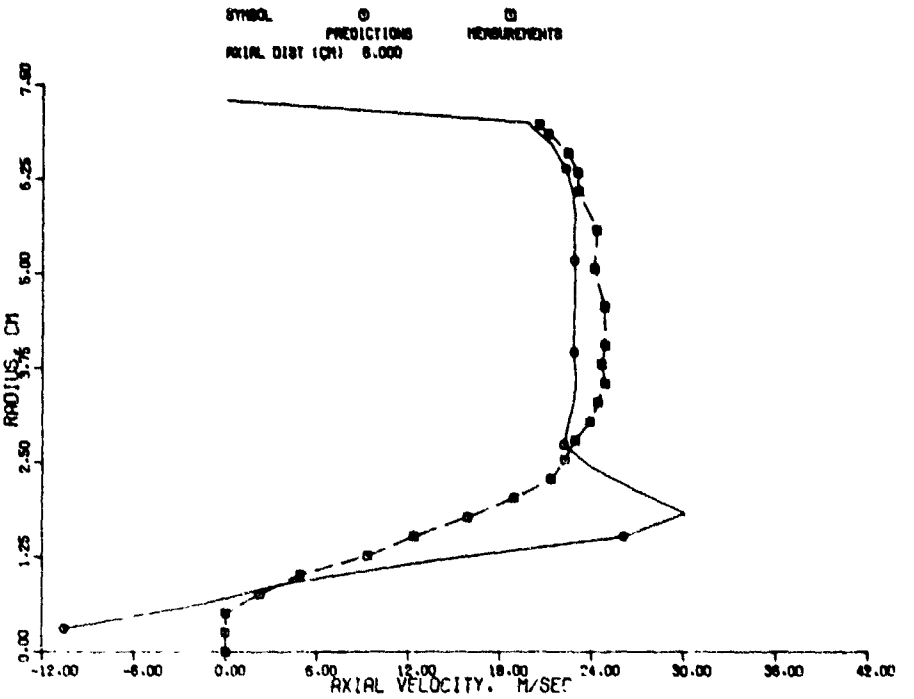

(g)

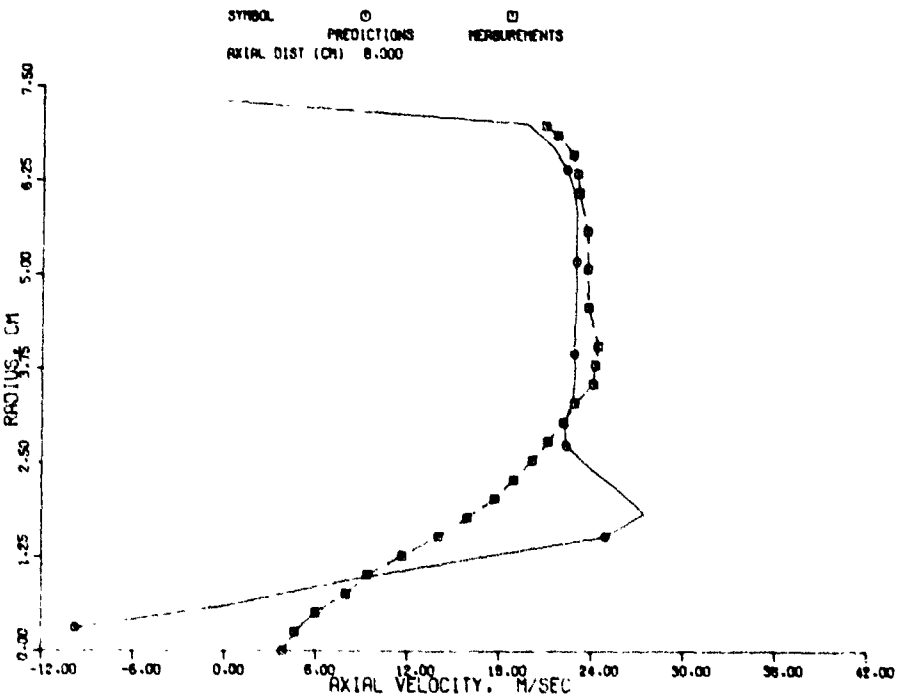

(h)

Figure 35. Axial Velocity Profiles for Counterswirl Case with Measured Inlet Profiles; Modified K-ε Model; $\alpha_{V_\theta} = -0.75$, $\alpha_C = -2.0$ (Contd).

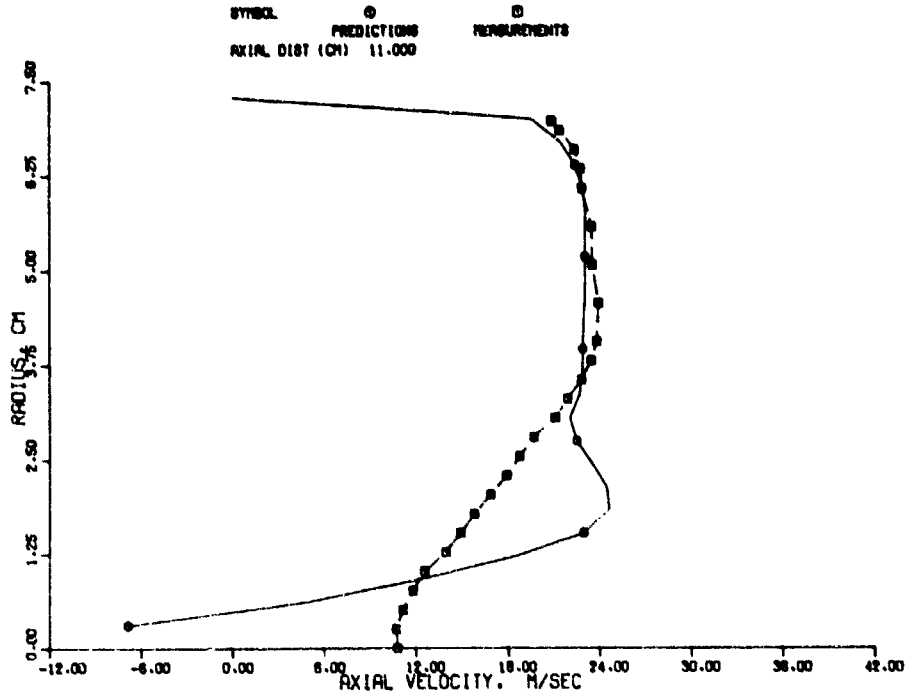

(i)

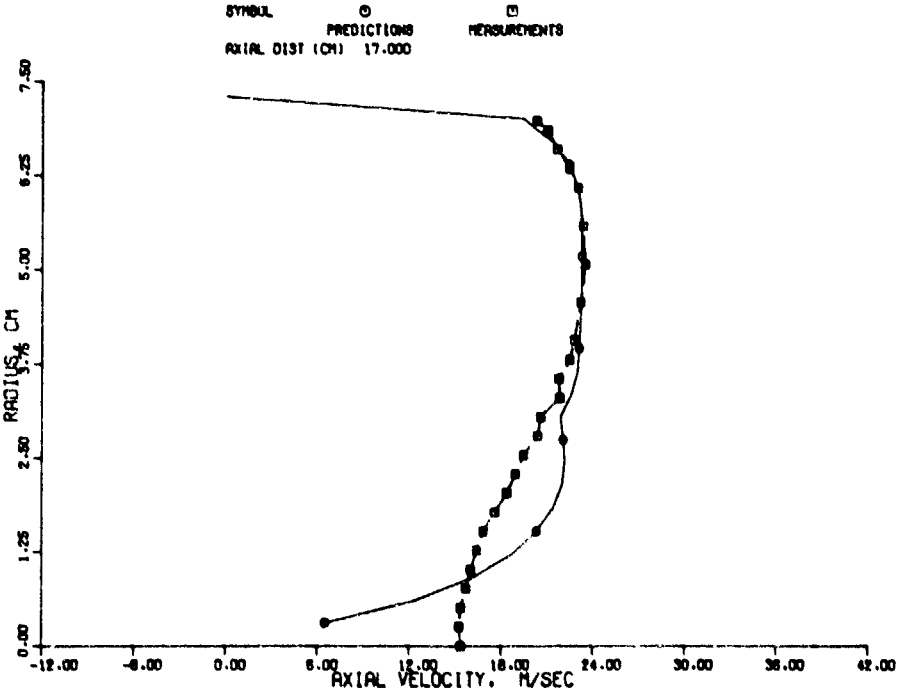

(j)

Figure 35. Axial Velocity Profiles for Counterswirl Case with Measured Inlet Profiles; Modified K-ϵ Model; $\alpha_{V_\theta} = -0.75$, $\alpha_C = -2.0$ (Contd).

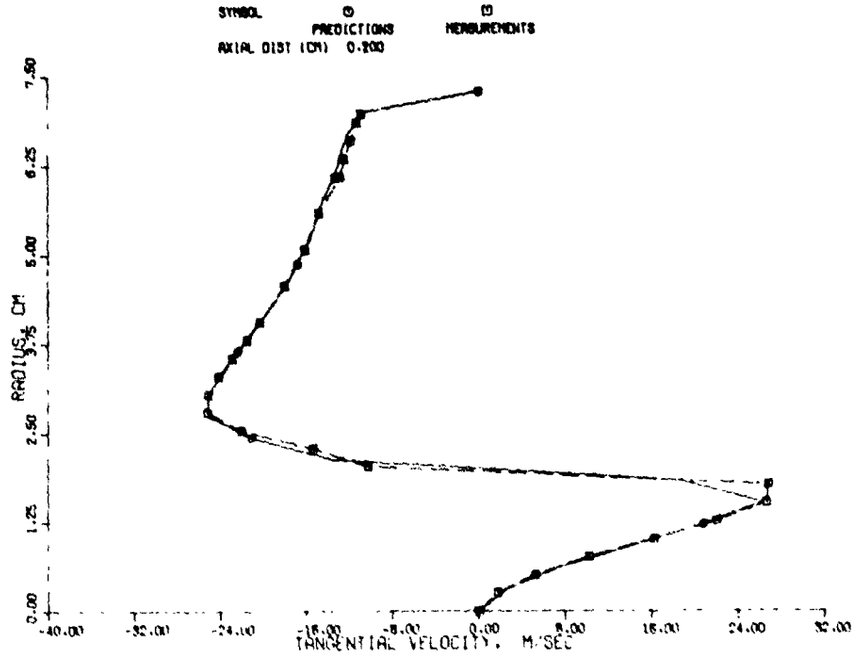

(a)

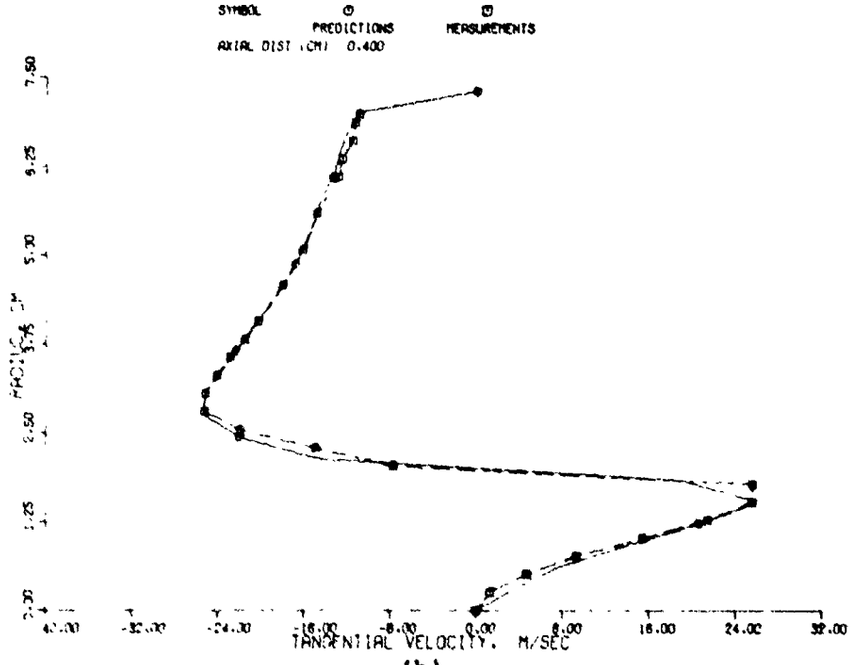

(b)

Figure 36. Tangential Velocity Profiles for Counterswirl Case with Measured Inlet Profiles; Modified K-ϵ Model; $\alpha_{V_\theta} = -0.75$, $\alpha_C = -2.0$.

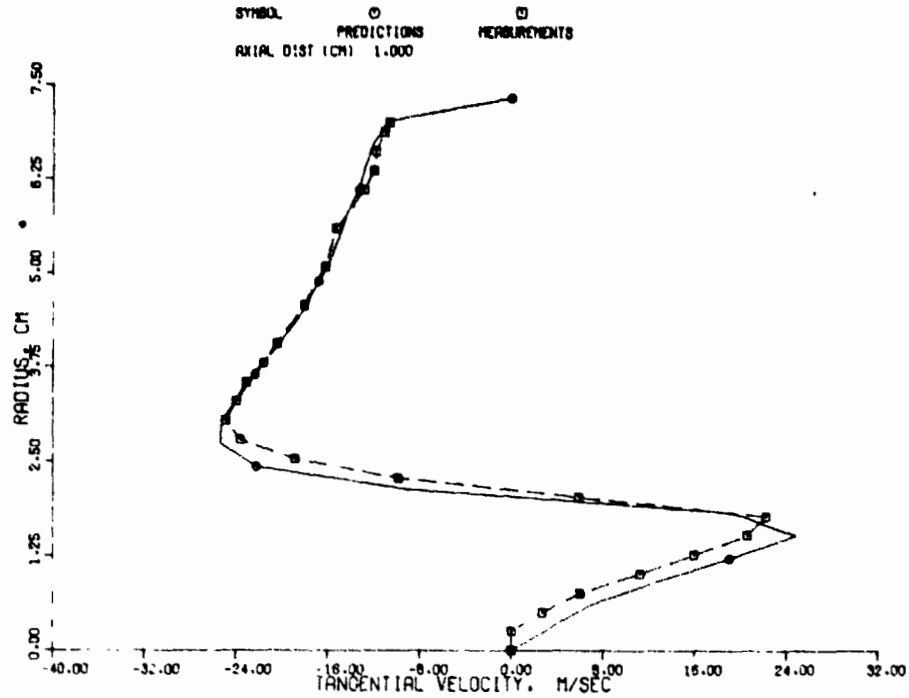

(c)

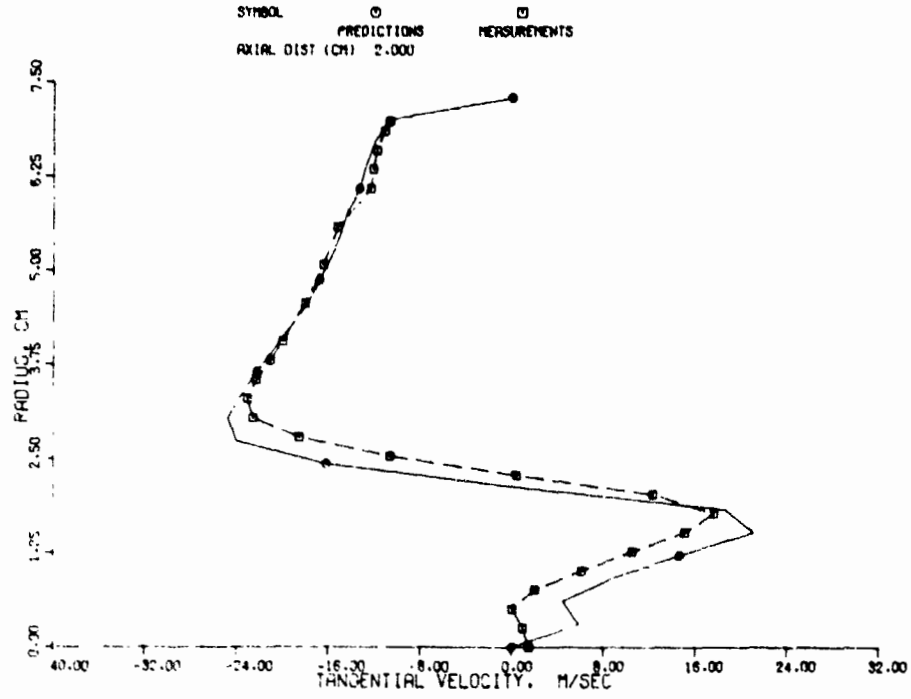

(d)

Figure 36. Tangential Velocity Profiles for Counterswirl Case with Measured Inlet Profiles; Modified K-ϵ Model; $\alpha_{V_\theta} = -0.75$, $\alpha_C = -2.0$ (Contd).

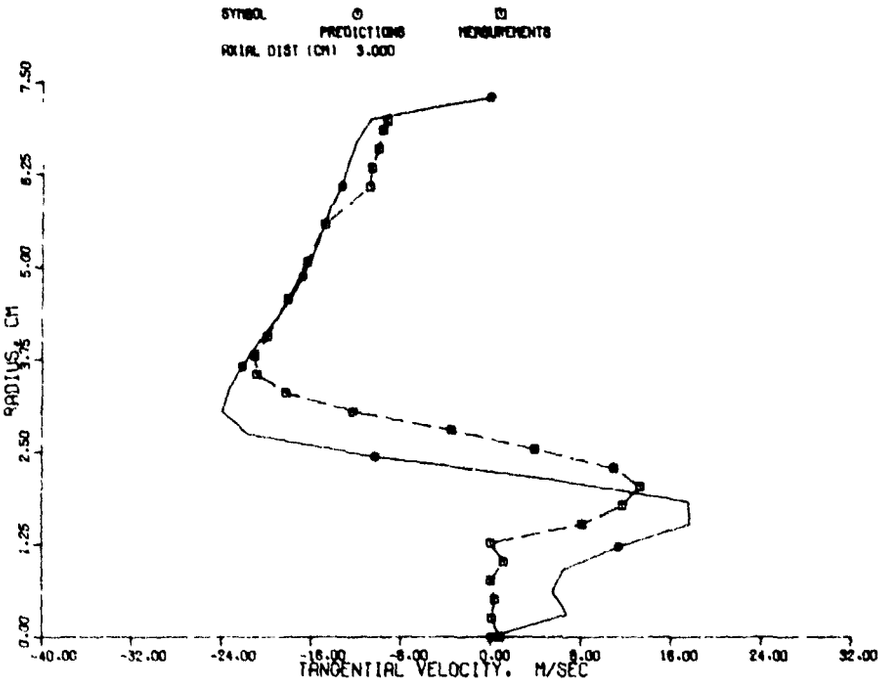

(e)

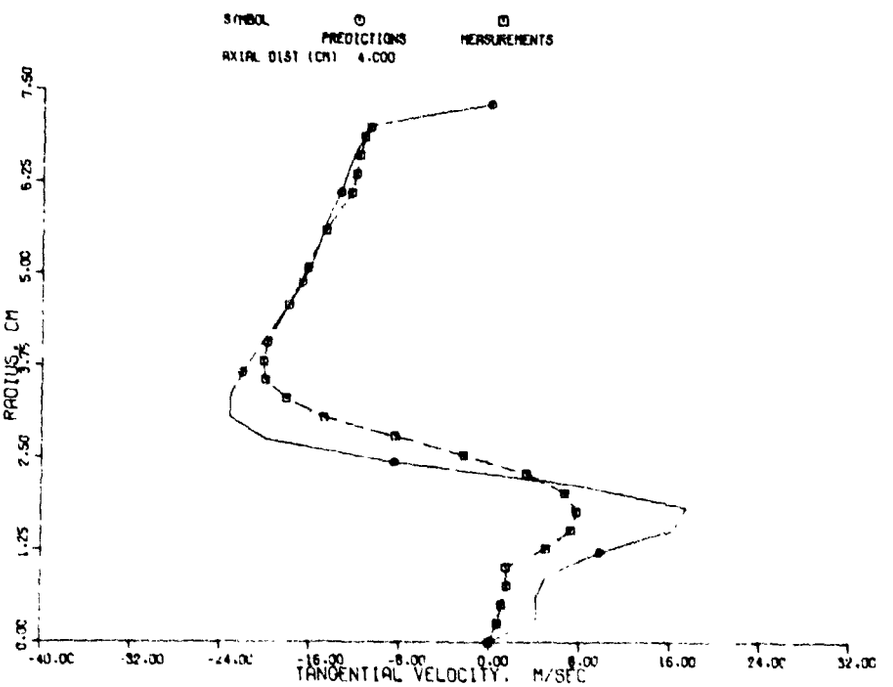

(f)

Figure 36. Tangential Velocity Profiles for Counterswirl Case with Measured Inlet Profiles; Modified K-ε Model; $\alpha_{V_\theta} = -0.75$, $\alpha_C = -2.0$ (Contd).

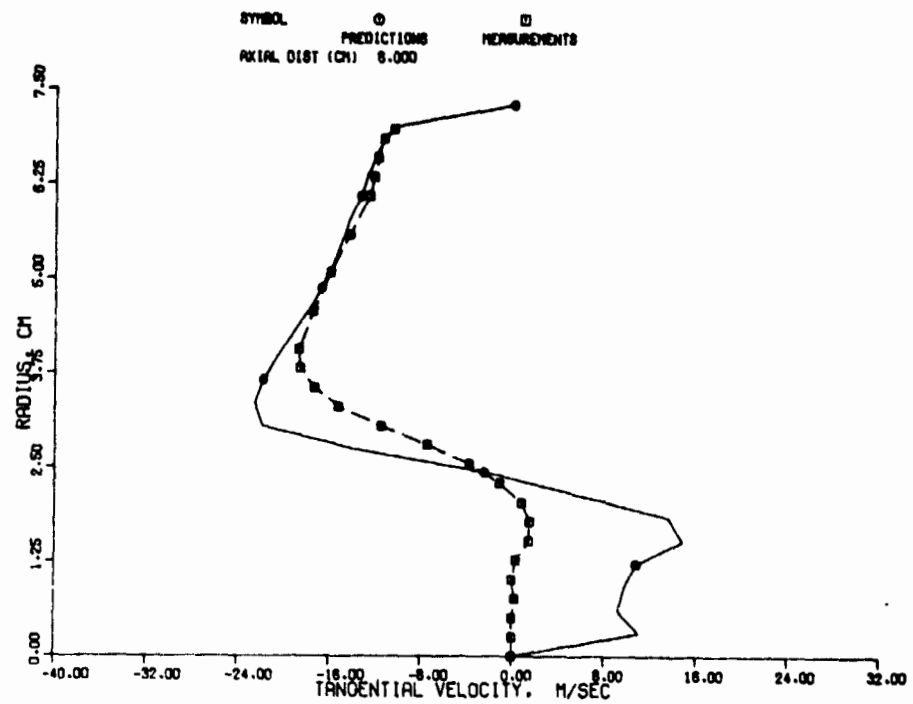

(g)

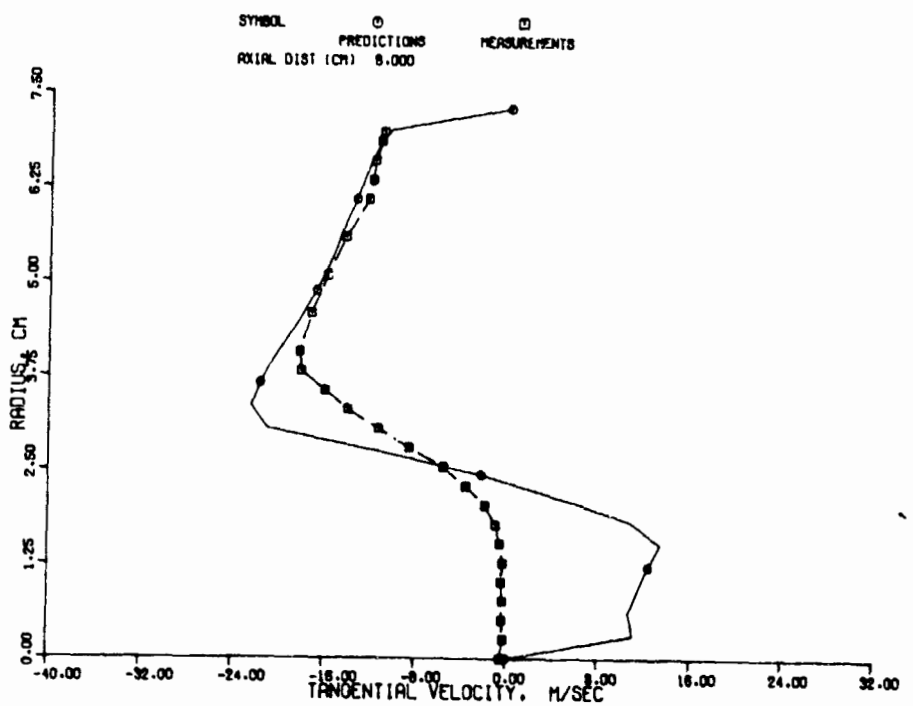

(h)

Figure 36. Tangential Velocity Profiles for Counterswirl Case with Measured Inlet Profiles; Modified K-ε Model; $\alpha_{V_\theta} = -0.75$, $\alpha_C = -2.0$ (Contd).

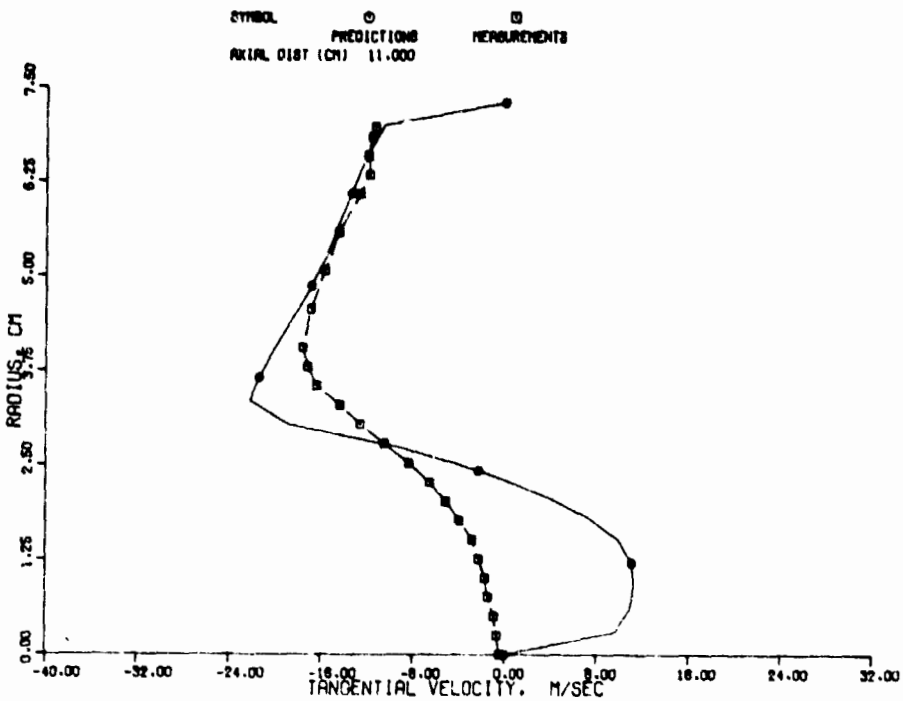

(i)

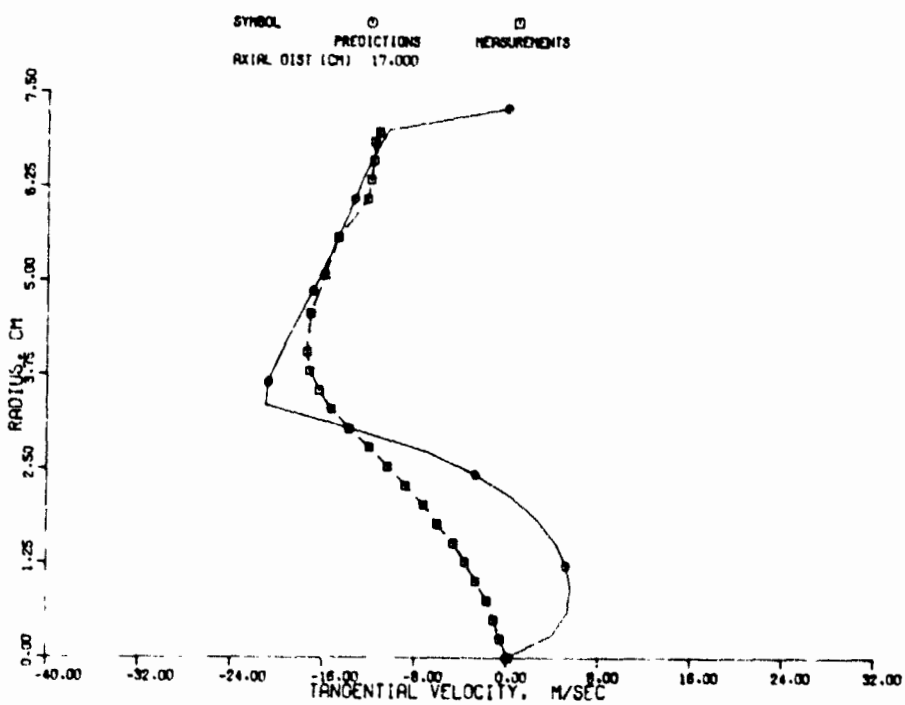

(j)

Figure 36. Tangential Velocity Profiles for Counterswirl Case with Measured Inlet Profiles; Modified K-ϵ Model; $\alpha_{V_\theta} = -0.75$, $\alpha_C = -2.0$ (Contd).

$$\ell_{inlet} = 0.02\, h_{inlet}$$

where h_{inlet} is the radius of the representative inlet ducts. The strongly converging outer flow passage is expected to result in a reduced turbulence intensity, and the characteristic length scale is also likely to be smaller then the fully developed values of turbulence kinetic energy and the length scale.

Several different runs were made with smaller inlet kinetic energy and length scale profiles to determine the effect of these inlet profiles. These test runs were made parametrically, to delineate the effect of each. Predictions were obtained with the original, as well as the modified k-ϵ model. The predictions did not show any major improvements in the mean velocity profiles. These results are not presented here for the sake of brevity.

The results obtained with the modified k- model demonstrate that the two equation turbulence model can be modified to yield more accurate predictions, especially in the recirculation zone. A closer look at the experimental data reveals that the structure of turbulence near the recirculation zone is quite anisotropic. This inference stems from the vastly different radial gradients of axial and angular momenta. The anisotropy implies the existence of multiple length scales in the turbulence structure. But, the k-ϵ model has the single length scale assumption built into the equations, and any simple modification of the turbulence model can not be expected to give very accurate predictions in the recirculation zone. Development of multiscale turbulence models is beyond the scope of this program. The inability of the original k-ϵ model in predicting recirculation in the counter-swirling case indicates a deficiency in the approach adopted thus far. The effects of pressure gradients on the flow development in the mixing region are not accounted for in Tasks I and II. In order to include these effects in the analysis, it was deemed necessary to simulate the geometry of the entire swirling flow assembly.

Task III-Results

A modified 2-D elliptic program was used in Task III in order to simulate the inner and the outer flow geometries as shown in Figure 37. The outer flow was simulated in the analysis as an axial injection station. The program is capable of handling any prescribed profiles for the axial injection. For the inner stream, the model assumed a uniform inlet axial velocity profile with a magnitude of 30.8 m/s from r = 0 to r = 1.86 cm and a uniform tangential velocity profile with magnitudes of 33.18 m/sec from r = 0.635 cm to r = 1.86 cm and zero for r < 0.635 cm. flow. The inlet profiles for the outer swirling stream were calculated by the AiResearch CAPS Program. The predicted axial and tangential velocities for the outer stream in the counterswirling arrangement is shown in Figure 38. The inlet radial velocity values were zero for both inner and the outer streams. Uniform inlet static pressure profiles were prescribed for both of the streams in Task III computations.

Figure 39 presents predicted axial velocity profiles for the flow assembly simulation (Figure 37) with the original k-ϵ model. These results may be compared with Task I computations, shown previously in Figure 15, to infer upstream effects of the outer stream on the inner stream flow development. The Task III computations are in good agreement with data even without modifying the k-ϵ model. The differences in the profiles in the region corresponding to the outer channel are attributed to the nature of the potential flow results employed for the inlet profile of the outer stream. The predicted recirculation zone, as identified by the negative axial velocity region, compares favorably with the Cornell data.

The tangential velocity profile predictions for this case are compared with the measurements in Figure 40. These profiles

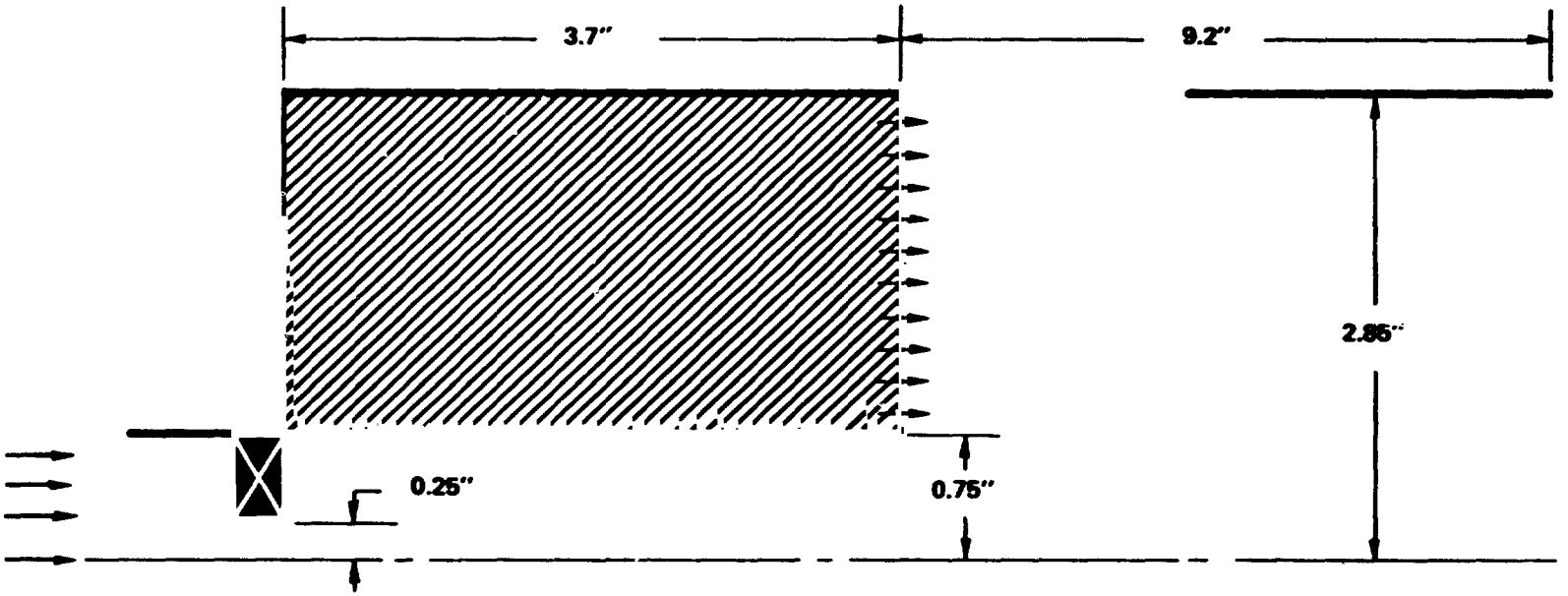

Figure 37. Co· ·ation of the Simulated Flow Assembly.

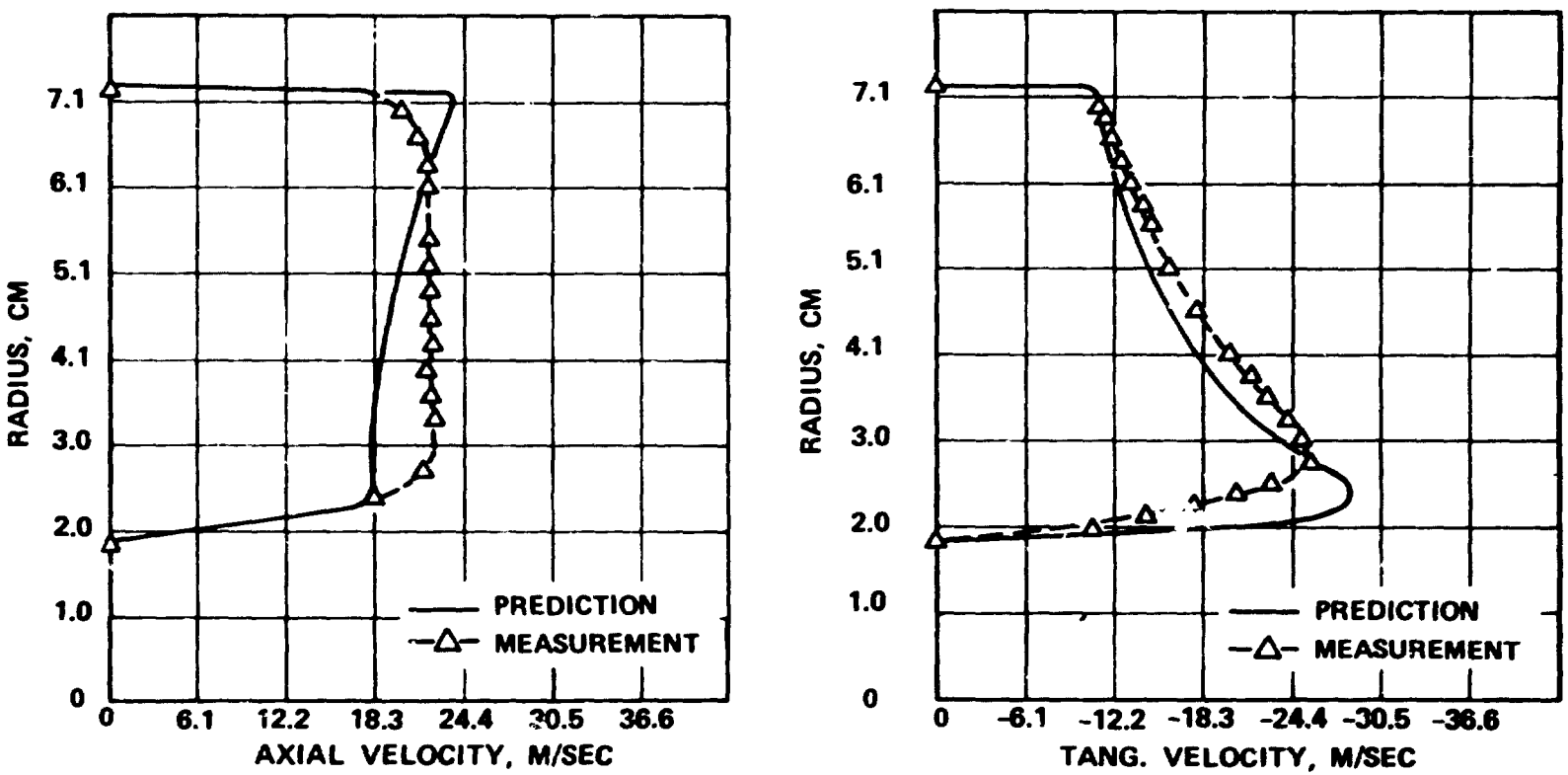

Figure 38. Comparison of Predicted Inlet Velocity Profiles with Test Data.

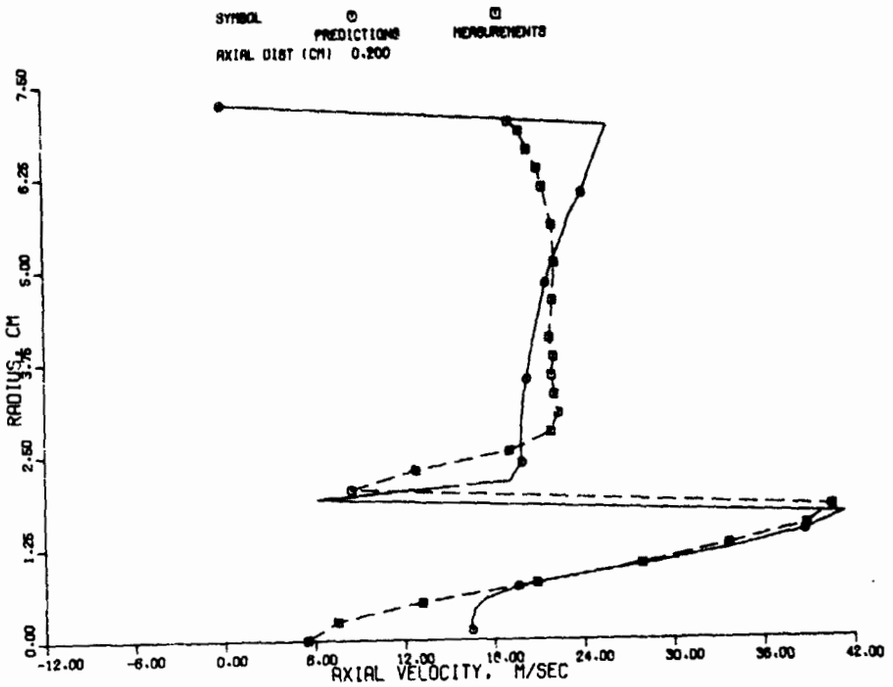

(a)

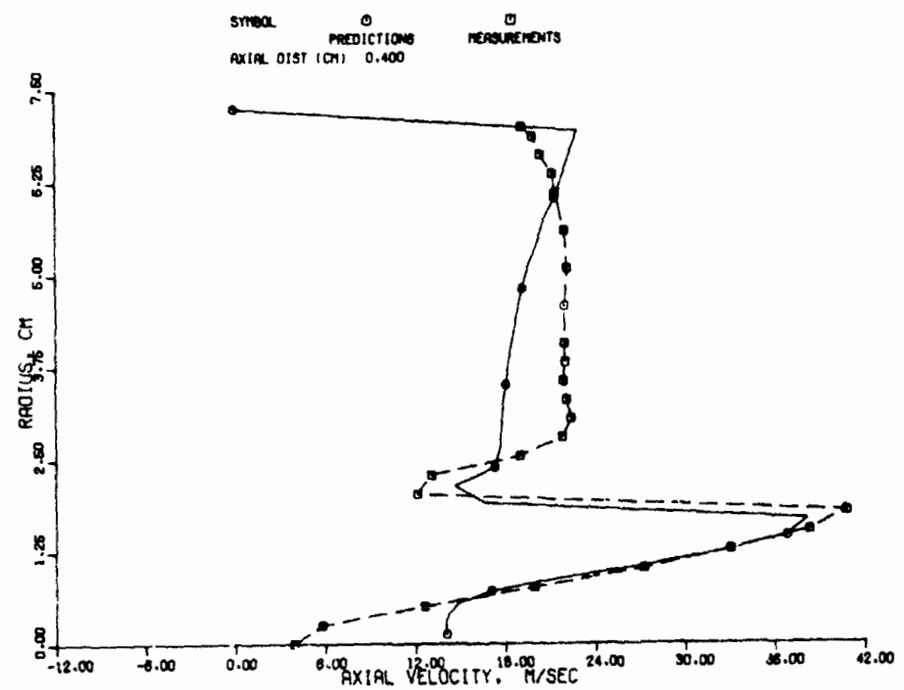

(b)

Figure 39. Axial Velocity Predictions of the Modified 2-D Elliptic Program for Counterswirl Case; Original K-ϵ Model.

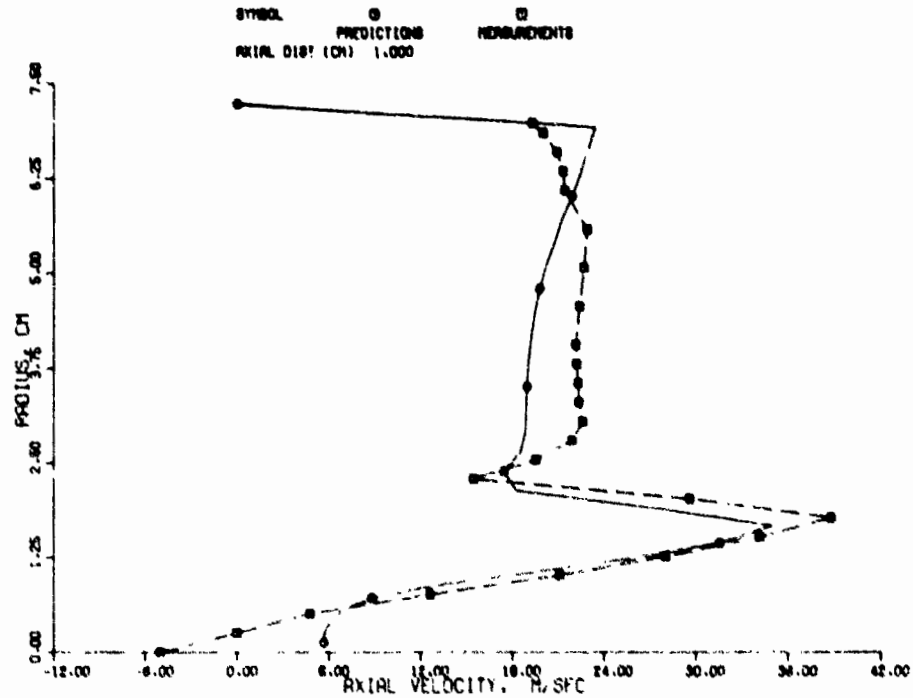

(c)

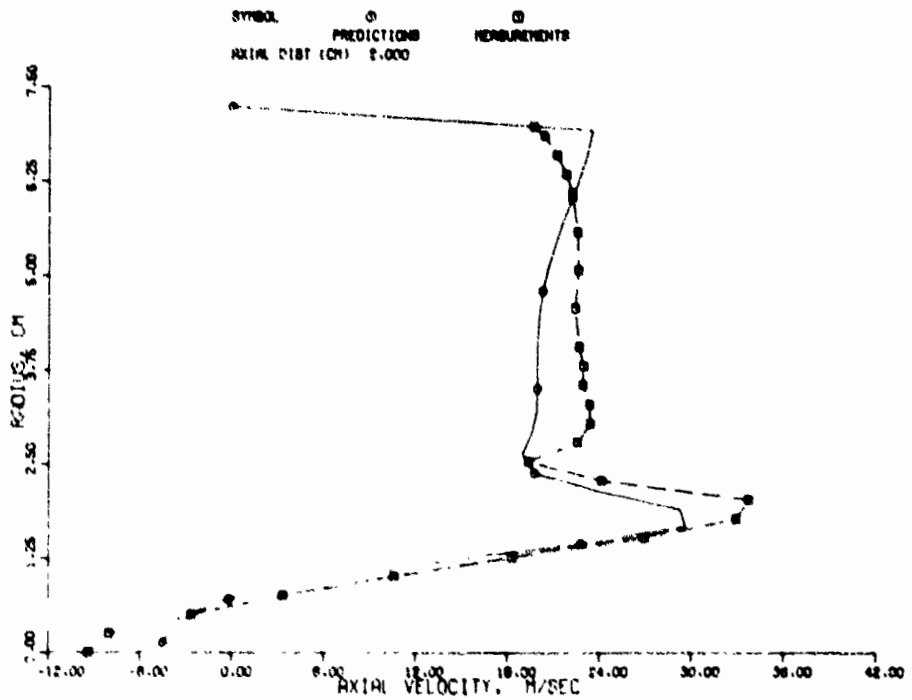

(d)

Figure 39. Axial Velocity Predictions of the Modified 2-D Elliptic Program for Counterswirl Case; Original K-ε Model (Contd).

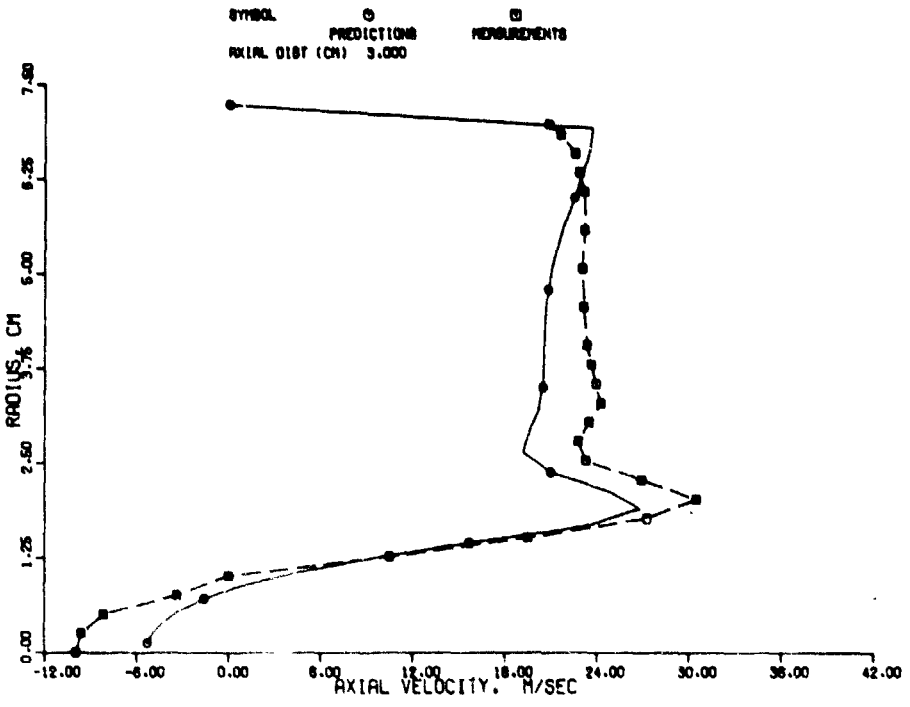

(e)

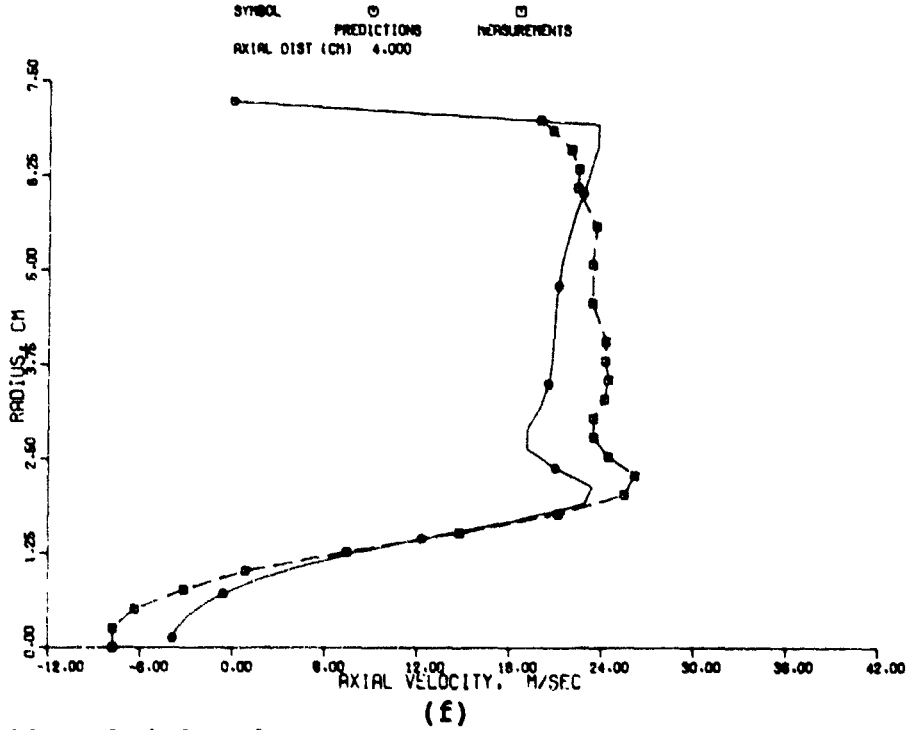

(f)

Figure 39. Axial Velocity Predictions of the Modified 2-D Elliptic Program for Counterswirl Case; Original K-ϵ Model (Contd).

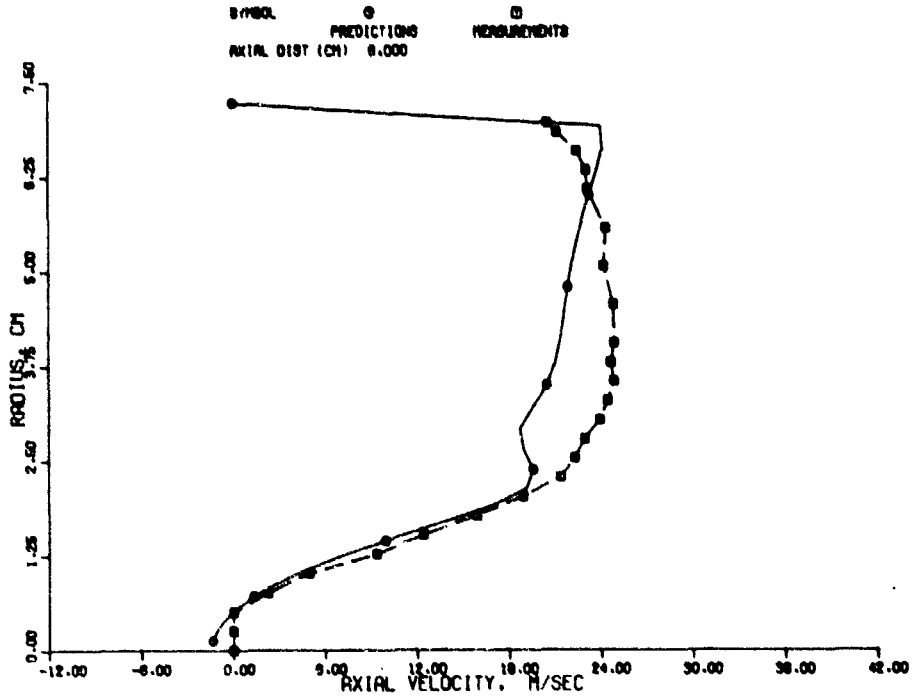

(g)

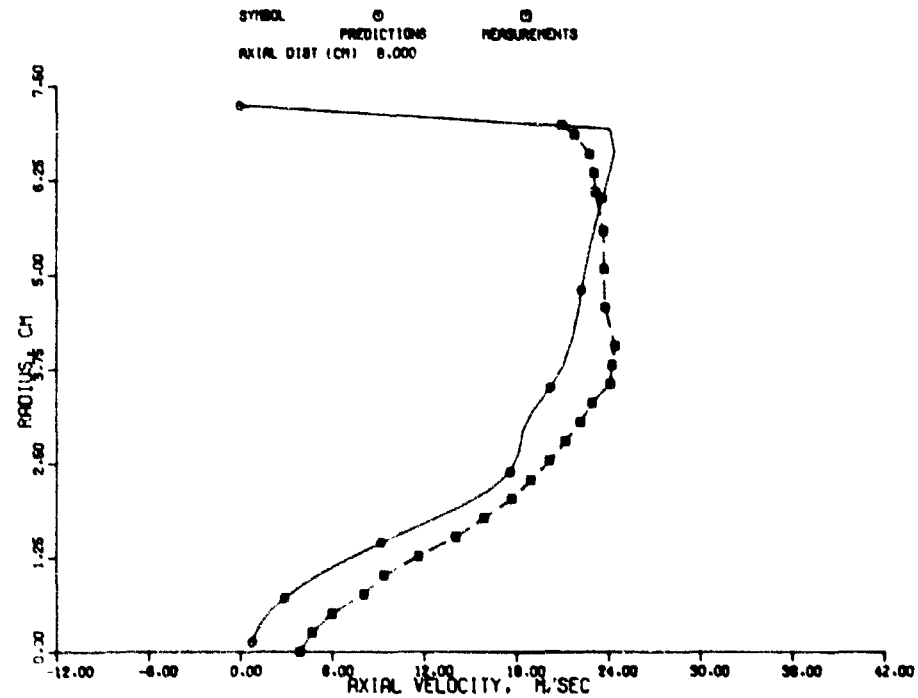

(h)

Figure 39. Axial Velocity Predictions of the Modified 2-D Elliptic Program for Counterswirl Case; Original K-ϵ Model (Contd).

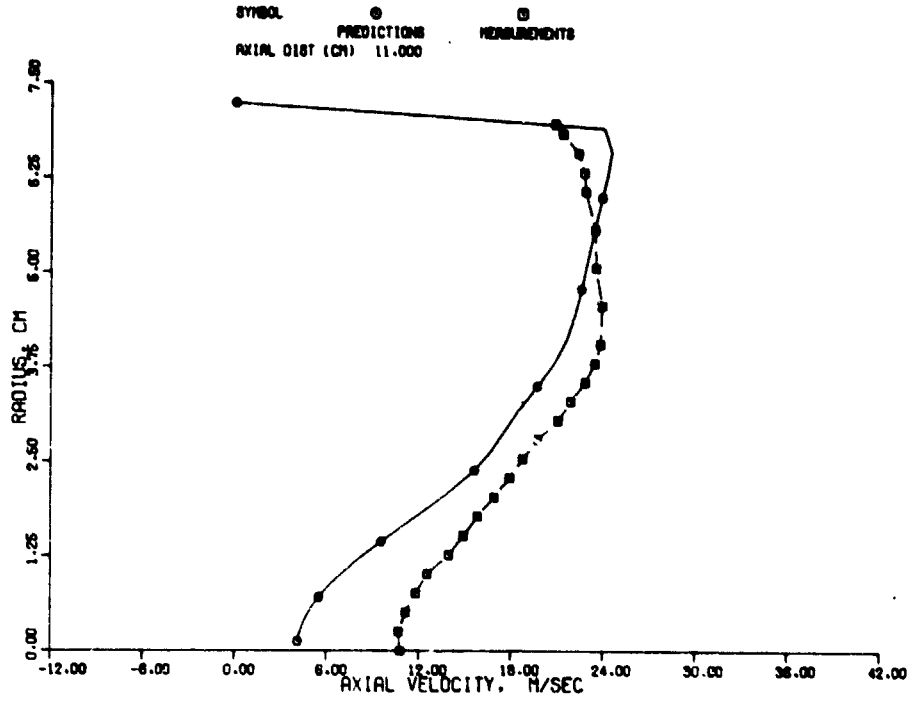

(i)

Figure 39. Axial Velocity Predictions of the Modified 2-D Elliptic Program for Counterswirl Case; Original K-ϵ Model (Contd).

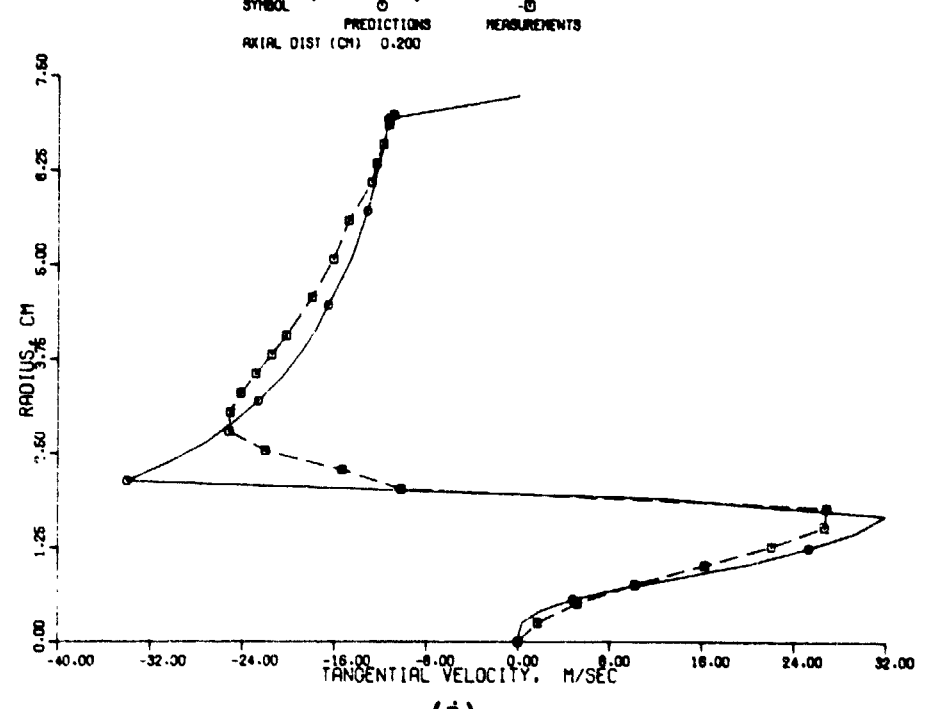

(j)

Figure 40. Tangential Velocity Predictions of the Modified 2-D Elliptic Program for Counterswirl Case; Original K-ϵ Model.

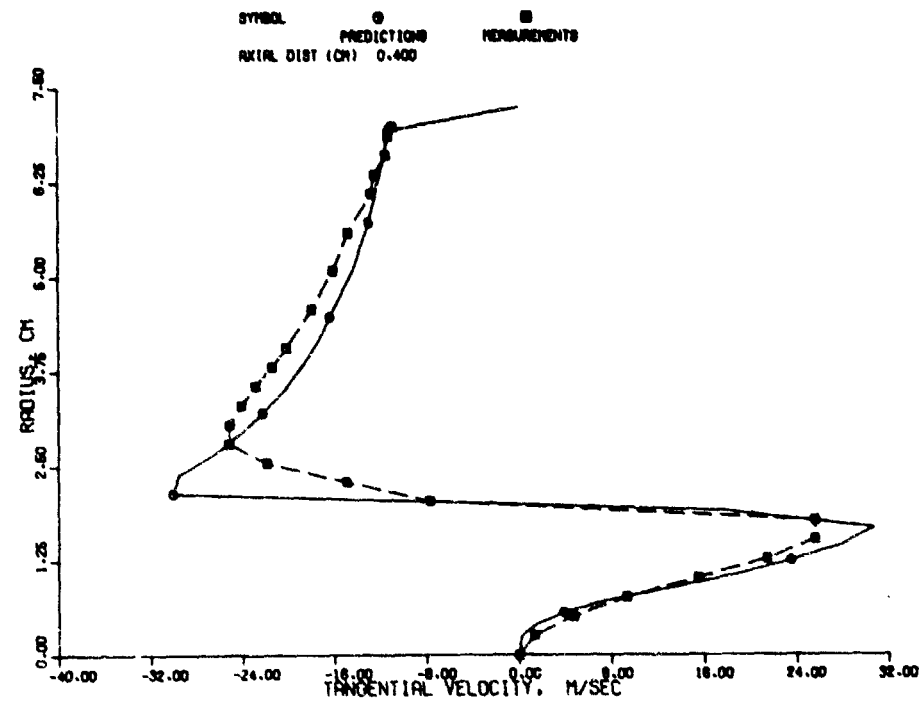

(b)

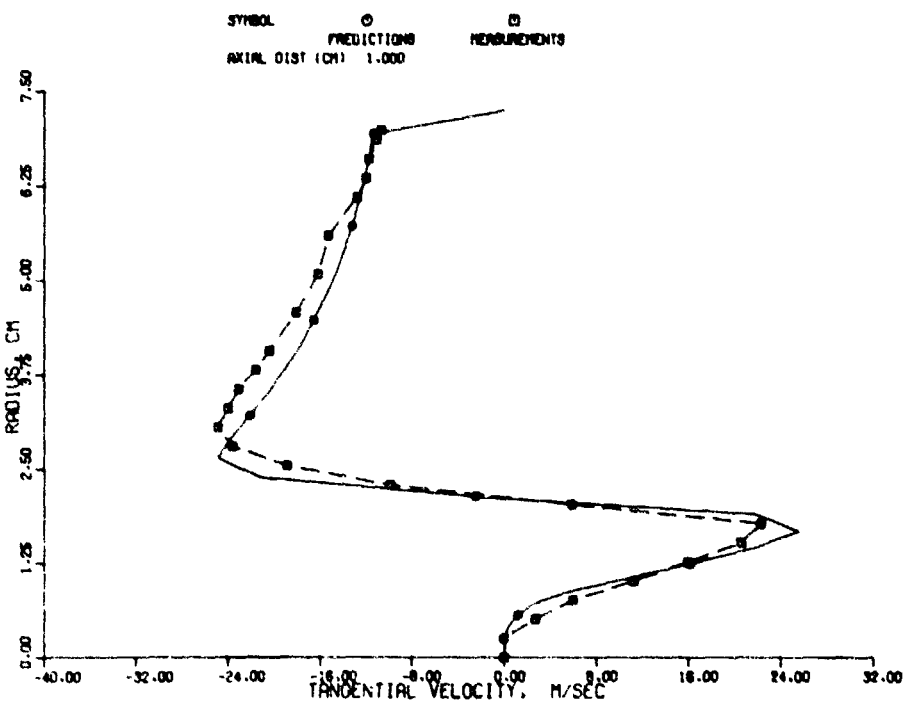

(c)

Figure 40. Tangential Velocity Predictions of the Modified 2-D Elliptic Program for Counterswirl Case; Original K-ϵ Model (Contd).

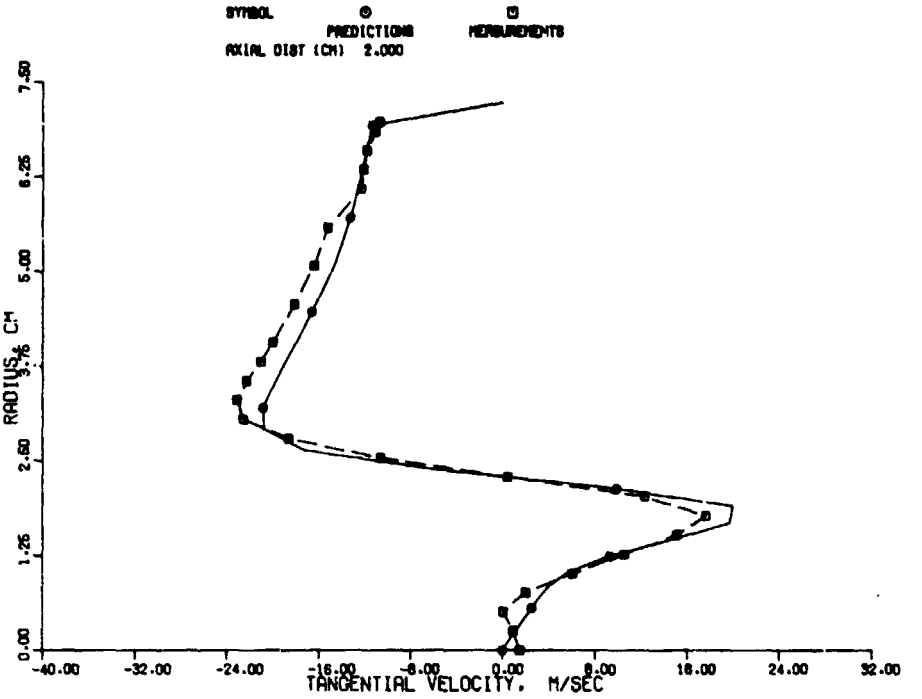

(d)

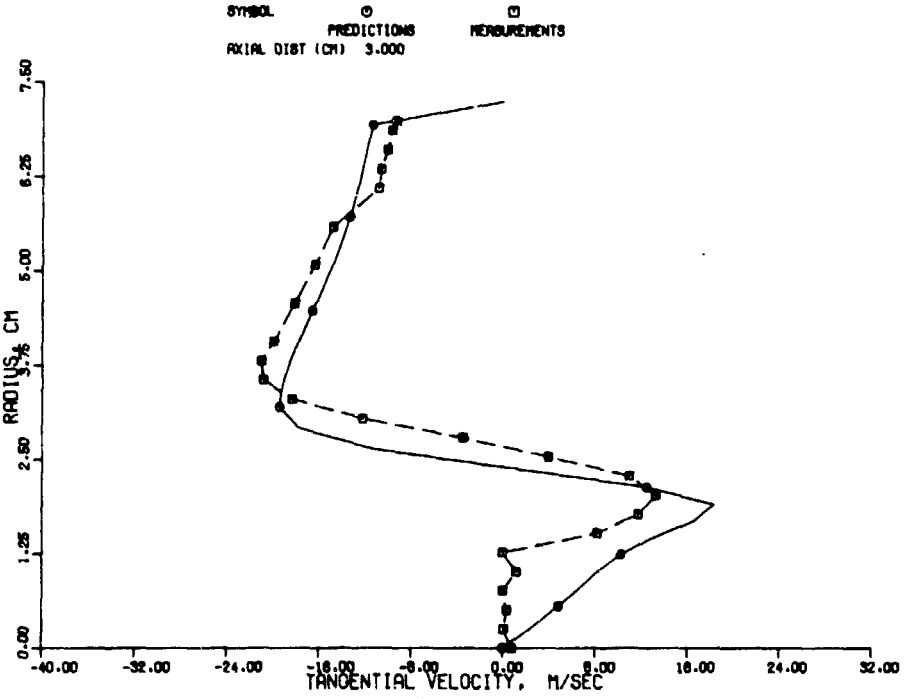

(e)

Figure 40. Tangential Velocity Predictions of the Modified 2-D Elliptic Program for Counterswirl Case; Original K-ϵ Model (Contd).

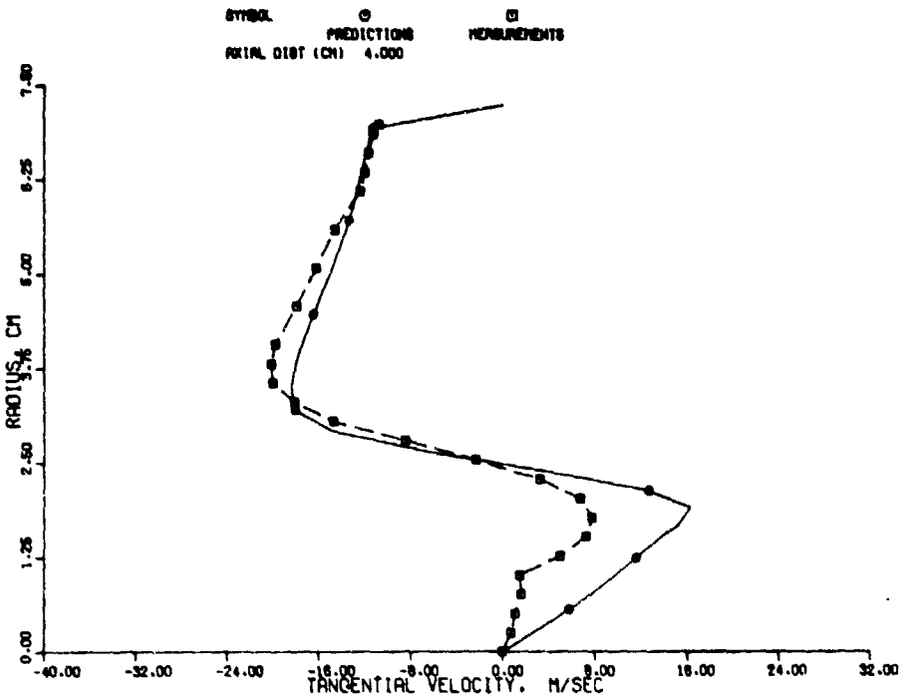

(f)

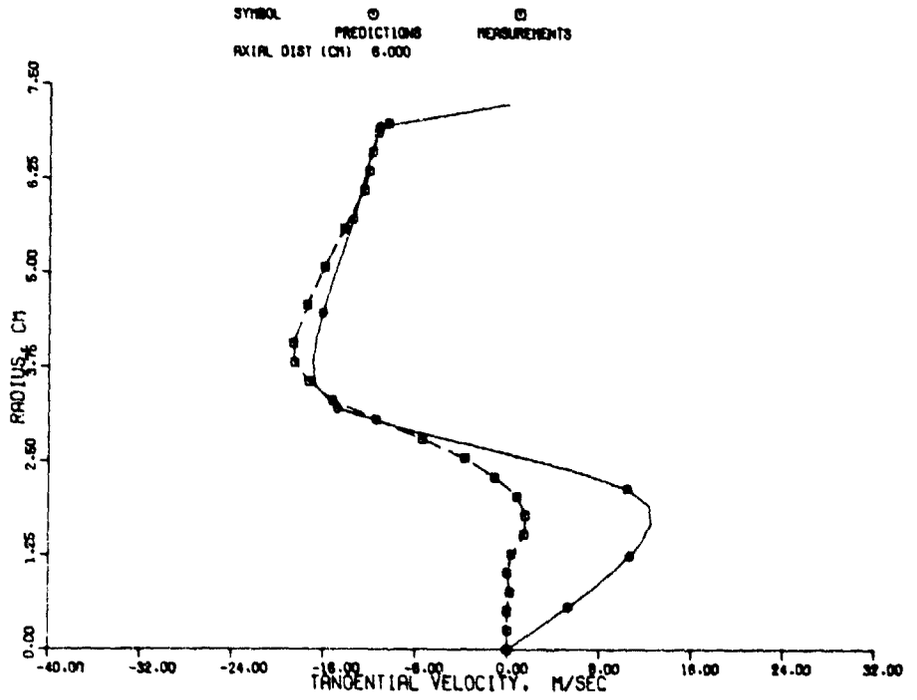

(g)

Figure 40. Tangential Velocity Predictions of the Modified 2-D Elliptic Program for Counterswirl Case; Original K-ε Model (Contd).

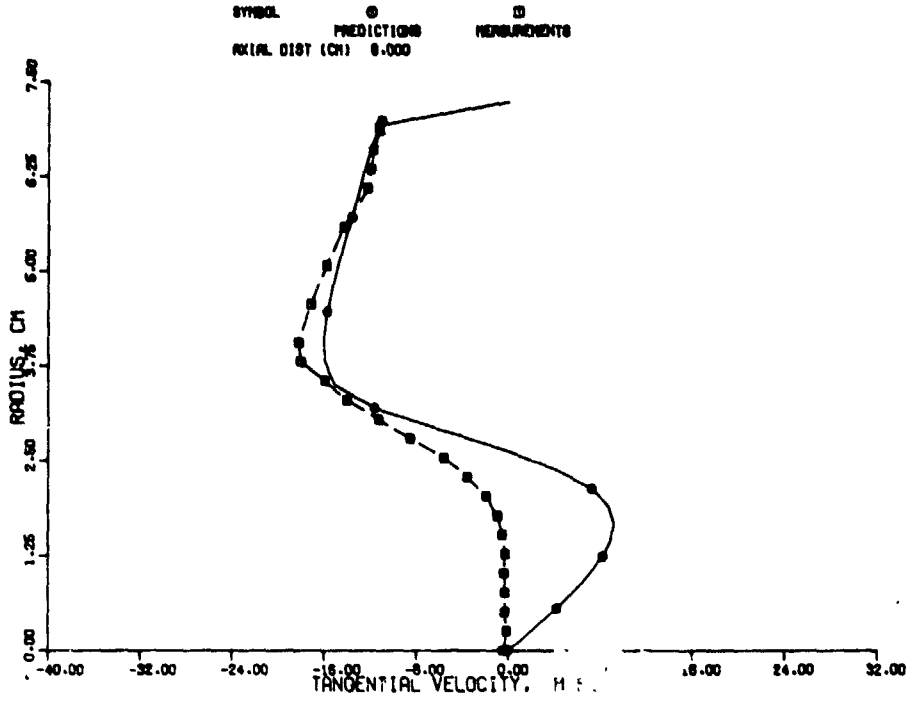

(h)

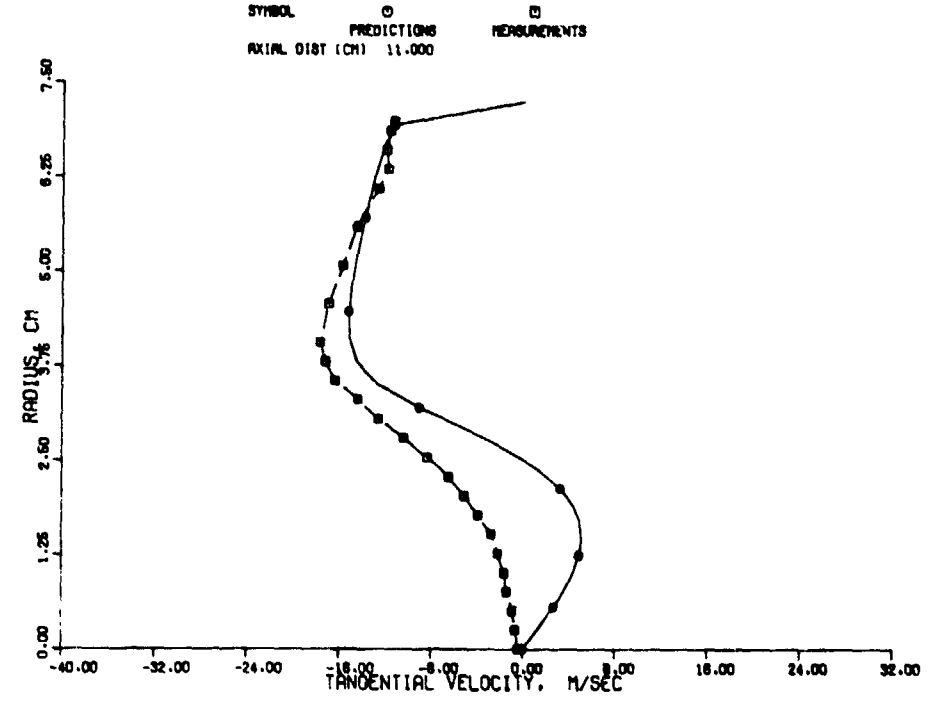

(i)

Figure 40. Tangential Velocity Predictions of the Modified 2-D Elliptic Program for Counterswirl Case; Original K-ϵ Model (Contd).

show very good agreement with the data. The CAPS program computes the tangential velocity by applying the free vortex structure (rV_θ = constant) to the outer swirling flow. The measurements seem to indicate that this structure is prevalent in the outer flow, with the exception of the regions near the tube walls. The tangential velocity profiles agree very well up to the beginning of the recirculation zone (X = 2 cm). Beyond this region, the agreement is not as good. Some of these differences are believed to be due to the deficiency of the k-ϵ model. The k-ϵ model assumes that the turbulence is isotropic, and hence a single length scale is associated with all three directions. In the vicinity of the recirculation zone, the production of turbulence kinetic energy should be very high due to the high local strain rates. It has been observed experimentally (ref. 34) that regions of turbulence kinetic energy production have highly skewed turbulence structure causing a large deviation from isotropy. The k-ϵ model is not expected to result in excellent agreement in the anisotropic regions near the recirculation zone. Furthermore, the measured data using pressure probes inside the recirculation zone are not likely to be very accurate.

The results presented in Figures 39 and 40 indicate that the pressure distribution resulting from the interaction between the inner and the outer streams plays a very important role in producing a recirculation region in the flow field. The extent of this interaction is illustrated in the total pressure distribution.

In a fully developed isoenergetic, nonswirling potential flow in a pipe, the static pressure is constant across the diameter of the pipe, and the total pressure distribution would depend upon the local velocity profiles. When swirl is introduced into this potential flow, the centrifugal acceleration caused by the swirl would tend to increase the static pressure near the pipe wall and reduce it near the centerline. The total

pressure variation across the pipe would alter accordingly. The effect of viscosity on the total pressure distribution would be to introduce sharp gradients in the viscous layer. In view of these qualitative trends, the radial total pressure distribution in the swirling flow field can shed some light on the areas where the k-ϵ model needs improvement.

A comparison between the measured and the predicted total pressure distribution for the counterswirling flow case is shown in Figure 41. These figures represent one-tenth of the difference between local total pressure and the total pressure at the pipe wall, $[P_T - (P_T)_{wall}]/10$. Figure 41 shows that the predicted profiles agree very well with measurements in the inner flow region near the centerline, while the agreement is not as good in the outer flow region. The lack of good agreement in the outer flow is attributed to the nature of the CAPS program predictions. Notwithstanding this difference, the predicted total pressure profiles are in very good agreement with measurements up to the beginning of the recirculation zone, and the comparison gets worse further downstream. The gradual deterioration in the quantitative agreement is due the k-ϵ turbulence model shortcomings and other potential numerical difficulties. Further, the accuracy of the measurements in the recirculating region is unknown.

Although the total pressure distributions describe how close the flow field is to a potential flow, the effect of interaction is revealed on the static pressure distribution. Since the static pressure distributions can be obtained from the total pressure and the velocity profiles, they are not presented in this report for brevity. However, it is interesting to obtain an idea of the axial variation of the static pressure. The centerline static pressure drop predicted by the modified 2-D elliptic program is compared with the values obtained from the Cornell data in Figure 42. The agreement between the predicted and the

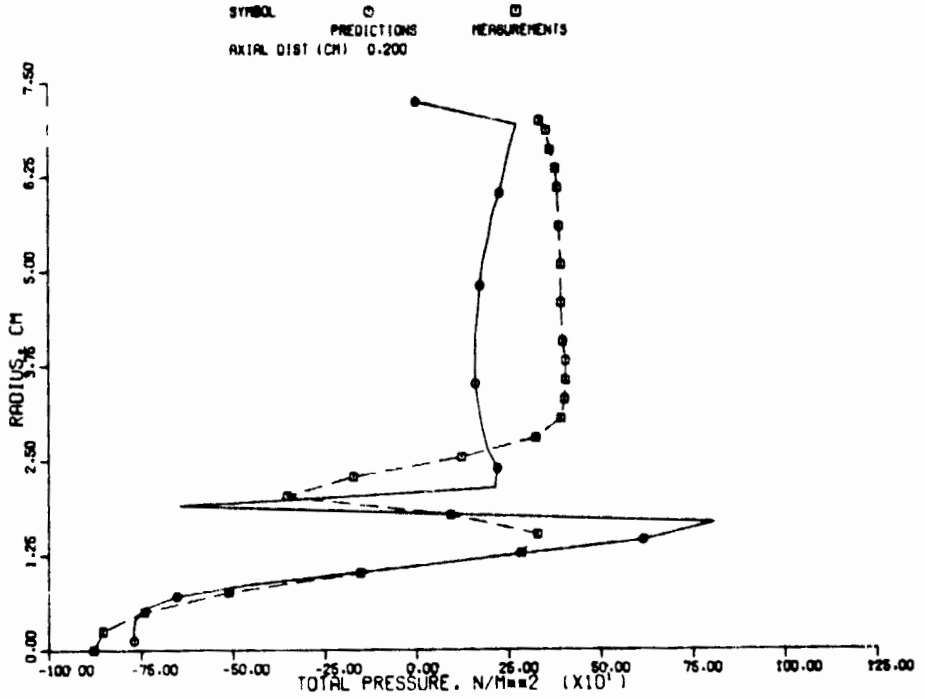

(a)

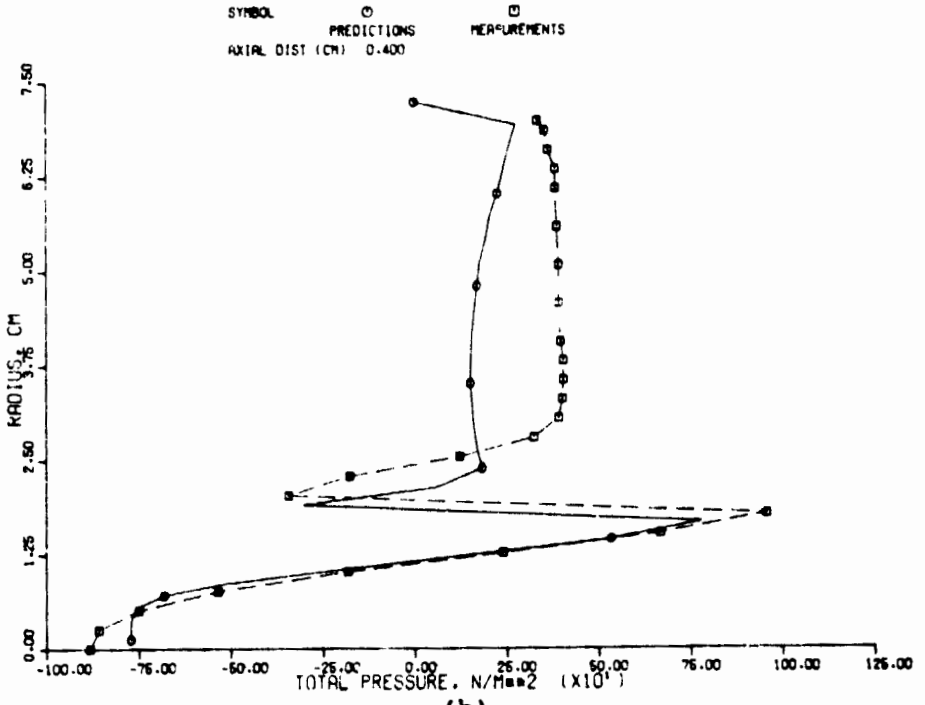

(b)

Figure 41. Total Pressure Predictions of the Modified 2-D Elliptic Program for Counterswirl Case; Original K-ε Model.

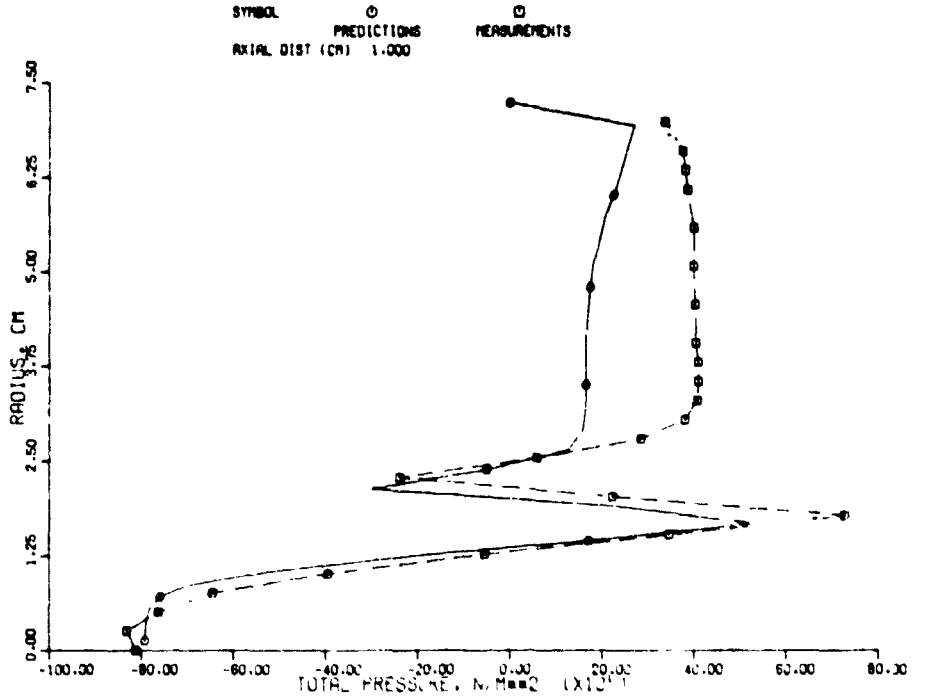

(c)

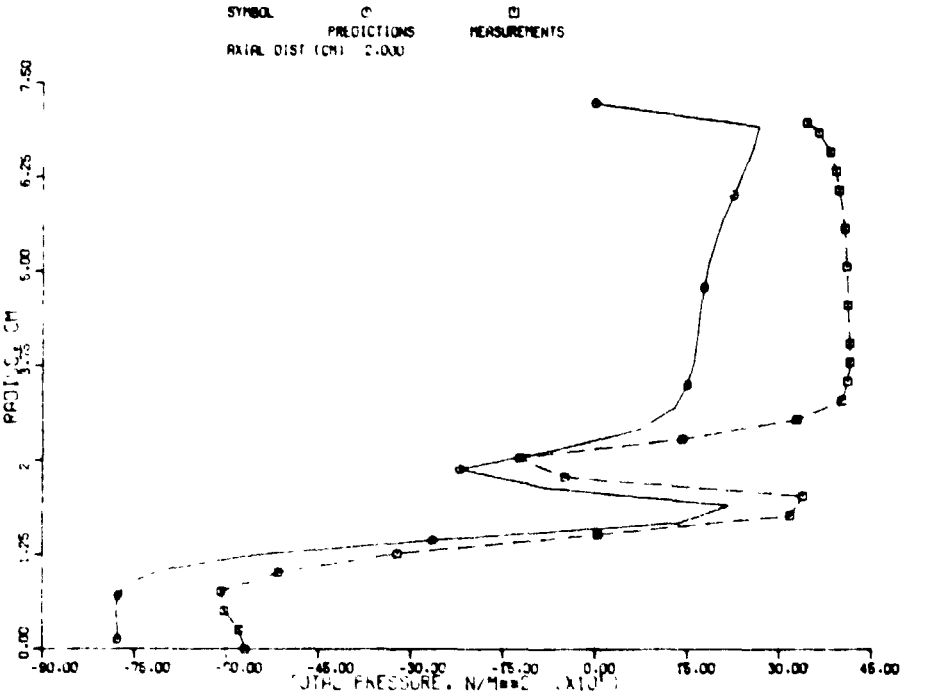

(d)

Figure 41. Total Pressure Predictions of the Modified 2-D Elliptic Program for Counterswirl Case; Original K-ϵ Model (Contd).

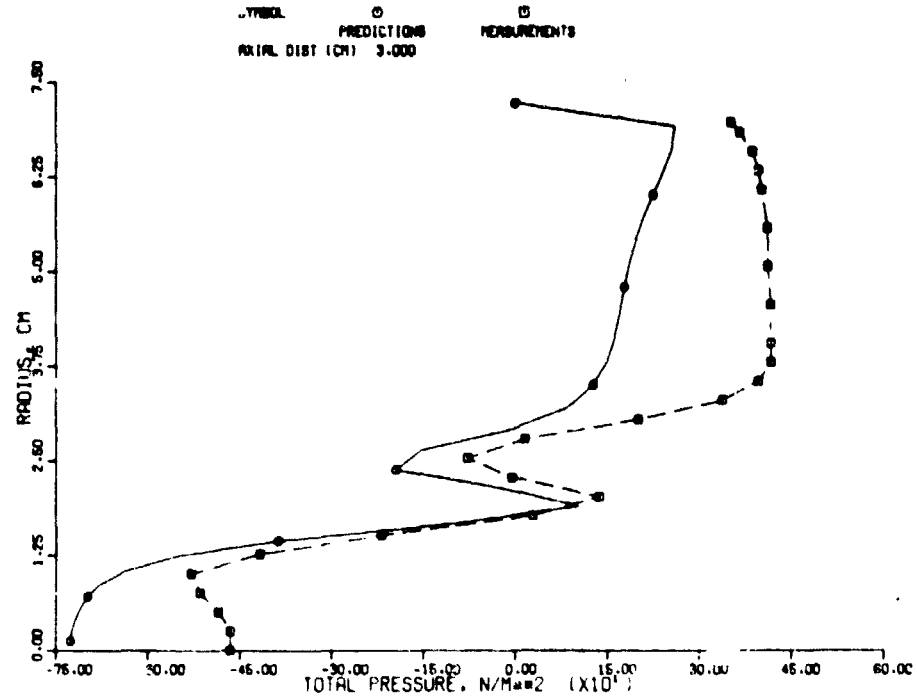

(e)

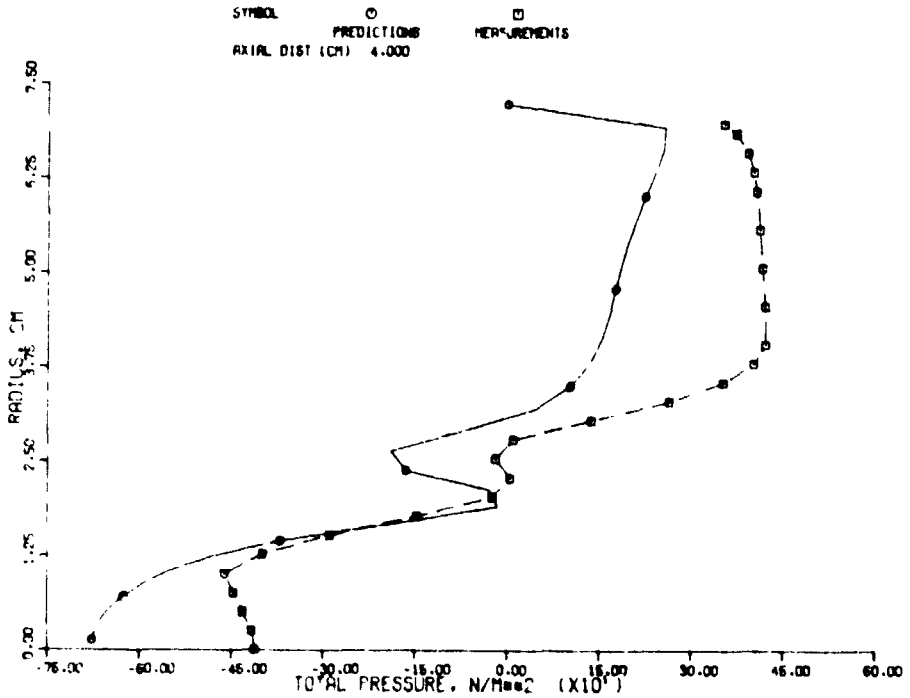

(f)

Figure 41. Total Pressure Predictions of the Modified 2-D Elliptic Program for Counterswirl Case; Original K-ε Model (Contd).

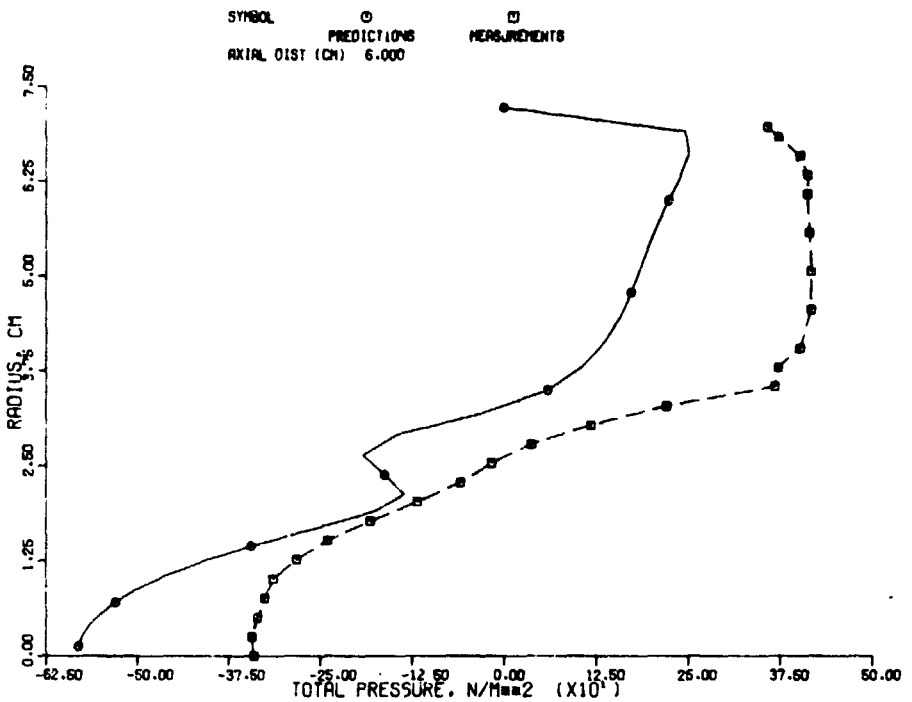

(g)

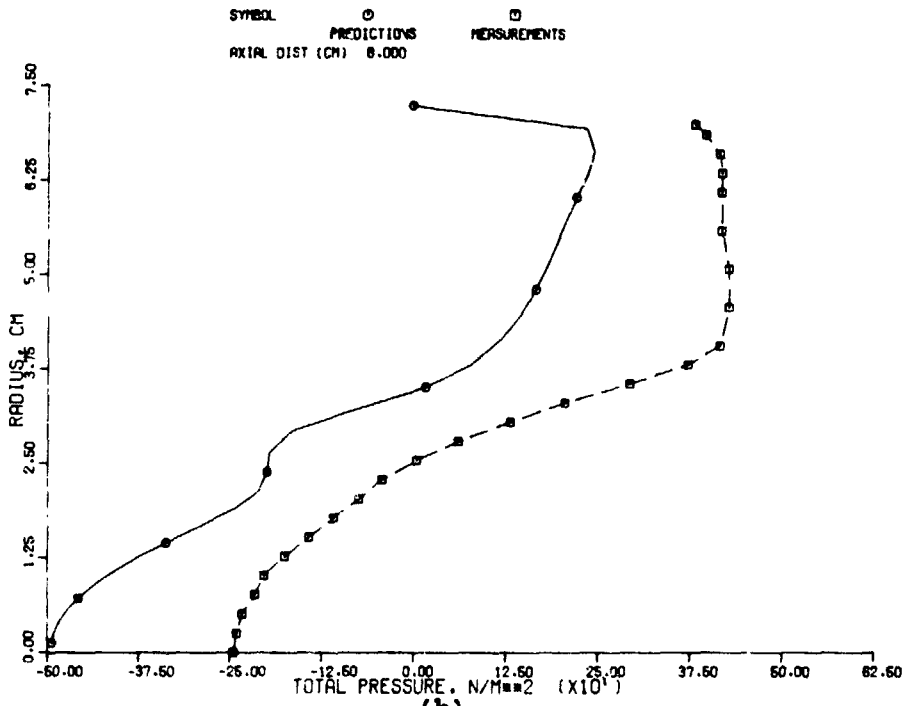

(h)

Figure 41. Total Pressure Predictions of the Modified 2-D Elliptic Program for Counterswirl Case; Original K-ϵ Model (Contd).

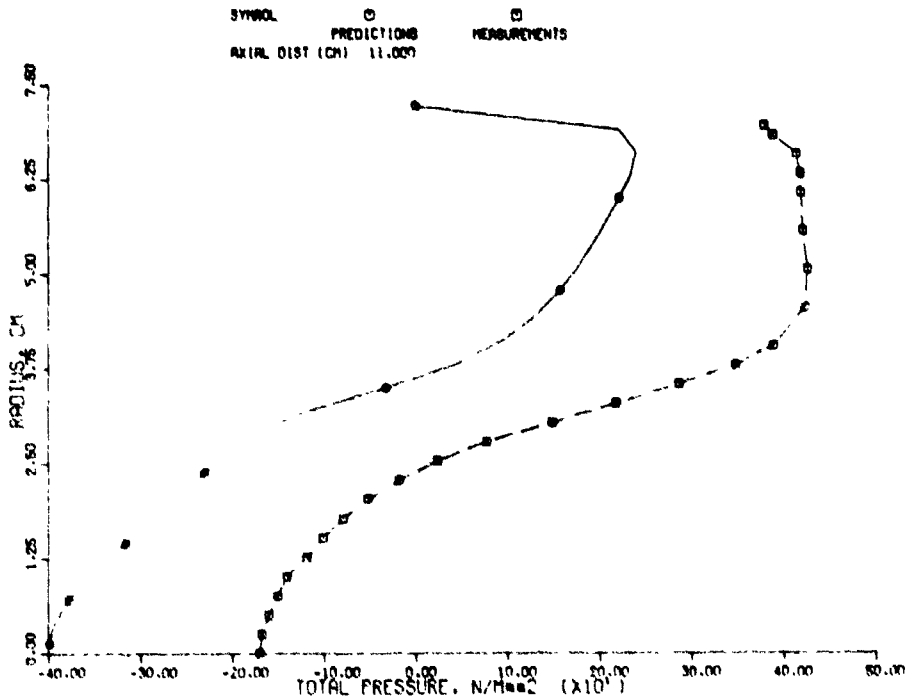

(i)

Figure 41. Total Pressure Predictions of the Modified 2-D Elliptic Program for Counterswirl Case; Original K-ϵ Model (Contd).

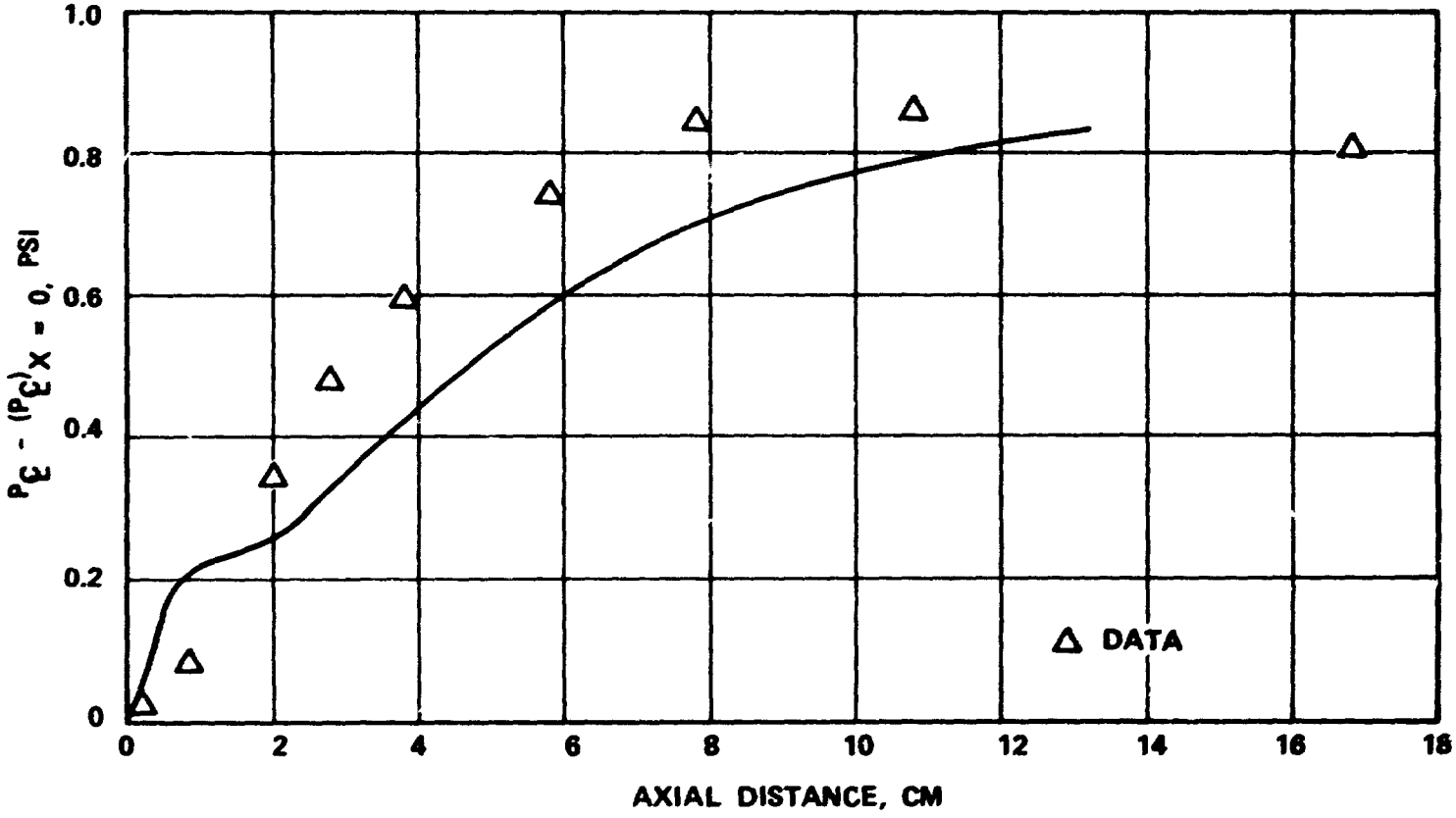

Figure 42. Centerline Static Pressure Variation for Counterswirl Case.

measured pressure drop is quite good. A similar comparison of the wall static pressure drop between the predicted and the measured results are shown in Figure 43. This figure, once again, shows that the two results are in good quantitative agreement. The k-ϵ model predictions on pressure drop in other regions are in a similar agreement with the measurements.

Figure 44 represents the comparison of the turbulence kinetic energy profiles predicted by the modified 2-D elliptic program and the measured longitudinal component of the turbulence kinetic energy, $1/2\langle U^2 \rangle$. The values of inlet turbulence kinetic energy used in the Task III computations correspond to the fully developed flows; namely, uniform k vales with magnitude 0.003 $(U_{av})^2$. This corresponds to a nondimensionalized turbulence intensity of 5.5 percent. In view of the accelerating outer flow passage, this value was considered to be a reasonable estimate.

The results presented in Figure 44 show that the predicted kinetic energy values are lower than those deduced from the data up to the end of the recirculation bubble, and beyond this zone, the magnitudes are in closer agreement. The experimental data on turbulence were obtained using a hot wire anemometer. These results indicate that the estimated values for the inlet turbulence kinetic energy of the outer flow is indeed reasonable. The relatively inferior agreement near the recirculation bubble is partially attributed to the isotropic assumption in the k-ϵ model. The agreements between predictions and the data in the outer flow region are uniformly good.

In swirling pipe flows, experimental observations (ref. 37) show that turbulent kinetic energy is produced directly from the mean flow on both longitudinal and transverse components. The production of the transverse component is increased near the outer wall and the large scale turbulence eddies generally roam

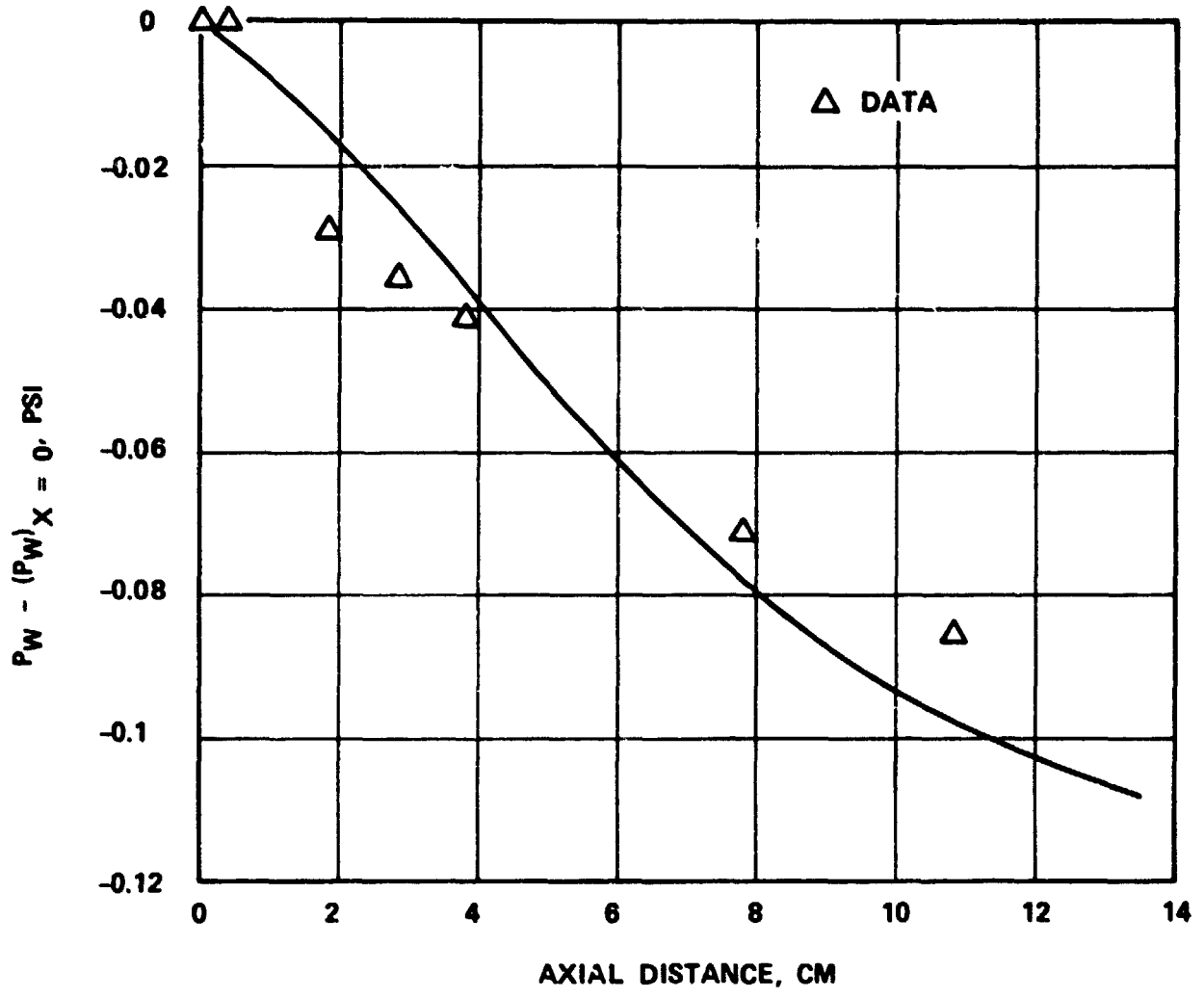

Figure 43. Wall Static Pressure Variation for Counterswirl Case.

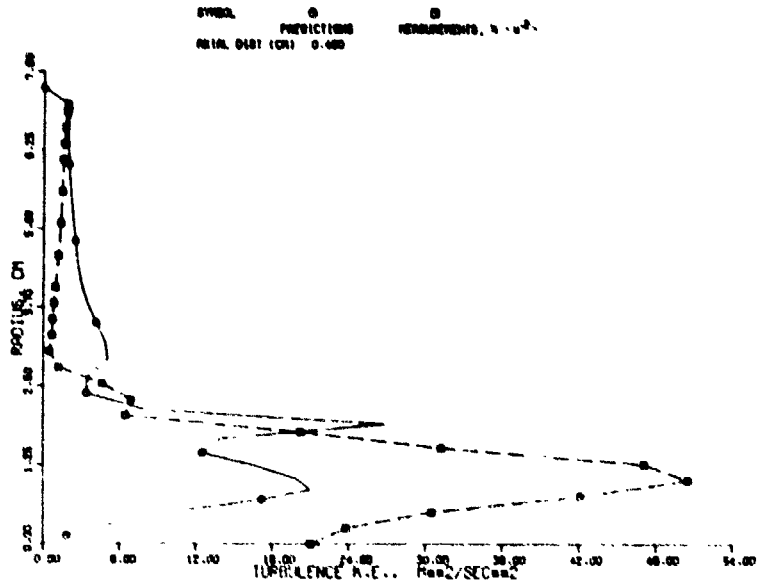

(a)

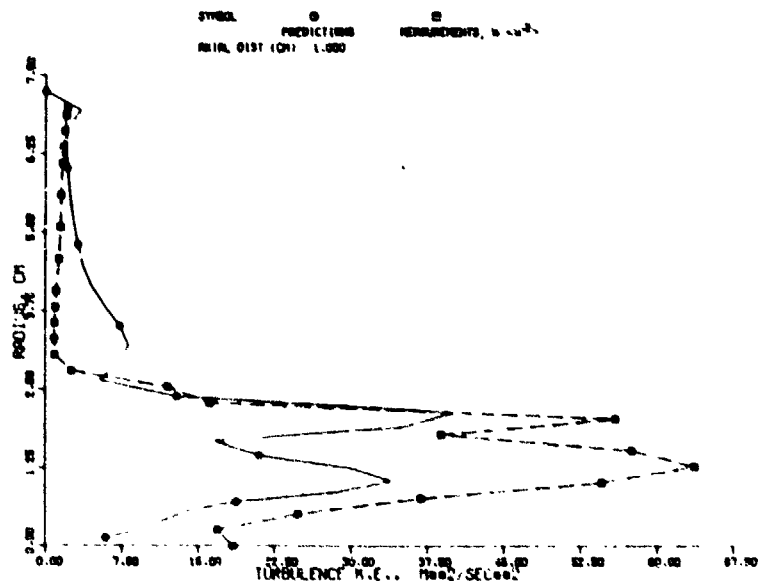

(b)

Figure 44. Turbulence K.E. Predictions of the Modified 2-D Elliptic Program for Counterswirl Case; Original K-ϵ Model.

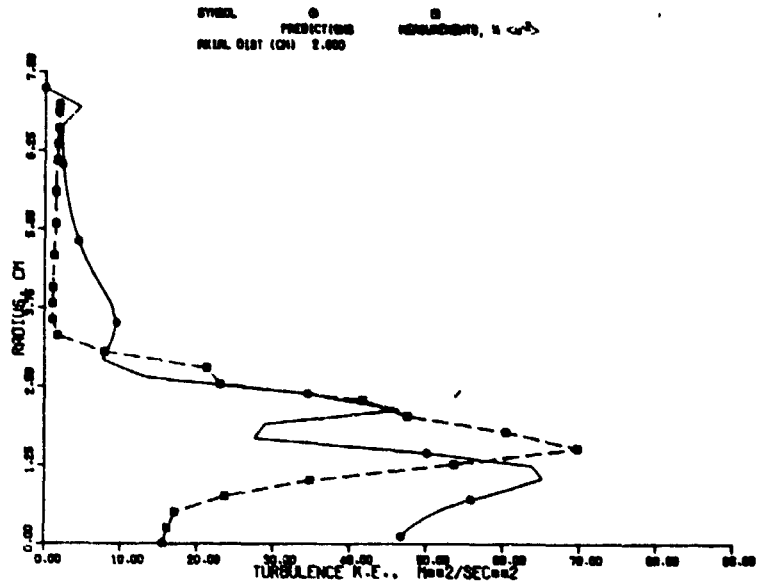

(c)

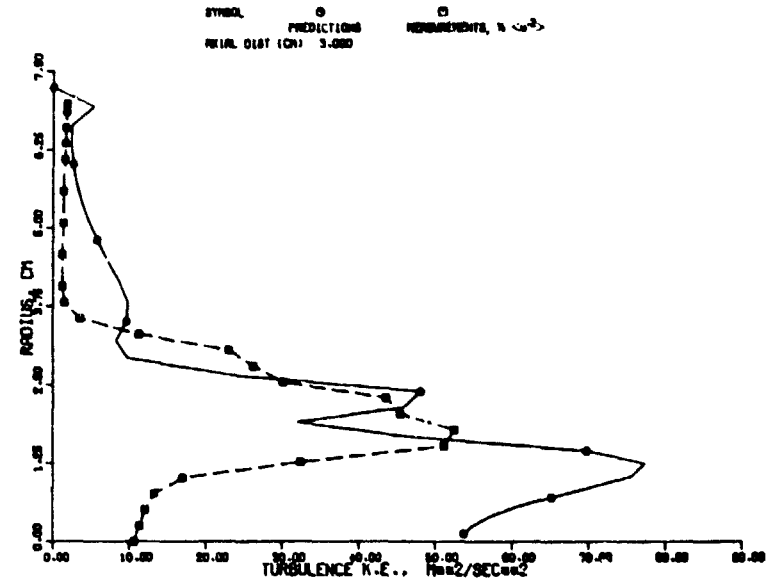

(d)

Figure 44. Turbulence K.E. Predictions of the Modified 2-D Elliptic Program for Counterswirl Case; Original K-ϵ Model (Contd).

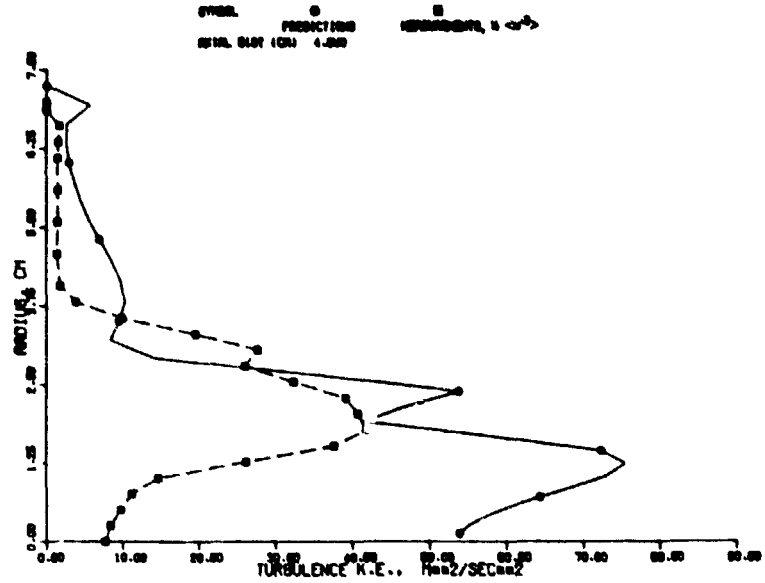

(e)

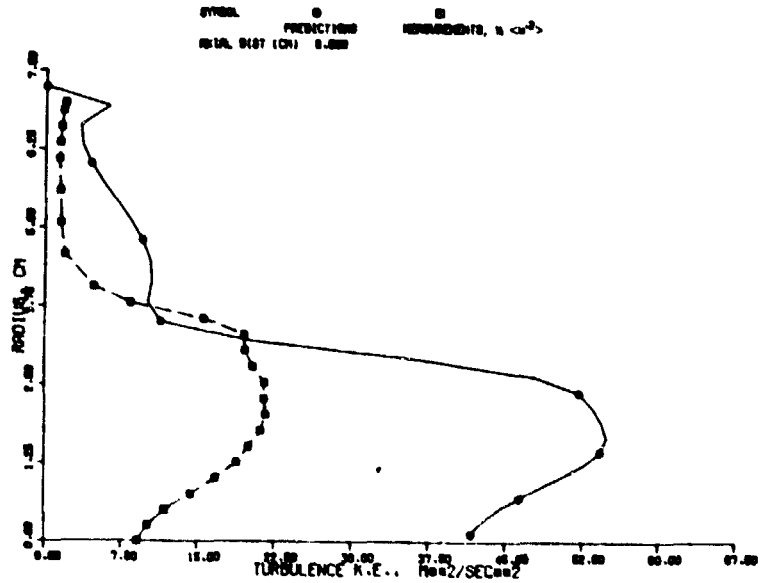

(f)

Figure 44. Turbulence K.E. Predictions of the Modified 2-D Elliptic Program for Counterswirl Case; Original K-ϵ Model (Contd).

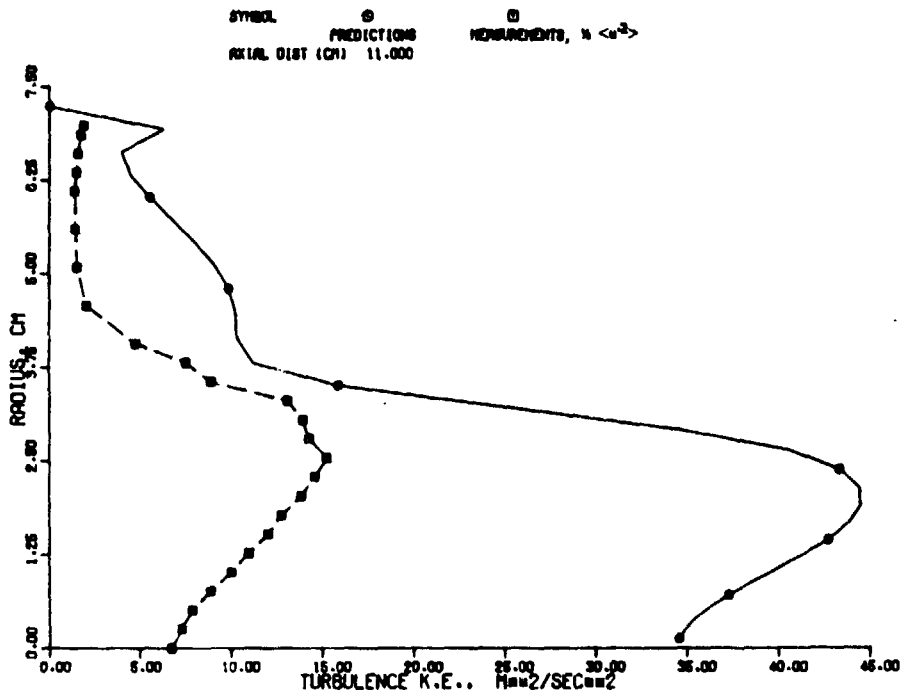

(g)

Figure 44. Turbulence K.E. Predictions of the Modified 2-D Elliptic Program for Counterswirl Case; Original K-ϵ Model (Contd).

radially back and forth in the outer half of the flow. This indicates a generally higher turbulence production near the outer wall than near the center.

In the present swirling flow assembly, the inner flow has a swirler vane whose hub radius is 0.635 cm and the tip radius is 1.86 cm. In the core of the flow, no swirl is generated. The flow development downstream should exhibit the effect of the shear layer from the hub region and an increased turbulence kinetic region near the tip radius of the swirler vanes. The shear layer produced by the shroud at the hub of the vanes would tend to decrease the turbulence kinetic energy in that region. These trends are clearly seen in the predicted results. The measured profile at X = 1 cm shows a similar behavior. The large gradients in the kinetic energy profile are gradually smeared out with increasing distance downstream.

From the point of view of analytical predictions, the most sensitive quantity in the model is the radial velocity. The radial velocity component, V_r in the present configuration, is quite small compared to the other mean velocity components. The radial velocity is also the most difficult to measure in the recirculation zone. The probe interference effects on radial velocity would be by far the most pronounced. Figure 45 shows the comparison between the predicted and the measured radial velocity components for the counterswirl case.

The modified 2-D elliptic program was also employed to analyze co-swirling flows. In this case, a uniform inlet axial velocity of magnitude 29.65 m/s was used for the inner flow. The inlet tangential velocity profile employed had a magnitude of zero from r=0 to r=0.635 cm and a constant value of 33.1 m/s from r=0.635 cm to r=1.86 cm. The profiles used for the outer stream were obtained from the CAPS program and are illustrated in Figures 14(a) and 16(a). The radial velocity component was set

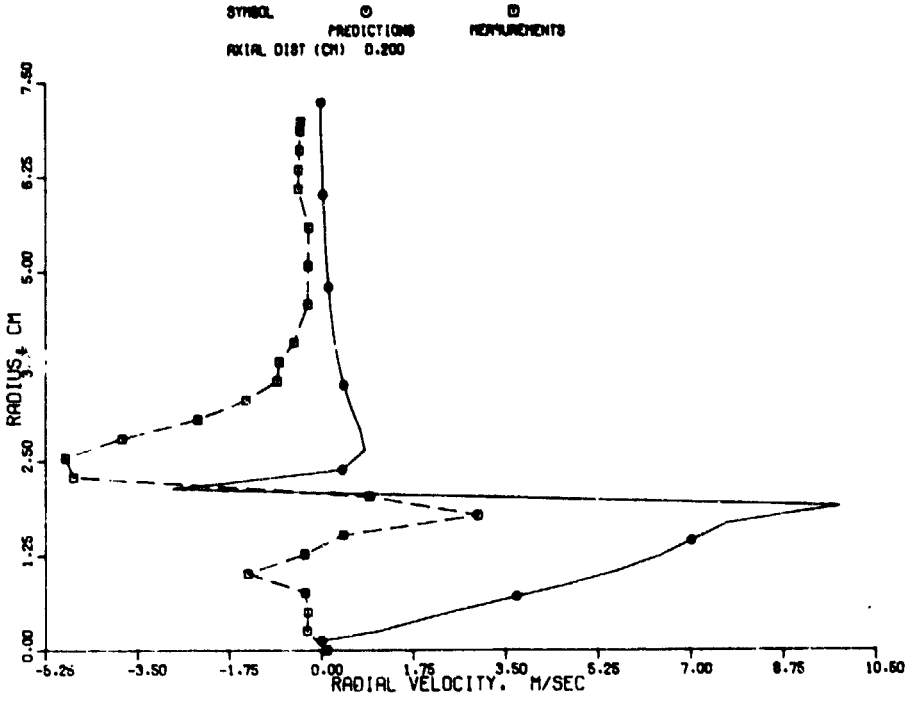

(a)

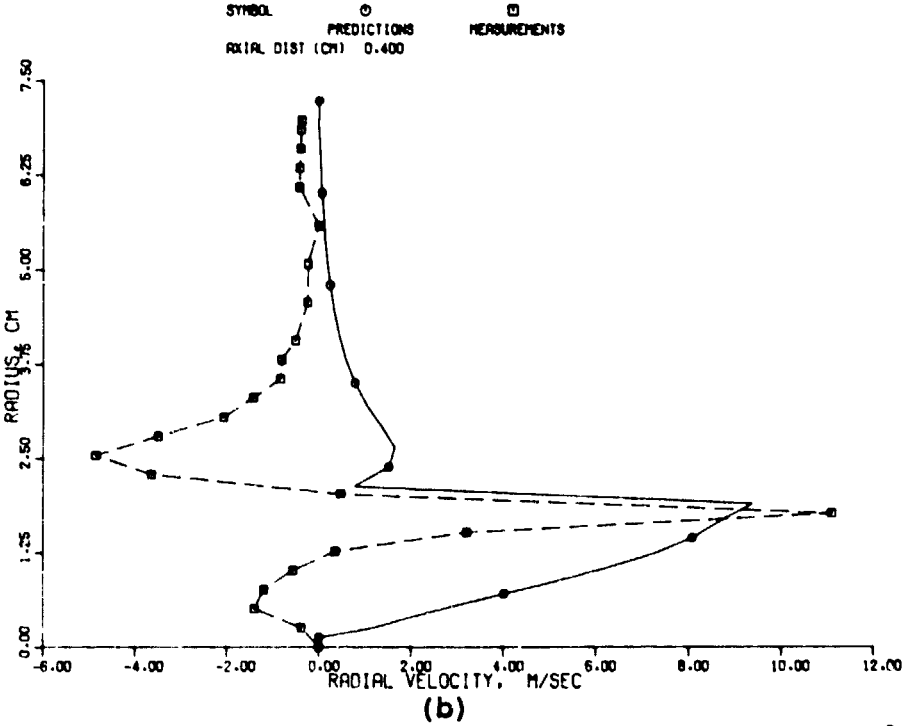

(b)

Figure 45. Radial Velocity Predictions of the Modified 2-D Elliptic Program for Counterswirl Case; Original K-ϵ Model.

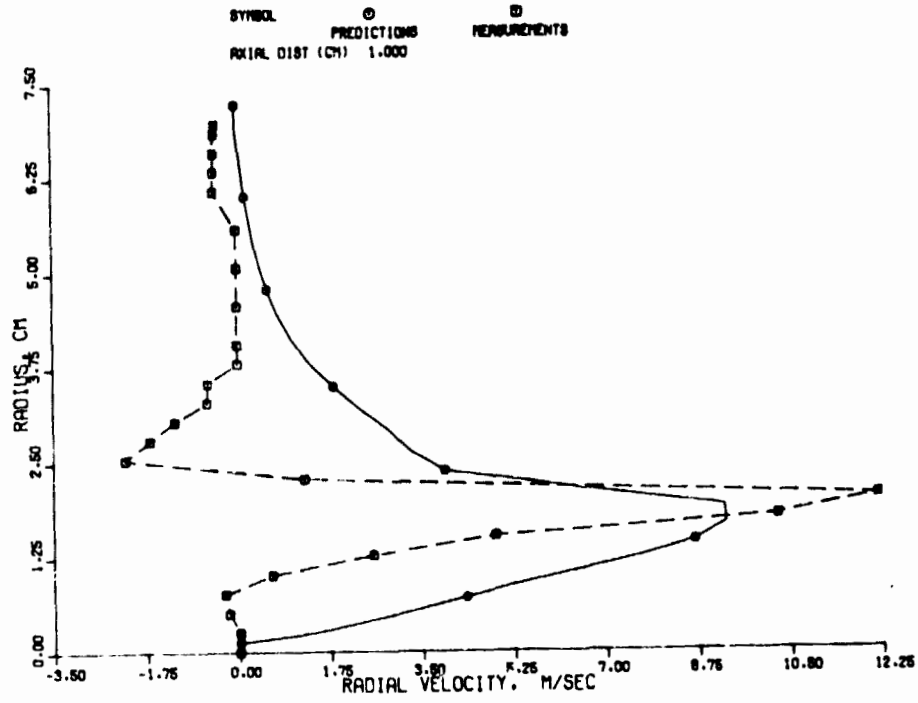

(c)

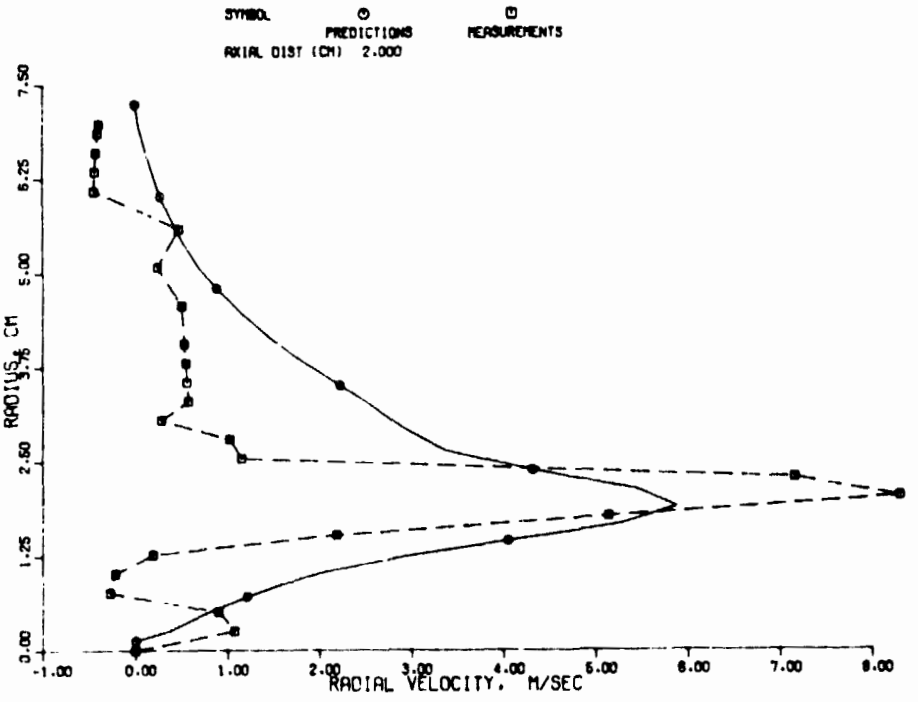

(d)

Figure 45. Radial Velocity Predictions of the Modified 2-D Elliptic Program for Counterswirl Case; Original K-ϵ Model (Contd).

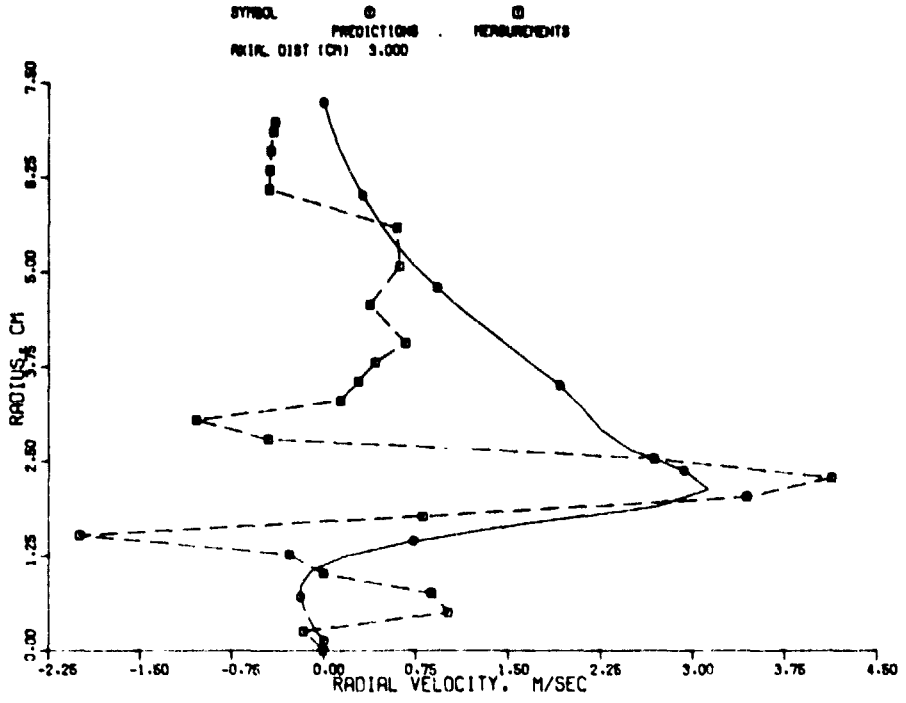

(e)

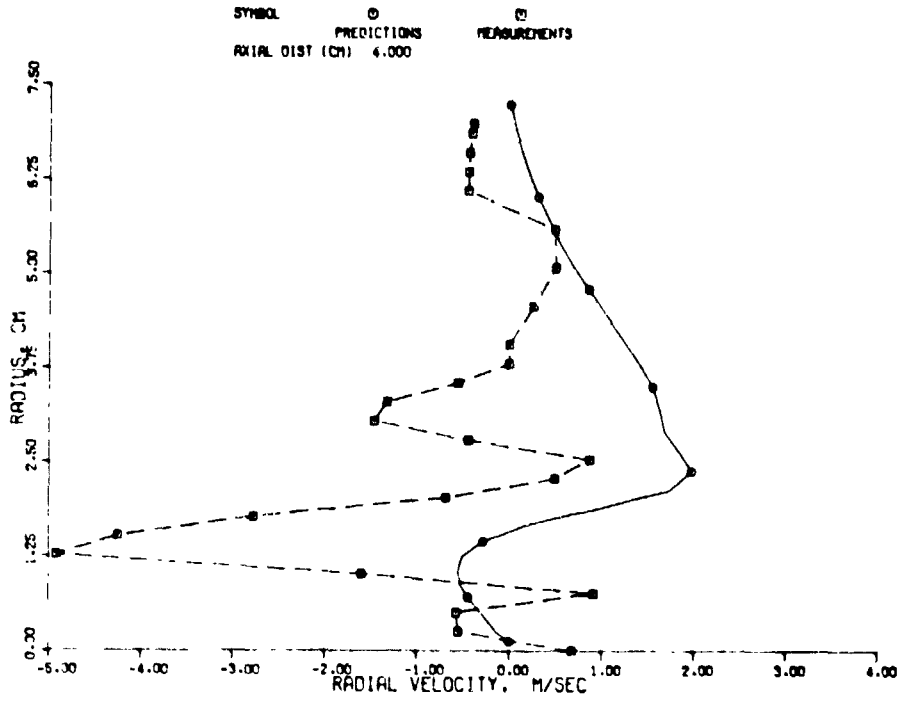

(f)

Figure 45. Radial Velocity Predictions of the Modified 2-D Elliptic Program for Counterswirl Case; Original K-ε Model (Contd).

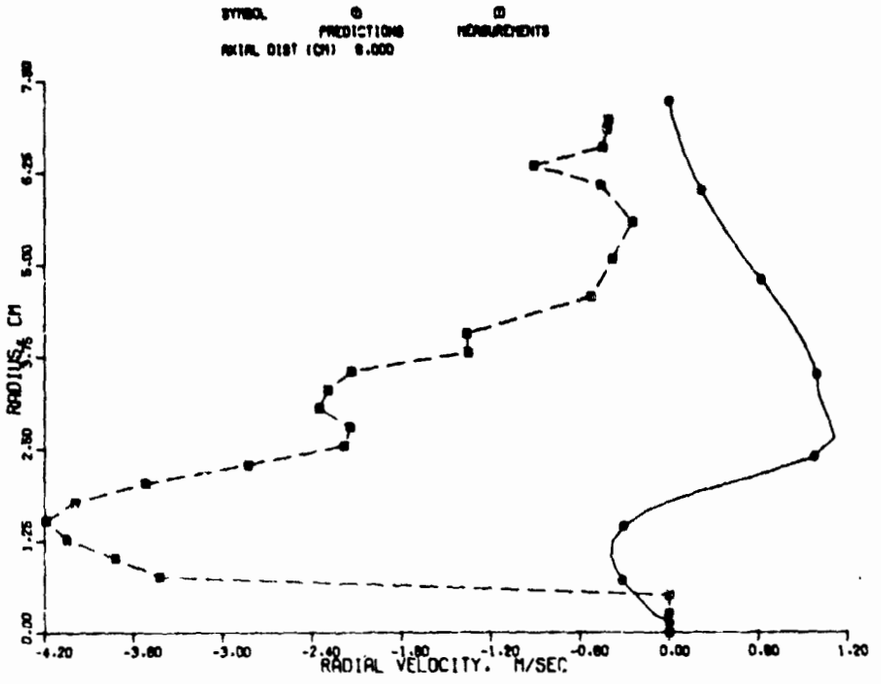

(g)

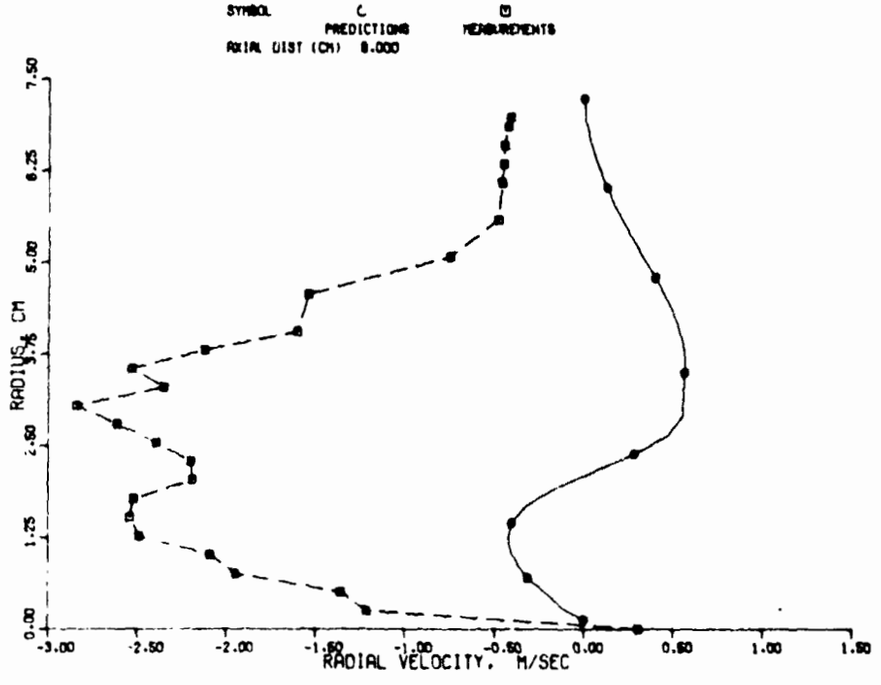

(h)

Figure 45. Radial Velocity Predictions of the Modified 2-D Elliptic Program for Counterswirl Case; Original K-ε Model (Contd).

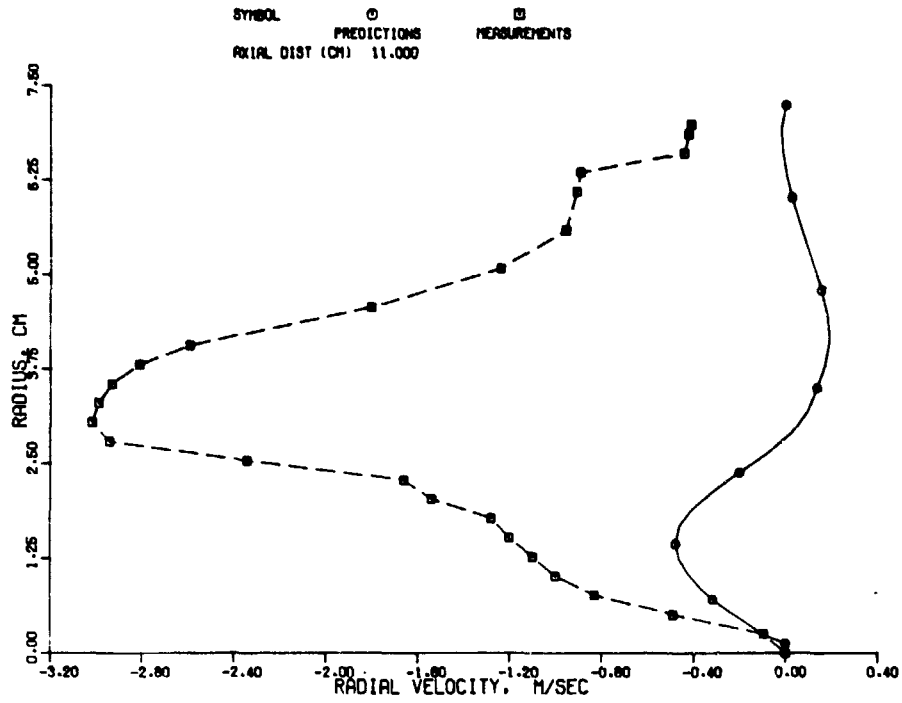

(i)

Figure 45. Radial Velocity Predictions of the Modified 2-D Elliptic Program for Counterswirl Case; Original K-ϵ Model (Contd).

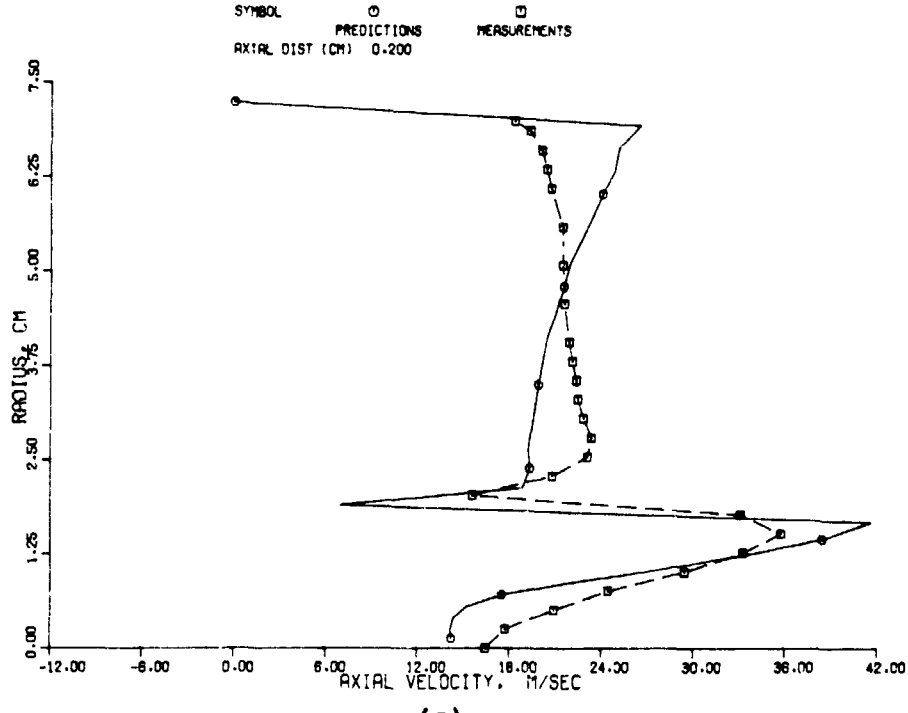

(a)

Figure 46. Modified 2-D Elliptic Program Predictions for Axial Velocity in Co-swirl Case; Original K-ϵ Model.

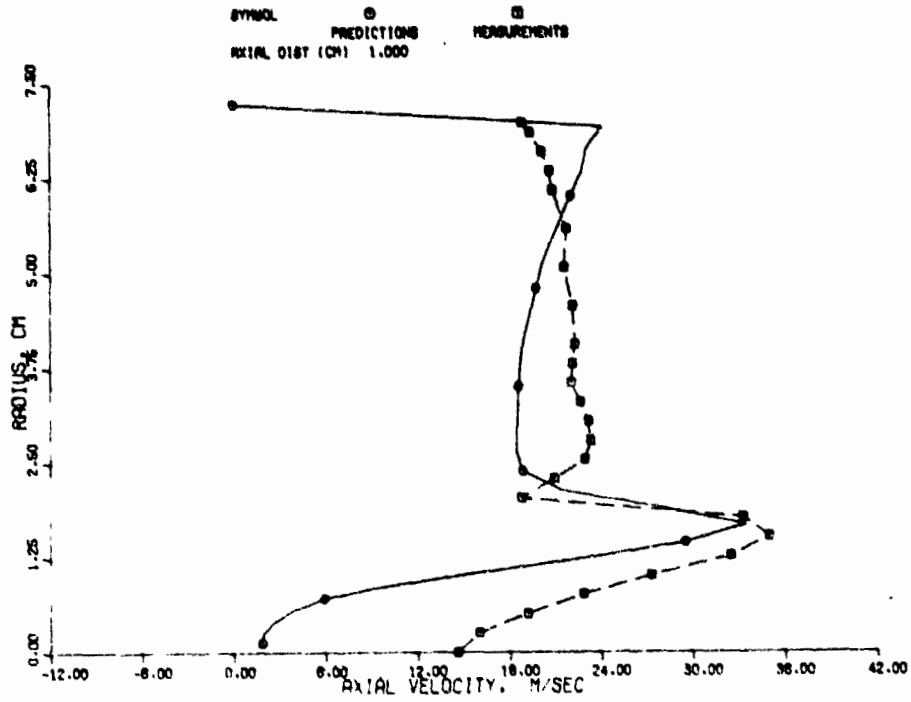

(b)

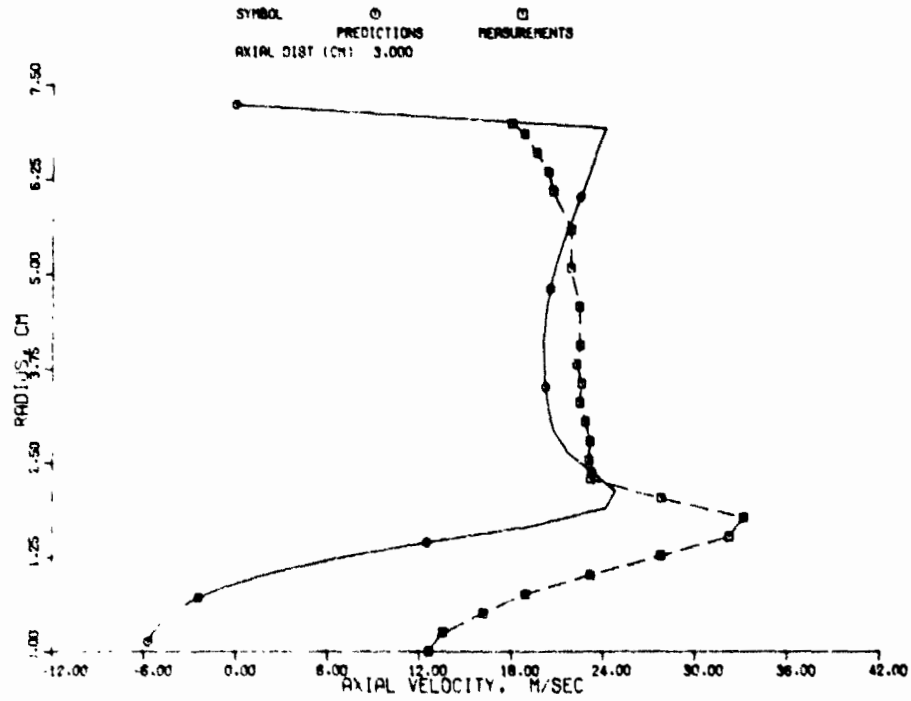

(c)

Figure 46. Modified 2-D Elliptic Program Predictions for Axial Velocity in Co-Swirl Case; Original K-ε Model (Contd).

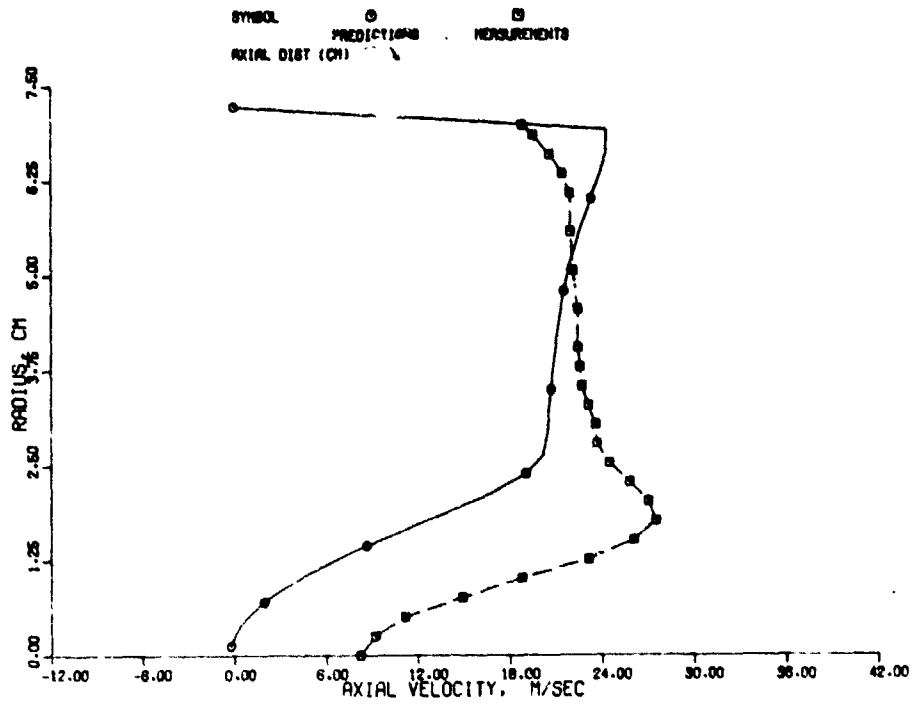

(d)

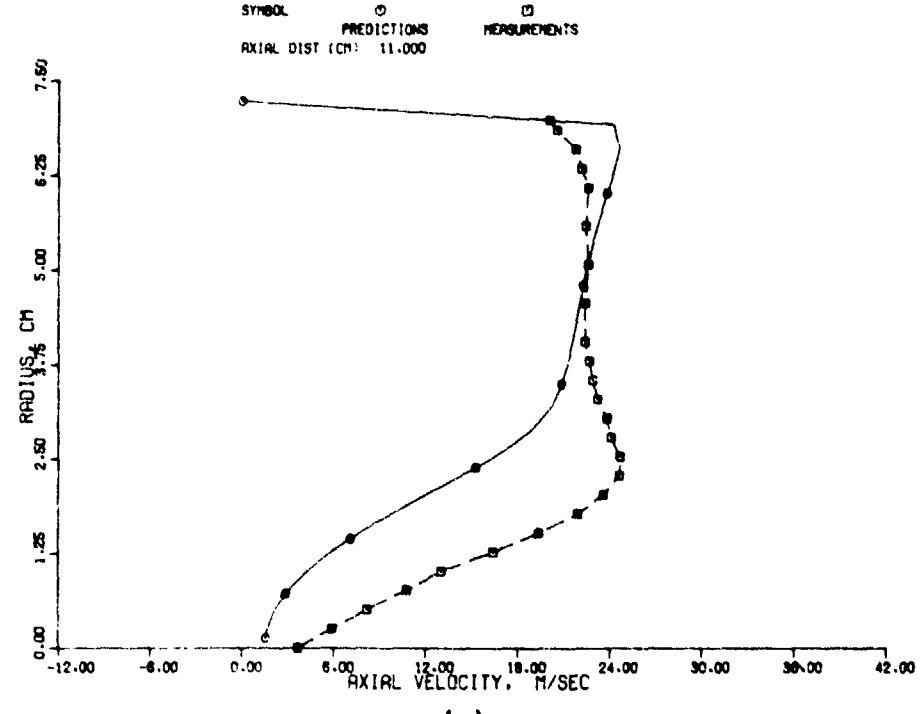

(e)

Figure 46. Modified 2-D Elliptic Program Predictions for Axial Velocity in Co-Swirl Case; Original K-ϵ Model (Contd).

equal to zero at the inlet plane and the inlet static pressure profile was assumed to be uniform for both the inner and the outer streams. The predictions in this case did not exhibit the same kind of agreement with measurements as in the counterswirl case.

Figure 46 affords a comparison of the axial velocity profiles in the co-swirling case. The solid line represents the predictions of the modified 2-D elliptic program, and the broken line represents the Cornell data. The two curves are in close agreement near the exit plane of the inner jet. Even though the measurements do not show any recirculation zone in the co-swirl case, the predictions do show the presence of a recirculation region. This recirculation region is smaller than that in the counterswirl case.

Figure 47 provides a comparison between the predicted and measured tangential velocity profiles. The agreement between these profiles is within about 10 percent in most of the region corresponding to the outer flow. In the inner flow region ($r < 2$ cm), the two profiles show significant differences downstream of $x = 0.2$ cm. As in the counterswirl case, the tangential velocity profiles in the outer flow region have the free vortex (rV_θ = constant) characteristics, except in the viscous region adjacent to the outer wall and the shear layer region near the inner tube wall.

The modified 2-D elliptic program predictions for turbulence kinetic energy are presented in Figure 48. The measured longitudinal component of the turbulence kinetic energy, $1/2\ \overline{u'^2}$, is also shown in this figure for comparative purposes. This figure indicates that the predicted value of turbulence kinetic energy in the core of the flow is smaller than that deduced from the data, and the values in the outer flow are comparable in magnitude.

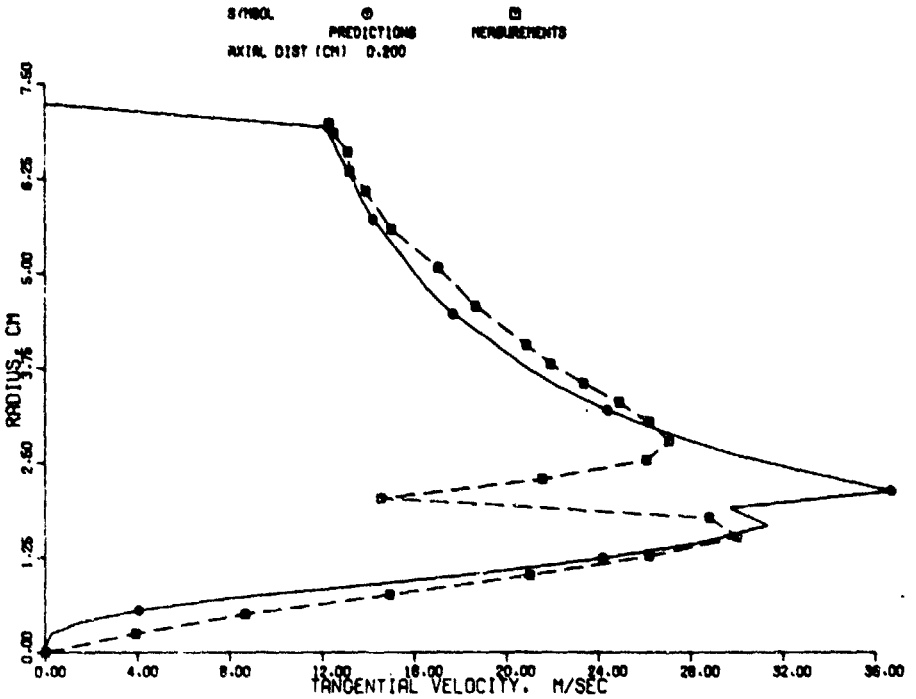

(a)

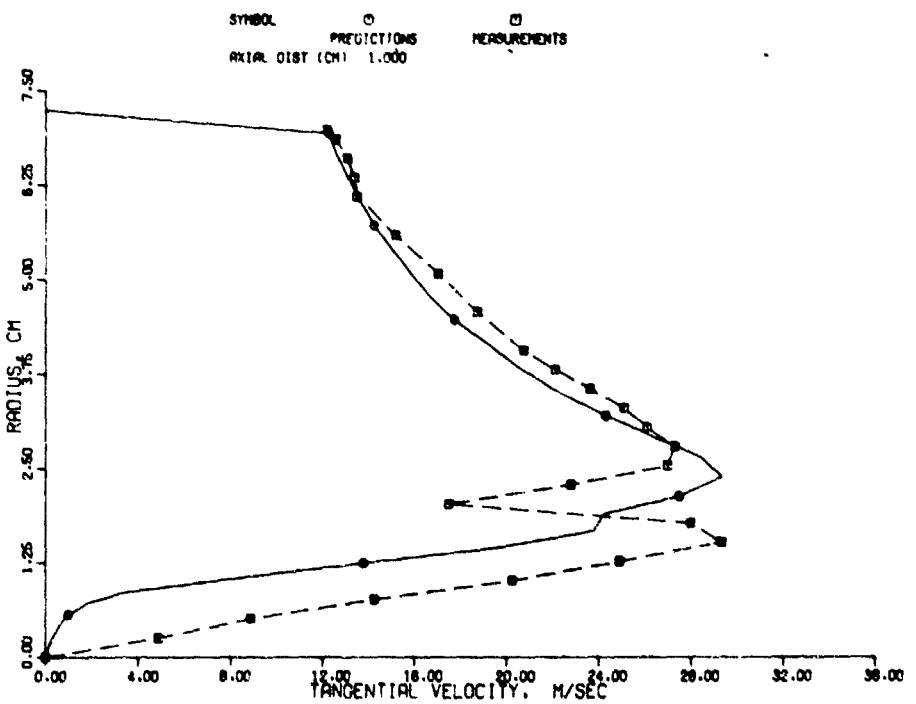

(b)

Figure 47. Modified 2-D Elliptic Program Predictions for Tangential Velocity in Co-Swirl Case; Original K-ϵ Model.

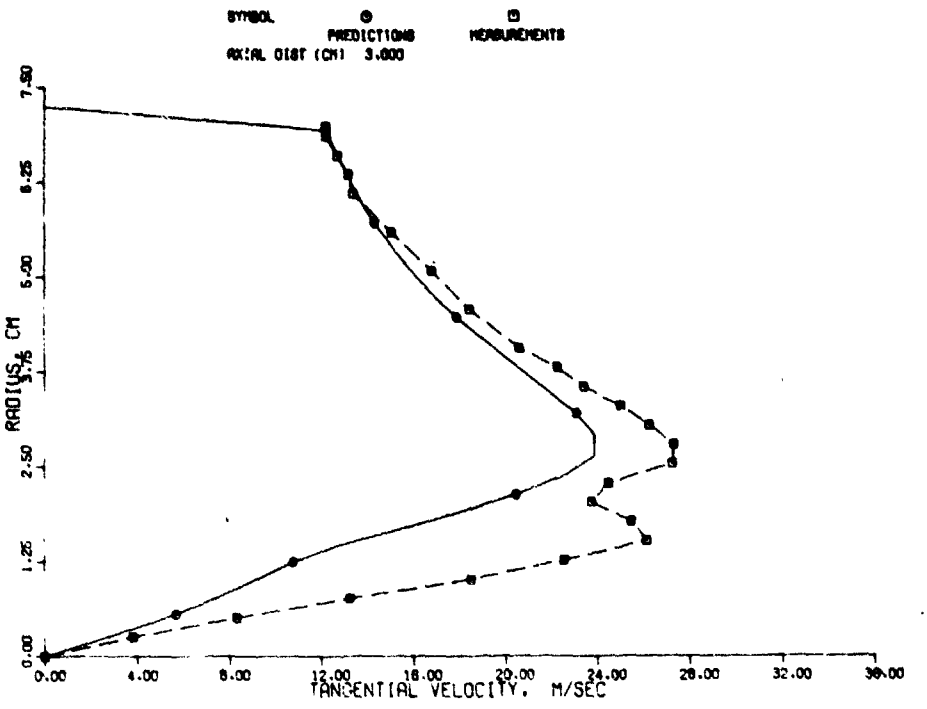

(c)

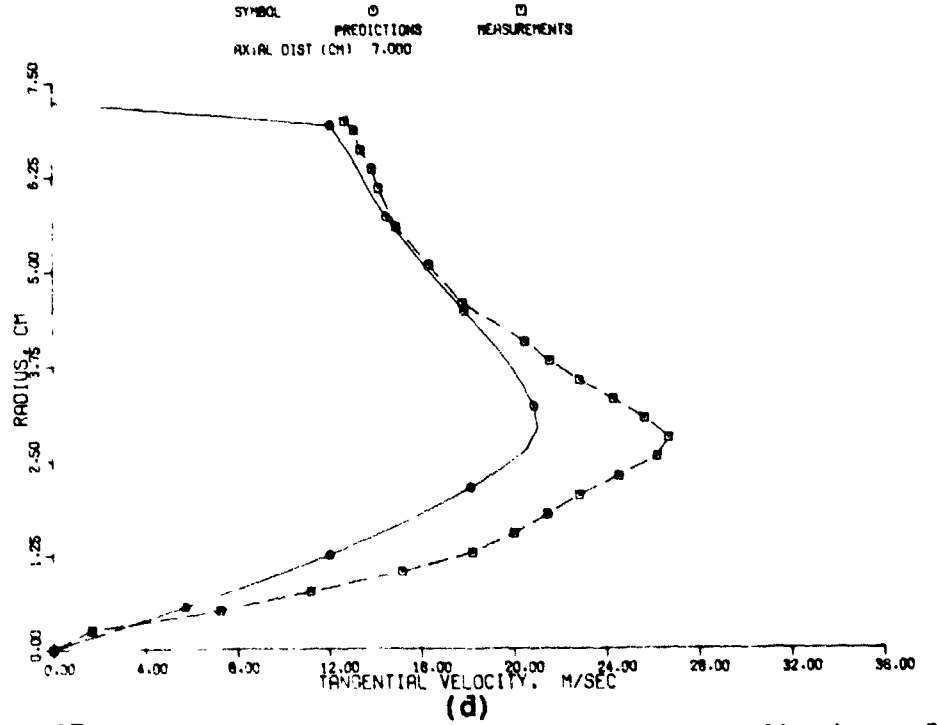

(d)

Figure 47. Modified 2-D Elliptic Program Predictions for Tangential Velocity in Co-Swirl Case; Original K-ε Model (Contd).

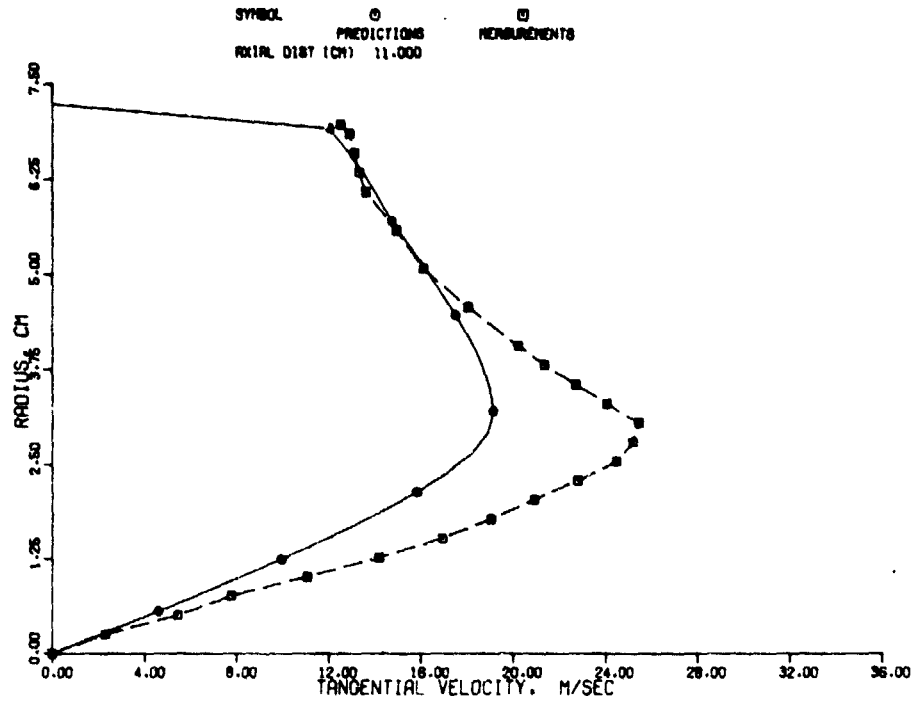

(c)

Figure 47. Modified 2-D Elliptic Program Predictions for Tangential Velocity in Co-Swirl Case; Original K-ϵ Model (Contd).

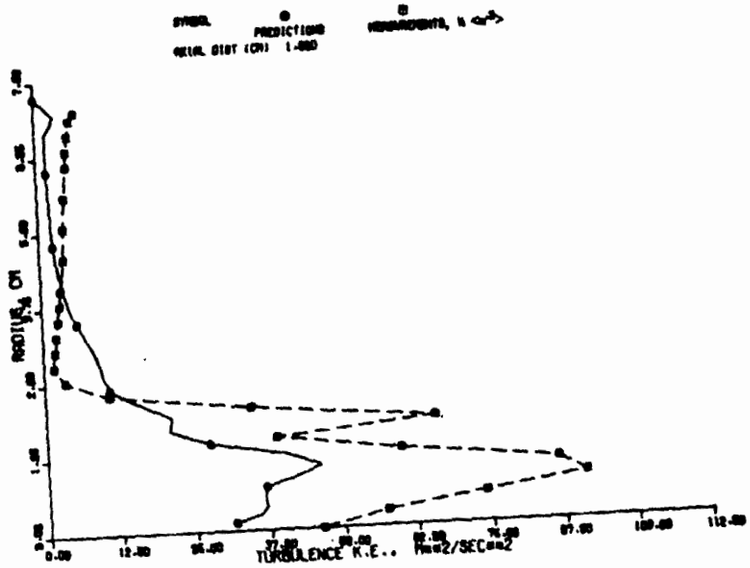

(a)

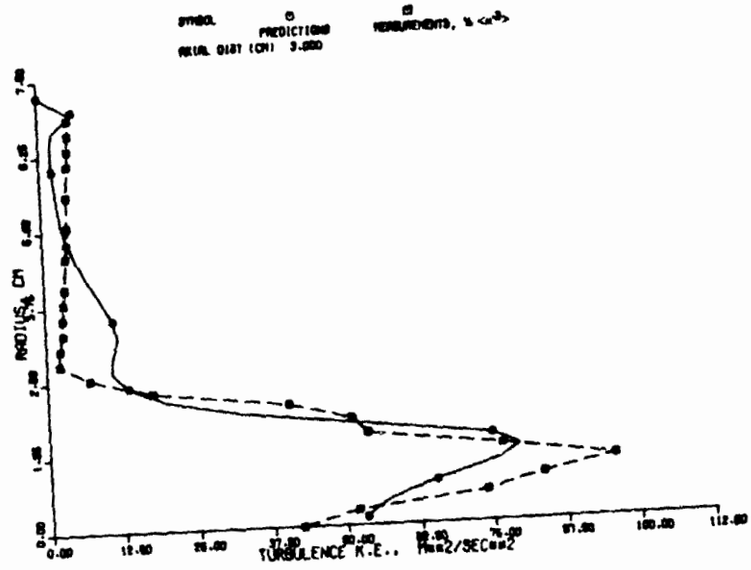

(b)

Figure 48. Modified 2-D Elliptic Program Predictions for Turbulence K.E. in Co-Swirl Case; Original K-ε Model.

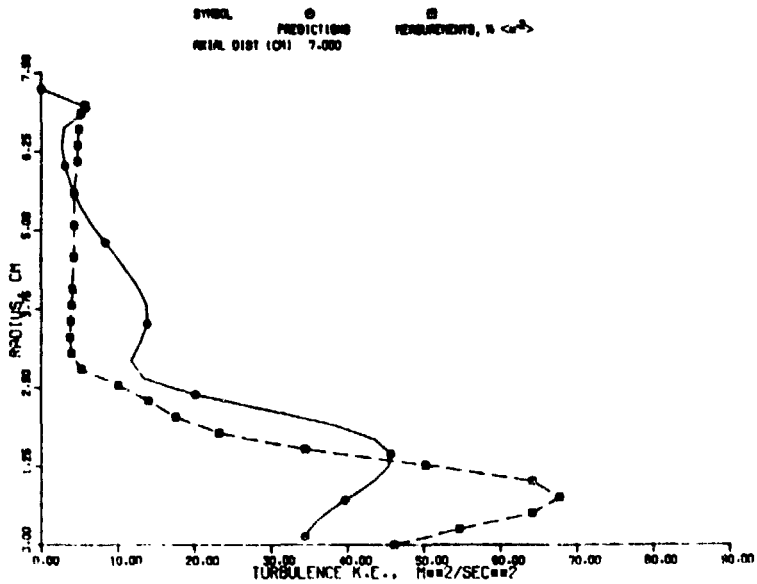

(c)

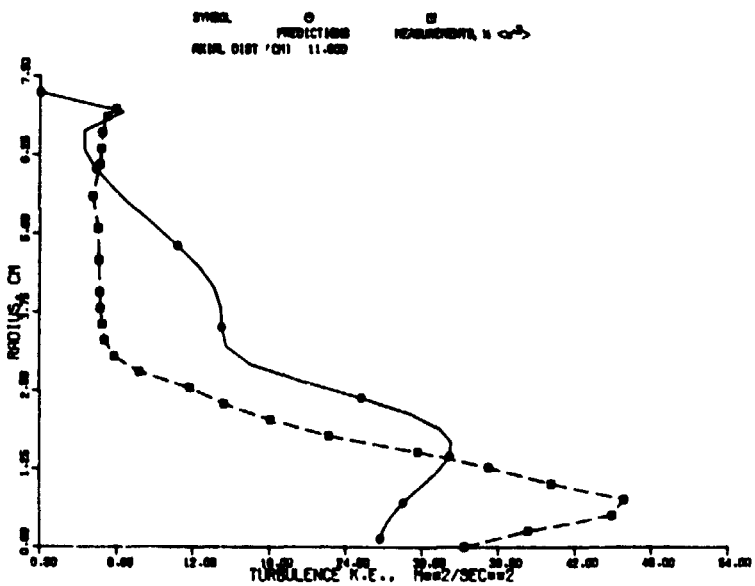

(d)

Figure 48. Modified 2-D Elliptic Program Predictions for Turbulence K.E. in Co-Swirl Case; Original K-ε Model (Contd).

This is partially due to the low inlet turbulence kinetic energy values.

A comparison of the predicted radial velocity profiles in the co-swirl case with the measurements are shown in Figures 49. These results are presented only for the purpose of providing qualitative comparison.

As alluded to earlier in this section, the CAPS results correspond to the potential flow solutions. When these results were employed for the outer stream, the 2-D elliptic predictions were not in very good agreement with the measurements in the outer flow regions. In an effort to get a better comparison with the test data, the outer duct was simulated more accurately in the next series of runs. The injection through the blockage was simulated in such a way that the outer stream had an entrance length of 1.35 inches (3.43 cm). Another objective of this effort was to determine the effect of the outer stream geometry on the interaction between the inner and the outer streams. The predicted results of this simulation with the original k-ϵ model were nearly identical to those shown in Figure 39, implying negligible effect due to the change in the simulated outer flow geometry.

Another series of computations were made for the counter-swirl case employing the modified K-ϵ model and the modified 2-D elliptic program. These computations were made to determine if the conclusions reached earlier with the modular approach were true when the interactive effects between the two streams were taken into account. The value for α_{V_θ} and α_C used in these runs was -0.5. A comparison of these results with those shown in Figure 39 showed that the modified k-ϵ model improved the comparison with the test data inside the recirculation zone. The modified k-ϵ model predictions exhibited trends similar to those reported in Figure 35.

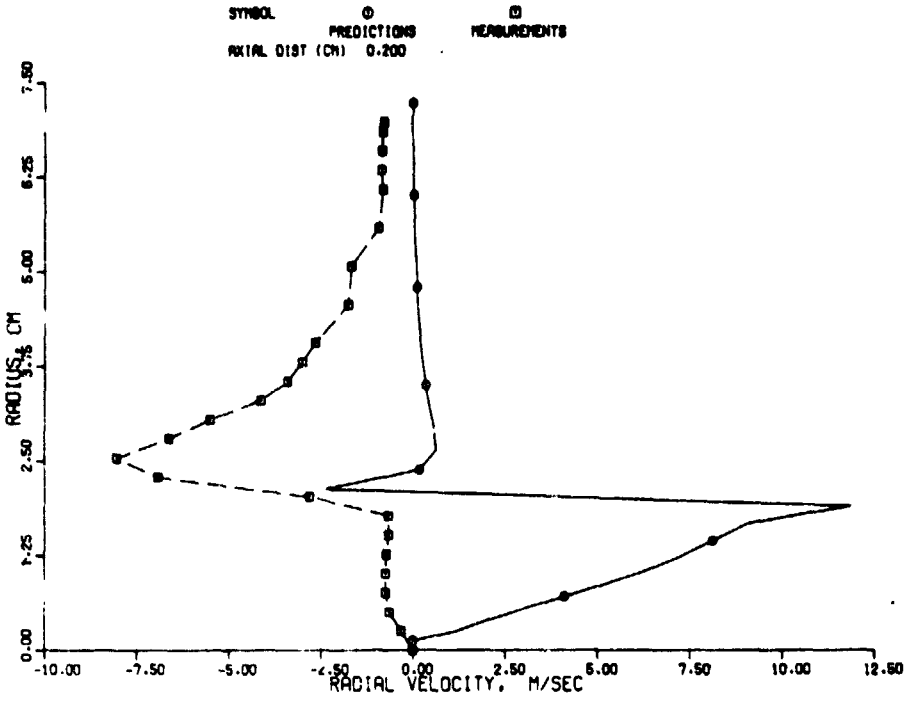

(a)

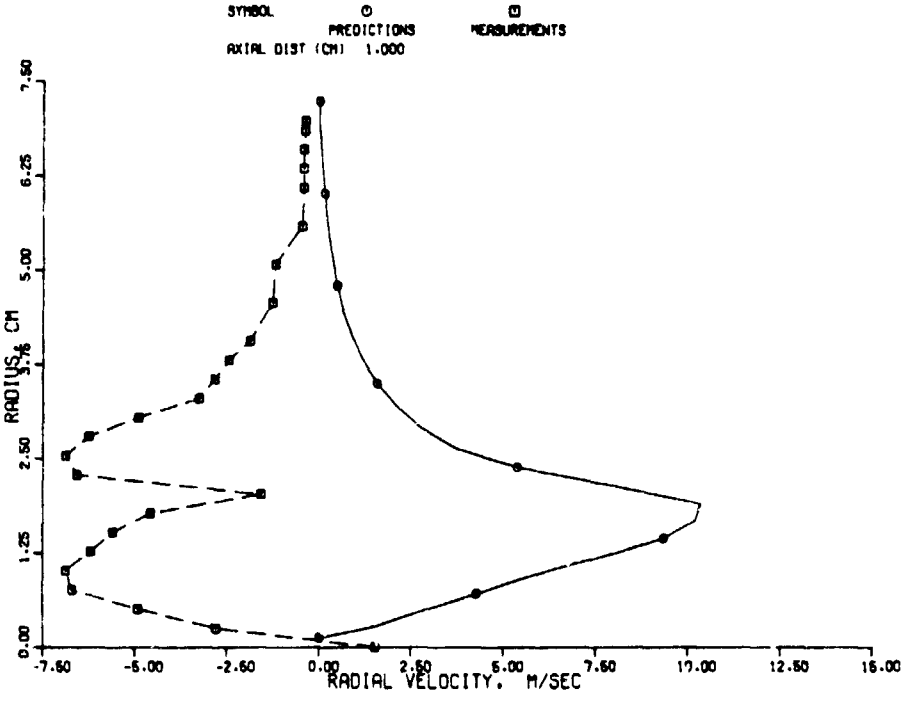

(b)

Figure 49. Modified 2-D Elliptic Program Predictions for Radial Velocity in Co-Swirl Case; Original K-ε Model.

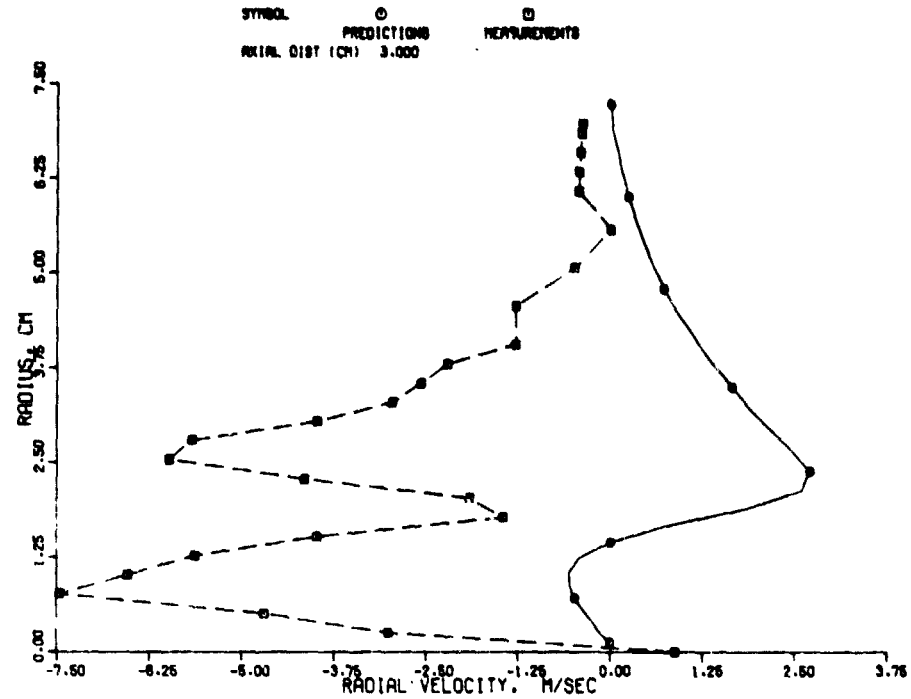

(c)

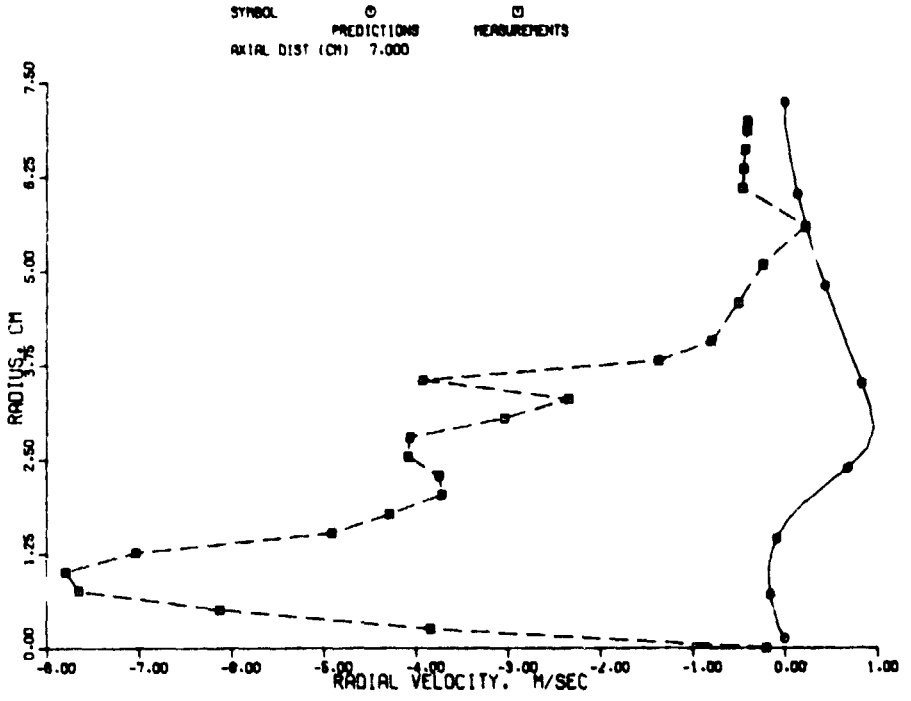

(d)

Figure 49. Modified 2-D Elliptic Program Predictions for Radial Velocity in Co-Swirl Case; Original K-ε Model (Contd).

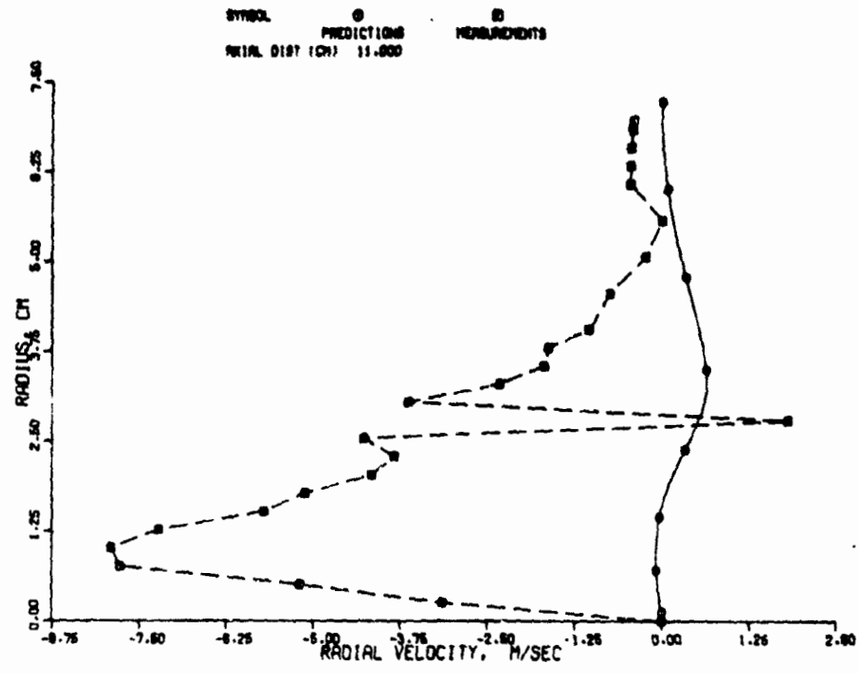

(e)

Figure 49. Modified 2-D Elliptic Program Predictions for Radial Velocity in Co-Swirl Case; Original K-ε Model (Contd).

A comparison of the predicted streamlines in the three tasks for the counterswirl case are shown in Figures 50 through 54. Figure 50 shows the predicted streamlines of Task I, wherein the inlet profiles of the mixing region were estimated from the mass flow rate and the swirler vane angle. These streamline contours do not show any recirculation bubble. However, the slight convex curvature of the streamlines near the centerline shows the effect of radial pressure gradients induced by swirl. Similar streamline isopleths were obtained even when the inlet profiles for the mixing region were obtained from test data. This point is illustrated in Figure 51 for the counterswirl case with the original k-ϵ model. However, when the modified k-ϵ model was used to analyze the flow, a relatively small recirculation bubble was predicted. The iso-streamline contours for the modified k- model predictions are shown in Figure 52. These results were obtained by using inlet profiles from test data and $\alpha_{V_\theta} = -0.75$ and $\alpha_c = -2.0$. The location of the leading edge of the recirculation bubble agrees quite well with the Cornell data. But the trailing edge of the bubble in this prediction is farther downstream than the data.

The predicted streamline contours using the modified 2-D elliptic program are shown in Figures 53 and 54. Figure 53 shows the predicted iso-streamlines from the modified 2-D elliptic program when the original k-ϵ model was employed. This figure shows the location and the size of the predicted recirculation region. The size as well as the location of the leading edge of the recirculation bubble agrees very well with those deduced from the test data. The predicted streamlines using the modified k-ϵ model, with $\alpha_{V\theta} = \alpha_c = -0.5$ are shown in Figure 54. This figure shows a much larger recirculation bubble than those seen in Figure 53. This bubble is larger in all directions than that obtained with the original k-ϵ model, as well as that corresponding to the test data. The geometry of the simulated outer flow duct with an entrance length is also shown in this figure.

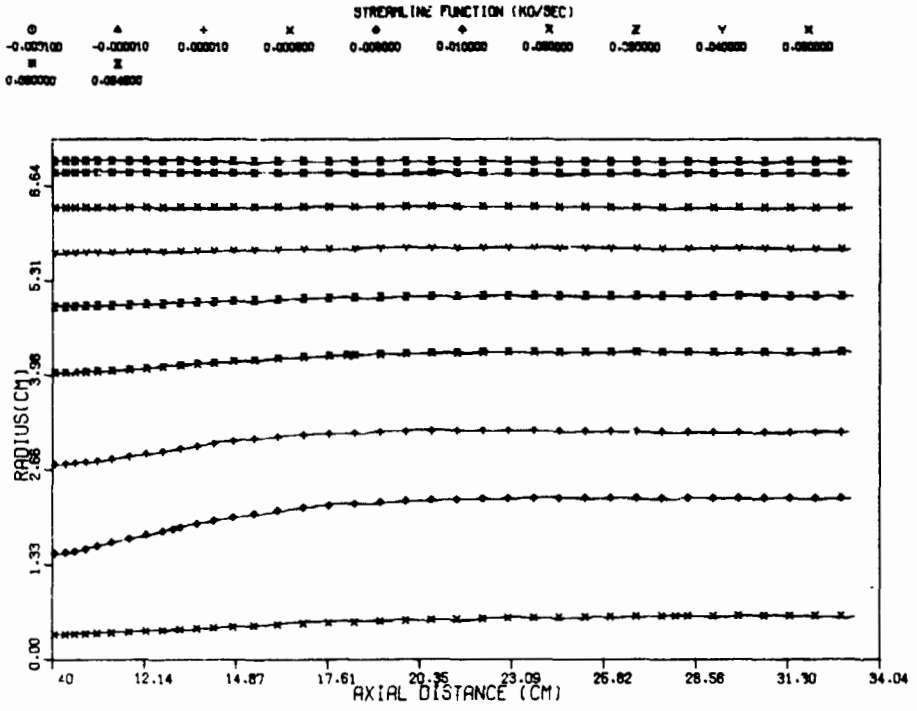

Figure 50. Streamline Contours for Counterswirl Case with Predicted Inlet Profiles; Original K-ϵ Model.

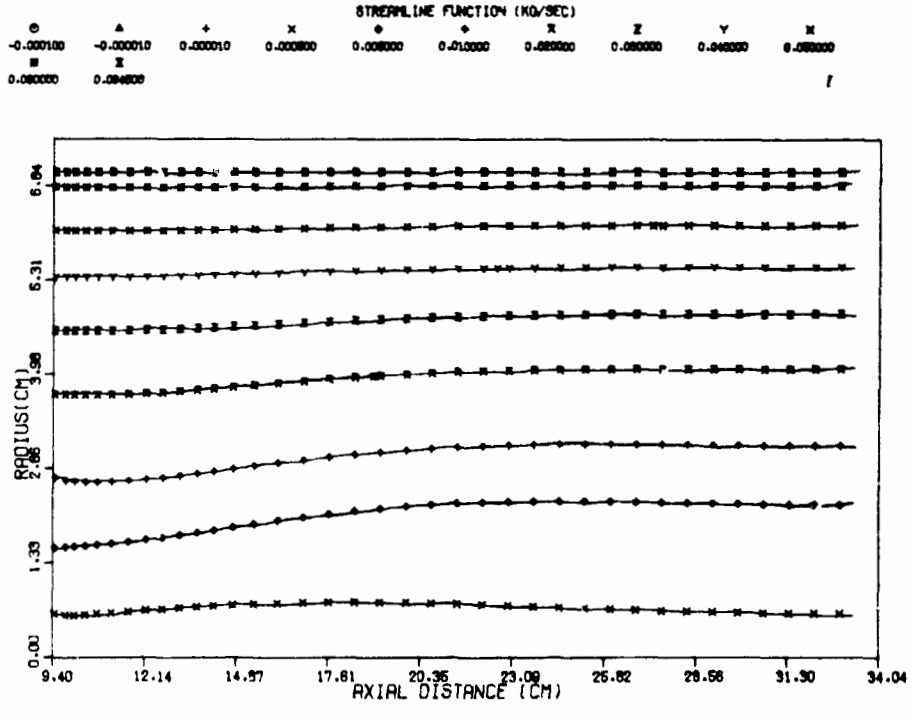

Figure 51. Streamline Contours for Counterswirl Case with Measured Inlet Profiles; Original K-ϵ Model.

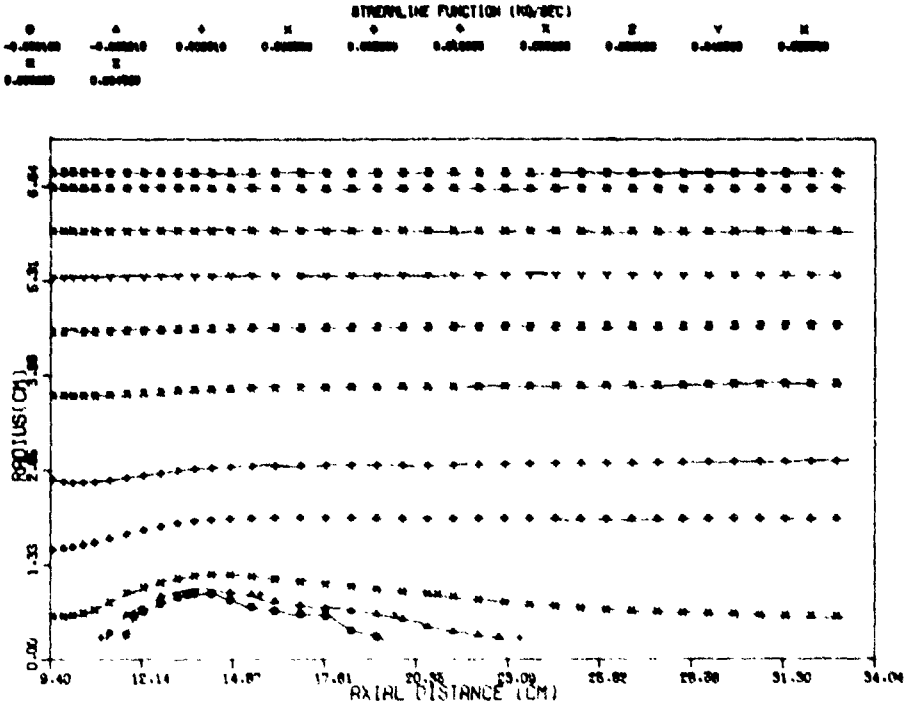

Figure 52. Streamline Contours for Counterswirl Case with Measured Inlet Profiles; Modified K-ε Model, $\alpha_{V_\theta} = -0.75$, $\alpha_C = -2.0$.

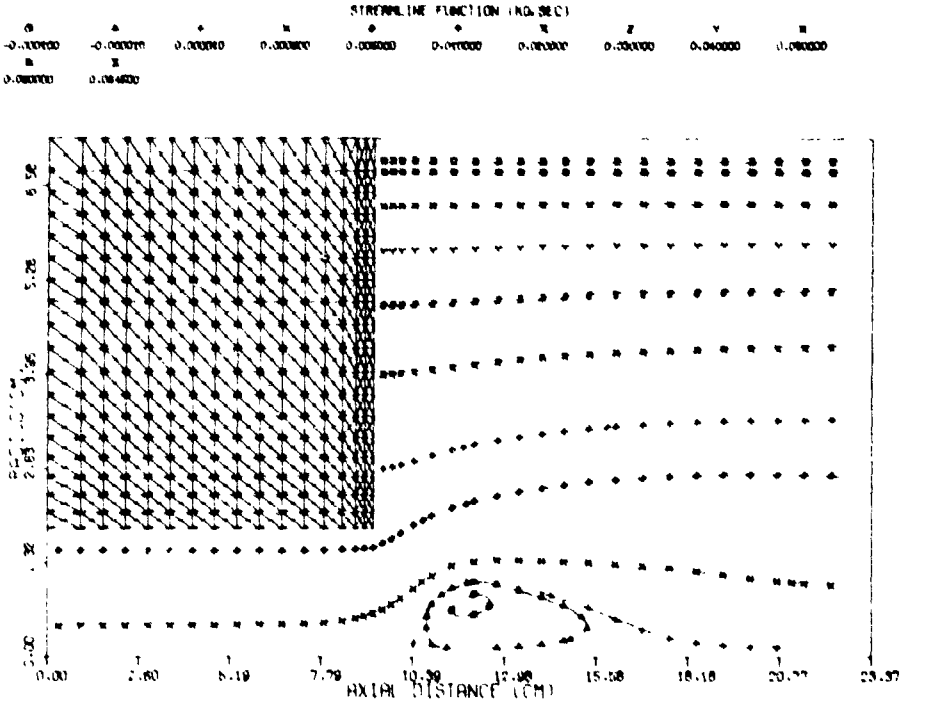

Figure 53. Streamline Contours of the Modified 2-D Elliptic Program Predictions for Counterswirl Case, Original K-ε Model.

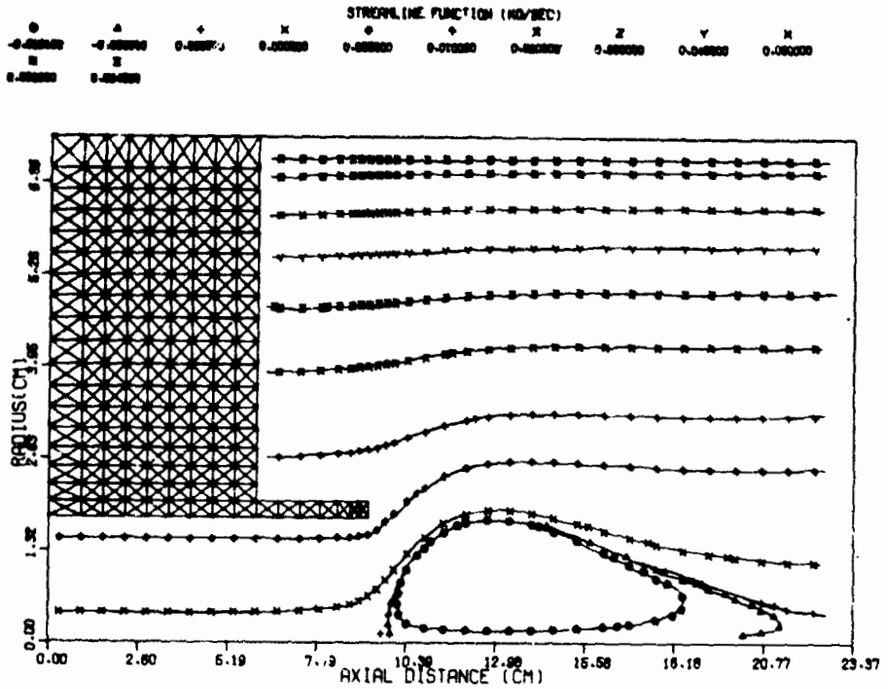

Figure 54. Streamline Contours of the Modified 2-D Elliptic Program Predictions for Counterswirl Case; Modified K-ϵ Model, $\alpha_{V_\theta} = \alpha_C = -0.5$.

The distance between the outer flow injection station, and the lip of the inner tube used in this computation was 1.35 inch (3.43 cm). The streamline contours deduced from the test data are shown in Figure 55 for comparison.

The computations were performed on a CDC Cyber 174 computer. The required average computer processing time on this system was approximately 0.9 seconds per equation for each iteration.

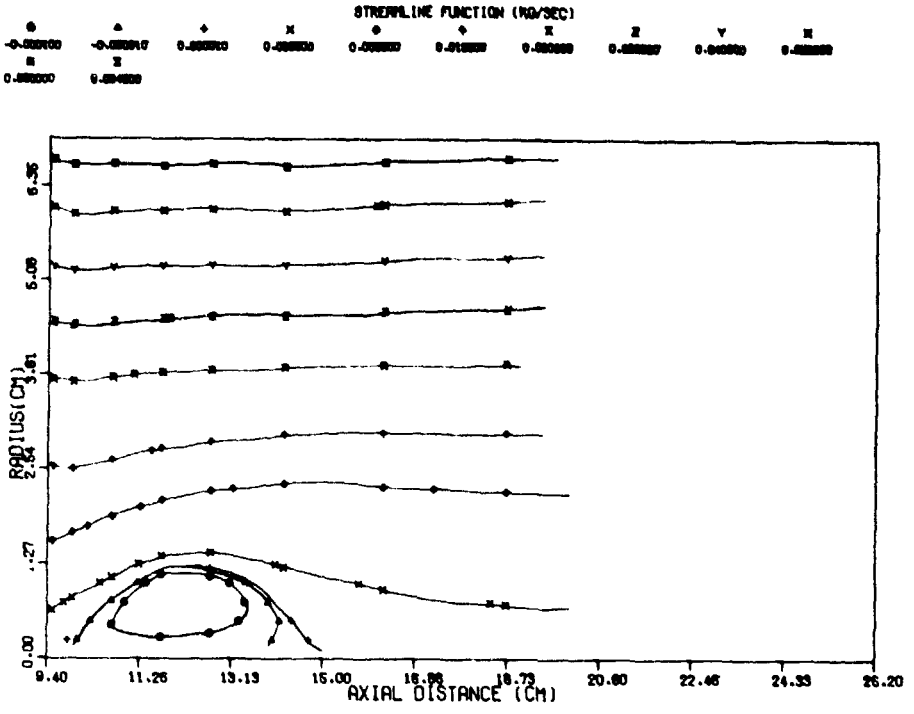

Figure 55. Streamline Contours Corresponding to Gouldin's Test Data.

CONCLUSIONS

- Predictions were obtained for the following tasks:

  Task I - Computations with given geometry of the mixing region, using original K-ϵ model for co- and counter-swirling cases.

  Task II - Computations with prescribed inlet profiles from measurements

  - Original K-ϵ model for co- and counterswirl cases
  - Modified K-ϵ model (Richardson number effects)
    - Improved correlations were obtained for the counterswirl case
    - Co-swirl computations failed to converge.

  Task III - Computations with modified 2-D elliptic program

  - Original K-ϵ model for co- and counterswirl cases.
  - Modified K-ϵ model
    - Counterswirl case, $\alpha_{v_\theta} = \alpha_c = -0.5$
    - Co-swirl computations failed to converge.

- In Task I, the inlet profiles for the mixing region were estimated by neglecting the elliptic effects of the interaction between the two co-axial streams. As a consequence of this, the estimated inlet profiles were incorrect near the axis of the tube and the predictions further downstream did not show any flow reversal.

- In Task II, the inlet profiles for the mixing region were prescribed from the test data. Even for this case, the original K-ϵ model did not predict any recirculation.

- The modified k-ϵ model predicted a recirculation bubble near the axis of the tube in the counterswirl case, when the measured velocity profiles were used as input. The predicted recirculation bubble was elongated in the axial direction. The modified k-ϵ model showed significant improvements over the original k-ϵ model predictions inside the recirculation zone. The modified k-ϵ model failed to converge for the co-swirl case and this highlights the need for further work in this area.

- The modified 2-D elliptic program predictions for the counterswirl case were in agreement with the Cornell data. In the proximity of the recirculation zone, higher intermittency is expected due to an increased turbulence kinetic energy production. In such regions, multiple turbulence scales are needed to accurately predict the flow field. Hence, the k-ϵ model predictions is not expected to be accurate in these regions. However, the k-ϵ model predictions for axial and tangential velocities were in agreement with the data within a maximum value of about 10 percent of the average flow velocity.

- In the co-swirl case, the modified 2-D elliptic program predicted a recirculation bubble, while the measurements did not indicate any flow reversal.

- The 2-D elliptic program is a very useful tool for analyzing swirling and recirculation flows. The predictions are, on the whole, in good qualitative agreement with available data. Additional experimental measurements and analytical work are needed to address the turbulence model deficiencies.

APPENDIX A

REFERENCES

APPENDIX A

REFERENCES

1. Chigier, N.A., and Beer, J.M., "Velocity and Static Pressure Distributions in Swirling Air Jets Issuing from Annular Divergent Nozzles", Journal of Basic Engineering, 86, No. 4, December, 1964, pp. 788-798.

2. Reynolds, R.S., Kuhn, T.E., and Mongia, H.C., "An Advanced Combustor Analytical Design Procedure and its Application in the Design and Development Testing of a Premix/Prevaporized Combustion System," Presented to 1977 Spring Technical Meeting of the Central States Section of the Combustion Institute, March, 1977.

3. Beer, J.M., and Chigier, N.A., Combustion Aerodynamics, Applied Science Publishers, London, 1972.

4. Chigier, N.A., "Gasdynamics of Swirling Flow in Combustion Systems", Astronautica Acta, 17, 1972, pp. 387-395.

5. Syred, N. and Beer, J.M., "Swirl Stabilized Combustion and its Application to Gas Turbine Combustors", ARC Paper No. 34787, Comb. 111, October 1973.

6. Patankar, S.V., and Spalding, D.B., "A Computer Model for Three-Dimensional Flow in Furnaces," 14th Symposium (International) on Combustion, The Combustion Institute, Pittsburgh, 1973, pp. 605-614.

7. Manheimer-Timnat, Y., Segal, A., and Wolfshtein, M., "Swirling Natural Gas Flames in Cylinderical Chambers", Proc. of Combustion Institute European Symposium, (Weinberg, F.J., ed.), Academic Press, London, 1973.

8. Anasoulis, R.F., McDonald, M., and Buggeln, R.C., "Development of Combustor Flow Analysis, Part I: Theoretical Studies", Technical Report, AFAPL-TR-73, 98, Part 1, Air Force Systems Command, Wright-Patterson AFB, Ohio, January, 1974.

9. Lilley, D.G., "Modeling of Combustor Swirl Flows", Acta Astronautica, Vol. 1, 1974, pp. 1129-1147.

10. Lilley, D.G., "Predictions of Inert Turbulent Flows," AIAA Journal, 11, No. 7, July 1973, pp. 955-960.

11. Lilley, D.G., "Turbulent Swirling Flame Predictions", AIAA Journal, 12, No. 2, February 1974, pp. 219-223.

12. Hall, M.G., "Vortex Breakdown", Annual Review of Fluid Mechanics, 4, 1972, pp. 195-218.

13. Leibovich, S., "The Structure of Vortex Breakdown", Annual Review of Fluid Mechanics, 10, 1978, pp. 221-246.

14. Wettendorf, F.L., "A Study of the Effect of Curvature on Fully Developed Turbulent Flow," Proceedings of the Royal Society, Vol. 148, 1935, pp. 565-598.

15. Rayleigh, J.W.S., "On the Dynamics of Revolving Fluids", Proceedings of the Royal Society, Vol. 6A, 1916, pp.148-154.

16. Eskinazi, S., and Yeh, M., "An Investigation on Fully Developed Turbulent Flows in a Curved Channel", Journal of Aerospace Sciences, Vol. 23, No. 1, January, 1956.

17. Margolis, D.P., and Lumley, J.L., "Curved Turbulent Mixing Layer", Physics of Fluids, Vol. 8, No. 10, Oct., 1965, pp. 1775-1785.

18. Bradshaw, P., "Effects of Streamline Curvature on Turbulent Flow," Agardograph 169.

19. Launder, B.E., and Spalding, D.B., Mathematical Models of Turbulence, Academic Press, London, 1972.

20. Launder, B.E., Reece, G.J., and Rodi, W., "Progress in the Development of Reynolds Stress Closure", Journal of Fluid Mechanics, Vol. 68, Part 3, 1975, pp. 537-566.

21. Rubesin, M.W., "Numerical Turbulence Modeling", AGARD Lecture Series No. 86 on Computational Fluid Dynamics, 1977.

22. Owen, J.M., "Flow Between a Rotating and a Stationery Disc", Ph.D. Thesis, 1969, University of Sussex, Sussex, England.

23. Patankar, S.V., and Spalding, D.B., Heat and Mass Transfer in Boundary Layers, Intertext Books, London, 1970.

24. Mongia, H.C., and Reynolds, R.S., "Combustor Design Criteria Validation", Vol. III, USARTL-TR-78-55C, 1978.

25. Patankar, S.V., "Numerical Prediction of Three-Dimensional Flows," Published in "Studies in Convection: Theory, Measurement and Applications", Vol. 1, edited by B.E. Launder, Academic Press, 1975.

26. Vu, B.T., and Gouldin, F.C., "Flow Measurement in a Model Swirl Combustor," AIAA paper No. 80.0076, presented at the AIAA 18th Aerospace Sciences Meeting, Jan. 1980.

27. Hunter, S.C., Johansen, K.M., Mongia, H.C., and Wood, M.P., "Advanced, Small, High Temperature Noise Combustor Program; Vol. 1, Analytical Model Derivation and Combustor-Element Rig Tests (Phase I and II)", AD778766, 1974.

28. de Vahl Davis, G., and Mallinson, G.D., "An Evaluation of Upwind and Central Difference Approximations by a Study of Recirculationg Flow", Computers and Fluids, VA, pp. 29-43, 1976.

29. Anonymous, "Proceedings of the Third AIAA Computational Fluid Dynamics Conference," Albuquerque, New Mexico, June 27-28, 1977.

30. Militzer, J., Nicoll, W.B., and Alpay, S.A., "Some Observations on the Numerical Calculation of the Recirculation Region of Twin Parallel Symmetric Jet Flow", Symposium on Turbulent Shear Flows, University Park, Pennsylvania, April 18-20, 1977.

31. Militzer, J., "Dual Plane Parallel Turbulent Jets: The Measurement and Prediction of the Mean Velocity Field", Ph.D. Thesis, University of Waterloo, 1977.

32. Raithby, G.D., "Skew Upstream Differencing Schemes for Problems Involving Fluid Flow", Computer Methods in Applied Mechanics and Engineering, Vol. 5, 1976, pp. 151-162.

33. Launder, B.E., "Turbulence Models and their Experimental Verifications, 2 Two-Equation Turbulence Models - I", Imperial College Report HTS/73/17, April 1973.

34. Kim, H.T., Kline, S.J., and Reynolds, W.C., Journal of Fluid Mechanics, Vol. 50, 1971, pp.133.

35. Yeh, H., "Boundary Layer Along Annular Walls in a Swirling Flow", Transactions of the ASME, Vol. 80, May 1958, pp. 767-776.

APPENDIX B
SYMBOLS AND ABBREVIATIONS

APPENDIX B
LIST OF SYMBOLS AND ABBREVIATIONS

C_1, C_2, C_D	Constants in the k-ϵ turbulence model
$C_{2_{V_\theta}}$	Empirical constant in Morse's model
G_K	Turbulence generation term, Eq. (6)
K	Turbulence kinetic energy
ℓ	Characteristic length scale of turbulence
p	Static pressure
r	Radial coordinate
R	Radius of curvature of streamline, Eq. (20)
Ri_c	Curvature Richardson number, Eq. (26)
Ri_{V_θ}	Swirl Richardson number, Eq. (24)
$S\phi$	Source term for the variable
$<u'^2>$	Axial component of turbulence kinetic energy
u	Axial velocity component
v	Radial velocity component
V_θ	Tangential velocity component
X	Axial coordinate
$\alpha_{V_\theta}, \alpha_c$	Empirical constants in the modified k-ϵ model
$\Gamma_{eff,\phi}$	Exchange coefficient for the variable, ϕ, Eq. (10)
ϵ	Turbulence dissipation rate
κ	Von Karman constant, 0.41
μ	Dynamic viscosity
μ_t	Turbulence (Eddy) viscosity
μ_{eff}	Effective viscosity
ρ	Density
$\sigma_{eff,\phi}$	Effective Prandtl, Schmidt number for the variable ϕ